Old Dominion University Research Foundation

DEPARTMENT OF ELECTRICAL & COMPUTER ENGINEERING
DEPARTMENT OF MECHANICAL ENGINEERING & MECHANICS
COLLEGE OF ENGINEERING & TECHNOLOGY
OLD DOMINION UNIVERSITY
NORFOLK, VIRGINIA 23529

NEW DEVICES FOR FLOW MEASUREMENTS: HOT FILM AND BURIAL WIRE SENSORS, INFRARED IMAGERY, LIQUID CRYSTAL, AND PIEZO-ELECTRIC MODEL

By

Griffith J. McRee Jr., Principal Investigator

A. Sidney Roberts Jr., Co-Principal Investigator

Final Report
For the period ended May 15, 1990

Prepared for
National Aeronautics and Space Administration
Langley Research Center
Hampton, Virginia 23665

Under
Research Grant NAG-1-735
Debra L. Carraway, Technical Monitor
IRD-Acoustics & Vibration Instrumentation Section

February 1991

Old Dominion University Research Foundation is a not-for-profit corporation closely affiliated with Old Dominion University and serves as the University's fiscal and administrative agent for sponsored programs.

Any questions or comments concerning the material contained in this report should be addressed to:

Executive Director
Old Dominion University Research Foundation
P. O. Box 6369
Norfolk, Virginia 23508-0369

Telephone: (804) 683-4293
Fax Number: (804) 683-5290

DEPARTMENT OF ELECTRICAL & COMPUTER ENGINEERING
DEPARTMENT OF MECHANICAL ENGINEERING & MECHANICS
COLLEGE OF ENGINEERING & TECHNOLOGY
OLD DOMINION UNIVERSITY
NORFOLK, VIRGINIA 23529

NEW DEVICES FOR FLOW MEASUREMENTS: HOT FILM AND BURIAL WIRE SENSORS, INFRARED IMAGERY, LIQUID CRYSTAL, AND PIEZO-ELECTRIC MODEL

By

Griffith J. McRee Jr., Principal Investigator

A. Sidney Roberts Jr., Co-Principal Investigator

Final Report
For the period ended May 15, 1990

Prepared for
National Aeronautics and Space Administration
Langley Research Center
Hampton, Virginia 23665

Under
Research Grant NAG-1-735
Debra L. Carraway, Technical Monitor
IRD-Acoustics & Vibration Instrumentation Section

Submitted by the
Old Dominion University Research Foundation
P.O. Box 6369
Norfolk, Virginia 23508-0369

February 1991

FINAL REPORT

NASA CONTRACT NAG-1-735

By
Griffith J. McRee, Jr. and A. Sidney Roberts, Jr.
Co-Principal Investigators

Experimental methods and computer simulations were used to develop diagnostic techniques in relation to heat transfer and boundary layer flows over aerodynamic surfaces employing hot-film sensors and infrared thermography. Reference is made to the several published and presented papers reporting the results of the research. Four graduate theses also document the details of the research discussed in the subject areas summarized below.

SPATIAL CHARACTERISTICS OF AN ARRAYED HOT-FILM SENSOR

Graduate student Mike Wusk, having the lead responsibility, analyzed the results of experiments which were completed in the Fall/Winter, 1988. Using a wing model mounted in the IRD small wind tunnel facility, the hot-film array was shown capable of detecting spanwise variations in a boundary layer flowfield. By employing small beads to trip the laminar boundary layer, spanwise vortical disturbances were induced, and the surface sensors were able to resolve the flow regime differences to within a 1.5 millimeter spacing. A full report of these results was compiled for a presented paper AIAA-88-4677-CP, and a complete description of the work was submitted as a masters thesis at Old Dominion University dated December, 1988. A copy of the AIAA paper is included in the Appendix.

TRANSIENT RESPONSE OF THE HOT-FILM SENSOR

Shock tube experiments were performed in order to determine the response of a single

sensor to transiently induced flow behind a normal shock wave. The 0.15 meter diameter shock tube facility at the Instrument Research Division of NASA LaRC was employed for this purpose, using ODU and NASA instrumentation. Graduate student Kelly Ortegies had the responsibility of interpreting the resulting transient heat transfer information. The experiments attempted to isolate the response as that due only to the change in convective heat transfer at the hot-film element, which was mounted on the side wall of the shock tube. Results showed an initial sensor response during shock front transit where the convective heat transfer is reduced due apparently to the abrupt rise in gas temperature just behind the shock front. Correlation of the data, within one millisecond after the gas (air) is set in motion over the sensor, with transient boundary layer theory suggests that there is a turbulent boundary layer development over the sensor. These results have been used to formulate a time-dependent heat transfer coefficient to be used as a forcing formation for the generalized hot-film instrument model simulator. A complete report of these results is found in the masters thesis of Mr. Ortgies dated May, 1989. A summary of essential results was published in ASME FED Vol. 92, and a copy of the paper is enclosed in the Appendix.

FLOWFIELD CHARACTERIZATION USING INFRARED SURFACE TEMPERATURE MEASUREMENTS

An extensive series of experiments was completed in the ODU low-speed wind tunnel where IR thermography was used to study flow separation over a NACA-0012 airfoil. A unique method was devised to simultaneously observe in the IR spectrum tufts motion and the clean surface temperature field as the angle of attack was varied from 0° to 14°. The experiments showed separation to occur at $\alpha=6°$ ($\alpha=7°$ accounting for wall proximity) compared with $\alpha=10°$ predicted by the Eppler code, an unviscid and viscous solver, for flows about airfoils.

As an additional area of interest the flat plate (α=0°) substrate diffusion, laminar boundary layer model was implemented by finite difference calculations. The model results agreed reasonably well with the thermal boundary layer experimental data which had been obtained earlier with the IR thermography technique.

The work to develop the IR flow field diagnostics has been well documented. A list of published papers is given below. A sampling of the papers is included in the Appendix, including AIAA-88-2523-CP relating to the laminar jet and laminar flat plate experiments. Also included is the paper, "Twenty-five Years of Aerodynamic Research with IR Imaging - A Survey," an invited paper to be presented at the April 1991, SPIE meeting in Orlando, Florida (The International Society of Optical Engineering). Dr. Ehud Gartenberg, who had responsible charge for this segment of the research, thoroughly documented the work in a doctoral dissertation which was accepted by the faculty of Old Dominion University, April, 1989.

MODELING OF HOT-FILM SENSORS WITH SUBSTRATE EFFECTS

A detailed mathematical model designed to investigate the frequency response of a hot-film anemometer system was constructed by David Judge, a Masters Degree candidate. Since several diverse factors affect the frequency response, the analysis was broken down into three main parts. Each part was represented by a detailed model. The first model consisted of the ordinary differential equations which model the electronics of the feedback system and heat transfer sensor. An important simplification in this model is that the rate of heat conduction from the sensor to its substrate is constant.

In the second model the unsteady state heat transfer properties of the substrate were examined by numerically solving the appropriate partial differential equation. A two pole equivalent circuit was constructed from the results of the second model. A third model resulted

from merging the first part with the equivalent circuit. In this model the rate of heat conduction from sensor to substrate was not assumed to be constant.

Three principle conclusions were drawn from this work. First, the frequency response of the fifth order sensor-electronic model can be adequately represented by a second order system. Using the system parameters of the particular system which was being used by Langley Research Center and studied under this contract, the natural frequency discovered as being appropriate was 10.3 KHz. The appropriate damping coefficient was found to be 0.065. The values for this frequency and damping coefficient will vary with the particular anemometry system being used. Non-linear effects were found to be negligible.

Second, the frequency response of the rate of heat conduction through the hot film substrate can be modeled by a second order system with cut-off frequencies at 1 and 100 Hz. Again these frequencies are a function of the particular system being used. In this case the substrate consisted of kapton tape over insulating foam.

Third, the effect of variable rate of heat conduction is insignificant for the substrate materials of the experimental model used here for frequencies down to 10 Hz. The substrate materials of this model were thermally insulating to a large degree. Models with a more thermally conductive substrate would demonstrate these effects at higher frequencies.

The results of this work are thoroughly described in Mr. Judge's thesis, "MODEL OF HOT-FILM SENSOR WITH SUBSTRATE EFFECTS", approved by the faculty of Old Dominion University. Much of the work also was described in a paper, "Model of Hot-Film Sensor with Substrate" presented at the International Congress on Instrumentation in Aerospace Simulation Facilities, June, 1987.

REFERENCES

Roberts, A. S., Jr., K. R. Ortgies, E. Gartenberg and D. L. Carraway, "Convective Response of a Wall-Mounted Hot-Film Sensor in a Shock Tube," Proc. of the International Symposium on Non-Steady Fluid Dynamics, ASME FED Vol. 92, Toronto, Canada, June 4-7, 1990, pp. 253-258.

Gartenberg, E. and A. S. Roberts, Jr., "Influence of Temperature Gradients on the Measurement Accuracy of IR Imaging Systems," Proc. SPIE Thermosense XII: An International Conference on Thermal Sensing and Imaging Diagnostic Applications, Orlando, Florida, April 18-020, 1990, pp. 218-224.

Gartenberg, E., A. S. Roberts, Jr. and Griffith J. McRee, Jr., "Infrared Imaging and Tufts Studies of Boundary Layer Flow Regimes on a NACA 0012 Airfoil," Proc. of the 13th International Congress on Instrumentation in Aerospace Facilities, Research Center Gottingen, West Germany, Sept. 18-21, 1989, pp. 168-178.

Gartenberg, E., A. S. Roberts, Jr., and Griffith J. McRee, Jr., "Aerodynamic Investigation by Infrared Imaging," Proc. of AIAA 6th Applied Aerodynamics Conference, Williamsburg, VA, June 6-8, 1988, pp. 121-128.

Gartenberg, E., A. S. Roberts, Jr., and V. Selby, "Infrared Surface Imaging as a Flowfield Diagnostic Tool," Proc. of the 12th International Congress on Instrumentation in Aerospace Simulation Facilities, The College of William and Mary, Williamsburg, VA, USA, June 22-25, 1987, pp. 343-349.

Gartenberg, E. and A. S. Roberts, Jr., "Phenomenological Aspects of Infrared Imaging in Aeronautical Research," Paper No. AIAA-88-4674, Conference on Sensors and Measurements, Atlanta, GA, Sept. 7-9, 1988.

McRee, Griffith J. Jr., and Judge, David M., "Model of Hot-Film Sensor with Substrate," Proc. of the 12th International Congress on Instrumentation in Aerospace Simulation Facilities, The College of William and Mary, Williamsburg, VA, USA, June 22-25, 1987, pp. 350-355.

Reprinted from PROCEEDINGS OF THE ICIASF RECORD — INTERNATIONAL CONGRESS ON INSTRUMENTATION IN AEROSPACE SIMULATION FACILITIES, Williamsburg, Va., June 22-25, 1987

MODEL OF HOT-FILM SENSOR WITH SUBSTRATE

Griffith J. McRee and David M. Judge

Old Dominion University

A detailed model is constructed to investigate parameters influencing a hot-film anemometer system used to study cross-flow phenomena on swept wings. This anemometer is designed to detect vortices set up by cross-flow. The nature of the vortices is not well known and a well-verified instrumentation model is essential to allow accurate interpretation of experimental results.

A vital element of the model is the equation which governs the energy balance at the sensor element. This equation accommodates energy flow to the adjacent gas, to the mass of the sensor film, and to the film substrate. Previous investigators have indicated that heat conduction to the film's substrate is significant. Two variations on the inclusion of substrate effects are discussed. In the first model the substrate is assumed to have a constant temperature throughout; in the second, more elaborate models, the temperature of the substrate is allowed to vary. The variation of substrate temperature is related to the convective heat removal at the substrate/gas interface.

I. INTRODUCTION

A. MOTIVATION

Hot-film anemometers are used experimentally for many purposes. These include detecting flow transition and measuring skin friction [1],[2]. The work discussed here was part of the development of a hot-film anemometer designed to detect and measure the characteristics of vortex phenomena associated with cross-flow on a swept wing. In order to accurately interpret the sensor information an effort has been made to develop a detailed mathematical model and numerical simulation of the anemometer. A primary motivation for conducting this analysis was to ascertain the frequency response of the sensor. Though so motivated these results are not limited to cross-flow vortex detection but relate to a large class of experimental situations. Constant temperature hot-film anemometers all work on the same basic principal. A moving fluid cools the electrically heated hot-film sensor. The slight drop in temperature of the film causes a drop in electrical resistance of the film. A wheatstone bridge detection and voltage difference amplification system respond by supplying more power to the film so as to return it to the target temperature. The voltage at the top of the bridge, the output of the instrument, then becomes an indication of the fluid velocity [3].

The frequency response of the sensor is a function of the dynamics of the feedback system, cable impedance and thermal inertia of the sensor. These effects have been modelled by many investigators. It is known that for a properly tuned system operating well below filter cut-off frequency, nonlinear effects are negligible [4]; however, there is one other effect that is not so easily modelled and can be significant at low frequencies. This effect is the variable rate of heat conduction from the sensor to its substrate [5].

The same fluid which cools the film itself also cools the surrounding substrate material, thus the rate of heat conduction from the film to its substrate will depend on the thermal inertia of the substrate materials and their geometry. Investigators have developed one-dimensional substrate flow approximations but suggest the solution of a 3-D model would give a much more accurate result [6].

B. OVERVIEW OF MODELS

For this paper two models were constructed. The first is a digital computer simulation of a hot-film sensor with a constant rate of heat conduction to the substrate. The model also includes cable and trim impedances and feedback with a low pass filter. The differential equations were solved using the ACSL software package [7]. The second model computes heat storage and flow in the substrate. It is a finite difference solution of the 3-D unsteady state heat flow problem. It includes the effects of having two materials layered under the sensor. In addition to indicating steady state conditions, the model will allow the analysis of transients such as system warm-up. In subsequent work these two models will be tied together.

The experimental system modeled is shown in Fig. 1. It consists of two rows of very thin (2000A) closely spaced nickel sensors at a 40°C

CH2449-7/87/0000-0350 $1.00

overheat controlled by a Dantec flow analyzer. To avoid thermal interference adjacent sensors are never heated simultaneously. The voltage output from the top of the wheatstone bridge within the analyzer is viewed on an oscilloscope (and recorded on other equipment). The sensor substrate consists of several different materials. Immediately beneath the nickle sensor is a strip of kapton tape and beneath that a layer of 3-M double backed tape. The 3-M tape adheres to the airplane wing model itself. The wing model consists of a hard resin coating, a layer of fiberglass and a core of highly insulating foam. Gold leads connect each sensor to wires which run inside the model and out of the other side to a coaxial cable connected to the analyzer.

The actual numerical solution of the three-dimensional unsteady state heat transport within the substrate was solved assuming two distinct materials. These were the kapton tape (material nearest the surface) and the insulating foam (greatest volume of material). The thermal properties of both the kapton and 3-M tapes were similar. The thermal properties of the resin and fiberglass could not be obtained with certainty, but the conductivity of both should be greater than that of any of the other materials.

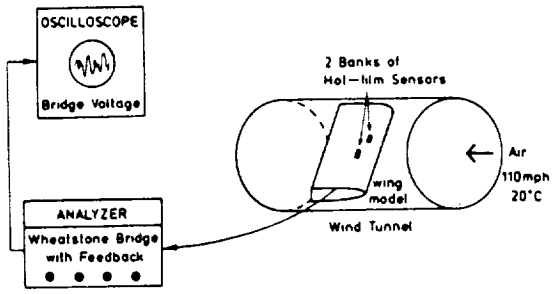

FIG. 1. EXPERIMENTAL SYSTEM

C. BACKGROUND

Cross-flow vortices have been observed for some time as a swept-wing phenomenon. If they are determined to be reliable predictors of flow transition, the ability to detect them will be very advantageous. Ginoux has determined that cross-flow vortices do penetrate the boundary layer. He also has obtained very large heat transfer rates locally, some even greater than that of mean free stream turbulence [8]. Thus it was decided that a reasonable forcing function for the sensor would be a sinusoidal variation of the convective heat transfer coefficient oscillating between the laminar and turbulent values of the free stream velocity.

The frequency response of hot-film anemometers has been investigated by many authors. Fremouth concluded that for a properly tuned cylindrical hot-film sensor non-linear effects are restricted to velocity fluctuations larger than 14% of the mean velocity in a frequency, range greater than 15% of the cut-off frequency of the anemometer. Fremouth's criteria do not apply directly to the model here because his work was for a cylindrical hot-film sensor and this is a flat thin film. A better frequency response is to be expected from a non-cylindrical film [4].

The distortion mentioned above by Fremouth does not include that from a variable rate of heat conduction to the substrate. This effect was first mentioned by Bellhouse and Schultz [5]. Experimentally they detected reduced dynamic sensitivity at low frequencies and attributed that to the thermal inertia of the substrate and heat conduction to areas not covered by the sensor. They constructed a one-dimensinonal heat transfer model to explain the observed attenuation. This model was extended by Fremouth to allow for attenuation greater than 0.5 which had been experimentally observed. Fremouth pointed out that he used only one dimension to maintain simplicity, and that the final step would be to compute the three-dimensional solution for an actual probe [6].

II. MODEL DESCRIPTIONS

A. LIST OF VARIABLES AND PARAMETERS

sensor surface area, As ($1.97\times10^{-3}cm^2$)
cable capacitance, Cc (508pf)
sensor heat capacity, C_p (4.56j/kgK)
lowpass filter cutoff frequency, fc (120kHz)
amplifier gain, G
convective heat transfer coeffcient, h
bridge inductor, L3 (1.27uh)
cable inductance, Lc (1.27uh)
rate of heat conduction from sensor to substrate, $\dot{Q}s$
bridge resistors, R1(50Ω),R2(500Ω),R3(Ω)
sensor reference resistance, Ro (8.422Ω)
sensor resistance, Rs(Ω)
ambient temperature, Ta (20^oC)
sensor reference temperature, To (21.1^oC)
sensor temperature, Ts
bridge output voltage, V
bridge offset voltage, Vo (0.6v)
sensor voltage, Vs
sensor volume, v ($3.94\times10^{-8}cm^3$)
sensor resistance/temperature coefficient, α($0.025\Omega/^oC$)
sensor density, ρ ($8.91\times10^{-3}Kg/cm^3$)

B. THE SENSOR AND ELECTRONIC MODEL

The first of the two models described in this paper is sketched in Fig. 2. It consists of the sensor resistance, cable impedance, wheatstone bridge and feedback loop. The feedback loop begins with a nonlinear voltage difference operator. The voltage difference is filtered with a first order lowpass filter. The filtered signal is then amplified and offset. The voltage V is the system output. The sensor resistance, Rs, is temperature dependent. The system input, a sinusoidaly varying heat transfer coefficient, causes Rs to vary all parameter values are set to approximate the actual experimental setup. On the actual instrument the amplifier gain G can be set to anyone of eleven different values. Setting three is used most often in our work so its values were used in the model. The gain rolls off with

frequency to increase the stability margin. The gain roll off is 10db/dec beyond 50Hz and is tabulated in Table I for the frequencies tested.

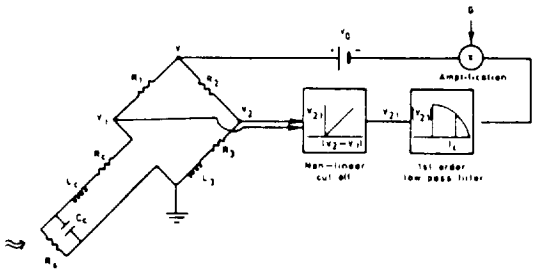

FIG. 2. SENSOR AND ELECTRONIC MODEL

FREQUENCY (H_z)	GAIN (G)
0-52	26,000
100	18,836
1,000	5,957
10,000	1,884
100,000	600

TABLE I

AMPLIFIER GAIN VS. FREQUENCY

Of key importance is the nonlinear relationship between the sensor resistance, voltage and heat transfer to the surroundings. This relationship is derived with a simple power balance. The electrical power to the sensor must either be dissipated by heat convection to the air, heat conduction to the substrate or be accumulated in the sensor as a temperature rise. Radiative power loss was calculated to be a very small fraction of the other energy terms and so was neglected. The power balance yields

$$\frac{V_s^2}{R_s} = \dot{Q}_s + hA_s(T_s - T_A) + \nu\rho c_p \frac{dT_s}{dt} \qquad (1)$$

The first order relationship between sensor temperature and resistance is shown in (2). The coefficient values used are those of an actual sensor. Substitution of (2) into (1) gives (3), a form that can be incorporated into the solution of the circuit equations.

$$R_S = I_O + \alpha(T_s - T_O) \quad (2a) \qquad dT_s/dt = 1/\alpha\, dR_s/dt \quad (2b)$$

In (3), Qs, the rate of heat conduction from sensor to substrate, is a constant. After the two models are tied together it will be a variable. In this model Qs is the heat transfer rate after a sensor warmup time of 10 seconds. This value is computed in the substrate model.

$$\frac{dR_s}{dt} = \left[\frac{V_s^2}{R_s} - hAs\left(\frac{R_s}{\alpha} - \frac{R_o}{\alpha} + T_O - T_A\right) - \dot{Q}_s\right]\left[\frac{\alpha}{\nu\rho c_p}\right] \qquad (3)$$

The system forcing function is the convective heat transfer coefficient h, shown in (4). By varying ω in (4) the response of the system can be tested at different frequencies. The laminar and turbulent values for h were estimated from correlations for air flow at 110 mph (wind tunnel speed) over a flat plate. The estimates were $0.005 w/cm^2 K$ for the laminar value and $0.0178 w/cm^2 K$ for the turbulent value [9].

$$h = ho(1 + B \sin\omega t) \qquad (4)$$

C. SUBSTRATE HEAT TRANSFER MODEL

The second of the two models described in this paper is that of modelling the unsteady state heat transfer within the substrate material under the hot-film sensor. A sketch of the model with its dimensions is shown in Fig 3. The inner radius of the sensor (r_i) is 0.0828cm, the outer radius of the sensor (r_o) is 0.0968cm. The radius of the model (r_m) is 3.07cm. The model has three types of boundary conditions. A small area at the surface is maintained at a constant temperature of 60°C to simulate the hot sensor. The rest of the surface allows convective heat transfer to the air at the ambient temperature of 20°C. The value of the convective heat transfer coefficient is that of constant laminar flow.

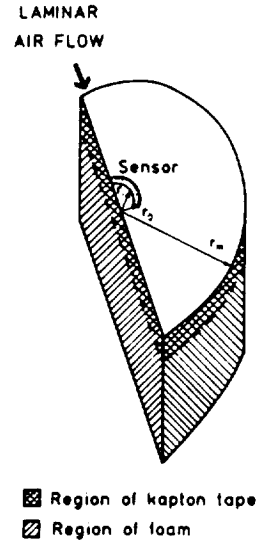

FIG. 3. SUBSTRATE MODEL

All other boundaries are assumed insulated. The justification for this assumption is different for different boundaries. One boundary is insulated because it is a plane of symmetry. The model sensor is shaped in a semicircle but the model exploits the midline symmetry and computes a solution for only half a sensor. The remaining boundaries are assumed to be insulated because they are far enough away from the hot sensor so that the temperature at these boundaries is almost equal to that of the initial/ambient temperature. The boundary nodes are checked to make sure that this is a good assumption.

The actual sensor is not perfectly cylindrical in shape, but to make computation easier a cylindrical model with an equivalent area was used. The model uses 3600 grid points in cylindrical coordinates. There are six nodes in the angular direction, 30 in the radial direction and 20 in the z direction. Grid point spacing in the r and z directions is variable, being farther apart at a greater distance from the sensor. The model contains two different regions with different thermal properties. The thickness of the kapton tape region is 0.16cm, that of the insultating foam region is 2.5cm. The explict method of finite difference is used for computing the solution [10].

III. SIMULATION RESULTS

A. SENSOR-ELECTRONIC MODEL

Simulations were conducted at several different frequencies. Sample outputs are shown in Figs. 4-7. These figures plot three different sine waves. One is a normalized wave with the same frequency as the forcing function. It represents the frequency and phase of the oscillating convective heat transfer coefficient over the sensor. The second wave plots the variation in resistance of the sensor, R_s. The third wave tracks the model output, V. The abscissa of Figs. 5-7 is milliseconds, that of Fig. 4 is ten times this. None of these four figures begin at zero time. The natural response of the system is a 10 kHz oscillation which is very poorly damped. Since it is the steady state values that are desired, the initial cycles are ignored to allow this start-up transient time to decay. The simulations at all frequencies displayed a transient of approximately 10kHz.

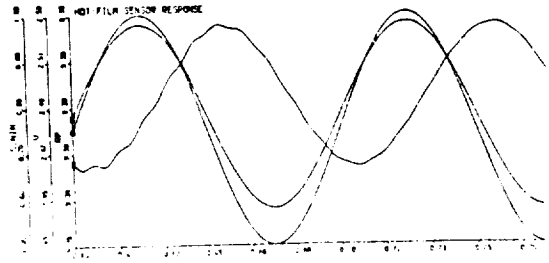

FIG. 4

SENSOR-ELECTRONIC MODEL RESULTS FOR 1 KHz INPUT

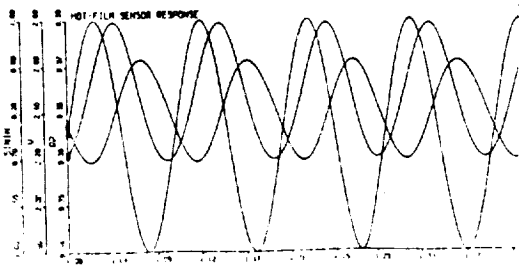

FIG. 5

SENSOR-ELECTRONIC MODEL RESULTS FOR 10 KHz INPUT

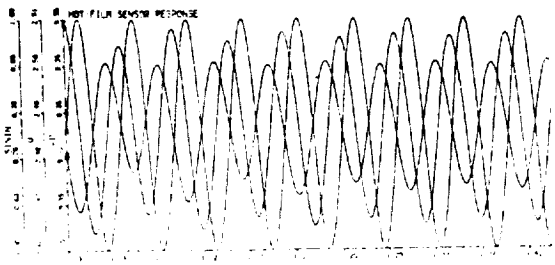

FIG. 6

SENSOR-ELECTRONIC MODEL RESULTS FOR 20 KHz INPUT

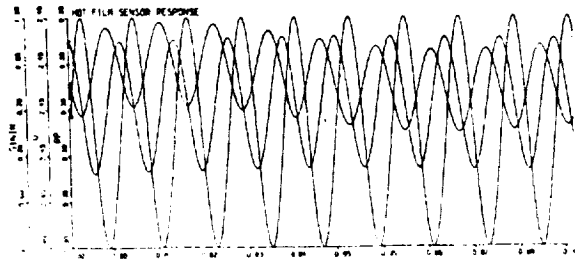

FIG. 7

SENSOR-ELECTRONIC MODEL RESULTS FOR 100 KHz INPUT

The significant results of the simulations are tabulated in Table II. Several qualifying remarks are necesary to understand the results in the table. The phase lag of the voltage wave from the input wave is defined in the usual sense, but that of the sensor resistance from the input wave is not. In the physical instrument when h, the input, rises, inducing greater convective heat transfer, the sensor resistance wave should decrease, because of a temperature drop. Thus, for the input and sensor resistance waves, a no phase lag condition in the physical sense is a 180 phase lag in the usual sense. The results in Table II are tabulated in the physical sense.

Freq (Hz)	500	1 K	10 K	20 K	100
V/h, Phase	-	360°	420°	532°	539°
R_s/h, Phase	-	295°	346°	452°	467°
Volt/Res Phase	-	65°	74°	80°	72°
Average V (v)	2.452	2.486	2.495	2.487	2.488
Pk/Pk V (mv)	-	80	570	27	0.74
Avg R_s (Ω)	9.388	9.385	9.373	9.352	9.301
Pk/Pk R_s (mw)	-	0.244	16.8	1.62	0.228

TABLE II
SENSOR-ELECTRONIC MODEL RESULTS

The mean and peak-to-peak values of the output voltage and sensor resistance are also tabulated in Table II. Both mean values follow a consistent pattern. The mean sensor resistance decreases with increasing frequency while the output voltage

increases with increasing frequency. The peak-to-peak values for the same variables are not so consistent. A possible explanation of this observation is that transients were still present: especially the 10kHz transient.

B. SUBSTRATE MODEL

The key result from the substrate model is shown in Fig 8. It is a plot of the rate of heat conduction from the sensor to the substrate as a function of start-up time. Zero time corresponds to the rate of heat conduction when the cold sensor is first turned on and assumed to be at 60°C while the substrate is at the ambient temperature of 20°C. When the sensor is first turned on there is a rapid drop in the heat transfer rate as the substrate material adjacent to the sensor heats up. Eventually the heat transfer rate levels off considerably, although it never reaches a true steady state. The shape of the curve is not exponential but can be approximated by an exponential curve with a time constant of 4.5msec.

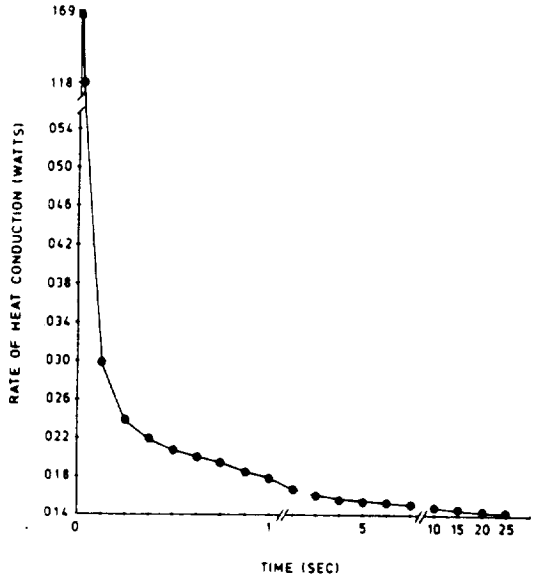

FIG. 8

SENSOR-SUBSTRATE HEAT CONDUCTION ($\dot{Q}_s$) vs TIME

IV. SUMMARY AND CONCLUSIONS

Two models have been constructed to aid in the investigation of cross-flow vortices using hot-film sensors. The models have not been subjected to rigorous experimental validation, but can be judged against results from the literature and from laboratory observations. The results of the two models appear consistent with these observations with two exceptions. The first exception is that the experimental results yield a dc voltage output of about 5v while our model yields only half of that value. A possible explation is that the substrate model underestimates the steady state heat flow. If there were to be a error in the model it would be on the low side. Of the several materials comprising the substrate the two most insulating were used. Also, heat transfer properties of these materials are inexact.

The second anomaly in the results is the high peak-to-peak values of voltage and resistance at 10kHz from the sensor model. This discrepancy is due to the 10kHz resonance.

Other results are consistent with observation or theory. The actual shape of the heat transfer curve from the substrate model agrees with that observed in practice. The engineer operating the experimental apparatus allows for a 5 second warm-up time. She selects five seconds becauses she observes an apparent steady-state condition on the oscilloscope. The plot of the rate of heat transfer from sensor to substrate, Fig. 8, is consistent with this observation.

The sensor electronic model shows an increasing phase lag with frequency, as is to be expected. Together, these two models provide a characterization of performance. When the two models are fused together the results should be most informative for low-frequency response.

V. FUTURE WORK

The next logical step will be to fuse the two models described above. The results will be most informative for low-frequency response. Systems analysis will benefit greatly by having a full model in place. Experiments in variation of system parameters such as sensor overheat will be studied. Another area appropriate for the use of this model is that of developing tuning procedures. Anemometers are generally tuned with electrical square pulses but this method ignores the effect of variable substrate conduction [11],[12],[13]. This model, being more complete and replicating closely the real test environment, will provide a more accurate procedure. Also, since a future experimental set up will use an aluminum wing model instead of an insulated wing, substrate heat calculations will be extremely important.

VI. ACKNOWLEDGEMENTS

From Old Dominion University the authors thank Yvonne Wilson, Susan C. Hoebeke, and Deborah Miller-Carson of the Office of Creative Services, for the graphics work, and thank Linda Evans and Janice Bella of the Department of Electrical and Computer Engineering for editing. The authors are also grateful to the many helpful persons of NASA's Langley Research Center, without whom this paper could not have been possible. Special thanks to Debbie Carraway of the Instrument Research Division for the many long hours spent familiarizing the authors with her sensor systems. Thanks are also due to the computer consultants of the LRC Computer Center, especially Pat Kerr, Savonne Etheridge and Pam Skillman. This

paper was made possible by a research grant from NASA.

VII. REFERENCES

[1] Chiles, H. and Johnson, B., "Development of a temperature-compensated hot film anemometer system for boundary-layer transition detection on high-performance aircraft", NASA Tech Memo 83732, August 1985.

[2] Reichert, J., Razad, "Wall shear stress measurement with a hot film in a variable temperature flow", Rev Sci Instrument, Vol. 48, No. 3, March 1977.

[3] Fingerson, L., Fremouth, P., Appendix 2, IFA 100 Intelligent Flow Analyzer, Instruction Manual, TSI Incorporated.

[4] Fremouth, P., "Extension of the nonlinear theory to constant-temperature hot-film anemometers", with comments, TSI Quarterly, August/September 3-6, 1978.

[5] Bellhouse, B. J. and Schultz, D. L., "The determination of fluctuating velocity in air with heated thin film gauges", J. Fluid Mech, Vol. 29, 289-295

[6] Fremouth, P, "Modelling of hot-films by an extended Bellhouse-Schultz Model," Flow, its measurement and control in Science and Industry, 2, 69-75, 1980.

[7] Mitchel and Gauthier Associates, 1981, Advanced Continuous Simulation Language (ACSL), User Guide/Reference Manual.

[8] Ginous, J. "Streamwise vortices in laminar flow, Agardograph 97, May 1965.

[9] Welty, Wicks,and Wilson, "Fundamentals of momentum, heat and mass transfer, 2nd ed., John Wiley & Sons, 1976.

[10] Suec, J., Heat transfer, (p247-266), Dubuque, Iowa: Brown, 1985.

[11] Borgos, J. A., "A review of electrical testing of hot-wire and hot-film anemometers", TSI Quarterly, Vol. VI, Issue 3, August/September 1980.

[12] Fremouth, P., Sine-wave testing of non-cylindrical hot-film anemometer according to the Bellhouse-Schultz Model", J. Phys E. 13, 96-102.

[13] Baker, C. B., "Hot film frequency response", Internal Memorandum, Applied Research Lab, Penn State University, File No. 76-174.

ABOUT THE AUTHORS

GRIFFITH McREE

Griffith J. McRee, Jr. received his BS degree from the United States Military Academy, West Point, NY, in 1956. He received his MS degree in Electrical Engineering from the University of Arizona, Tucson, Arizona, in 1960 and his PhD in Electrical Engineering from the University of Virginia, Charlottesville, Virginia in 1967.

He is currently an Associate Professor in the Department of Electrical and Computer Engineering, and Associate Dean of Research and Graduate Programs for the College of Engineering and Technology, Old Dominion University, Norfolk, Virginia. He retired from the US Army Signal Corps having spent eleven years on active duty and nine years in the active reserve. While on active duty he taught at the US Military Academy and spent time in Europe and Vietnam.

His principle areas of research interest lie in automatic control, system simulation, and intelligent systems. He has done extensive research for NASA's Langley Research Center in the areas of space systems and aircraft control. For three years he was Director of the NASA/ASEE Summer Faculty Fellowship Program.

He is a member of IEEE, Sigma Xi and Eta Kappa Nu.

DAVID M. JUDGE

David M Judge received the B.S. degree in chemical engineering from Washington University,St.Louis,Mo. in 1979.It was here that he first became interested in automatic control and analysis of complex systems. After studying medicine for two years he served in the U.S. Navy for three years as a Radiation Health Officer.While in the Navy he studied undegraduate electrical engineering in night school at Old Dominion University,Norfolk,Va. and now is a masters degree candidate.

AIAA'88

AIAA-88-4677-CP

An Arrayed Hot-Film Sensor For Detection Of Laminar Boundary-Layer Flow Disturbance Spatial Characteristics

M.S. Wusk; D.L. Carraway; B.J. Holmes
NASA Langley Research Center,
Hampton,VA

AIAA/NASA/AFWAL Sensors & Measurement Technologies Conference
September 7-9, 1988 Atlanta, Georgia

An Arrayed Hot-Film Sensor For Detection Of Laminar Boundary-Layer Flow Disturbance Spatial Characteristics

M.S. Wusk*, D.L. Carraway**, and
B.J. Holmes***

NASA Langley Research Center
Hampton, VA 23665

Abstract

An arrayed hot-film sensor has been developed for use in laminar boundary-layer research for the detection of crossflow or Görtler vortices. This sensor has been developed to detect spatial variations in heat transfer which are characteristic of crossflow or Görtler vortices. The sensor is ultimately intended for flight research applications. This paper describes the sensor, its principles of operation, signal analysis techniques, and experimental results illustrating the spatial detection capabilities of this specialized hot-film device. Discretely placed spheres placed in the boundary layer created alternating regions of undisturbed and disturbed laminar flow over a prototype sensor. Flow visualization results were correlated with the sensor output to demonstrate the ability of the sensor to determine the spatial boundaries of localized disturbances in laminar flow. This work represents the intial steps toward the validation and calibration of an arrayed hot-film sensor for the detection of crossflow or Görtler vorticity wavelength and/or wave frequency.

Nomenclature

AC	alternating current
CTA	constant temperature anemometer
DMM	digital multimeter
FM	frequency modulation
ft/sec	feet per second
hp	horsepower
NLF	natural laminar flow
R	Reynolds number
RMS	root-mean-square
RPM	revolutions per minute
U	velocity
Λ	sweep angle
Ω	resistance, ohms

Subscripts:

k	conditions at top of sphere
t	conditions at which transition occurs
∞	free stream condition

* Research Engineer
Flight Applications Branch
** Research Engineer
Instrument Research Division
*** Senior Member, AIAA;
Head, Flight Applications Branch

Introduction

It is important to understand the development of the crossflow and Görtler instability modes which amplify in laminar flow in order to develop and validate prediction methods for laminar boundary-layer stability and transition. Several advancements in arrayed hot-film devices have provided researchers with improved detail on boundary-layer transition phenomena (ref. 1-4). In research applications the frequency and/or spatial behavior of the flow is measured and compared with theoretical predictions from laminar stability theory. These correlations provide validation of the theory.

Two kinds of laminar instabilites involve growth of streamwise vortices in the laminar boundary layer. The first instability involves small co-rotating crossflow vortices which develop due to the spanwise pressure gradients present on wings with substantial leading-edge sweep, and can be a dominant mode of transition on swept wings. Crossflow vortices form when the slower flow close to the wall moves in the direction of the decreasing pressure (spanwise), while the faster flow in the outer part of the boundary layer is less affected by the lateral pressures and maintains a flow direction closer to that of the freestream (fig. 1). The resulting three-dimensional velocity profile of the boundary layer is inflected, creating the necessary conditions

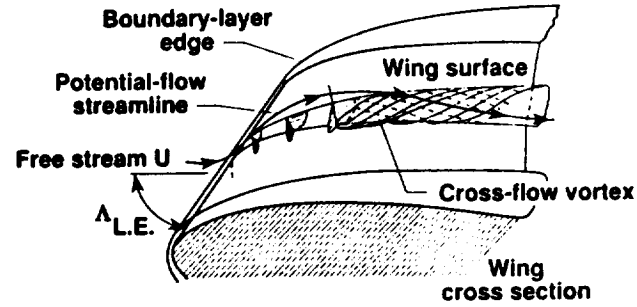

Figure 1. Crossflow vortices over swept wing.

for the formation of vortices. These stationary or moving vortices grow in the laminar boundary layer at exponential rates, eventually leading to transition and a turbulent boundary layer. The second

instability phenomenon is caused by Görtler vortices which form on concave surfaces in two- or three- dimensional flows. In two-dimensional flow these vortices are stationary, counter-rotating, streamwise vortices (fig. 2) formed due to the imbalance between pressure and centrifugal forces present on concave surfaces. The formation of these vortices is governed by the relationship between the Reynolds number and the radius of curvature. The Görtler vortices also grow at exponential rates in the laminar boundary layer, eventually leading to transition and a turbulent boundary layer.

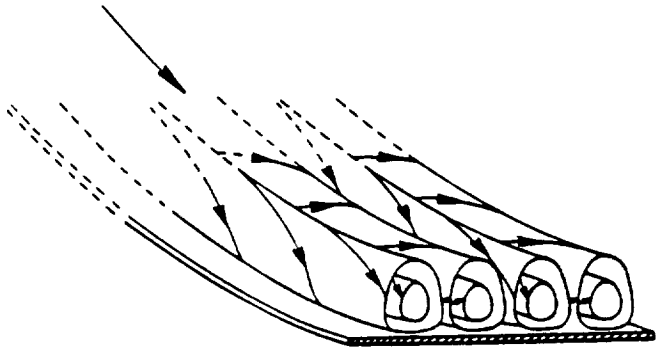

Figure 2. Görtler vortices over concave surface.

Theory predicts the spatial and temporal behavior of streamwise vortices; however, the ability to experimentally measure and make observations of these phenomena has been difficult in the past, especially in flight. Few experiments (no known flight experiments) document the development, structure, and breakdown of the crossflow or Görtler disturbances. Current research is directed at the development of sensors and instrumentation that can be used to gain more understanding of the physics involved in the transition process (ref. 1). The arrayed hot-film vorticity sensor is one such device under development.

As streamwise vortices develop in the laminar boundary layer, local spanwise variations in convective heat transfer occur. These variations can be detected with a sensitive device such as a surface hot film. With a closely spaced array of hot-film elements, the spanwise distribution in heat transfer can be detected. This information provides the investigator with the vortex spacing and/or the frequency of the crossflow or Görtler disturbances. The geometric arrangement of the elements is intended to capture the periodic nature of these variations in heat transfer, in addition to giving such information as whether or not the vortices are moving or stationary. For the moving crossflow vortices, a time series analysis of the sensor signals is necessary to provide the frequency of the most amplified crossflow disturbance. However, in the work reported here only steady-state sensor signals were recorded which show that the sensor can discriminate different convective flow regimes and thereby distinguish between disturbed and undisturbed laminar boundary layers.

A prototype sensor was fabricated and a test was conducted in a low-speed wind tunnel to experimentally validate the hot-film vorticity sensor concept. The test was designed to determine the spatial resolution capability of the sensor in measuring laminar boundary-layer disturbances. This was accomplished by creating lateral variations in the heat transfer in the flow over the sensor using surface imperfections.

The arrayed hot-film sensor has been developed for use in laminar boundary-layer stability research for detection of crossflow or Görtler vortices. Ultimately, the sensor will be used to detect crossflow or Görtler vortices in flight to measure the instability frequency and/or wavelength. This paper describes the sensor, its principles of operation, signal analysis techniques, and experimental results illustrating the sensitivity of the sensor to spatial heat transfer variations in the laminar boundary layer.

Arrayed Hot-Film Sensor and Data Acquisition System

The vorticity sensor was an array of closely spaced hot-film elements on a substrate of thin polyimide film. The pattern of hot-film elements was applied to the polyimide film by a vapor deposition technique. The thin nickel elements were V-shaped (fig. 3) in order to minimize the dependence of the instrument sensitivity on local flow direction. The wide, equal length nickel leads were gold plated in order to help minimize lead resistance. Wires were

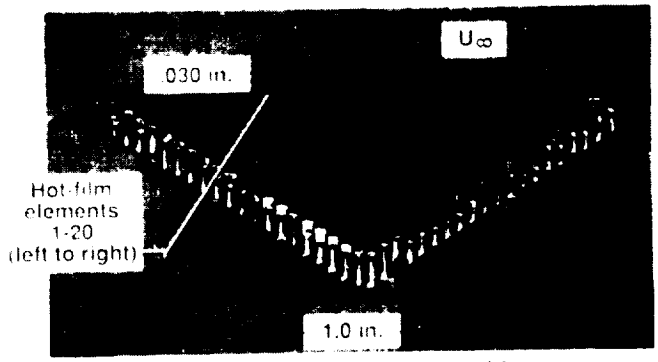

Figure 3. Prototype arrayed hot-film sensor.

connected to the ends of the gold leads and routed back into the airfoil model used in the tests (see "Experimental Set-up" section) and out the bottom of the tunnel floor. Connections were then made to coaxial cables which carry the signals to the data acquisition system. A layer of thin double-backed tape adhered the sensor to the model surface. The center-to-center element spacing of the sensor was 0.03 inches. This small spacing was chosen to provide as many as 5 elements per wavelength for most streamwise vorticity studies of interest in future planned flight applications.

A block diagram of the multichannel hot-film data acquisition system is shown in figure 4. The components of the system include the constant temperature anemometers (CTAs) used to drive the hot films, a desk-top computer, a switching network, four digital multimeters (DMM), a scanner, AC amplifiers, an oscilloscope, and an FM tape recorder. During this test a desktop

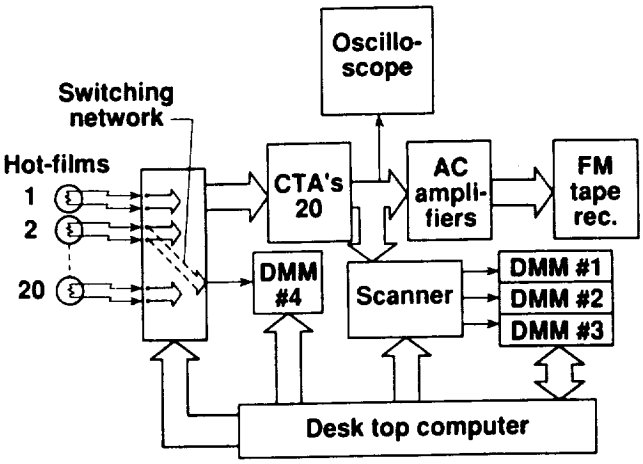

Figure 4. Diagram of 20-channel hot-film data acquisition system

computer controlled the instrumentation, acquired, stored, and reduced the data. The switching network, under computer control, switched the hot films sequentially into DMM #4 for a resistance measurement. The switches, when disabled, restored the hot films automatically to their individual and respective CTA. The CTAs provided current to the hot films, and the output voltages from the CTAs were scanned and sampled with the scanner and the DMM for on-line data reduction. The output voltages were also viewed on the oscilloscope, and recorded on FM tape for further processing and analysis.

A simplified schematic of a single channel of the annemometry circuitry is shown in figure 5. It consists of two parts, a 10 to

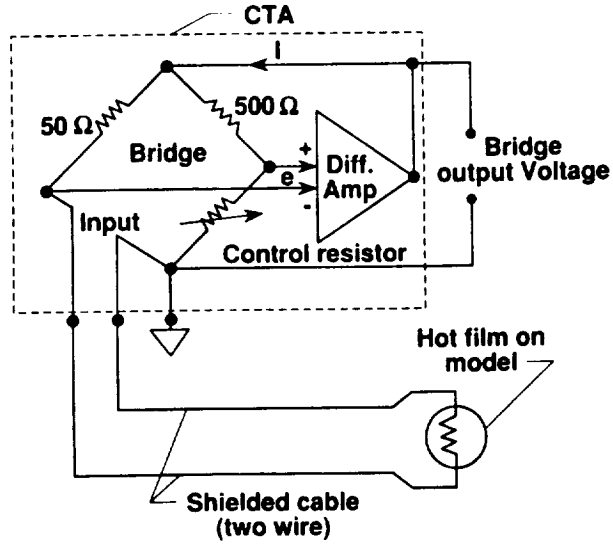

Figure 5. Single channel of hot-film anemometry.

1 resistance-bridge network, of which the hot film is a component, and a very high gain, differential amplifier, with feedback to the bridge. The bridge funtions in a quasi-balanced mode by forcing the hot film to be a resistance value determined by a control resistor. The hot film's intial resistance, referred to as the "cold resistance", indicates the unheated local temperature of the film and is a reference value in the determination of the overheat resistance of the film. The overheat is defined as the ratio of the hot (i.e., heated hot film) resistance to the cold resistance of the hot film. This overheat ratio determines a film's sensitivity to temperature and velocity fluctuations in the flow. During this experiment each film was operated at a relatively high overheat ratio of 1.3. This allowed the film's sensitivity and response to velocity fluctuations to dominate while minimizing substrate heating between the simultaneously heated elements.

Once the overheat is set into the control resistor, the film is at its control resistance value and is sensitive to the fluctuations in the boundary layer (i.e., changes in heat transfer). When the film senses fluctuations in the boundary layer, there is a slight change in the hot-film resistance which results in a small imbalance in the bridge. The imbalance in the bridge causes the differential feedback amplifier to increase or decrease the current to the bridge, maintaining the film at a constant temperature. These fluctuations in the bridge current, and hence voltage from the feedback amplifier, can be translated directly to: (1) the root-mean-square (RMS) voltage, and (2) the mean voltage, at the bridge output. The root mean square and mean voltages from the hot-film anemometers are sequentially scanned, averaged, and stored in real-time (i.e., on-line) with the desktop computer.

Experimental Set-up

The tests were made in the 17- by 22-inch test section of the Instrument Research Division's (IRD) Small Calibration Facility, shown in figure 6. A 50 hp motor drives a squirrel cage blower at either 885 revolutions per minute (RPM) or 1780 RPM, resulting in test section speeds between 8 and 280 feet per second. Speeds above 160 feet per second are reached by use of the high blower-speed setting. Control of the test section velocity is accomplished by opening and closing 12 radial damper vanes located downstream of the diffuser. During

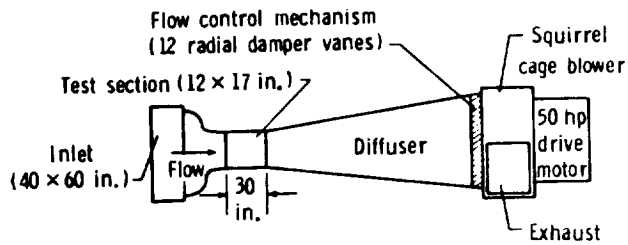

Figure 6. Schematic of IRD small calibration facility.

this experiment all tests were conducted using the low blower-speed. Test points were recorded at the following test section speeds: 8.4, 28.9, 34.5, 41.7, 48.7, 70.4, 112.4, 127.4 feet per second. This range in speed allowed an adequate coverage of the predicted Reynolds numbers needed to cause the desired boundary-layer behavior. Turbulence intensity in the test section ranged between 0.7% at low speeds to 0.3% at higher speeds. No test section turbulence spectral data are available for this facility.

An existing airfoil model was used as a surface on which to test the hot-film vorticity sensor. Figure 7 shows the model mounted in the wind-tunnel test section. The model was a one foot chord section of the NASA NLF(1)-0414 natural laminar flow airfoil (ref. 5). This model has exhibited

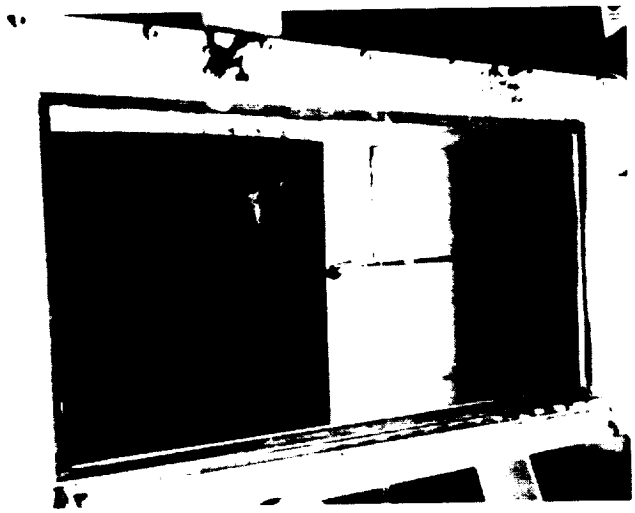

Figure 7. NASA NLF(1)-0414 airfoil mounted in test section of IRD small calibration facility.

laminar flow to as far back as sixty percent chord in previous tests (ref. 2). The model is constructed of a foam core with an outer fiberglass skin, resulting in a hard, smooth finish. The model surface was painted flat black to enhance the flow visualization techniques used. The model was mounted vertically in the tunnel test section, and was bolted to the turntable section of the tunnel floor. The scope of this experiment did not include angle of attack as a variable. Instead, the model was set as close to a zero angle of attack as possible and remained fixed throughout the remainder of the experiment.

Glass microspheres were used to generate streamwise vorticity disturbances in the laminar boundary layer, thus creating spanwise variations in the heat transfer. Theoretical sizing criteria by Braslow (ref. 6) and practical handling considerations were used in determining a range of sizes that would be appropriate for this experiment. The glass spheres were glued on to the airfoil surface, upstream of the sensor location. A horseshoe vortex system (fig. 8a) propagated downstream from each sphere (ref. 7) and passed over the sensor. At sufficient speed, each of these horseshoe vortex systems caused a local transition to turbulent flow. Through spanwise contamination, the turbulence would spread laterally forming a turbulent wedge as it propagated downstream (fig. 8b). Placing

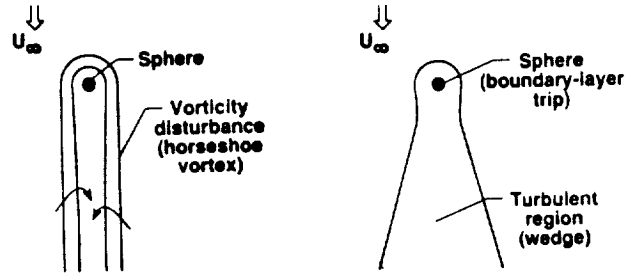

a) Horseshoe vortex

b) Turbulent wedge

Figure 8. Boundary-layer disturbances shed from spherical roughness particle.

these microspheres in the appropriate locations allowed the investigator to dictate the spacing and number of disturbances encountered by the sensor, and thus provided an inexpensive, simple, and easily-altered method to create the needed aerodynamic input for the steady-state sensor calibration.

Sublimating chemicals were used for flow visualization (ref. 8,9). The sublimating chemical method provided a detailed pattern of boundary-layer transition that could be examined and photographed both during and after the testing. The chemical Naphthalene was chosen for the tests because of its suitability to the speed and temperature of the experiment range.

Preliminary tests were conducted to determine the best size and configuration for the spherical roughness particles. Various bead sizes, groupings, spacings, and chord locations were tested. The configurations were subjected to a range of increasing velocities using sublimating chemical flow visualization techniques to determine the critical velocities for the various arrangements. A bead diameter of 0.033 inches proved to be the most effective size. A single bead of this diameter provided a clearly visible, tightly contained vortex pair behind the bead at test speeds starting as low as about 25 feet per second. Boundary layer thickness ranged from 0.062 inches at U_∞=30 ft/sec to 0.030 inches at U_∞=130 ft/sec according to laminar boundary-layer theory. These produced roughness-height Reynolds numbers (R_k) of approximately 390 and 2000 respectively. A critical Reynolds number of $R_{k,t} \approx 600$ is required for a spherical particle to cause transition at the roughness. Thus, a turbulent wedge could be produced at the the top end of the speed range. A group of these beads provided a disturbance width of any size desired.

During the sensor experiments there were four different bead set-ups for each test speed. The first was a no-bead or laminar flow condition. The second was a cluster of beads denoted as the one-bead group. The other two set-ups used three and four individual discretely placed beads and were denoted as the three-bead and the four-bead set-ups, respectively. The one-bead group allowed for a single wide disturbance area which covered several neighboring hot-film elements. Beads were placed approximately 1 inch directly upstream of hot-film element numbers 10 through 12. The elements were numbered 1-20, from left to right, as seen in the figure 3. The other set-ups allowed various numbers of discretely spaced regions of disturbed flow to pass over the sensor area. The three-bead set-up positioned beads upstream of elements number 1, 11, and 20. The four-bead set-up positioned beads upstream of element numbers 2, 8, 14, and 20. This arrangement provided flow fields of different disturbance spacing that could be accurately measured, changed and controlled.

Data Reduction and Results

The sensor's output was analyzed using two techniques. First, the RMS voltage output of the CTA was used to determine the transition intermittency at a hot-film location (ref. 10). Second, the mean voltage level at the output of the CTA was used to determine a level of heat transfer, in the form of power dissipated from the element, at a hot-film location (ref. 11). Both methods proved to be effective, with individual advantages and limitations.

Figure 9 shows the normalized RMS voltages versus test section flow velocity for element 11. The RMS voltage outputs were a measure of the local velocity flucuations above the hot-film element. For the presentation of RMS data, the RMS values were normalized by the corresponding mean voltage values (ref. 10). The data of figure 9 show the low, relatively constant RMS values obtained when the element remained in an undisturbed laminar region. The data also indicate the RMS values when the element was in a boundary-layer flow that transitioned from laminar to turbulent (caused by an upstream sphere).

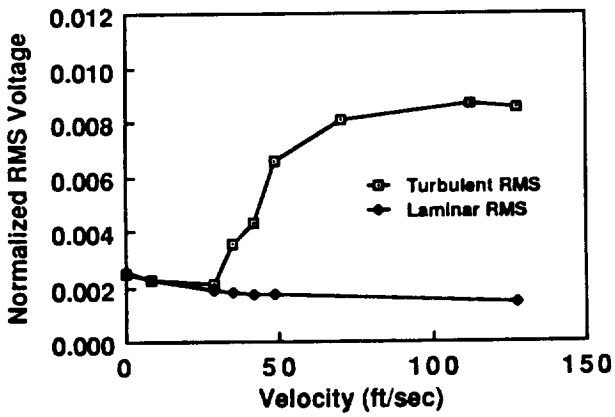

Figure 9. Normalized RMS output for element number 11.

The turbulent RMS signal shown in figure 9 indicates the onset of transition with a sharp increase in the RMS voltage resulting from turbulent spots that occur in the flow. At the peak RMS signal, the turbulent spots were at their maximum occurrence and the boundary layer was approximately 50 percent laminar and 50 percent turbulent. Tunnel operating conditions did not permit data to be obtained beyond this peak intermittency. Figure 10 shows a theoretical example of expected normalized RMS voltage output for a complete cycle from fully laminar to fully turbulent flow. After the peak RMS signal,

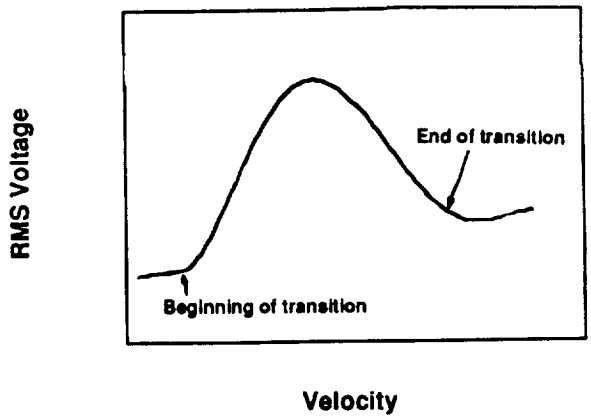

Figure 10. Theoretical expected RMS output for a single hot-film.

one would expect a rapid reduction of the RMS voltage level with an occasional laminar burst or interval in what would then have become a predominately turbulent boundary layer. At the end of transition (i.e., fully turbulent boundary layer), the RMS voltage has a nearly constant value (in some instances with a small increase), but at a level that is slightly elevated from the laminar boundary layer level. Because of this peaking in the RMS levels, spanwise comparison of different hot-film elements, each covered by a flow of different and unknown level of turbulence, becomes a difficult task because it is not known which side of the peak value the signals are indicating. The RMS signal does, however, provide clear indications of vorticity at lower speeds or in flows where the disturbances are still tightly contained, such as vortical flow. Also, if the development of transition is observed from the onset (i.e., the signal is monitored as the flow velocity is increased), it is easy to determine when this peak value occurs.

The electrical power dissipated (derived from the mean voltage output) by one individual hot film, over a range of test speeds, is shown in figure 11. This figure shows the increases in the power level corresponding to increases in velocity for hot-film element number 11 during the laminar flow, no-bead test set-up. Similar

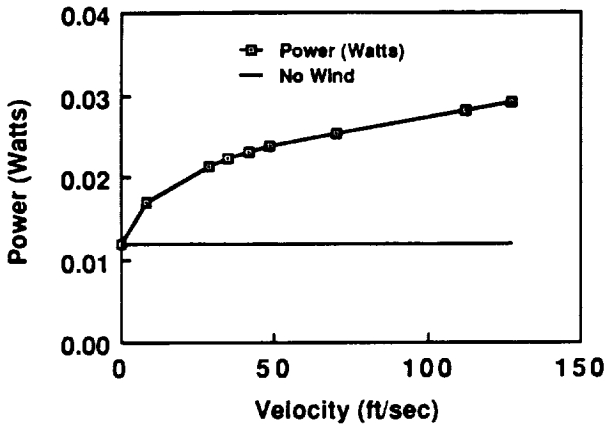

Figure 11. Power output calibration curve for element number 11.

calibration graphs for each hot-film element in the array demonstrated that although all the elements in this particular sensor do not exhibit the same power levels, they react approximately the same to changes in the flow velocity. The differences were due to the thermal heating effects of the model substrate and slight physical differences that existed between individual hot-film elements. By applying two corrections, the no-wind power correction and the element offset correction, these two effects were removed.

The calibration procedure for this sensor assumes that the ideal output of each hot-film element in a laminar flow condition would be to have the exact same voltage level across the array. The uncorrected experimental electrical output of the sensor from the laminar flow test condition is shown in figure 12. The figure shows the uncorrected power output for three different velocities. The lowest curve in figure 12 is the power output for the no-wind condition.

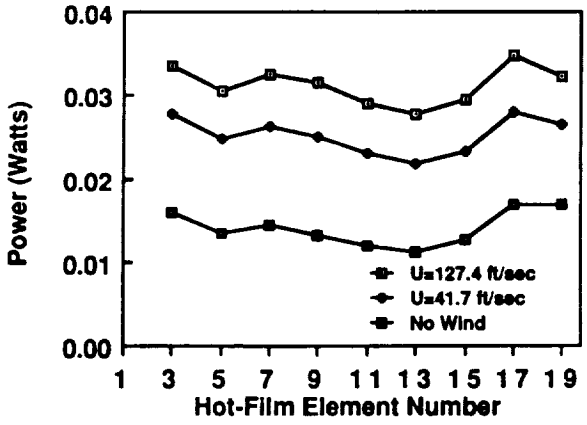

Figure 12. Uncorrected laminar power output for hot-film sensor.

This is the electrical power required to maintain the sensor's overheat in a zero velocity flow condition. Assuming that radiation heat transfer and free-convection heat transfer are negligble, the no-wind power represents energy lost through conductive heat transfer to the substrate. This lost energy is of no use in determining information about the airflow. It also causes a heating of the substrate material around the sensor area, which creates differences in output power levels as each hot-film element tries to maintain its pre-set constant overheat temperature in a changed thermal environment.

Curves which more closely represent the heat transfer due to convection into the airflow can be see in figure 13. These data have the no-wind power correction applied to them. By subtracting, element by element, the no-wind power value from each flow condition power value, the portion of the energy lost to the substrate is eliminated from the output. The power levels that remain give a much better indication of the convection heat transfer from each hot-film element.

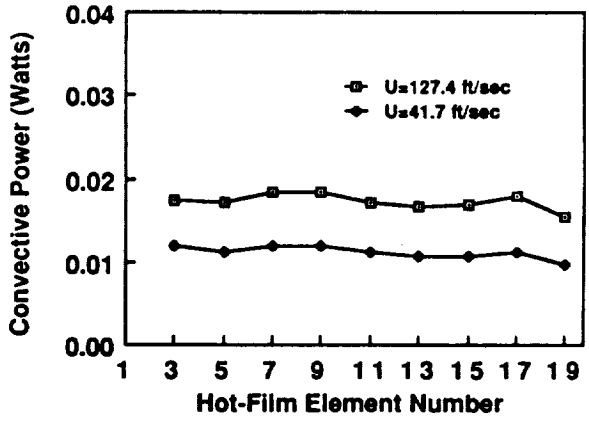

Figure 13. Laminar convective power output for hot-film sensor.

The curves of figure 13 have not been corrected for differences between indivdual elements. These differences occur in the output power levels because each hot-film element has slightly different physical characteristics and each CTA operates slightly differently. So there is some unique error in maintaining the exact overheat desired. Consquently, there can be relative differences in absolute power levels from element to element in addition to any thermal interaction effects. These differences are inherent characteristics of each individual CTA and remain fairly constant. Therefore, assuming again that in laminar conditions every element should be at the exact same power level, an offset correction from a laminar baseline can be found for each particular element at each

specific velocity. Figure 14 shows the data from figure 13 with the corrections for element differences applied to the data. This offset correction is applied as a calibration factor to each respective hot-film element during any measurement.

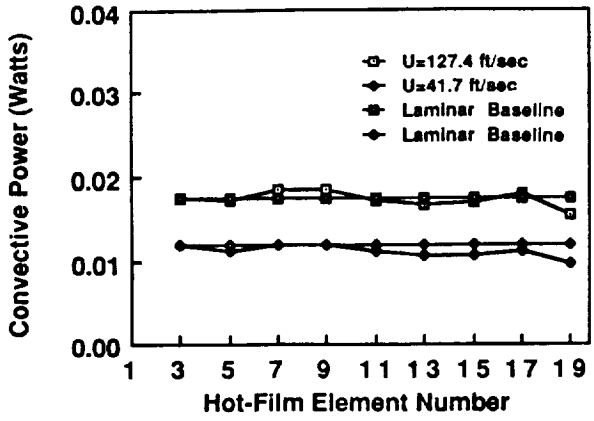

Figure 14. Laminar convective power with laminar baselines.

By applying the foregoing corrections to the power output, the resulting values more closely represent the actual trends in the convective heat transfer. Thus the sensor can be made more sensitive to spatial variations in flow (i.e., crossflow vortices). This characteristic can be seen in the following example. Figure 15 shows the power outputs from the three-bead, 34.5 feet per second flow condition. Flow visualization showed that element 11 was the only odd-numbered element covered by the vorticity disturbances (fig. 15a). The data show the uncorrected electrical power output of the sensor, and corrected output power employing the data reduction method previously descibed (fig. 15b). The areas of disturbed flow are much more distinct in the corrected data.

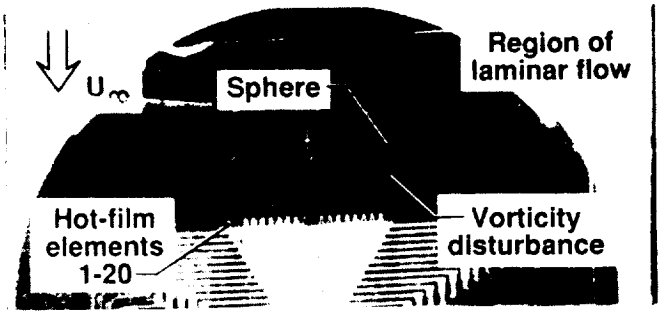

a) flow visualization

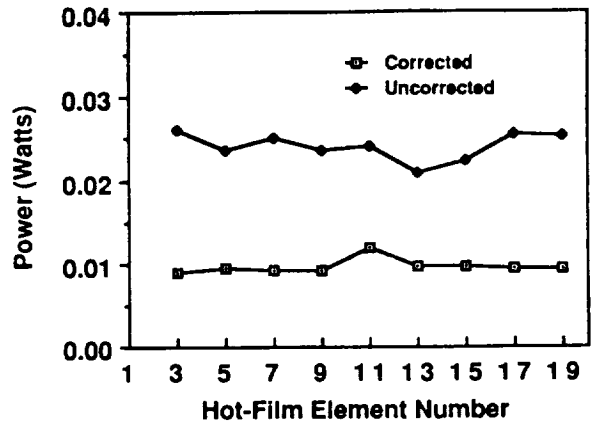

b) Sensor power output

Figure 15. Uncorrected and corrected senor output, 3-bead, U_∞=34.5 ft/sec

In order to compare results from different velocities, the power values obtained from each bead configuration are normalized by their respective laminar baseline values. The normalized graphs show laminar flow, regardless of test speed, as a value of 1.0. A value greater than 1.0 is an indication of a disturbance existing in the boundary layer. Normalized results are presented for two test speeds. These speeds represent the highest tunnel speed obtained during the testing (127.4 ft/sec) and an intermediate speed (41.7 ft/sec) at which vorticity disturbances in the laminar boundary layer, due to the spheres, start to appear. The results are presented in each figure set as: (a) picture of the flow visualization, (b) graph of the normalized RMS voltage from the hot-film elements versus element spanwise position, and (c) graph of the normalized convective heat transfer versus hot-film element spanwise position. For the results presented, only the odd numbered elements were powered. Also, element number one was not working.

Figure 16 shows the results of the one-bead group, 127.4 feet/second test run. The flow visualization picture (fig. 16a) shows elements 9-13 were covered by the area of disturbed (turbulent) flow. The RMS curve (fig. 16b) clearly shows that highly elevated output levels were present for only those three sensors. Likewise, the normalized heat transfer curve (fig. 16c) also shows that the same three elements (9,11,13) were at an elevated level.

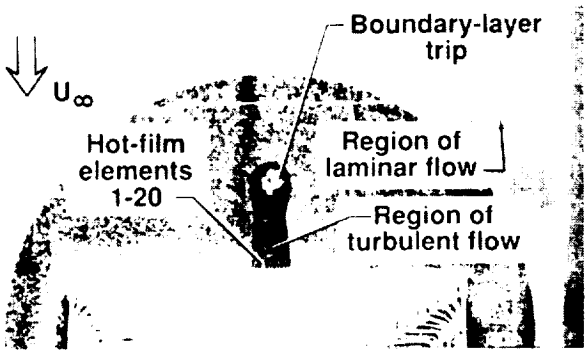

a) flow visualization

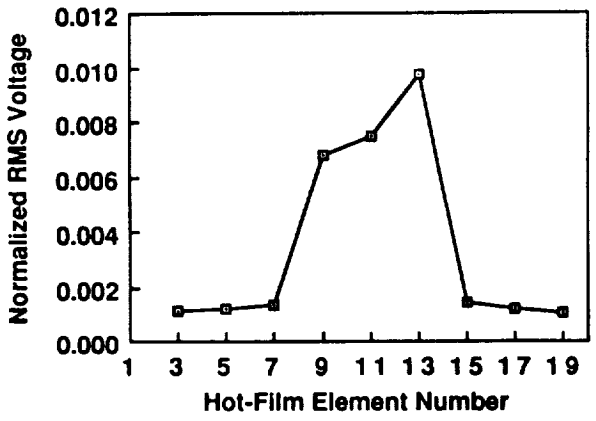

b) RMS output for hot-film sensor

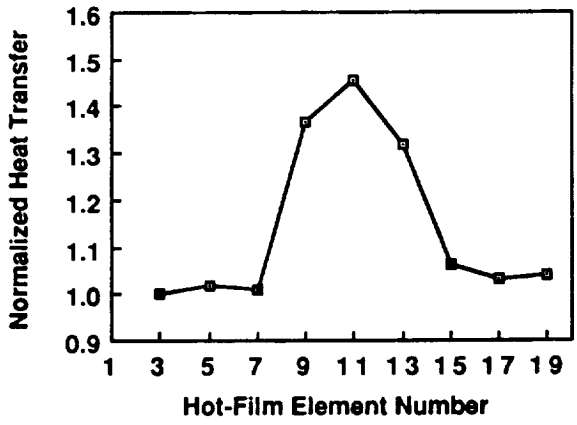

c) normalized-power sensor output

Figure 16. One-bead group, U-=127.4 ft/sec

The same bead set-up at the 41.7 feet per second test speed is shown in figure 17. Element 11 was the only one affected in both the normalized RMS (fig. 17b) and the normalized heat transfer (fig. 17c) output levels, as the generated vorticity disturbance in the laminar boundary layer was much more contained than at the higher speed (simulated picture shown for fig. 17a).

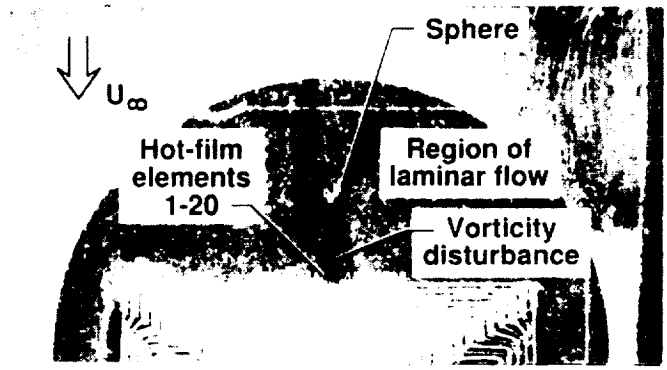

a) flow visualization (Simulated picture)

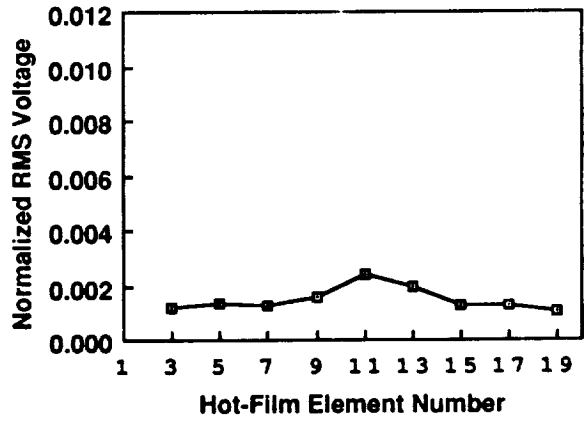

b) RMS output for hot-film sensor

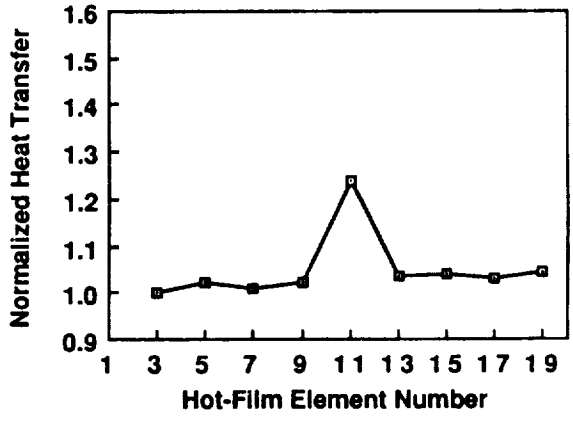

c) normalized-power sensor output

Figure 17. One-bead group, U-=41.7 ft/sec

Results from the three-bead set-up at a test speed of 127.4 feet per second are shown in figure 18. The flow visualizaton (fig. 18a), the normalized RMS (fig. 18b) and the normalized heat transfer (fig. 18c) show that elements 3,9,11,19 were in a turbulent region. Element 13 was also partially affected by this turbulent flow.

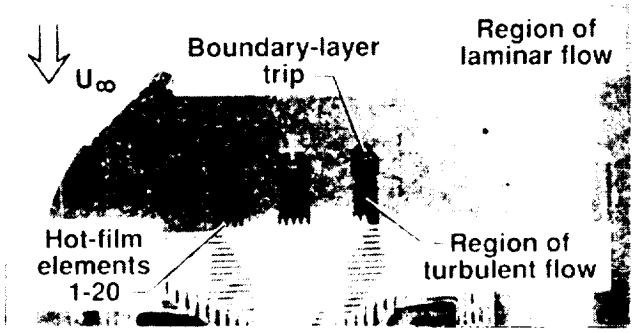

a) flow visualization

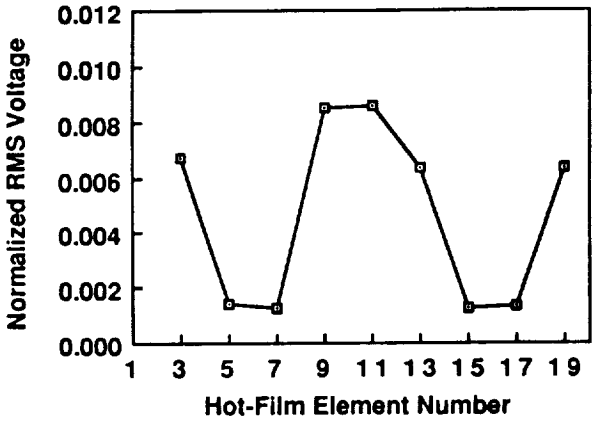

b) RMS output for hot-film sensor

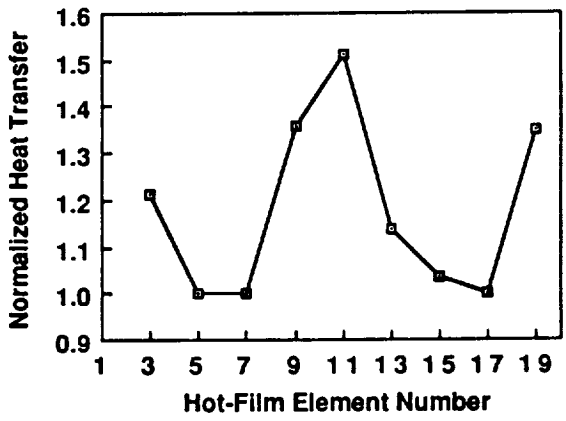

c) normalized-power sensor output

Figure 18. Three-bead group, U_∞=127.4 ft/sec

For the 41.7 feet per second test speed, the vorticity disturbances in the laminar flow appeared to only partially cover elements 3 and 19 while element 11 was immersed (fig. 19a). This condition is apparent in the graphs (fig. 19b and 19c) as element 11 was the only one to indicate any vorticity disturbance in the laminar boundary layer.

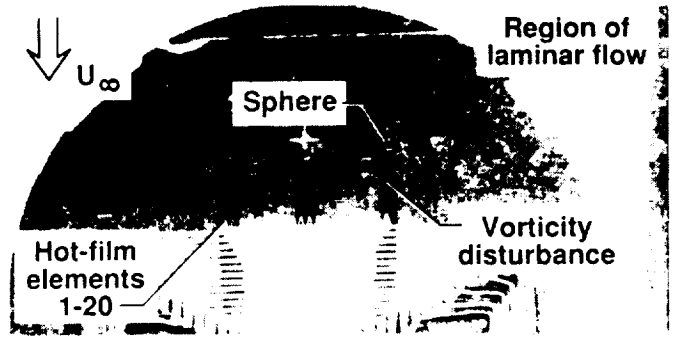

a) flow visualization

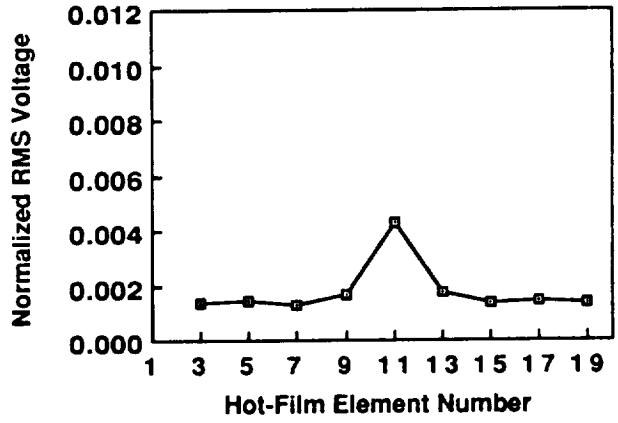

b) RMS output for hot-film sensor

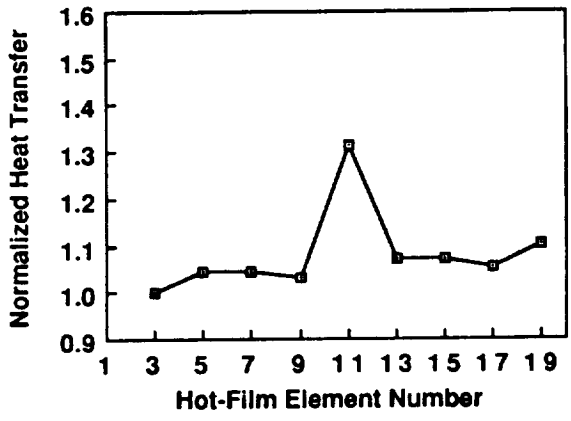

c) normalized-power sensor output

Figure 19. Three-bead group U_∞=41.7 ft/sec

The four-bead case results are shown in figure 20. Flow visualization (fig. 20a) for the 127.4 feet per second test condition, indicated the turbulence had spread until it completely covered the whole sensor array. The normalized power (fig. 20c) showed a overall increase in turbulence level. The RMS graph (fig. 20b) shows four low spots corresponding to the bead locations. These were lower RMS levels because the RMS signals in these areas were past the peak value (i.e., the core regions of turbulence were more than 50% intermittent).

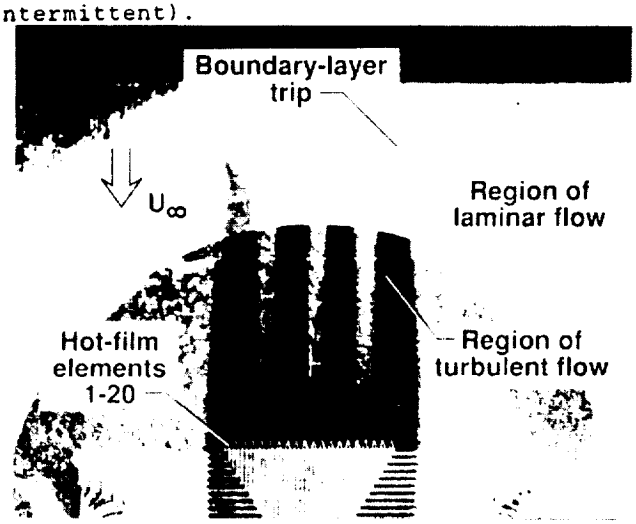

a) flow visualization

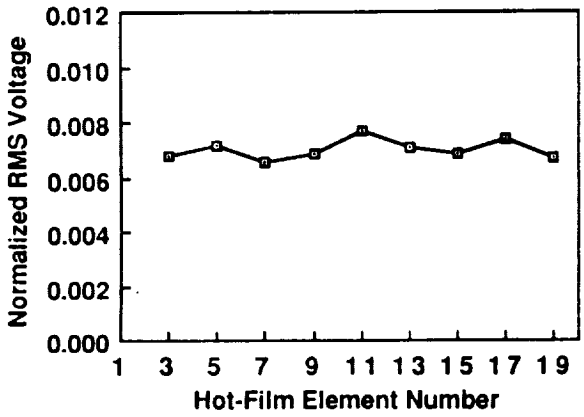

b) RMS output for hot-film sensor

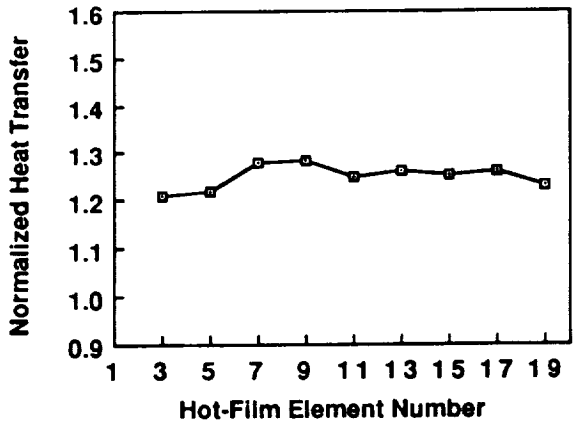

c) normalized-power sensor output

Figure 20. Four-bead group, U_∞=127.4 ft/sec

The data for the four-bead test set-up at a speed of 41.7 feet per second are shown in figure 21. Flow visualization (fig. 21a) indicated very tightly contained vorticity disturbances. Four peaks, corresponding to the four beads, are easily visible in both the RMS and the normalized heat transfer graphs (fig. 21b and 21c).

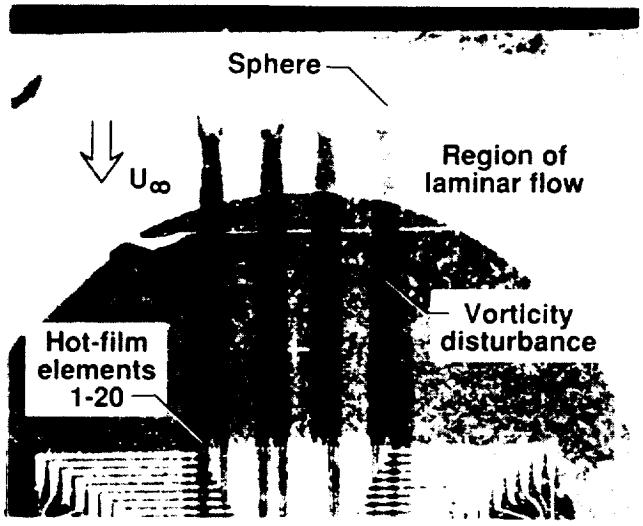

a) flow visualization

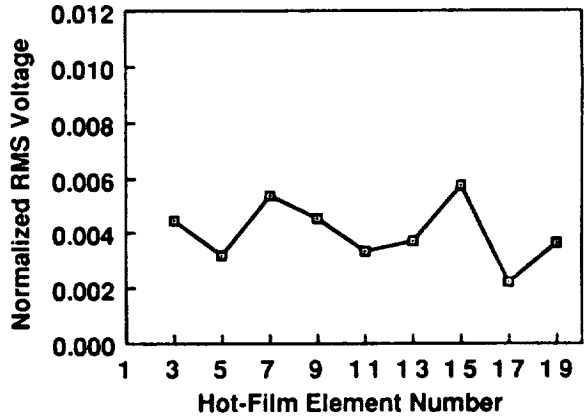

b) RMS output for hot-film sensor

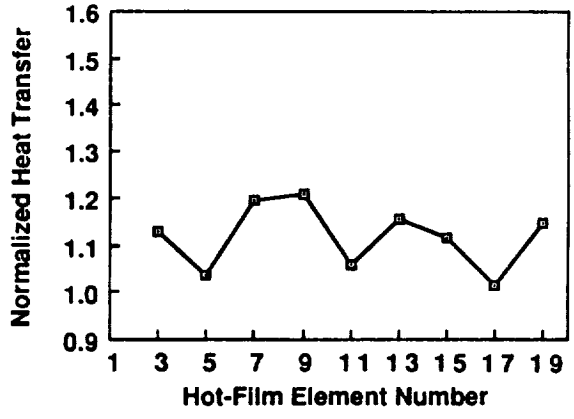

c) normalized-power sensor output

Figure 21. Four-bead group, U_∞=41.7 ft/sec

Future Plans

Further wind-tunnel and flight experiments are planned to fully develop research procedures with the sensor. A swept cylinder crossflow vorticity wind-tunnel experiment will be conducted to document the performance of the sensor in an actual crossflow environment. This experiment should provide both steady state (stationary vortices) and, possibly, dynamic (moving vortices) experience. Flight experiments are planned on a gloved test surface on an existing NASA transonic research aircraft to validate sensor performance in flight. Ultimately, supersonic and hypersonic flight applications of the device are invisioned for transition mode determination.

Concluding Remarks

A surface mounted arrayed hot-film sensor has demonstrated the ability to detect spanwise variations in a flow field by measuring both the RMS voltage and the mean voltage variations at individual hot film locations. This test was conducted in a controlled, steady-state environment with artificially created three-dimensional laminar vorticity and turbulent flow disturbances. The ability to change and control these areas of disturbance demonstrated the capability of the sensor to resolve the flow boundaries to within a 0.06 inch spacing. The sensor tests demonstrated the ability to detect vorticity disturbances in laminar boundary layers and to detect transition and turbulence.

These tests have resulted in the following advances in crossflow hot-film sensor research:

(1) The development of the data reduction methods.

(2) The steady-state operation and calibration of the sensor device.

(3) The development and definition of the operating test requirements for future testing of the sensor in an actual crossflow environment.

References

1 Holmes, B. J.; Croom, C. C.; Gall, P. D.; Manuel, G. S.; Carraway, D. L.: Advanced Transition Measurement Methods for Flight Applications. AIAA Paper No. 86-9786, Presented at the 3rd Flight Testing Conference, Las Vegas, Neveda, April 2-4, 1986.

2 Manuel, G. S.; Carraway, D. L.; Croom, C. C.: The Laminar Seperation Sensor: An Advanced Transition Measurement Method for Use in Wind Tunnels and Flight. SAE Paper No. 871018, Presented at the General Aviation Aircraft Meeting and Exposition, Wichita, Kansas, April 28-30, 1987.

3 Croom, C. C.; Manuel, G. S.; Stack, J. P.: In-Flight Detection of Tollmien-Schlichting Instabilities in Laminar Flow. SAE Paper No. 871016, Presented at the General Aviation Aircraft Meeting and Exposition, Wichita, Kansas, April 28-30, 1987.

4 Stack, J. P.; Mangalam, S. M.; Berry, S. A.: A Unique Measurement Technique to Study Laminar-Separation Bubble Characteristics on an Airfoil. AIAA Paper No. 87-1271, Presented at the AIAA 19th Fluid Dynamics, Plasma Dynamics and Laser Conference, Honolulu, Hawaii, June 8-10, 1987.

5 McGhee, R. J.; Viken, J. K.; Pfenninger, W.; Beasley, W. D.; Harvey, W. D.: Experimental Results for a Flapped Natural-Laminar-Flow Airfoil with High Lift/Drag Ratio. NASA TM 85788, May 1984.

6 Braslow, A. L.; Knox, E. C.: Simplified Method for Determination of Critical Height of Distributed Roughness Particles for Boundary-Layer Transition at Mach Numbers from 0 to 5. NACA TN 4363, August 1958.

7 Gibbings, J.C.; Goskel, O. T.; Hall, D. J.: The Influence of Roughness Trips upon Boundary-Layer Transition. II-Characteristics of Single Spherical Trips. Aeronautical Journal, vol.90, November, 1986.

8 Holmes, B. J.; Obara, C. J.; Yip, L. P.: Natural Laminar Flow Experiments on Modern Airplane Surfaces. NASA TP 2256, June, 1984.

9 Obara, C. J.: Boundary-Layer Visualization for Flight Testing. NASA CP 2413, 1986, presented at NASA/SAE/AIAA/FAA Laminar Flow Certification Workshop, Wichita, Kansas, April 15-16, 1985.

10 Johnson, C. B.; Carraway, D. L.; Hopson, P.; Tran, S. Q.: Status of a Specialized Boundary- Layer Transition Detection System for use in the U.S. National Transonic Facility. ICIASF Paper No. 87CH2449-7, Presented at International Congress on Instrumentation in Aerospace Simulation Facilities, Williamsburg, Va., June 22-25, 1987.

11 Bellhouse, B. J.; Schultz, D. L.: Determination of Mean and Dynamic Skin Friction, Seperation and Transition in Low-Speed Flow with a Thin-Film Heated Element. Journal of Fluid Mechanics, Vol. 24, Pt. 2, 1966.

Published in, Proc. of the International Symposium on Non-Steady Fluid Dynamics, ASME FED Vol. 92, Toronto, Canada, June 4-7, 1990, pp. 253-258.

CONVECTIVE RESPONSE OF A WALL-MOUNTED HOT-FILM SENSOR IN A SHOCK TUBE

A. Sidney Roberts, Jr.,[1] Kelly R. Ortgies[2] and Ehud Gartenberg[3]
Department of Mechanical Engineering and Mechanics
Old Dominion University, Norfolk, Virginia USA

and

Debra L. Carraway[4]
NASA Langley Research Center
Hampton, Virginia USA

ABSTRACT

Recent efforts with arrayed hot-film sensors, maintained at constant temperature and mounted flush with an airfoil surface, are directed toward detecting the various modes of change in the boundary layer flow regimes. Shock tube experiments have been performed in order to determine the response of a single hot-film element of a sensor array to transiently induced flow behind weak normal shock waves. The experiments attempt to isolate the response due only to the change in convective heat transfer at the hot-film surface mounted on the wall of the shock tube. The experiments are described, the results being correlated with transient boundary layer theory and compared with an independent set of experimental results. One of the findings indicates that the change in the air properties (temperature and pressure) precedes the air mass transport, causing an ambiguity in the sensor response to the development of the velocity boundary layer. Also, a transient, local heat transfer coefficient is formulated to be used as a forcing function in an hot-film instrument model and simulation which remains under investigation.

INTRODUCTION

Shock tube experiments have been performed to determine the response of one element of an arrayed hot-film sensor, mounted flush on the side-wall of the tube, to the flow induced by weak normal shock waves. The experiments attempt to isolate the response of the anemometer due only to the change in convective heat transfer at the hot-film surface. The work is the result of collaborative efforts with NASA Langley Research Center, Hampton, Virginia, USA, where a primary goal has been the refinement of a hot-film sensor able to detect the development of perturbations in the laminar boundary layer.

The continuing effort to develop this type of constant temperature hot film sensor is specifically aimed at the detection of the various types of identified modes of boundary layer instability, for example Tollmein-Schlichting waves, Goertler and crossflow vortices (Wusk, et al., 1988). The particular effort with the arrayed sensors, concentrating on both the sensor design, fabrication and signal processing, is intended to provide an experimental tool capable of detecting spanwise patterns of vortical striations with a spatial resolution better than two and one-half millimeters (0.1 inch) per wavelength and a frequency response up to 1×10^5 Hz (Wusk, et al., 1988 and Ortgies, 1989). The ultimate goal is to qualify these sensors for flight tests in order to gather data concerning laminar boundary layer instabilities under operational conditions. Among the performance parameters characterizing the sensor, the limit of its time response is the most difficult one to predict. A local variation in the convective heat transfer characteristic of the airflow will influence both the sensor and the surrounding areas of the substrate. An analytic effort to understand the influence of the substrate involvement on the arrayed sensor response was carried out by McRee and Judge (1987), who set out to model the complete instrument behavior starting with both convection and conduction heat dissipation modes and ending with an electronic circuit response. Initially, this model used a sinusoidally varying convective heat transfer coefficient as a forcing function in order to predict the anemometer (sensor, substrate and circuit) response to a cyclical change in the flow conditions. However, to make a prediction of the sensor's response due to vortical flow conditions, it was necessary to input a time dependent convective heat transfer coefficient characteristic of vortical flows, but such a function was not available.

In order to produce some characteristic values of the convective heat transfer coefficient resulting from actual transient flow conditions, recourse was made to shock tube testing. This decision was supported by the fact that the flowfield induced by the moving compression wave approximates a step velocity change with respect to time. Furthermore, the flow behind the shock wave both in the free

[1]Professor
[2]Graduate Research Assistant
[3]Research Assistant Professor
[4]Aerospace Engineer

stream and in the boundary layer, is amenable to analytic treatment (Anderson, Jr., 1982, and Mirels, 1955 and 1956 respectively).

The following sections describe in turn the experimental methods, analysis of the results, and the conclusions drawn. The experiments were carried out in a 15.2 cm (6 inch) diameter shock tube at the Instrument Research Division of NASA Langley Research Center. The hot-film sensors were mounted on a plug fitted flush with the inside surface of the cylindrical test section wall as described below. The flow velocity was deduced from piezoelectric pressure transducer data, the change in convective heat transfer from the hot-film anemometer, and the results were compared with those from Mirels' transient boundary layer theory (Mirels, 1956) and the experimental shock tube data of Davis and Bernstein (1969).

EXPERIMENTAL METHOD

An array of four nickel film sensors (0.51x0.76 mm each) was mounted on an insulating foam plug inserted through the cylindrical wall of the shock tube. Only one sensor was active, and maintained at constant temperature during the experiments. The built-up sensor presented a roughness element of 0.1 mm or less at the inside wall surface in the test section. A piezoelectric pressure transducer was mounted opposite the hot-film sensor plug. Another piezoelectric pressure transducer was mounted 61.0 cm upstream from the hot-film sensor, allowing an independent time-of-flight measurement of shock motion. Figure 1 is a schematic diagram showing the shock tube layout, position of sensors, and the instrumentation assembly. It may be noted that the 7.62 cm (3 inch) diameter driver section is followed immediately by a diverging section with an area ratio of 4. At low supersonic shock speeds, where the induced free stream flow is subsonic, this diverging section acts as a subsonic flow diffuser.

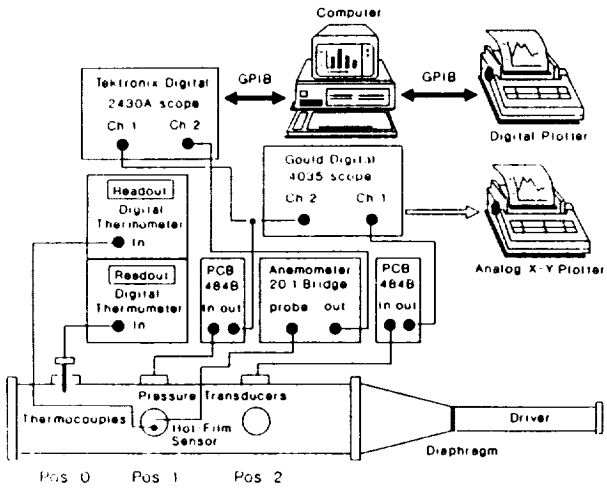

Figure 1. Equipment Schematic for Shock Tubes Tests

The sensor was set to a nominal temperature of 380 K (an overheat of about 85 K above ambient) and allowed to reach a thermal steady state with the plug and the ambient air prior to breaking a Mylar diaphragm in the driver (air) section. The sequence of tests was performed at three sensor temperatures, corresponding to overheat ratios (ratio of the heated sensor resistance to the cold sensor resistance) of 1.3, 1.4 and 1.5. The effect of increasing the sensor temperature was to increase the anemometer sensitivity to flow fluctuations and increase the frequency response of the anemometer. The substrate temperature, measured at the thermocouple location on the plug surface, maintained approximately the same average temperature (22.8 ± 0.6 °C) throughout the series of tests for all three overheat ratios.

Before each test, the end plate of the shock tube was removed and the debris remaining inside the tube due to the diaphragm rupture was blown out, in order to minimize the amount of flow disturbance present during a test. The Mylar diaphragm was cut from a sheet with thickness corresponding to an estimated driver rupture pressure, and the diaphragm was inserted into its holder and placed in position in the shock tube (see Fig. 1). A computer program was implemented to initialize the Tektronix Oscilloscope parameters and store the anemometer digitized voltage signals and position 1 pressure transducer response data. After these procedures were completed, the driver section was pressurized until the diaphragm ruptured. At the time of the diaphragm rupture, the maximum driver pressure attained was recorded from a Wallace and Tierman pressure gauge. Subsequently, the oscilloscope captured the transient anemometer and "position 1" pressure transducer response data as the shock passed the hot-film sensor. Tests were conducted at driver gauge pressures of approximately: (1) 179 kPa (26 psig), (2) 338 kPa (49 psig), (3) 386 kPa (56 psig), to (4) 545 kPa (79 psig). In most tests of interest, the ratio of the shocked gas to undisturbed air pressure, P_2/P_1, was 1.3. At each of the driver pressures, tests were repeated for which the time base of the oscilloscope was changed from 500 μs/div to 20 μs/div. The maximum experiment time, determined by the arrival of the reflected shock, was about 3 milliseconds.

The active hot-film sensor in the constant temperature anemometer circuit was found to have a frequency response (weakly variable with overheat ratio) of about 100 kHz, using a 30 kHz square wave test. Data acquired by the oscilloscope for each test, the passage of the shock front across the sensor station, was down-loaded to a floppy disk. Knowing the anemometer circuit and overheat parameters, the voltage versus time values were transformed to convected power versus time values (or local Reynolds numbers) as an indication of the time dependent convection heat transfer coefficient. The initial conduction and radiation heat transfer rates prior to shock passage remained essentially unchanged as the transient boundary layer flow developed over the sensor, because of the large thermal inertia of the sensor substrate and the constancy of the sensor temperature.

RESULTS

Figure 2 displays the anemometer response versus time along with the corresponding pressure transducer response. Incident and reflected shock transients are clearly distinguished, and on an expanded time base both transducers demonstrate a rise time corresponding to $1x10^5$Hz (see Figure 5). The shocked gas pressure (P_2), taken from Figure 2 (a), in ratio with the ambient pressure (P_1) are used to determine the shock speed from normal shock tables for air; the deduced speed agrees to within one percent with the values from the independent time-of-flight measurements of the shock front between the pressure transducers. Test or experiment numbers are designated by the prefix, "Exp." in the figures. As noted previously,

the anemometer voltage signals (Figure 2 (b)) are transformed to convected power-versus-time results. The convected power results appear the same as those shown in Figure 2(b) after the dc-level reference power, prior to shock arrival, is subtracted. Two interesting features of the anemometer response received further study: the leading dip in convected power (reduced heat transfer from the sensor), and the initial decrease in the power convected away from the sensor surface during the first millisecond after the incident shock passes across the sensor. From shock speed measurements, the transit time of the shock across the sensor is about 2.0 microseconds. It is hypothesized that as the incident wave passes across the sensor, the step change in the shocked gas temperature precedes the development of the velocity boundary layer that begins to grow more slowly due to a mass transport lag. These effects are discussed in detail below.

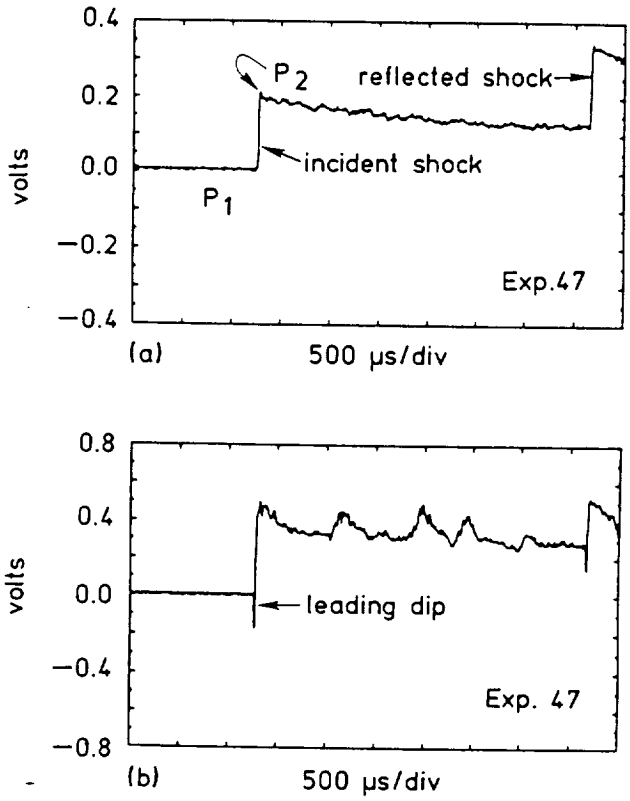

Figure 2. Signal Response at a Driver Pressure of 183 kPa (26.5 psig) for the (a) Pressure Transducer, and (b) Anemometer

Most of the data presented here are results from experiments performed at a low shock pressure ratio, P_2/P_1 = 1.28, which is the basis for the anemometer response in Figure 2. Figure 3, however, shows how the anemometer response dramatically changes when a stronger shock (P_2/P_1 = 1.60) is induced. While not well understood, the case in Figure 3(b) suggests a fully developed turbulent flow, quite different from the lower frequency, intermittent response found at the lower shock speed in Figure 3(a). A recent paper (Johnson and Carraway, 1989), describing experiments with hot films on flat plates in supersonic flow, attributes the intermittency to boundary layer transitional effects, and the lower amplitude, higher frequency signal to fully developed turbulent flow. The thrust herein is to treat the evidence for boundary layer development during the first millisecond of the low pressure ratio runs, and to correlate the data with boundary layer theory due to Mirels (1956).

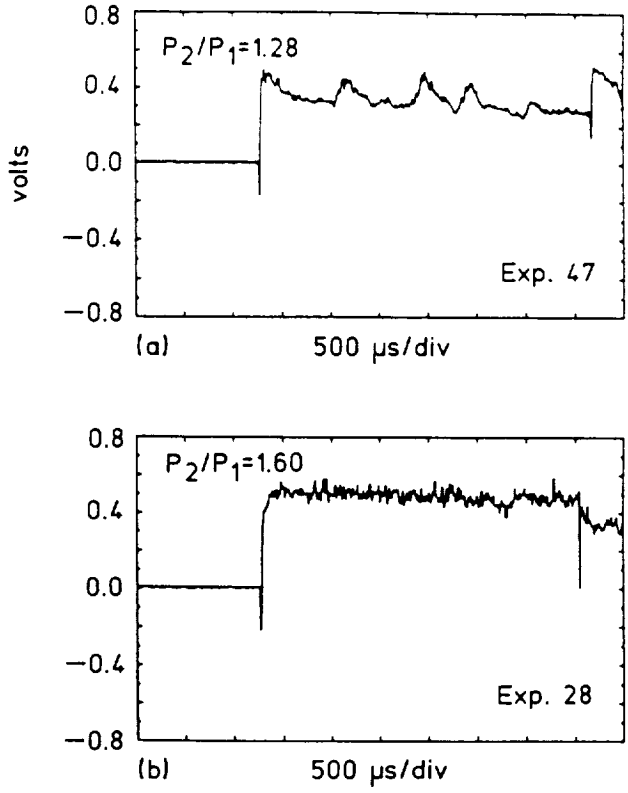

Figure 3. Comparison of Anemometer Response at Driver Pressures of (a) 183 kPa (26.5 psig), and (b) 543 kPa (78.8 psig).

Table 1 summarizes pertinent experimental findings in terms of directly measured quantities and deduced, calculated quantities.

The value P_4 is the driver gas pressure; P_1 is the undisturbed gas pressure; T_b is ambient temperature; T_{sub} is the substrate temperature (essentially unchanged during experiments); T_w is the sensor surface temperature, U_w is the shock speed; P_2/P_1 is the shocked gas pressure ratio; $\overline{U}_e$ is the induced freestream speed of flow behind the shock; T_e is the shocked gas temperature; T_r is the recovery temperature; and, $h^*(t)^{0.2}$ is the calculated theoretical convective heat transfer coefficient (Ortgies, 1989) for a turbulent boundary layer. The interpretation of a transient, turbulent boundary layer development during the first millisecond of the experiment shown in Figure 3(a) is based on Mirels' theory (1955 and 1956), where a steady boundary layer problem may be solved in the frame of reference of the moving shock. When the convected power versus time data, which according to the theory should be a power law relationship, is graphed logarithmically a straight line fit is found. In nondimensional Stanton number — Reynolds number form slope parameters of –0.17, –0.25, –0.18 are found respectively for the three cases reported in Table 1, and the corresponding correlation coefficients (r^2) are 0.827, 0.879 and 0.889. A comparison with the Mirels' theory, where the slope should be, -0.20, for turbulent

Table 1. Measured and Calculated Experiment Parameters†

Exp. No	P_4 (kPa) gauge	P_1 (kPa) absolute	T_b (K)	T_{rub} (K)	T_w (K)	U_w (m/s)	P_2/P_1	Over Heat Ratio	$\bar{U}_e$ (m/s)	T_e (K)	T_r (K)	$h^* \cdot t^{0.2}$ (W $ms^{0.2}/m^2K$)
	Measured								Calculated			
22	186	103	295	296	380	385	1.29	1.3	65	318	320	220
39	185	103	295	296	400	383	1.29	1.4	62	317	319	216
47	183	103	295	296	421	383	1.28	1.5	62	317	318	214

†Expected error in the parameters in implied by the number of significant figures reported.

boundary layer development, is shown in Figure 4. It is seen from Figure 4 that the experimental Stanton number is higher than theory predicts for the same Reynolds number. This trend is repeated for the other two test cases, which are not shown. Plotted with the theoretical and experimental heat transfer correlations in Figure 4 is the Stanton number correlation which fits the Davis and Bernstein (1969) experimental data set. There was no evidence of a laminar-to-turbulent transition, seen in the current work, even though the results fall well below the critical Reynolds number for flat plate boundary layer flow.

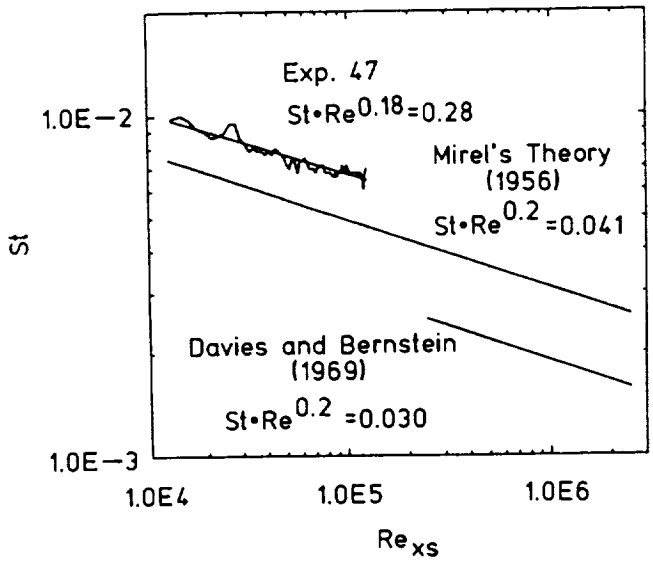

Figure 4. Comparison of Experimental and Theoretical Heat Transfer Results. Re_{xs} is a Reynolds Number Measured with Respect to the Shock Position

As noted earlier, an interesting development occurs as the shock passes the hot-film sensor. A very pronounced dip occurs in the anemometer signal a few microseconds after the shock front reaches the sensor. Figure 5 shows the experimental data record on a 20μs/div time-base for an expanded view. Excited by the transient, the hot-film sensor response drops negatively until it reaches a minimum. It then increases sharply to realize a maximum within the 25μs time frame. During the course of the experiments, the magnitude of the voltage drop was seen to increase with increasing driver pressure P_4, as illustrated in Figure 5. As seen in Figure 5(a), when P2/P1 = 1.28, the drop was approximately 0.27 V. In Figure 5(b), where P2/P1 = 1.61, the drop was 0.55V. The data obtained was repeatable and the trend was without exception. No other experimental works have been found which discuss this leading negative-going pulse in the hot-film sensor response.

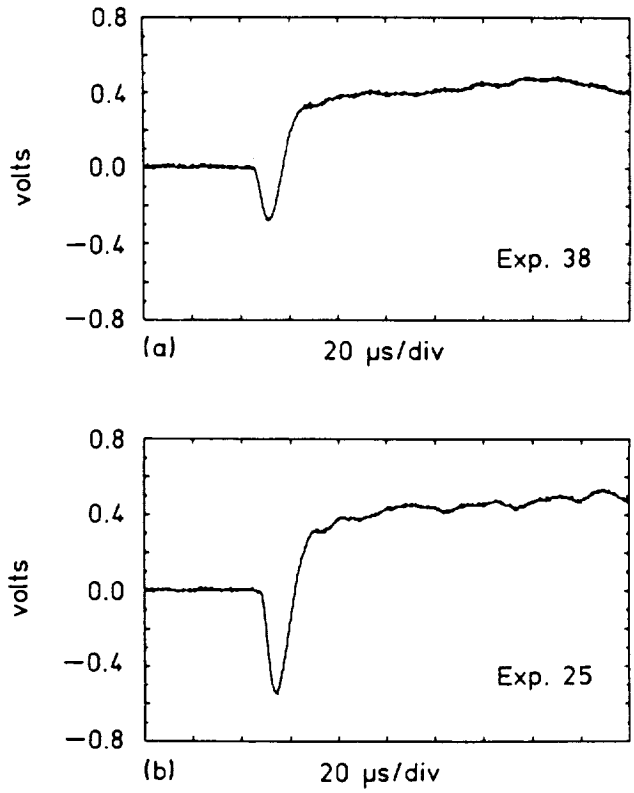

Figure 5. Anemometer Response Showing Wave Transit Effect, P_4 = (a) 181 kPa, and (b) 531 kPa Gauge Pressure

A hypothesis is generated in order to explain the phenomenon of this drop in voltage, which corresponds to a decrease in the convective heat transfer from the hot-film sensor. It is known that as the shock passes across the hot-film sensor, the temperature of the

free stream gas behind the wave rises abruptly. It is further hypothesized that the step change in free stream temperature across the shock wave precedes the development of the velocity boundary layer because of a mass transport lag. Consequently, natural convective conditions may prevail just prior to the build-up of the shocked gas velocity boundary layer, but sensor/substrate to free stream gas temperature differences are now less. Thus, a smaller temperature difference along with natural convective heat transfer produces a sudden decrease in the heat flux from the sensor. Note that the substrate adjacent to the sensor maintains a temperature, T_{sub}, some 22°C below the shocked gas temperature, T_e (see Table 1). The current supplied to the hot-film sensor to maintain its constant operating temperature is decreased, which produces the initial drop seen in the experimental results for the first few microseconds of the test. At the start of the velocity boundary-layer growth the heat flux from the sensor is a maximum since the forced convective heat transfer coefficient becomes large. As the velocity boundary layer grows, the heat flux from the sensor decreases and the anemometer supplies less current to maintain the constant operating temperature of the hot-film sensor, which is the effect detected during the first millisecond and seen more clearly in Figure 3(a).

The estimate of a natural convective heat transfer coefficient is made by assuming a characteristic length equal to the area of the sensor divided by the length of the sensor (0.762 mm). It is also assumed that this characteristic length can be associated with a small wire (horizontal cylinder). With these assumptions, Morgan (1975) defines a natural convective correlation for various ranges of Grashof numbers. After calculating the Grashof number (approximately 0.12) and applying the correlation given by Morgan (1975), an estimate of the natural convective heat transfer coefficient is made yielding a value of $8.0 \times 10^1 W/m^2 \cdot K \pm 25$ percent due to the uncertainty in the correlation.

The transient convective heat transfer coefficient is divided into three parts. The first is an estimate of the amount of natural convection occurring before the start of the test from the initial power being supplied to the sensor to maintain its operating temperature. Second, a heat transfer coefficient is needed from time t=0 to approximately t=25 μs which is based on the prior hypothesis. Finally, the transient response derived from Mirels (1956) for turbulent boundary layer development is used for times greater than measured shock transit times.

During the time that the output voltage drops dramatically and rises again ($0<t<25\mu s$), the heat transfer coefficient is assumed to be a constant. The calculated time for the shock to pass across the sensor ranges from 1.8 to 2.0 μs at the tested driver pressures, based on time-of-flight measurements. The measured time half-way across the negative anemometer pulse is on the order of 5 to 12 μs. A discrepancy exists between the calculated shock transit time across the sensor and the anemometer measured transit time. This discrepancy may be attributed in part to the lag associated with the mass transport of the gas behind the shock, but is more probably related to the response time of the anemometer. The inverse transit time of the shock moving across the sensor is larger by a factor of 5 than the frequency response of the anemometer (~100 kHz). Consequently, the anemometer may not be responding fast enough to capture the full effect of the shock transit.

The natural convective value of heat transfer coefficient is assumed valid during the shock transit time. The transient portion of the convective heat transfer coefficient is of the form shown in Table 1 for a turbulent boundary layer. By combining the three portions, a complete heat transfer coefficient is estimated for a given set of test conditions. Figure 6 shows a convective heat transfer coefficient curve for Exp. 47. Thus, a computer model can simulate the shock tube test cases using the combined heat transfer coefficient as a forcing function.

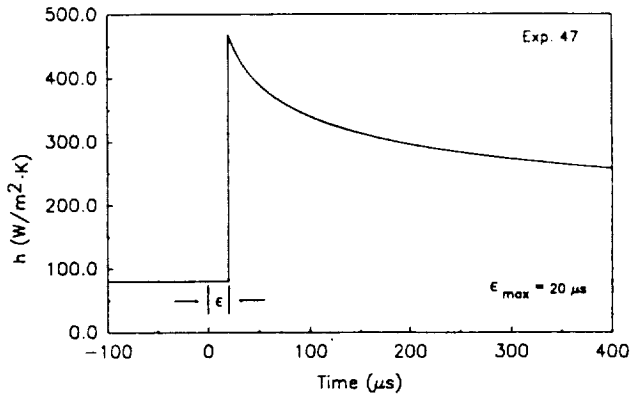

Figure 6. Transient Convective Heat Transfer Coefficient

CONCLUSIONS

The transient response of the hot-film anemometer has been analyzed with a combination of results. First, repeatable data is easily obtained over the range of driver pressures used. The experimental comparison of the data with transient, turbulent compressible boundary layer theory seems to be valid within the first millisecond of experiment time at driver pressures of approximately 179 kPa (26.0 psig). Even at these driver pressures with statistically valid curve fits, the theoretical Stanton number for turbulent flow is less than the Stanton number obtained from the experimental data. The slopes are similar (see Figure 5), but the coefficients have different values, and the current results find a turbulent boundary layer at Reynolds number below 1×10^5. After the first millisecond the anemometer response becomes intermittent at the lower pressure ratios. This may be due to flow disturbances occurring inside the shock tube due to the diffuser, microcavities from the ports in the walls, or unsteady turbulent free stream flow.

The comparisons with other experimental work (Davies and Bernstein, 1969) indicate qualitative agreement. The analysis of the anemometer response at the higher driver pressures must be left to future testing under more strictly controlled conditions. A surprising result of this work is the occurrence of reduced convected heat transfer as the shock wave passes over the sensor. This effect has not been clearly demonstrated in the other experimental works examined by the authors. While an hypothesis is offered, further investigation is needed to fully understand this phenomenon.

The computer simulation of the anemometer response (McRee and Judge, 1987) is to be investigated in an extension of this project with hope that agreement between these experimental results and

predicted anemometer response will tend to validate the hot-film anemometer model.

ACKNOWLEDGEMENT

The study reported here was partially supported by NASA Langley Research Center grant NAG-1–735, managed by the Old Dominion University Research Foundation.

REFERENCES

Anderson, Jr., John D., 1982, Modern Compressible Flow, McGraw-Hill Book Co., New York, N.Y, Chap. 7.

Davies, W. R. and Bernstein, L., 1969, "Heat Transfer and Transition to Turbulence in the Shock-Induced Boundary Layer on a Semi-Infinite Flat Plate," J. Fluid Mechanics, Vol. 36, pp. 87–112.

Johnson, C. B. and Carraway, D. L., 1989, "A Transition Detection Study at Mach 1.5, 2.0, and 2.5 Using a Micro-Thin Hot-Film System", Proc. of the International Congress on Instrumentation in Aerospace Simulation Facilities, ICIASF '89, Goettingen, West Germany, pp. 82–94.

McRee, G. J. and Judge, D. M., 1987, "Model of Hot-Film Sensor with Substrate," Proc. of the International Congress on Instrumentation in Aerospace Simulation Facilities, ICIASF '87, Williamsburg, VA, pp. 350–355.

Mirels, H., 1955, "Laminar Boundary Layer Behind Shock Advancing into Stationary Fluid," NACA TN 3401, Washington, D.C..

Mirels, H., 1956, "Boundary Layer Behind Shock or Thin Expansion Wave Moving into Stationary Fluid," NACA TN 3712, Washington, D.C.

Morgan, T., 1975, "The Overall Convective Heat Transfer from Smooth Circular Cylinders," Advances in Heat Transfer, Vol. 11, Academic Press, New York.

Ortgies, K., 1989, "Transient Hot-Film Sensor Response in a Shock Tube," Masters thesis, Department of Mechanical Engineering and Mechanics, Old Dominion University, Norfolk, VA; also, NASA CR 181838.

Wusk, M. S., Carraway, D. L. and Holmes, B. J., 1988, "An Arrayed Hot-Film Sensor for Detection of Laminar Boundary-Layer Flow Disturbance Spatial Characteristics," AIAA Paper 88–4677–CP, AIAA/NASA/AFWAL Sensors and Measurement Technologies Conference, Atlanta, Georgia.

INFRARED SURFACE IMAGING AS A FLOWFIELD DIAGNOSTIC TOOL

by Ehud GARTENBERG, A. Sidney ROBERTS, Jr., and Gregory V. SELBY

Department of Mechanical Engineering and Mechanics
Old Dominion University
Norfolk, Virginia 23508 USA

Abstract

An infrared imaging system supported by a dedicated image processing system was evaluated as a diagnostic tool for aerodynamic research. The results reported herein characterize the system's capability in performing a variety of experimental investigations such as: temperature transients, air velocity distrubutions, capture of vortices, boundary layer flows and separated flows over a flat plate with a two-dimensional rearward-facing step.

1. INTRODUCTION

Infrared imaging systems are proving to be convenient experimental tools for surface temperature mapping. Their main advantages over the classical methods may be summarized as follows:

1) They are non-intrusive, thus permitting measurements without interfering with the phenomenon under investigation and also without the need to expose the sensor itself to potentially hostile environments.

2) They map continuously the whole region of interest (rather than discrete points), thus producing "frozen" pictures of the entire field, a feature of great importance when studying unsteady phenomena.

3) They have the output displayed on video screen, permitting real-time evaluation of the results, and allowing the investigator the flexibility of corrective actions while running the experiments.

The use of these systems has been extended to heat transfer research, e.g., from buildings to their surroundings [1]. There, the actual conditions were simulated by scale models in a stratification wind tunnel. Thereafter, the experimental data gathered as temperature contours were used to calculate local heat transfer coefficients. a logical follow-up is to apply this method to aerodynamic research by taking advantage of the inherent heat exchange phenomena between an aerodynamic surface and the surrounding fluid flow.

Basically speaking, there are two radically different ways of heating an aerodynamic surface and obtaining temperature distributions due to the energy interaction with the free stream. One method is through passive heating due to recovery of the freestream temperature in the stagnation areas and the boundary layer [2]. The other is by uniform active heating (e.g. by electrically heated elements) and variable local cooling due to the flowfield interaction with the surface.

For quantitative assessment, the raw IR data is digitally processed by dedicated software for image enhancement, allowing the capture of small local differences in temperature, that are barely detectable by the human eye in the original image [3].

The work reported herein was aimed at exploring the feasibility of using IR imagery in aerodynamic research, using actively-heated surfaces as targets, an AGA system for detection and imagery and image processing software for data extraction.

2. THE IR IMAGING AND PROCESSING SYSTEM

The nucleus of the IR imaging system is an AGA Thermovision 782 camera equipped with 20°x20° lens coated for optimal response in the short wave (5 μm) infrared spectrum. At 0.5-m distance, the field of view is 0.15 x 0.15-m. Throughout the reported experiments, the aperture was kept at f/1.8. The optical scanning system is syncronized such that four fields of 100 horizontal lines each, produce one interlaced frame. The scanning rate is 25 fields per second. The scanned field is reproduced on a specially-designed black-and-white video display unit, which facilitates direct or relative thermal level measurements. The angular resolution of the system in the above configuration is 0.003 radians.

Proceeding of the 12th International Congress on Instrumentation in Aerospace Simulation Facilities (Sponsored by IEEE)
The College of William and Mary
Williamsburg, Virginia
June 22-25, 1987

The digital image processing is performed on a dedicated BMC IF800, model 20 personal computer with 64K bytes main memory plus an extra 128K bytes RAM PCB and two 5 1/4" disk drives. The color CRT display has graphics capability.

A DISCO 2.0 software package is used for the image processing and completely occupies a floppy disk in a read-only storage mode. Up to 36 individual images can be stored on the second floppy disk in a read-and-write access storage mode. The automatic aquisition capability of the system permits continuous recording of up to 16 images at an approximate rate of 1.5 Hz or lower. Although both the field and frame aquisition modes are available, only the field mode was used. A key feature of this program is the gradual assignment of eight tones of artificial colors (from black through blue, green, red, etc., to white), for corresponding grey shades in the original image. Such a display produces a color shade for each temperature band scanned by the camera. The user has the choice of getting temperature measurements at a certain point or along specified rows or columns, for given values of the input parameters (emittance, transmittance, ambient temperature, etc.). Also, the user can concentrate on a given range of temperatures, depending on the area of interest. The program is quite versatile and offers an abundance of processing and filtering choices; however, only the essentials have been reported herein.

3. FEASIBILITY STUDIES

The IR imaging system can be used in conjunction with actively-heated aerodynamic surfaces in two ways. One way is to suspend a thin heated wire across a flowstream and to monitor the temperature variations along it. Assuming that the heat conduction along the wire is negligible compared to the forced convection, this method is particularly effective in capturing wakes and vortices. The other approach is to bond heated wires or strips on aerodynamic surfaces and to proceed with the measurement as in the previous case. The latter method is particularly well suited for detection of separated-flow regions. When trying to apply these methods, the experimentalist is presented with some obstacles that are described below:

1. The wire material choice: The search for a suitable wire material was defined in terms of commercial availability in a variety of sizes, price, electrical resistivity, specific heat, temperature coefficient of electrical resistivity, thermal expansion and chemical stability. According to the aforesaid criteria, Chromel emerged as the best practical choice, followed by Constantan.

2. The emittance problem: Since Chromel wires and strips are supplied with polished surfaces, they have very low emittances (approximately 0.05 at room temperature). This fact raises two problems; first, because of the low emittance (and hence, high reflectance), one may get false signals from reflections of heat sources in the vicinity of the target. The likelihood of this phenomenon increases with the dimensions of the target (wire or strip). The second problem arises when the heated element is bonded to a substrate with a much higher emittance (e.g., wood). In this case, even though the substrate is at a temperature equal to or lower than the heated element, it will appear on the IR display as a much "brighter" and hence hotter object. This fact may cause severe problems in data reduction as the IR image is processed into an actual temperature field.

3. In the same context of a heated element bonded to a substrate, it is important to remember that the substrate is actively involved in the heat transfer process both in the conduction mode with the heated element and in the convection mode with the flowfield, thus inducing a phase lag in the target's time response. This complex coupled heat-transfer analysis in conjunction with measurements involving hot-film sensors is treated in [4].

4. The resolution problem: In terms of measurement accuracy, the best approach is to work with a target (heated wire) as thin as possible. This arrangement gives a faster time response and minimizes the heat conduction along the wire, background reflection, flow contamination and boundary-layer tripping. However, such a choice is highly detrimental from the IR imaging system's point-of-view. The problem arises when the angle through which the target is viewed by the camera falls below its angular resolution. This means that the camera's IR detector will get less photons from the target than it would get from a target wide enough to fill a whole pixel. Practically, this translates into reported temperatures lower than the actual ones. The low emittance of the wires only aggravates the problem. A possible solution to this problem is to assign emittances lower than the actual ones in order to compensate the detector for its lack of saturated target area. This corrected emittance can be determined by calibration versus a known target temperature. It must be realized that since the result of the calibration is influenced by:

a. target distance
b. target size
c. target true emittance
d. the lens' field of view,

a specific calibration is good only for the particular conditions under which it was performed. Therefore, each test configuration requires its own calibration.

5. The out-of-focus background: When scanning targets at very close distances, the background may be out-of-focus, causing its emitted photons to be "smeared" out, contributing an erroneous signal at the detector. This may cause

abnormally (false) low temperatures to be attributed to the background. While a solution was not found for this situation, one should be aware of its existence.

6. The flow regime influence on heat transfer coefficients: When making measurements of convective heat transfer phenomena, one has to remember that the flow may be laminar or turbulent, thus exhibiting different heat transfer coefficients in the same field of view. Therefore, differences in temperatures should be analyzed carefully in order to trace them back to their origin; namely, either changes in velocity or changes in flow regime or both.

The aforesaid points illustrate the range of problems that were encountered during this experimental research. Simple flowfield experiments were initially chosen in order to ease the task of resolving the IR imaging and data reduction problems.

4. EXPERIMENTAL RESULTS

Several different experiments were performed in order to demonstrate the various possible applications of the IR imaging system. In what follows, the experiments and their objectives will be presented to illustrate the experimental method.

1. Air-jet heated suspended wire:

The purpose of this experiment was to check the dynamic capability of the AGA system by monitoring a temperature transient. The general experimental layout is shown in Figure 1. A 0.003" Chromel-Constantan uninsulated thermocouple wire was placed 0.33-m above the nozzle of a heat-gun. At time t=o, the power switch was turned from the "heat" position to the "cool" position, while the air continued to flow cooling the heating element of the heat-gun. The airflow was aimed at the region of the thermocouple junction, thus enabling a comparison of the data obtained through the AGA system with the thermocouple output. Sixteen consecutive frames of the suspended wire were taken at 0.7 sec. intervals. In parallel, the thermocouple output was recorded on a strip chart-recorder. The results are displayed in Figure 2, where one can see qualitative agreement between the results obtained with the two independent instruments. The discrepancy at t=o is due to the relatively slow initial time response of the chart-recorder. Ten more identical experiments were carried out at different times with similar results, thus proving their repeatability. However, when the same experiment was run with much larger diameter wires (0.015"), the results obtained were not satisfactory, with the AGA system consistently showing, during early times, higher temperatures than the thermocouple readings. This was explained by the possible interference of the heat-gun IR radiation which reflected from the wire to the camera.

2. Electrically heated suspended wire locally cooled by an airstream:

The purpose of this experiment was to check the resolution capability of the AGA system in monitoring temperature gradients along the wire. The test system for this experiment was identical to that shown in Figure 1, except for the fact that the 0.003" thermocouple wire was heated by an electric current, and the local cooling was achieved with a low-speed airjet (1.5 cm in diameter), flowing perpendicularly to the wire. The effective air velocity at the wire was checked with a Pitot probe and found to be $\approx$ 2.5 m/sec, which gives at 22C a Reynolds number based on the wire diameter of $Re_D \approx 11.5$. In this regime the flow is laminar and the Nusselt number from a standard correlation [5] is about 2.0, giving a heat transfer coefficient of h = 725 W/m^2K. Alternatively, from the IR image as shown in Figure 3, the area of maximum effective cooling is about 1 cm long, and the wire temperature ($\sim$ 42C) is about 20C above the jet temperature. With an applied voltage of 22V and a total wire resistivity of 152 Ω, the current through the wire was 0.144 A, which resulted in a heat dissipation rate of 0.034 W at the location of maximum cooling. The subsequent local heat transfer coefficient of 726 W/m^2K is in fortuitous agreement with the result determined from the correlation.

This experiment and the crude calculation comparing its result with a standard correlation for forced convective heat transfer suggests that through Stanton number correlations, flowfield velocity variations can be traced back to local temperature measurements.

3. Measurements in the wake of a cylinder:

Measurements were made in the wake of a 0.1-m diameter cylinder. These tests were conducted in a 3'x4' low-speed wind tunnel. The 0.003" wire was placed perpendicularly to the flow direction and to the axis of the cylinder at 0.3-m from the wind tunnel floor and parallel to it. The cylinder was placed five diameters upstream of the wire and the IR camera was located 0.5-m downstream of the wire, looking upstream at both the wire and the cylinder as shown in Figure 4. At a freestream velocity of 14.3 m/sec, the Reynolds number $Re_D \approx 90000$. The thermocouple wire could be used alternately as a thermocouple and as an electrically heated sensor wire. The wire's thermal dissipation maintained its temperature at about 50C above the freestream value. Figure 5 shows the result of the experiment. Although the mean air velocity in the wake is lower than in the freestream, the heat transfer coefficient is higher due to the turbulent vortical flow. In particular, it is interesting to observe the effect of the main vortices at the wake's edges where the heat transfer rate is visibly higher than at its core. In a related experiment, a 2-cm diameter cylinder

was placed 24 diameters upstream of the heated wire at an air velocity of 14 m/sec. The temperature distribution along the wire is presented in Figure 6. Such experiments were carried out with wires placed between 8 to 32 diameters downstream of the cylinder. The wake's signature on the wire was very visible on the IR display, proving the system's capability of capturing the effect of wakes even with wires at relatively large distances behind the source of the disturbance.

4. Flat plate measurements:

The last two experiments to be reported herein were aimed at reproducing two classical experiments in aerodynamics: the laminar velocity and thermal boundary layer development along a flat plate at zero angle-of-attack and flow over a rearward-facing step. For this purpose, a vertical flat plate with a 1.0-m span, 0.3-m chord and a sharp leading edge was placed vertically in the wind tunnel previously described. A 0.003" Constantan wire was wrapped three times around the plate chordwise and at 1-cm pitch. A 2" wide aluminum tape was applied over the wires, from the leading to the trailing edge to ensure uniform surface texture and heating. The wires were heated by a constant electrical current. The IR camera was placed laterally 0.5-m from the target plate, behind another plate (parallel to the first one) with a circular hole in it through which the camera could view the target. This was done in order to prevent vortices shedded from the camera from interfering with the flow over the target plate. The result for a velocity of 14 m/sec. is presented in Figure 7. The Reynolds number at a distance x=16-cm from the leading edge is 131000, so that the boundary layer is laminar all along the plate [6]. The temperature irregularity at the leading edge of the plate was due to IR background reflections from the aluminum tape. The result obtained is self evident. For comparison purposes, one may use Reynolds' analogy (i.e., Prandtl number of unity) and therefore assume similarity between the velocity and thermal boundary layer growth. Such a comparison with the data available in the literature [7] shows that the measured profile is qualitatively correct, indicating the true potential of the IR imaging system, i.e., simultaneous temperature mapping along a line, and ultimately over a surface, with minimal effort on the part of the investigator.

Finally, qualitative data relating to flow over a rearward-facing step will be reported. On the same flat plate described earlier, a 30-degree wedge terminating with a 5-cm long and 2-cm high step was fixed to the plate, thus creating a rearward-facing step geometry for the flow. The step was placed over the heated strip reported earlier, and was covered with aluminum tape in order to maintain a uniform emittance in the target area. The results for an air velocity of 14 m/sec. are shown in Figure 8. One can clearly observe the increase in the flat plate's temperature due to the low velocities just behind the step. As the flow approaches the reattachment point, the temperature goes down once again until the minimum is achieved in the vicinity of the reattachment point, in agreement with the expected behavior. Further downstream, the temperature goes up as the boundary layer starts redeveloping. An interesting point to note is that the flow reattachment occurs about 12-cm downstream of the step (about 6 height steps), which is in good agreement with results reported in the literature [8].

5. SUMMARY

The infrared imaging system, when properly and carefully used, has proven to be a viable experimental tool applicable to aerodynamic research. The scanning of actively-heated aerodynamic surfaces can produce very useful data on forced heat transfer, velocity distribution, boundary-layer flows, separated flows and wakes. The method also has a limited capability for capturing transients. This limitation is not conceptual but is due primarily to the low scanning and data aquisition rates characteristic of the available hardware.

Typical results have been reported here for a series of simple aerodynamic experiments. Confidence has been gained in the use of IR surface imaging as a flow diagnostic device, especially since the relatively crude initial experiments display good data repeatability for both steady-state and transient temperature fields. Work is continuing in order to develop the technique as a low-speed quantitative tool with obvious extensions to high-speed aerodynamics.

ACKNOWLEDGEMENT

The authors wish to acknowledge Mr. E. W. Cronce and Mr. K. Ferguson from the College of Engineering and Technology at Old Dominion University for their dedicated technical support of this research.

This research was supported in part by NASA grant NAG-1735.

REFERENCES

1. Meroney, R. N., Studying the Convective Heat Transfer from a Building Model with Infrared Camera Techniques, ASME Paper No. 78-WA/HI-58.

2. Schmitt, R. L. and Chanetz, B. P., Experimental Investigation of Three Dimensional Separation on an Ellipsoid-Cylinder Body at Incidence, AIAA-85-1686.

3. Bouchardy, A. M. Durand, G. and Gauffre, G., Processing of Infrared Thermal Images for Aerodynamic Research, Applications of Digital Image Processing, April 19-22, 1983, Geneva, Switzerland, pp. 304-309.

4. McRee, G. J. and Judge, D., Proceedings of the 12th International Congress on Instrumentation in Aerospace Simulation Facilities, College of William and Mary, Williamsburg, Virginia, June 22-25, 1987 (present Congress).

5. Wong, H. Y., Handbook of Essential Formulae and Data on Heat Transfer for Engineers, Longmans, 1977, p. 76.

6. Schlichting, H., Boundary Layer Theory, McGraw-Hill, 6th ed., 1968, p. 39.

7. Schlichting, H., Op. Cit., p. 132.

8. Selby, G. V., Phenomenological Study of Subsonic Turbulent Flow over a Swept Rearward-Facing Step, Ph.D. Dissertation, University of Delaware, June 1982.

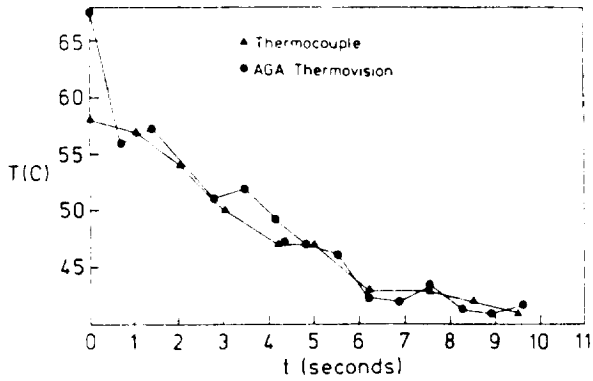

Fig 2: Heat—gun airstream cool—down process as monitored through a 0.003" thermocouple wire suspended at 33 cm above the nozzle

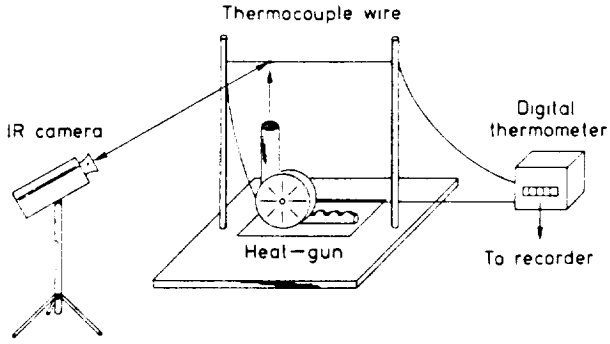

Fig 1: Experimental set—up for the air—jet heated suspended wire.

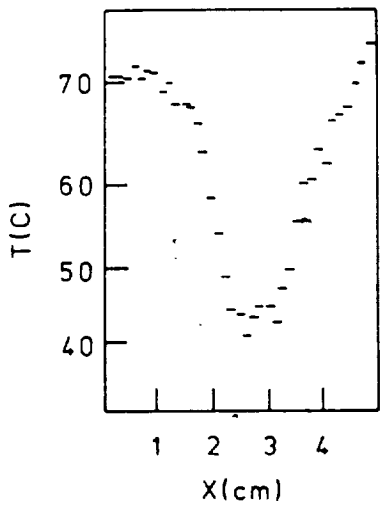

Fig. 3: Temperature variation along a 0.003" electrically heated wire placed in a 2.5 m/sec. airjet at 24C.

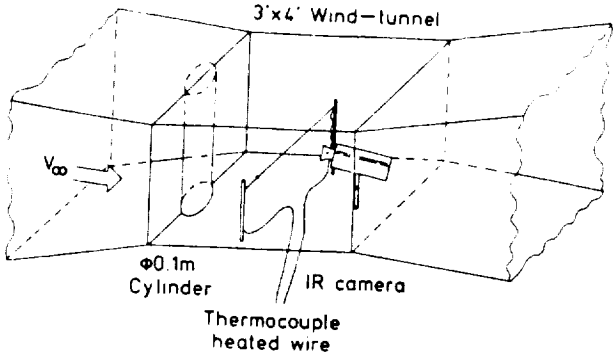

Fig. 4: Experimental layout for IR measurements of a heated wire in the wake of a cylinder

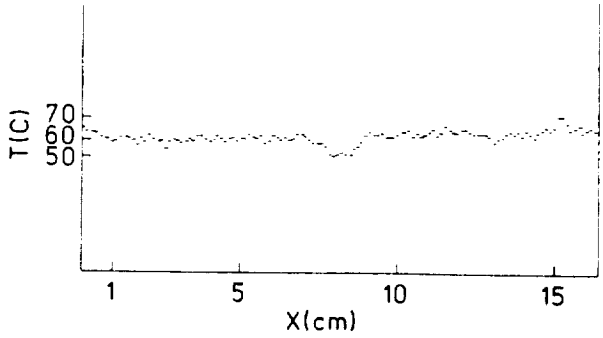

Fig. 6: The wake of a 2 cm diameter cylinder as captured on a 0.003" electrically heated wire placed 24 cylinder diameters downstream. $Re_D = 18,000$.

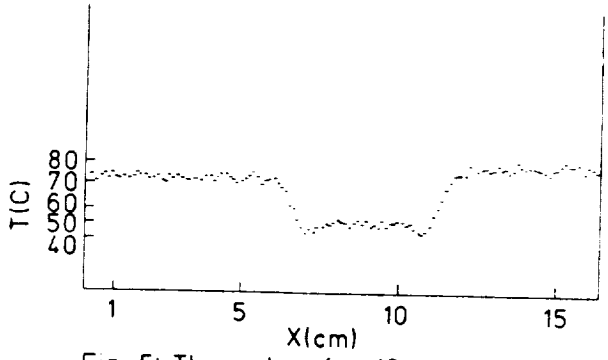

Fig. 5: The wake of a 10 cm diameter cylinder as captured on a 0.003" electrically heated wire placed 5 cylinder diameters downstream. $Re_D = 90,000$.

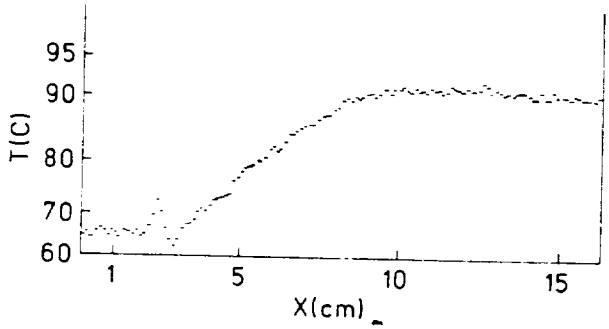

Fig. 7: Temperature distribution along a heated flat plate. $V_{air} = 14$m/sec.

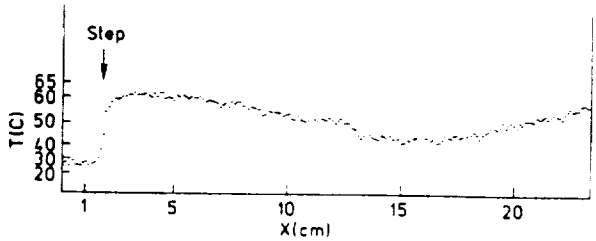

Fig. 8: Temperature distribution over a heated plate with a rear facing step. $V_{air} = 16$m/sec. Step height=2 cm

Ehud Gartenberg, B.S. and M.S. in Aeronautical Engineering from the Technion, Haifa, Israel; currently a Ph.D. student at the Department of Mechanical Engineering and Mechanics, Old Dominion University. His professional experience is mainly in testing aeronautical and propulsion systems.

A. Sidney Roberts, Jr., with B.S. and Ph.D. degrees in Nuclear Engineering from N.C. State University and the M.S. in Mechanical Engineering from the University of Pittsburgh, PA, USA, has general interests in power/energy conversion systems and particular interests in experimental fluid mechanics and heat transfer. At Old Dominion University, where he is Professor of Mechanical Engineering and Mechanics, research has been accomplished recently in the areas of the melting problem, creeping flows, energy and mass transfers in buildings, and the development of infrared imaging for flow field detection.

Gregory V. Selby has a B.S. degree in Aerospace Engineering from the University of Virginia and M.S. and Ph.D. degrees from the Mechanical and Aerospace Engineering Department of the University of Delaware. His professional experience includes 12 years with NASA performing engineering analyses on sounding rocket systems and conducting research in fluid mechanics. He is currently an assistant professor at Old Dominion University with research interest primarily in the areas of flow visualization, low-speed drag reduction and control of separated flows.

AIAA'88

AIAA-88-2523-CP
Aerodynamic Investigation by Infrared Imaging

Ehud Gartenberg, A. Sidney Roberts Jr. and Griffith J. McRee, Old Dominion Univ., Norfolk, VA

AIAA 6th Applied Aerodynamics Conference

June 6-8, 1988/Williamsburg, Virginia

AERODYNAMIC INVESTIGATION BY INFRARED IMAGING

88-2523-CP

Ehud Gartenberg*, A. Sidney Roberts, Jr.**
and Griffith J. McRee***

Old Dominion University
Norfolk, Virginia 23529-0247

Abstract

Infrared imaging systems can be used to measure temperatures of actively heated bodies immersed in an airstream. This monitoring of the convective heat transfer process, provides also information about the interaction between the body and the flow. The concept appeals to Nusselt/ Reynolds numbers relations in order to produce data of interest from surface temperatures. Two test cases are presented and reference is made to analytical results: the mapping of a laminar jet and the temperature distribution along a constant power heated flat plate in laminar boundary layer regime. Although this research is currently focused on low speed aerodynamics, the extension to high speed aerodynamics, where the body undergoes frictional heating is of interest in this context, too.

Nomenclature

k	thermal conductivity
$\dot{q}_o''$	heat flux (per unit time per unit area)
T	absolute temperature
U	freestream velocity
X	coordinate value in stream-wise direction
θ	differential temperature ($= T_{wall} - T_\infty$)
ν	kinematic viscosity
Nu	Nusselt number
Pr	Prandtl number
Re	Reynolds number

1. Introduction

The traditional experimental tool in aerodynamics is the Pitot tube. Using the exchange principle between the kinetic energy of the flow and its pressure, this device measures pressures from which corresponding velocities can be determined. These measurements are by their very nature, pointwise valid and intrusive. For mapping a region of interest, the choices are either to move the probe from point to point within the flowfield, thus introducing uncertainties associated with time-dependent phenomena, or to introduce into the flow a pressure rake consisting of an array of individual probes, thus perturbing the flow exactly at the points of interest.

An alternative approach may use the principle of thermal exchange between the configuration of interest and the surrounding flow. Starting from this principle, one may assume that by measuring the temperature distribution over an aerodynamic surface, the local freestream velocity may be deduced through a Nusselt-Reynolds type relation approach. This concept is diagrammatically shown in Figure 1. With the renewed interest in high Mach number flows, where the aerodynamic and the thermal loads (with the resulting structural response) are coupled, the infrared imaging technique arises as a natural experimental choice. The advantages it offers are that it's non-intrusive, area-scanning, readily available and has plenty of supporting software and hardware that is developed not necessarily for aerospace applications, thus reducing instrument development costs.

In this research use was made of actively heated bodies and very low speed airflows in attempting to isolate every factor that may influence the measurements and assess quantitatively its influence on the final results. The main factors include:

1) The flow velocity
2) The heat exchange rate and surface overheat
3) The target material and its surface properties
4) The lens field of view
5) The camera distance to the target
6) The ambient temperature

With increasing airflow velocities and the respective Mach numbers, the concept of active heating should be discarded in favor of passive heating due to the increasingly higher recovery temperatures at the wall. The latter concept is valid as long as the gas in the immediate vicinity of the configuration stays radiatively non-participating. In the high Mach-number flow regimes (super-and-hypersonic) when the surrounding gas starts to be radiatively participating (and eventually chemically unstable), this technique maintains its vitality provided the sources of radiation are properly associated with their respective measured temperatures. However, in this paper results are reported for actively heated surfaces and low speed flows.

The target surfaces may be of two distinctive types:

* Ph.D. student, Aeronautical Engineer, Member AIAA
** Professor of Mechanical Engineering
*** Associate Dean, College of Engineering and Technology

1) They may be the aerodynamic configurations themselves, the data obtained being influenced also by boundary layer behavior, i.e., laminar, turbulent, transitional or separated.

2) They may be very thin (heated) wires, interfering to a minimum with the surrounding flow and thus particularly well suited to detect or map wakes, jets, shear-flows or any other non-uniform flows.

In the early phase of this investigation a series of experiments were designed and carried out in order to check qualitatively how this concept works. Widely different types of flow such as laminar jets, wakes, laminar boundary layer growth and separated flows over a rear-facing step were mapped with very promising qualitative results[1].

2. The IR Imaging and Processing System

The nucleus of the IR imaging system is an AGA Thermovision 782 camera equipped with 20°x20° lens coated for optimal response in the short wave (5 μm) infrared spectrum. At 0.5-m distance, the field of view is 0.15 x 0.15-m. Throughout the reported experiments, the aperture was kept at f/1.8. The optical scanning system is syncronized such that four fields of 100 horizontal lines each, produce one interlaced frame. The scanning rate is 25 fields per second. The scanned field is reproduced on a specially-designed black-and-white video display unit, which facilitates direct or relative thermal level measurements. The angular resolution of the system in the above configuration is 0.003 radians.

The digital image processing is performed on a dedicated BMC IF800, model 20 personal computer with 64K bytes main memory plus an extra 128K bytes RAM PCB and two 5 1/4" disk drives. The color CRT display has graphics capability.

A DISCO 2.0 software package is used for the image processing and completely occupies a floppy disk in a read-only storage mode. Up to 36 individual images, which can be either fields or frames, can be stored on the second floppy disk in a read-and-write access storage mode. The automatic aquisition capability of the system permits continuous recording of up to 16 images at an approximate rate of 1.5 Hz or lower. Although both the field and frame acquisition modes are available, only the field mode was used. A key feature of this program is the gradual assignment of eight tones of artificial colors (from black through blue, green, red, etc., to white), for corresponding grey shades in the original image. Such a display produces a color shade for each temperature band scanned by the camera. The user has the choice of getting temperature measurements at a certain point or along specified rows or columns, for given values of the input parameters (emittance, transmittance, ambient temperature, etc.). Also, the user can concentrate on a given range of temperatures, depending on the area of interest. The program is quite versatile and offers an abundance of processing and filtering choices; however, only the essentials have been reported herein.

3. The Laminar Jet Experiment

The laminar jet experiment was intended to test the capability of mapping flows with position-dependent velocities using the heated wire concept.

In this experiment, the infrared camera mapped the temperature distribution along a thin, electrically heated Chromel wire, part of which was diametrically placed at the exit of a pipe from which a laminar jet discharged into the atmosphere. The measured temperatures were used in conjunction with heat transfer correlations in order to obtain the air velocity distribution within the jet.

The Chromel wire 0.003 inch in diameter (0.0762 mm.) was part of a Chromel-Constantan thermocouple assembly that was previously used for wire emittance calibrations as shown in Figure 2.

Those calibrations were performed as follows: A working heat-gun was aimed at the thermocouple's junction, thus getting a direct reading of the wire's temperature. This temperature was double-checked with a mercury thermometer. In parallel, the wire was thermographed by the AGA system and the temperature of the Chromel wire adjacent to the thermocouple's junction was analysed with the Disco 2.0 software on the system's microcomputer. The emittance input of the wire was adjusted until the result from the computation equaled that of the thermocouple readout. This result was checked with another software package supplied by AGA and run on an HP-41 CV programmable calculator with identical results. The Chromel wire length was 40 cm. and the Constantan wire length was 10 cm. The thermocouple assembly was hung between two vertical bars 50 cm apart. The length to diameter ratio of the Chromel wire was 5250:1, so that the influence of the heat conduction (in the area of interest) to the supports can be neglected. The wire was heated by a D.C. electric current passing through it. The laminar flow pipe exit was placed at 1 mm. distance from the heated wire, at the center of the Chromel section, as shown in Figure 3. The air-supply pipe had a 0.545 inch (13.353 mm) internal diameter and a straight section of 80 cm., thus getting a length to diameter ratio of 60. The air was supplied by a standard 100 psi low-pressure supply system (of the type that is usually found in laboratories and workshops). The air mass-flow rate was determined by taking total pressure and temperature measurements upstream of a sonic nozzle. Three fine-mesh screens, (each rotated at 45° with respect to the others) were placed at the entry of the straight section of the tube in order to break down any large vortices or non-uniformities that might exist in the flow. The nominal mean air velocity in the tube was about 2 m/sec, and the corresponding Reynolds number based on the pipe's diameter was about 1700, which is well under the critical Reynolds number of 2300.

The infrared camera was placed at a distance of 0.5 m from the wire. The experiments were carried-out at four different levels of heating corresponding to dissipation rates of 3.97, 9.71, 6.17 and 9.33 watts/m of Chromel wire.

For each separate experiment, 9 consecutive fields were taken at a rate of 1.5 Hz and their average was stored as a single frame on the computer's diskette for latter analysis. During each experiment, the range and level of the camera were carefully set according to the target's luminosity in order to minimize the background noise and at the same time to prevent the detector from being under or overexposed (saturated) to the target's photons. In either case the output result ceases to be proportional to the target's temperature.

The results of the experiments at the three lower heating rates are presented in Figure 4 while the result of the experiment carried out at the highest heating level is presented in Figure 5. The darkened symbols are given for comparison and represent the expected temperature distribution along the section of the wire directly exposed to the laminar flow. The air velocities were calculated assuming parabolic velocity distribution as predicted by the viscous-flow theory. The respective temperatures were deduced from the

$$Nu = 0.795\ Re^{0.384} \qquad 1 < Re < 35 \qquad (1)$$

cross-flow correlation[2]. In this case the Reynolds number at the computed points varied roughly between 4 to 20. The most striking feature of these results, is the ever increasing discrepancy between the measured versus the expected temperatures predicted by correlation (1), for decreasing Reynolds numbers. Since this correlation accounts only for forced convective heat transfer, a first thought was to check the possible contribution of the other two heat transfer modes, namely conduction and radiation. The radiation effect can be discarded from the onset. Assuming that the emittance and the absorptance of the wire's material are the same, one gets for an overheat of 80° K above the room ambient that the radiation effect is three order of magnitudes lower than the generated heat. For evaluating the possible heat conduction contribution, the temperature profile of the wire exposed to the highest overheat was approximated by a cosine-type function fit between 0 and π radians. With a maximum temperature gradient of 2524 °K/m and a mean conductivity coefficient of 50 W/m°K, the maximum conductivity loss for a wire element between two adjacent sampling points is still two order of magnitudes lower than the generated heat; therefore, this mechanism can be discarded too. One possible conclusion may be that the forced convective heat transfer correlations reported in the literature may not be applicable all along the specified range of Reynolds numbers, even though the conditions themselves seem at least a priori, to fall within the validation limits of the correlation.

In this context, it is of interest to check how well the experimental results are correlated. A quick look at Figures 4 and 5 shows that the scatter of the measured temperatures decreases as the overheat level increases, a fact that may be attributed to a better signal to noise ratio. However, in spite of the apparent advantages of high overheating, it should be remembered that it may cause changes in surface emittance, excessive wire elongation (that may induce high amplitude vibrations) and thermal contamination of the flow. Thus, the overheat value should not be abused.

Further evidence that for lower Reynolds numbers the assumed correlation fails to reproduce the reality is provided by the fall of velocity toward the jet's edge. Starting approximately at Re=5, the predicted temperature is higher than that measured on sections of the wire outside the jet plume were the natural convection was the more significant heat removal mechanism. This result repeated itself on all four experiments, and is of course unacceptable.

The deduction of the velocity profile from the measured temperature profile through Nu-Re correlations is also possible. This time, the process is reversed and using the same correlation, the differential temperature is assumed known when calculating the velocity that would produce it. The results as deduced from the experiment with the highest heating rate are presented in Figure 6. The explanation for the increasing departure of the deduced velocity data (Fig. 6) from the theoretical profile, compared to that of the temperature data from which it was deduced (Fig. 5) lies in the behavior of the Nu-Re correlations. These correlations assume a behavior like $Nu \sim Re^n$, $0 < n < 1$. In the former case one gets $\Delta T \sim U^{-n}$, while in the latter $U \sim (\Delta T)^{-1/n}$, thus causing the deduced velocity behavior U to be quite sensitive to the scatter of the temperature measurements. In spite of this fact the results of these experiments show that for Reynolds numbers above 15, good velocity estimations can be obtained even with the existing correlations.

The encouraging aspect of this approach is that as the Reynolds number increases with the velocity, so does the heat transfer coefficient, on a power law basis[2]. The net result of this feature is to increase substantially the accuracy of the velocity predictions from the temperature measurements.

4. The Flat Plate Experiment

The second experiment to be reported herein was aimed at reproducing another classical experiment in aerodynamics: the laminar velocity and thermal boundary layer development along a flat plate at zero angle-of-attack.

The target flat plate measured 32 cm. chordwise, 90 cm. spanwise, was made of wood and had a sharp leading edge of the type assumed in the Blasius analysis of the boundary layer. The IR camera was placed laterally at 55 cm. from the target, behind a second plate (parallel to the first one), with a circular hole through which the camera could view the target. This was done in order to prevent the vortices shedded from the camera from interfering with the flow over the target plate. As shown in Figure 7, the entire

assembly was placed vertically in the department's 3' x 4' low speed wind tunnel where the experiments took place.

The target flat plate was placed in the wind-tunnel at $0^{-0.5}$ degree angle of attack, so that the surface under investigation was at most accelerating minutely the external flow.

The active heating of the target plate was achieved locally, at one third of the span, by wrapping chordwise a 0.00397" Constantan wire three times around the plate at 2 mm. pitch and connecting it to a power supply. To ensure uniform surface texture and roughness, these wires and the entire surrounding area in the field of view of the camera were covered chordwise with three adjacent strips of 2" wide duct tape. At 85 mm. from the leading edge, a Chromel wire was soldered to the Constantan wire and its lead was taken to the back of the plate through a very small hole that was drilled in the wood. This layout enabled emittance calibrations of the duct-tape surface by providing the true surface temperature. Hence, the Constantan wire played a dual role in this experiment, as a heating element when connected to the power supply, or as a thermocouple element when connected to a digital thermometer. The desired function was selected by switching between the circuits. Direct measurements performed during the experiments show that heat was dissipated at a rate of 949 W/m^2 over that area of the flat plate that was affected by the testing.

The guiding rule in performing these experiments was to make them as short as possible. There were two reasons for this, one concerning the wind-tunnel operation, the other concerning the substrate participation in the heat transfer process. Since the wind-tunnel used in this experiment is of closed circuit type, the longer the operation period the higher is its air temperature. This phenomenon has a negative influence on the heat transfer process from the flat plate to the fluid and in general is disruptive to infrared measurements. The other concern was that long periods of heating, would effect the substrate to an unknown degree resulting in long cooling times between runs and irreproducible results. In this respect, the thermocouple used for emittance calibrations proved to be of significant help in establishing the substrate initial conditions for each test.

A total of 20 tests were performed. Of these, eleven tests were recorded. Since the results of all the runs were very much alike, only the last three were picked-up for data analysis. The reproducibility of the results ensured that no further benefit would have come out of analyzing more profiles, except perhaps to establish a statistical variation measure for the data set.

The chordwise temperature profiles as obtained from the last three runs are shown in Figure 8. The camera's field of view in this configuration was 16.5x16.5 cm, and the Reynolds number of that area of the plate scanned by the camera varied between zero (at the leading edge) to about 217000. This means that the phenomena addressed are all under the laminar boundary layer regime.

The data as presented in Figure 8 displays the temperature profile along the plate reduced by the airflow temperature, versus the chordwise coordinate. A primary evaluation of these profiles will reveal the following:

1) The information gathered from all three runs was quite reproducible and the data points obtained from the different experiments almost coincide.
2) The general qualitative behavior of the temperature profile theory meets the expectations based on laminar boundary layer theory.
3) The temperature distribution exhibits some irregularity around the coordinate X=8 cm. This is the region where the thermocouple junction was placed, a fact that caused a slight "bumpiness" on the overlaying duct tape surface. It is assumed that this geometrical feature may have initiated a directional emittance factor, which is usually lower than its normal counterpart. This effect, not being taken into account by the system's softwave, is ultimately (and falsely) interpreted as a local drop in temperature.
4) The leading edge experiences an abrupt increase in its temperature, due to its sharpness. This geometrical feature causes a finite amount of heat to be absorbed by a theoretically infinitesimal substrate mass, with the consequent real increase in temperature. The effect is further augumented by the fact that the heating wires being wrapped around the plate, the leading edge is well heated from all around its contour.

As a result of these considerations, it was decided to proceed with the analysis of the experiments, using only the data points starting at the coordinate X = 1.9 cm from the leading edge (the first 1.52 cm. from the leading edge were ignored). The numerical values of these coordinates resulted from the fact that the data was extracted at each third consecutive pixel, which on the plate is equivalent to an interval of 3.8 mm.

In search for a model against which the experimental results can be evaluated, the physical reality of constant power heating at the wall, suggests using the flat plate laminar boundary layer model with constant heat flux at its surface as the prescribed boundary condition. The model assuming a general heat flux distribution chordwise and its analytical solution was formulated by Tribus and Klein[3]. When simplified to the constant heat flux assumption, the solution reads:

$$\theta(x) = 2.2019 \frac{\dot{q}_o''}{k} Pr^{-1/3} \left(\frac{\nu}{U}\right)^{1/2} x^{1/2}$$

$$= \text{const} \cdot x^{1/2} \qquad (2)$$

According to this model when the flat plate corrected temperature distribution is plotted against the square-root of the distance from the leading edge, the slope of the line is an indication of the heat flux convected into the airstream. When this plotting is done for the present case, as shown in Figure 9, its analysis shows that although the data is well correlated, the assumed linear behavior of the data is not uniform all along the coordinate scale. A closer look suggests one linear regression for the first 14 stations and another for the last 18 stations, leaving 6 stations in between as a transition zone. The question is what causes this change in the pattern behavior. A possible answer lies in the actual physical process taking place with this experimental set-up and its departure from the assumed model. As shown in Figure 10, the theory assumes a flat plate "pumping" a constant amount of heat flux into the airstream. For a desired constant value of this heat flux, a certain prescribed temperature distribution should be maintained (or obtained) in order to compensate for the fact that the boundary layer thickens and heats up streamwise. In this case, the constant heat generation rate is shared mainly by two participating media, the wooden substrate by conduction and the airflow by convection. Heat transfer by radiation is also taking part, but to a lesser degree. Since the air cooling by convection is very effective on the forward part of the plate, (due to the thin boundary layer), the heat transfer by conduction to the substrate is much less than on the aft part of the plate, where the boundary layer is thick and the convective heat transfer is much poorer. The estimation of the boundary layer behavior will show that between the first and the last station of the first data group, it thickens by 90% (from 0.60 mm. to 1.15 mm) while with respect to the second data group, it continues to thicken but only by 30% (from 1.35 mm. to 1.75 mm.). Therefore, the heat conduction mechanism to the substrate will play a more prominent role on the aft part of the plate and contribute to the change of the trend exhibited over its leading part. Looking again at Figure 9, one may further observe that the general trend of the slope of θ vs. $X^{1/2}$ is to decrease gradually from the leading edge downstream, a feature that may add additional evidence to the ever increasing participation of the substrate due to the gradual decreasing effectiveness of the convective cooling.

The thermal energy analysis performed on the flat plates is summarized in Table 1 which clearly shows the gradual shift in the energy transfer mechanism from the predominantly convective mode in the leading edge area to the predominantly conduction mode to the substrate over the downstream regions of the plate. This happens in spite of the fact that the wood qualifies as a heat insulator. The radiative heat transfer mode, although playing a minor role in this configuration, cannot be ignored. Even though the overheat degree was relatively moderate 10 to 20°C, its contribution to the total heat transfer dissipation was about 9%. Theoretically, with different surface conditions and identical overheat values, its contribution could be as small as 1% or as high as 12%.

Table 1: Mean values analysis of the heat transfer modes on a flat plate heated at constant wall power generation placed in an airstream at zero angle of attack. $Re_x = 1.233 \times 10^6 X(m)$.

Data points	X (1)	$\frac{\dot{q}''_{o\ conv}}{\dot{q}''_{o\ gen}}$	$\frac{\dot{q}''_{o\ rad}}{\dot{q}''_{o\ gen}}$ (2)	$\frac{\dot{q}''_{o\ cond}}{\dot{q}''_{o\ gen}}$
All	1.9 → 159.9	42%	9%	49%
1st group	1.9 → 68.5	64%	8%	28%
2nd group	95.2 → 159.9	19%	11%	70%

1. distance from the leading edge (mm)
2. $\dot{q}''_o$ conducted = $\dot{q}''_o$ generated - ($\dot{q}''_o$ convected + $\dot{q}''_o$ radiated), mean value (W/m^2)

conv - convected
gen - generated
rad - radiated
cond - conducted

This experiment shows in a primitive but very fundamental way the potential of using infrared imaging in experimental aerodynamics. Firstly, no other method can supply the temperature distribution so quickly and easily, with no interference with the flowfield, the temperature field, or the geometry of the surface. Secondly, the flat plate temperature profile analysis in a direction perpendicular to the direction of the flow, provided a very easy means to determine very accurately the effective area of heat exchange. The knowledge of this area is critical in establishing the correct value of the heat flux for cases where active heating is employed. Thirdly, the analytical method may be also applied in an identical way to find the freestream velocity U assuming the heat flux is known. This mode will require either a solution to the participation of the substrate in the heat transfer process, or use of a substrate which is highly insulative thermally. Recently, a work which models and simulates highly time dependent coupled convective and conduction heat transfer, was accomplished with regard to hot-film time response investigation[4].

The need to understand the substrate's participation will become more accute in the high-speed regime, where the active heating will give way to frictional heating and the surface temperature distribution might serve as an indication of the aerodynamic loading.

5. Conclusions

The infrared imaging method emerges as a very useful tool in experimental aerodynamics. It can be used to measure temperatures along thin, long, heated wires to map flowfield velocities. A high heating rate of the wire will generally give higher signal to noise ratios, but it can also induce oscillations in the wire due to its thermal elongation. Thus, the optimum operating condition should be a compromise between the two conflicting requirements. Another possibility is to map surface temperatures of aerodynamic configurations to deduce thermal loadings, heat exchange processes and eventually flow velocities. This method gave encouraging results when it was applied to determine the temperature distribution of a constant power heated flat plate in the laminar boundary layer regime. In general, this experimental method focused the attention on the need of better understanding the heat transfer process associated with the coupling between the flowfield forced convection and the substrate participation by conduction.

Acknowledgement

This research was supported by NASA Langley Research Center grant NAG-1-735.

The authors wish to acknowledge Mr. E. W. Cronce and Mr. K. Ferguson from the College of Engineering and Technology at Old Dominion University for their valuable technical support of this research.

References

1. Gartenberg, E., Roberts, A. S., Jr. and G. V. Selby, Infrared Surface Imaging as a Flowfield Diagnostic Tool, Proceeding of the 12th International Congress on Instrumentation in Aerospace Simulation Facilities (Sponsored by IEEE), The College of William and Mary, Williamsburg, Virginia, June 22-25, 1987.

2. Morgan, V. T., The Overall Convective Heat Transfer from Smooth Circular Cylinders, Advances in Heat Transfer, Vol. 11, Academic Press, 1975.

3. Klein, J., and Tribus, M., Forced Convection from Non-Isothermal Surfaces. University of Michigan Engineering Research Institute, August 1952 Project M 992-B.

4. Judge, M. D., Model of Hot-Film Sensor with Substrate Effects, Master of Engineering Thesis, Department of Electrical and Computer Engineering, Old Dominion University, December 1987.

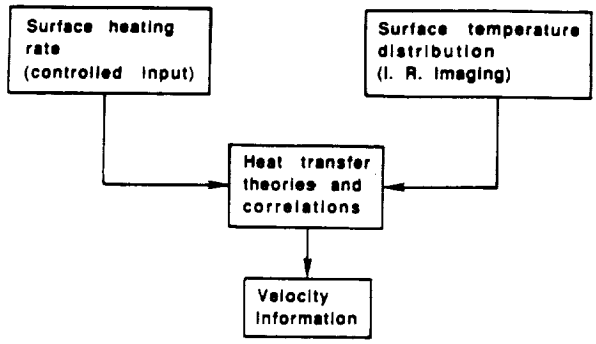

Fig. 1. The concept of flowfield velocity deduction through infrared imaging of the surface

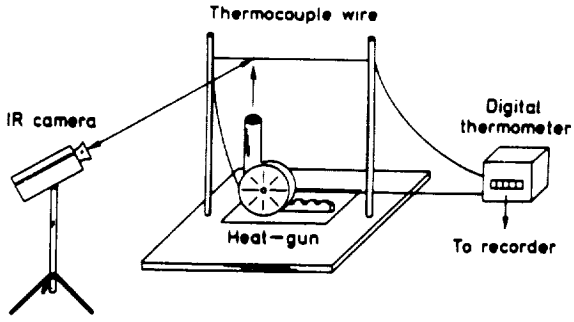

Fig. 2. Experimental set-up for wire emittance calibration

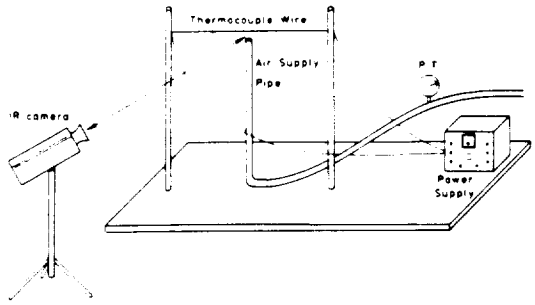

Fig. 3. Set-up for the heated wire laminar jet experiment

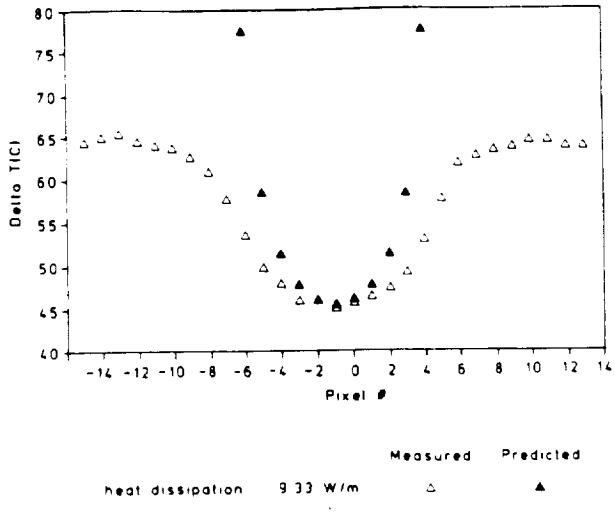

Fig. 5. Heated wire temperature distribution when exposed to a laminar jet.
U_{max} = 4 m/sec; 1 pixel = 1.154 mm
Prediction based on
$Nu = 0.795\ Re^{0.384}$

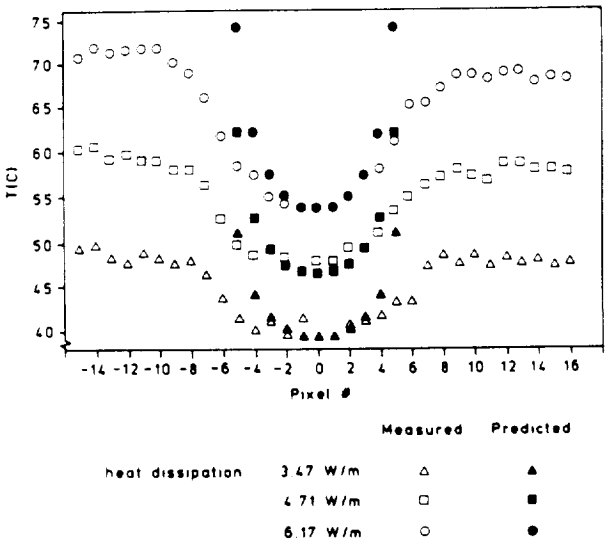

Fig. 4. Heated wire temperature distribution when exposed to a laminar jet.
U_{max} = 4 m/sec; 1 pixel = 1.154 mm
Prediction based on
$Nu = 0.795\ Re^{0.384}$

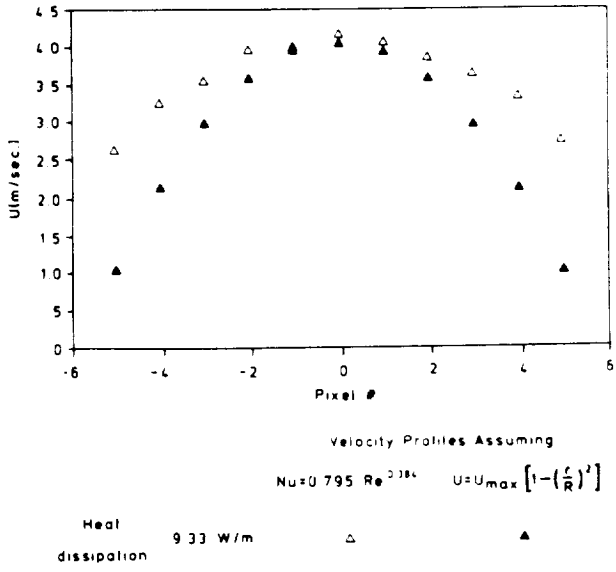

Fig. 6. Velocity profile as deduced from the heated-wire laminar-jet measurements: Nu-Re correlation versus viscous theory solution.

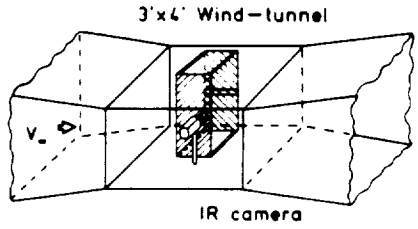

Fig. 7. Layout for infrared imaging surface measurements of a heated flat plate in a uniform freestream.

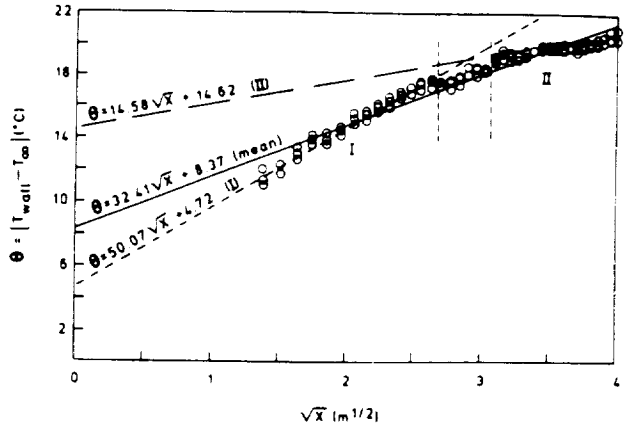

Fig. 9. Constant power heated flat plate experiment: adjusted temperature profile vs. square-root of distance from the leading edge.
$Re_x = 1.233 \times 10^6 X(m)$

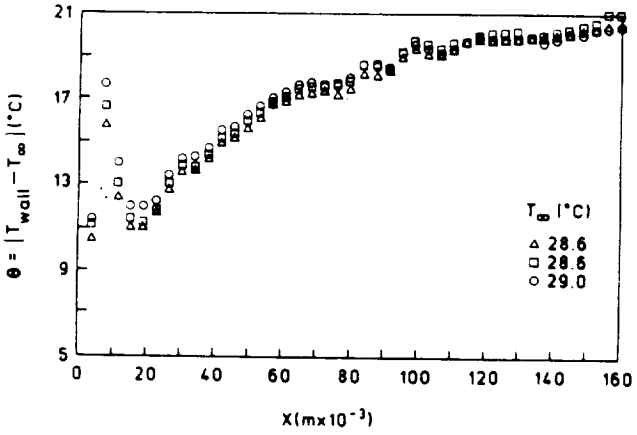

Fig. 8. Constant power heated flat plate experiment: adjusted temperature profile vs. distance from leading edge. $Re_x = 1.233 \times 10^6 X(m)$

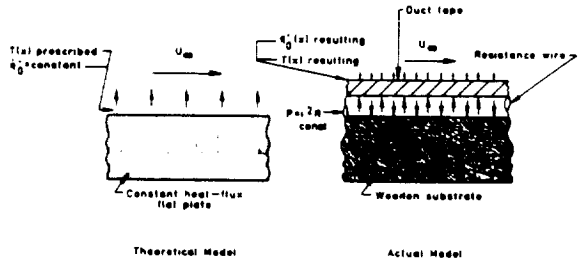

Fig. 10. Heated flat plate experiment: comparison between the theoretical constant heat flux model and constant power reality.

1647

N91-20452

SPIE 1467-59

Twenty-five Years of Aerodynamic Research with IR Imaging
- A Survey -

Ehud Gartenberg and A.S. Roberts, Jr.
Old Dominion University
Norfolk, Virginia

Thermosense XIII
An International Conference on Thermal Applications and Image Diagnostic
April 3-5, 1991, Orlando, Florida

Twenty-five Years of Aerodynamic Research with Infrared Imaging

Ehud Gartenberg and A. Sidney Roberts Jr.

Old Dominion University, Department of Mechanical Engineering and Mechanics
Norfolk, Virginia 23529-0247

Abstract

Infrared imaging used in aerodynamic research evolved during the last 25 years into a rewarding experimental technique for investigations of body - flow field viscous interactions, such as heat-flux determination and boundary layer transition. The technique of infrared imaging matched well its capability to produce useful results, with the expansion of testing conditions in the entire spectrum of wind tunnels, from hypersonic high-enthalpy facilities to cryogenic transonic wind tunnels. With unique achievements credited to its past, the current trend suggests a change in attitude towards this technique: from the perception as an exotic, project-oriented tool, to the status of a routine experimental procedure.

Abbreviations Used for Establishments

AEDC	Arnold Engineering and Development Center, USA
DFVLR	Deutsche Forschungs-und Versuchsanstalt fur Luft-und Raumfarht, Germany
DLR	Deutsche Forschungsanstalt fur Luft-und Raumfahrt, Germany
NASA	National Aeronautics and Space Administration, USA
ONERA	Office National d'Etudes et de Recherches Aerospatiales, France

1. Introduction

Throughout the history, aeronautical engineers faced the need to know more about boundary layer flows or ignoring the need, were forced to pay the price. At times, the capability to define and integrate boundary layer effects in a new design may impact on the success of an entire project. The commercial introduction of infrared (IR) imaging systems in the mid sixties, opened the possibility to visualize viscous interactions between a body and the surrounding air flow by mapping the surface temperature distributions on configurations of interest. The momentum and heat exchange occurring accross the boundary layer were related classically through the Reynolds analogy.[1] Invoking this analogy, surface temperature distributions are known to contain information related to both the heat transfer and the skin friction processes occurring at the wall. Therefore, the capability of IR imaging systems to produce in real-time thermograms that can be interpreted both globally and locally makes them attractive for skin friction and heat transfer aerodynamic studies.

Space exploration activities sparked interest in high-supersonic and hypersonic flight, and inevitably motivated the need to measure and define thermal loads. Most notable are the re-entry conditions of the Space Shuttle. Starting in the early seventies, the increase in fuel price had a deep impact on the air transportation industry. The response to the challenge of improving flight economy in the subsonic and transonic regimes was initially focused on power plant efficiency. Later, the attention turned toward the aerodynamic efficiency through drag reduction, with the friction component getting much attention.

The resurrection and the success of activities addressing all flight regimes depend critically upon the evaluation and understanding of the viscous flow effects. In the supersonic and hypersonic regimes, the boundary layer status affects both the friction drag and the thermal loading of the structure, two items of high consideration in any design. In the sub- and transonic regimes, sustaining laminar flow over a significant part of the wings, is a major challenge of current aerodynamic interest.

In spite of the significant potential demonstrated by IR imaging systems for aerodynamic research, the method was not widely accepted and recognized for its full capability until relatively recently. Two problems delayed acceptance of the method in its earlier stages of development. The first was a lack of easily accessible capability to store and manipulate data. This drawback was naturally solved with the commercial introduction of video cassette recorders (VCR's) and personal computers. The second was the realization that the temperature information contained on thermograms results from a multi-faceted process encompassing aerodynamics, heat conduction, geometry, and radiation.[2]

The reduction of the experimental data, from temperatures to heat flux distributions via the thermal response of the substrate, can be simplified if the the physical reality can be mathematically modeled based on assumptions leading to analytical solutions. At one end are models made of thermal insulating materials, where it is plausible to assume that deep in the substrate there is a layer that virtually keeps its temperature constant throughout the test (if its duration is not too long). This case is known as the "semi-infinite slab" model, for which the heat conduction equation can be solved analytically for the heat flux as a function of the transitory surface temperature distribution. At the other end there are hollow, "thin skin" models, where it can be assumed that the heat flux is uniformly absorbed in-depth the material with the temperature changing uniformly across the model skin. This case can be approximated by the "thin skin" model of the thermal energy equation. Other types of model construction may fall in between these two classifications, as they are affected by the filler or the spar underneath the skin. It follows that understanding the direct and indirect factors influencing an experiment and its results, is critical for the determination of the data reduction technique. Therfore, designing aerodynamic experiments based on IR imaging and extracting data from the thermograms are very challenging processes.

Utilization of the technique has yielded a wealth of experience and aerodynamic results, but the subject has not been adequately reviewed. As recently as 5 years ago, a paper on developments in flow visualization[3] mentioned only two references about aerodynamic research performed with IR imaging systems, although by that time the method was known for 21 years. This paper is a wide ranging review of the applications IR imaging has seen in aerodynamic research. It should benefit in particular those contemplating the use of the method. After a brief description of IR imaging systems, a few overview papers will be mentioned describing and analyzing the IR imaging technique for aerodynamic research. Attention will turn then to super- and hypersonic, and in turn sub- and transonic applications, two areas where these systems made distinctive contributions. The survey will then proceed to some specific applications in flow visualization, propulsion, fluid mechanics and heat transfer. Before concluding, a quick look will be taken at current trends and expected developments in the application of IR imaging to aerodynamic research.

2. IR Imaging Systems and Data Processing

Most of the commercial IR imaging systems are similar in concept to those built 25 years ago. A single detector, usually cooled by liquid nitrogen, is exposed to the incoming radiation from the target on which the objective lens is focused. To obtain an image of the objective lens field of view (FOV), the camera scans the scene both horizontally and vertically, with rotating prisms or mirrors, producing the display lines for the video display. The area projected at any single time on the detector is subtended in the instantaneous field of view (IFOV). The output of the detector is transmitted to a black-and-white video display, where lighter shades are associated with higher temperatures. Usually, a single pixel displays the sensor output from one IFOV. To give some specific numbers,[4,5] commercial imagers are

sensitive to IR radiation either in the 3- to 6-micrometer (short wave) or in the 8- to 12-micrometer (long wave) bands, also identified as infrared atmospheric windows. Shorter wavelength imagers are better suited to scan high temperature targets and vice versa. The field-of-view of commercial objective lens ranges between 2.5 to 40 degrees. One complete scanning of a scene is called a field. To improve the visual quality of the display, two or four fields are usually interlaced to produce a frame. Thus, the camera produces fields, but the human eye perceives frames. A field has usually fewer than 200 lines, each line having usually less than 200 pixels. The scanning rate may vary between 25 to 60 fields per second. Gauffre and Fontanella.[6] give particularly concise and useful description of IR imaging systems that introduces the reader to camera figures of merit, including sample calculations.

The systems can be connected to VCRs for analog recording and play-back and to personal computers equipped with dedicated software for digitizing, storing, and processing of individual fields or frames. A key feature of such software is the gradual assignment of artificial colors (from black through blue, green, and so on to red, yellow, and white) for corresponding gray shades in the original image, thus producing a visual sensation of the temperatures over the scanned target. Recent IR imaging models have false coloring option built in their display units. Under some circumstances, the thermograms may have to be enhanced when their quality is not adequate for data interpretation or presentation. Simple ad-hoc methods, such as averaging frames or images integration may produce satisfactory results.[7] In more problematic cases, more complex processing methods are required, such as smoothing contours and time-based interpolation.[8]

As it frequently happens, the information contained on a thermogram will not make sense to the experimentalist and he may be constrained to evaluate the actual performance and limitations of his IR imaging and data acquisition system. In those rare cases where the target temperature distribution is considered well behaved and known, the system may be evaluated on an input-versus-output basis.[9] In other cases, specific performance functions, e.g., the Modulation Transfer Function (MTF) of the system may have to be evaluated, to account for missing information, and allow data restoration.[10]

In most aeronautical applications, the camera is installed either outside the wind tunnel, scanning a model in the test section or, inside an airplane cabin or cockpit, scanning the wing. For the radiation to pass through, the wind tunnel or the airplane need special windows transparent to IR radiation. There is a large selection of commercial IR transparent materials.[11] The choice will depend upon the transmittance in the waveband of the specific sensor used, mechanical considerations, environmental compatibility, and cost. Antireflective coating may improve the transmittance of some of these materials, but at the expense of the reflectance.

3. Method Reviews

Some of the papers documenting aerodynamic or fluid mechanics experiments feature lengthy introductions describing IR imaging systems, data acquisition and processing hardware, specific peripherals, theoretical underlying principles, general and specific applications, etc. While the main value of the papers is found in the rather specific work done by the authors, some of them are a good starting point for forming an idea about this technique.[12-23] Some references document studies that were repetitively presented with additions, changes and refinements. These successive publications present before the reader the development of the technique, as they give the feeling of the obstacles that were overcome in gaining mastery and implementation. Some of the above references originated in lecture notes and were published later elsewhere.

4. Super- and Hypersonic Studies

The first documented use of IR imaging in aeronautical research was reported in 1967 by Thomann and Frisk[24] of the Aeronautical Research Institute of Sweden. In a wind tunnel experiment performed at Mach=7, the temperature distribution on an elastomeric paraboloid was measured as it evolved in time. From the temperature rate of change, the heat flux at the model surface was deduced using the "semi-infinite slab" solution[25] for the unsteady heat conduction equation. The short test run (seconds) combined with the low thermal diffusivity material justify use of that solution. This data reduction concept was borrowed from the fusible paint technique,[26] and it is still in use. The experiment showed the IR imaging to be as accurate as other competing techniques for heat flux determination, with the advantage that without requiring surface preparation before or in-between runs, it is quite expedient. More than a decade later, Balageas and Ory[27] proposed a data reduction method that incorporated the finite thickness of the skin and the boundary conditions at the internal wall, expanding the applicability of the technique to thin-skin models.

After this technique was shown to work, there were more attempts to evaluate and improve it, e.g., scanning the model against a water cooled plate to reduce the background radiation noise.[28] However, for a few years the method was far from being productive enough to be directly applicable to project designs. Compton[29] at the NASA Ames Research Center realized that the bottleneck of the technique was the data acquisition, storage, and processing. One should realize that the heat flux distribution is calculated from the temperature readings on a pixel-by-pixel basis that was generated at rates of approximately 88000 IFOVs per second. The solution was devised to record the data on an analog tape, to digitize and read it into a computer for processing, and thereafter to display and plot the results. This engineering concept set the pattern for similar systems to this very day. Automating the data processing system gave access to all the information produced during a test. In particular, it was understood that monitoring the history of the heating rate for relatively long periods of time, could indicate if the boundary-layer transition front moved on the model during the test.

In 1973, the Arnold Engineering Development Center (AEDC) embarked on a large-scale program to develop the capability of extensive heat transfer testing in the hypersonic regime with an IR imaging system.[30,31] The von Karman facility was designated for that purpose, and engineering modifications were made to allow hosting an IR imaging system for test series that extended over long periods of time. An automated data processing system was developed that accepted input from the IR camera, thermocouples on the model, and temperature and pressure probes providing the operational parameters of the wind tunnel. In parallel, materials used for model manufacture were screened for compatibility with the technique and the environment, and their thermal and radiative properties were documented. Accurate numerical values of these properties are critical for processing the output data from the IR imager, and deducing of the temperature distributions on the model. To assess the accuracy of the technique, calibration procedures were developed; the repeatability of the measurements was evaluated; and, a measurement error model was implemented.[32,33] The results were confirmed also by other experimental means and were found to agree well with theoretical predictions. On the negative side, it was found that step changes in the temperature distribution could not be resolved, the response being to "smear" or blur the result over a few adjacent pixels. Moreover, the camera displayed a consistent measurement error when the target temperature gradient exceeded a certain value. These shortcomings were blamed on the relatively large size of the imager's IFOV, but this aspect was not pursued enough to a full understanding. While a smaller IFOV will allow a better capture of abrupt changes in the temperature distribution, the blur effect will always occur, because of the Optical Transfer Function (OTF) of the camera.

The infrastructure and expertise developed at AEDC in the 1970's was used to measure convective heating rates on a 0.04-scale model of the Space Shuttle orbiter under flow conditions prevailing during the re-entry phase (Fig. 1). The test flow conditions were typically: Mach=8, temperature 1300 R, Reynolds number $0.5X10^6$ to $3.5X10^6$ per foot, angle of attack 30 to 45 degrees. The data obtained were incorporated in the design of the thermal protection system of the orbiter.[34,35] Besides project-oriented applications, general heating studies of elastomeric materials were carried out,[36] the results giving insights to phenomena that were harder to access with other diagnostic tools. For example, in a

testing program run at Mach=10, the surface heating was observed to be nonuniform to a greater extent than could have been forecast. Hot streaks that may be have been caused by wing-tip crossflow effects were detected, and increased heating rates were observed when bubbles caused by local failure of adhesive bonds formed in the substrate. Even though part of the data could not be reduced using the "semi-infinite slab" solution, the underlying assumptions being no longer valid, some of these effects could still be quantified, and operational conclusions could be drawn.

Tests under rarefied flow conditions at very high Mach numbers, say Mach=20, are characterized by a short duration of a very few seconds and heat fluxes that may get as low as 0.5 kW / m^2. In these cases, solid models may no longer be acceptable because the relatively long time required for the temperature pattern to become established is unavailable. For this application, thin skin models and a conforming data reduction model may be the only way to get useful results.[16] Balageas et al.[13-15] extended the use of thin skin models to low Mach numbers (down to Mach=2.0) through "stimulated thermography". According to this concept, the model in the wind tunnel is heated by a bank of lamps over a pre-set period of time, and the heat transfer coefficient is determined from the temperature response of the model integrated over a period of time. This approach is less susceptible to curvature effects of the surface and noise, the data reduction being based on integration and not on differentiation.

Next to determination of heat fluxes, location of boundary layer transition to turbulence was always a major subject of interest to aerodynamicists. Turbulent boundary layers have higher skin friction than the laminar ones. On the other hand, the laminar boundary layer is more susceptible to separation, especially in the super- and hypersonic regimes where shock-wave interaction can cause strong adverse pressure gradients. With the increase in skin friction, the transition to turbulence also induces higher heat fluxes, and under some speed and flight time combination, the structure may require special thermal protection. Therefore, the capability to detect boundary layer transition may have far-reaching consequences for the development and verification of designs.

The thermal signature of transition on a model can be caused by one of two effects. The first is the near term thermal response of the model, occurring as long as it does not reach thermal equilibrium with the recovery temperature in the boundary layer. Under these circumstances, heat transfer takes place between the flow and the model, the area exposed to the turbulent regime changing its temperature faster.[37] The second effect is the long term response, occurring when the model and the surrounding flow come to quasi-steady thermal equilibrium. In this case, the wall temperature tends towards the adiabatic value, the latter being higher under the turbulent-versus-laminar boundary layer regime.

Peake at al.,[38] carried out a boundary layer transition detection test in a blow-down tunnel at Mach number 3.85 using a stainless steel flat plate equipped with a bakelite insert surface. The transition location appeared on the thermograms as a localized hot front that was attributed to the difference in the recovery temperature between the laminar and the turbulent regime; it was also confirmed by other experimental means. In a subsequent experiment, an all stainless steel flat plate painted black was used as target, but the distinct transition pattern could not be observed anymore. The inadequacy of the IR imaging technique to detect transition on stainless steel models is caused by the relatively high thermal diffusivity of the metal that levels-out temperature differences along and in-depth through the model. In cases where the surface is polished, the situation is further aggravated. The high reflectance and the low emittance of the surface decrease the signal-to-noise ratio on the thermograms to an extent that renders the method useless. It may be speculated that at high Mach numbers the very intense heat transfer may offset the detriments of polished stainless models by raising very rapidly the surface temperature to relatively high values. Collier et al.[39] tried this approach on a polished stainless steel cone at Mach=14 but, unfortunately no reliable temperature readings could be obtained.

Identifying the indication of transition on thermograms with a precise locus inside the evolving transition process is critical in evaluating the merit of the method. In more concrete terms, the problem is that on thermograms the transition to turbulence appears to happen abruptly, while actually the process may develop over a significant portion of the aerodynamic surface. Hall et al.[40] compared the diagnosis of transition from an IR imaging system with that of hot films

on a flat plate at Mach numbers 1.5, 2.0, and 2.5. The results indicate that on thermograms the transition appears at various stages of its development. As expected, it always appears before the 50% intermittency; this intermittency value decreases as the Mach number increases.

Besides transition, flow separation and reattachment are features of much interest, especially on configurations of longitudinal symmetry. As the angle of attack increases, the flow will separate along the sides of the models, developing into large-scale vortices that reattach on the leeward side. These features are detectable through the surface temperature variation, minimum at separation and maximum at reattachment, and are induced by the respective behavior of the skin friction and heat transfer. Bandettini and Peake[41] carried out a separation detection study on a 10 degree fiberglass cone at different angles of attack at Mach=1.8, comparing the results with oil-flow visualization. Although the IR imaging and the oil flow visualization were performed at somewhat different Reynolds numbers ($3x10^6$ for the former and $9x10^6$ for the latter, based on the model length), the vortices separation and reattachment could be identified on the thermograms as areas of higher and lower temperatures. An investigation of a somewhat more complicated flow pattern was carried out by Arai and Sato[42] on a 12.84/7-degree, bent-nose biconic made of epoxy resin at various angles of attack at Mach=7. This geometry is a leading candidate for the forebody of the Aeroassisted Orbital Transfer Vehicle. Arai and Sato [42] results are very similar to those of Bandettini and Peake,[41] confirming that vortical flow reattachment can cause heating on the leeward side at positive angles of attack.

The experiments reviewed so far address temperature signatures of flow fields on models of circular geometry or longitudinal symmetry. Lately, Henckels and Maurer[43] published the results of an experiment addressing a Mach=8.7 flow along a corner, produced by the intersection of two perpendicular plates, at various pitch and yaw angles. This is highly three dimensional flow, involving interaction of two perpendicular shock waves originating at the leading edge of each plate, and the formation of an embedded vortex underneath the slip surface produced by the interacting shocks. The thermograms were used to deduce heating rates on the walls, with the stipulation that the influence of the flow scaling on the results could not be inferred.

Space Shuttle Flight Experiments

The Space Shuttle program deserves a special place in the history of IR imaging in aerodynamic engineering and research. As it was previously mentioned, the method was used during the engineering phase of the program to determine the atmospheric re-entry heating rates on its forebody. After the orbiters became operational, they were designated for two daring IR imaging flight experiments aimed at mapping their surface heating during the actual re-entry phase.

In the InfraRed Imaging of the Shuttle (IRIS) experiment,[44-46] the windward side of the Space Shuttle re-entering the atmosphere was observed from below through an astronomical IR telescope mounted on a "chasing" C-141 aircraft, known as the Kuiper Airborne Observatory. In spite of useful and promising results regarding the evolvment of the actual heating rates and the progression of the boundary-layer transition front,[47] this experiment was discontinued because of its cost, the complex coordination work, and restricted availability of the airborne observatory.

In the on-going Shuttle Infrared Leeside Temperature Sensing (SILTS) experiment, an IR imaging camera installed atop the vertical stabilizer of the Space Shuttle Columbia (Fig. 2), is scanning the leeside of that vehicle during the atmospheric re-entry phase of its flight.[48,49] Zones of intense heating were observed along the leading edge and the upstream part of the wing, the inboard/outboard elevon gap, and the orbital maneuvering system pod (Fig. 3), atop which the vertical stabilizer is mounted.[50,51] In general, the heating pattern indicates a highly vortical flow, convecting high temperature compressed air from the windward side of the orbiter to its leeside. This behaviour is typical to delta-like configurations at high angles of attack experiencing leading edge flow separation. The real pay-off from this

experiment will materialize when the heating patterns observed in flight will be reproduced in numerical simulations of the flow. Thereafter, the in-depth thermal response of the wing substrate could be analyzed in detail, promoting the understanding necessary for future thermal protection designs.

5. Sub- and Transonic Studies

The possibility of using IR imaging for sub- and transonic aerodynamic research was raised only in the early eighties.[7] Since then, the application of this technique got to the point where some industrial wind-tunnels offer IR imaging diagnosis as part of their standard data acquisition process.[52] The interest in thermography for these flow regimes is mainly for boundary layer transition research. The method is particularly attractive because it produces global views of the configurations of interest, mainly airfoils and wings, where the behaviour of the boundary layer can be deduced through a quick visual inspection.

The preoccupation with laminar flow for drag reduction reappears periodically in the aerodynamic research. In the past, it was used mainly as a means for range extension. More recently, the global energy crisis has caused the subject to resurface. New designs of transport airplanes are required to reduce their fuel consumption and their resulting direct operating costs. One avenue that can be used to achieve this goal is to design the wings to sustain laminar boundary layer to the largest possible extent. In the current laminar flow research, the IR imaging technique is an integral part of the effort to make this aerodynamic technology available. The effort encompasses wind tunnel technology,[53] wind tunnel and flight testing,[54-56] and aerodynamic design philosophies.[57-59]

In 1983, Bouchardy, Durand and Gauffre[7] from ONERA Chatillon reported the first transition detection study in a thermally stable wind tunnel. They addressed the effect of positive step change in the adiabatic wall temperature induced by the difference in the recovery temperature of the turbulent- versus-laminar regime. Using models fabricated of thermally insulating materials, current IR imaging systems are sensitive enough to detect transition down to Mach=0.5, at ambient conditions. For lower air velocities, down to Mach=0.1, the transition detection is still feasible through image processing enhancement of the thermograms. Among the thermally passive approaches to transition detection, this is the only aerodynamic effect that can be used in open circuit or thermally stable wind tunnels, where the stagnation temperature is considered constant.[60] The first systematic investigation of transition detection in wind tunnel and flight testing was publisheded by Quast from DFVLR Braunschweig.[61] He pointed out that the increased heat transfer coefficient of the turbulent-versus- laminar regime is a remarkably useful attribute that makes the transition detectable on raw thermograms even at very low speeds, if the temperature of the model is different from the temperature of the flow. When exposed to this effect, the area underneath the transitional and turbulent boundary layer will change its temperature faster than its counterpart under the laminar regime, thus enhancing the temperature contrast between the two areas on the thermogram. In fact, the heat transfer effect is dominating over the recovery temperature influence, and today it is used in the majority of transition detection experiments. It is convenient in use and interpretation, especially implying the Reynolds analogy between convective heat transfer and skin friction coefficients. This effect occurs in closed circuit wind tunnels, where the air heats naturally during their operation.[62] It can also be observed in wind tunnels equipped with a cooling system.[61] Another option is to use electrical[19,20,63] or laser[64] heating of the model surface, or to blow hot air through a hollow model,[17,18] and to observe the cooling effect of the flow. In flight testing, this effect occurs naturally when an airplane is flying an ascent or descent path through the atmosphere.[55] Although active heating of the substrate is very attractive and simple to implement, the surface overheat value should be kept at the absolute necessary minimum to prevent a premature triggering of transition.

When the significance and potential of IR imaging became evident for boundary layer research, the effort turned towards a full evaluation of the diagnostic capabilities of the method. In an effort to make the method more quantitative, it was shown that the active heating method can identify changes in the boundary layer regime by tracking the behavior of the

experimentally deduced heat transfer coefficient. Provided laminar boundary layer is established downstream of the leading edge, the maximum heat transfer coefficient is indicative of transition to turbulence, and its following minimum occurs at separation.[17-20,63-65] If the passive method is applied, the transition is identified visually at the location of the step change in the surface temperature.[7,12,55,61,62,66,67] At higher incidence, the onset of turbulent separation is identified by the emergence of a second zone of increased heat transfer caused by local vorticity shedding.[62]

The next step was to apply the IR imaging method to boundary layer transition research, that eventually would lead to "laminar" airplane designs. For this application, one must be able to identify on the thermograms the various modes of boundary layer transition, since the development of each mode can be attributed to a particular design feature of the wing under consideration. Generally speaking, at low Reynolds numbers and no sweep, the laminar boundary layer will separate under adverse pressure gradient, the subsequent expansion of the flow will reattach the boundary layer as turbulent, and a laminar separation bubble (Fig. 4) will be contained in-between the two regimes.[61,62] This bubble can be identified on thermograms as a narrow, elongated region of low heat transfer preceding the turbulent regime. At zero to moderate sweep and higher Reynolds number (but outside the critical conditions for attachment line transition), the transition will be caused by Tollmien-Schlichting waves characterized on the thermograms by a relatively smooth transition line (Fig. 5a).[68] As the sweep angle increases beyond a certain limit, the cross flow mechanism will prevail, with the transition front on thermograms resembling a "saw-teeth" pattern (Fig. 5b).[69]

The main obstacle to getting wider acceptance for this method, especially in the aeronautical industry, is that models are usually made of aluminum or stainless steel of high quality surface finish. The problems mentioned with this type of models in the previous section, i.e., high thermal diffusivity, and low emittance and high reflectance, only render the method more difficult to apply. In some cases, the problem may be solved satisfactorily by applying an insulating film, 1 or 2 mm in thickness, in specially machined grooves.[69] Crowder[66] suggested as a partial solution to this problem to cover the model with an insulating paint, and to spray liquid nitrogen into the tunnel, upstream the test section. The rapidly cooling flow produces on the metallic surface a thermal effect that is strong enough to make transition visible (Fig. 6).

Viewed in the perspective of a very few years, it seems that the IR imaging technique opened new horizons in the laminar flow research and applications. The method was used extensively in wind tunnel and flight test programs in Germany by the DLR and Deutsche Airbus,[68,70-74] in France at ONERA,[69,75] and in USA at NASA,[55,67] to investigate the occurrence of the various transition modes. The DLR / Deutsche Airbus program was a particular large-scale effort. It combined flight tests on small- and medium-sized airplanes with laminar flow gloves mounted on the wings, with wind-tunnel tests performed in different facilities. As part of this effort, an extensively instrumented VFW-614 twin jet medium-sized aircraft designated the Advanced Technologies Testing Aircraft System (ATTAS) was dedicated to laminar flow research over a period of a few years (Fig. 7a&b). The unique capability of IR imaging to provide repetitively global views of the transition pattern on the wing, allowed an immediate identification of the prevailing mechanism under given test conditions (Fig 7c). The combined use of IR imaging with hot films throughout the program helped elucidate the correlation between the actual mechanisms of transition development and numerical predictions designed to verify the e^N method. At NASA, the effort focused on comparative flight testing of different competing, or suplementing, methods for transition research.[55] At ONERA, the technique was used to confirm designs specifically aimed at obtaining significant runs of laminar flow on aerodynamic surfaces.[69] Unfortunately, none of these experiments illuminated the question surrounding the identification of the precise location in the transition process that is detected by this technique.

The main drawback with transition studies made in conventional wind tunnels is the scale of the models and the resulting inconsistency between the Reynolds number of the model and that of the real flying airplane. This discrepancy is pivotal in the search for ground testing methods capable of generating high Reynolds number flows. There are two main reasons for concern about this subject. The first is that transition, being a viscous effect, is critically influenced by the Reynolds

number of the airplane in flight. The second is that as of yet, there are no proven scaling methods for flows, especially not at large Reynolds numbers. To solve this problem cryogenic wind tunnels have been devised, where combinations of low temperatures, down to 100 K, and moderate pressurization can generate flows with Reynolds numbers in excess of 10^8 per meter. For these wind tunnels, non-intrusive, global and productive transition detection techniques are of fundamental importance. Despite the physical laws governing IR radiation working against this application, the IR imaging method showed promising results[76] and, so far, transition was detected at total flow temperatures down to 170 K.[77]

6. Propulsion Studies

The application of IR imaging to propulsion studies is very diverse in nature, the technique being used in cold and hot flow environments for studies ranging from flows in turbine cascades, through heat transfer measurements, to hot flows and plumes visualization.

Cold Flows

One of the earliest applications to jet engine research was to to study the effectiveness of film cooling for turbine blades.[78,79] In these applications the relative temperatures of the main flow and of the film flow are reversed. The "cooling air" that is injected through transpiration holes in the turbine blades is heated, to be visualized by IR imaging. This effect is possible because both the carbon dioxide and the water vapor in the air start to emit IR radiation at relatively low overheat temperatures. IR imaging was also used to inspect the film-cooled nozzle of a high-temperature wind tunnel for blockage areas on the transpiration surface.[80]

Brauling, Quast, and Dietrichs[81] used IR imaging to study boundary layer - shock interaction in a cascade flow simulating a jet engine turbine. This is an extension of transonic flow studies, the complex geometries very much complicating the flow and its diagnosis. The study succeeded to identify laminar and turbulent boundary layers, shock waves, separation bubbles and longitudinal vortices on the blades, but more work will be required to elucidate the findings.

Hot Flows

Combustion gases present another opportunity for IR imaging research. Sterby,[82] mapping the flow temperatures in an operating ramjet combustor, presented the temperature distribution of the reacting gases through topographic plots that greatly helped analyze and interpret the data. Byington et al.[83] used IR imaging to visualize and study the effectiveness of transpiration cooling in the hydrogen injection area of a supersonic combustor at flow temperatures up to 2000 K. Their investigation produced a very detailed picture of the flow, including the upstream shock interaction between the injected fuel and the main flow, the cool core of the injected fuel, and the lateral and downstream extent of the fuel mixing zone.

IR imaging systems also have been used to visualize exhaust gases of jet engines. There was special interest in surveying the plumes of VTOL aircraft hovering close to ground[84,85] because the interaction of the hot gases with the surrounding flow largely determines the aerodynamic capability and stability of these vehicles at take-off and landing. In a different application, the exhaust plume of a fighter airplane on the ground was visualized to identify flow structures causing radiation of low-frequency acoustic waves.[86] Presumably, those waves were the source of trouble for electronic testing equipment placed nearby.

7. Heat Transfer Studies

Relative to the obvious qualifications of the method for heat transfer studies, the scarcity of applications is relatively surprising.

Meroney[87] made a wind tunnel study of convective heat transfer of buildings using an actively heated model. The heat transfer coefficients were estimated, but lack of a data acquisition and processing system hampered progress on the work. Page et al.[88] investigated the flow of a radial jet on a stagnation surface. Using a heated jet impinging on a cold surface, they inferred the heat transfer occurring in the stagnation region from thermograms of the heated surface. Carlomagno and de Luca,[19,89] performed a similar investigation with interest in the heat transfer of both a single jet, and an array of jets. In this case, however, a cold air flow impinged on a heated metallic foil. Another jet impingement experiment was performed by Eppich and Kreatsoulas.[90] In their case, the surface upon which the jet impinged was a thin layer of an insulating material laid atop a constant temperature substrate. Therefore, they could deduce the heat flux across the top layer directly from the measurements of the surface temperature, the thickness of the top layer and the constant temperature of the substrate. Gartenberg and Roberts[9] proposed a method of mapping velocities by measuring the temperature distribution along a thin electrically heated wire placed across the flow of interest. The velocities can thus be derived from established, convective heat transfer correlations, provided the error measurement of the IR imaging system is known, especially when the wire displays high temperature- gradients in the scanner field of view. Spence[91] examined the possibility of determining heat transfer coefficients on vanes used for missile thrust vector control from wind-tunnel tests on a model vane under identical flow conditions. Henry and Guffond[92] made temperature measurements on a helicopter blade in an icing tunnel to validate computer code predictions of de-icing effectiveness of blade heaters. Other examples of heat transfer applications include convective heat transfer from a heated cylinder at moderate Reynolds numbers,[93] and external mapping of the temperatures of a gun barrel during firing.[94]

8. A View to the Future

A review of past achievements must end with a view to the future. Further progress in this field will be contingent on two factors: the technical developments in IR imaging technology, and the continuation of experimental exploration and aerodynamic research based on this technique.

Current trends in the electro-optic and semiconductor industries point to future IR imaging systems incorporating focal plane detector arrays. Such systems will offer improved performance in terms of spatial resolution, temperature sensitivity, and frame rate generation. Optionally, they will trade higher frame rates for lower temperature sensitivity. In parallel, as increasingly powerful personal computers become available, they will be used to increase the frame rate acquisition and storage. This option will allow capture of faster thermal transients and promote the application of the method in very short test duration facilities.

The testing needs at high Reynolds numbers in cryogenic wind tunnels at low temperatures will require imaging systems built around detectors sensitive to longer wavelength IR radiation, up to 30 micrometers.[95] In parallel, there will be requirements for window materials with high transmittance in selected bandwidths; good mechanical, thermal, and chemical properties; and compatible antireflective coatings.

At the hot-end of aerothermodynamic research, nonequilibrium, reactive, and high-temperature flow research will require multi-spectral IR imaging for measurement of wall thermal response, flow visualization, and tracing of the evolving concentration of chemical species through their absorption bands.

In aerodynamic testing, the challenge is either to solve the transition detection on metallic models or to compromise with other materials, either as inserts at locations of interest, or as model skins. The exact location where the transition is indicated on thermograms is still far from being defined. More comparative work is needed to define which phase of the transition process is detected, and to determine what flow, substrate, and IR imaging system parameters are that influence the identification of that location.

In general, each flow feature has a thermal signature of its own that should be identifiable on thermograms of models of interest. As the use of this technique expands, new features appearing on thermograms will puzzle engineers in their quest to identify their cause. Separation, shock waves, and vortices have already been observed and identified in the past, and continuing research will lead the IR imaging technique to become a widely accepted diagnostic tool in aerodynamic research.

9. Conclusions

In the years that have passed since 1967, the infrared imaging of aerodynamic surfaces gained recognition as an experimental tool with unique capability for fast mapping of surface temperatures. This capability is used in hypersonic research to determine heat flux distributions from local temperature measurements and in subsonic research to give a global view of the boundary layer transition to turbulence. With time, other flow features were identified on thermograms such as shock waves, separation, reattachment, and vortices. The use of the technique was gradually expanded to other disciplines, most notably propulsion and basic heat transfer research.

The technique had a relatively slow start, due to sporadic experiments, obscure documentation, and lack of data processing capability. When viewed in the perspective of the long period of time it took to mature and get recognition, it seems the technique was "invented" too soon. However, the ever-increasing number of publications reporting use of IR imaging in aerodynamic research is a convincing proof that the method has passed through the development stage and is assuming the status of a routine experimental procedure.

10. Acknowledgments

This research was supported under NASA Langley Research Center grant NAS 1-18584-58.

The authors wish to thank the following persons for their help in supplying sample photographs and / or granting permission to reproduce them: David Throckmorton and Vincent Zoby, NASA Langley; Armin Quast, DLR Braunschweig; George Gauffre and Volker Schmitt, ONERA Chatillon; James Crowder, Boeing; John Newbauer, AIAA; George Helfrich, NASA Langley.

The first author wishes to thank George B. Boyles, Jr., from NASA Langley Research Center for his daily untiring help and support.

11. References

1. Schlichting, H., Boundary Layer Theory, 7th ed., McGraw-Hill, New York, 1979, pp. 286, 706.
2. Gartenberg, E. and Roberts, A.S. Jr., "Phenomenological Aspects of Infrared Imaging in Aeronautical Research," AIAA Paper 88-4674, September 1988.
3. Settles, G.S., "Modern Developments in Flow Visualization," AIAA Journal, Vol. 24, August 1986, pp. 1313-1323.
4. Lloyd, J.M., Thermal Imaging Systems, Plenum Press, New York, 1975.
5. Gaussorgues, G., La Thermographie Infrarouge, 3rd ed., Technique et Documentation-Lavoisier, 1989.
6. Gauffre, G. and Fontanella, J-C., "Les Cameras Infrarouges: Principes, Characterization, Utilization," La Recherche Aerospatiale, ONERA, No. 1980-4, pp. 259-269; available also in English edition.
7. Bouchardy, A.-M., Durand, G. and Gauffre, G., "Processing of Infrared Thermal Images for Aerodynamic Research," Applications of Digital Image Processing, SPIE Vol. 397, April 1983, pp. 304-309.
8. Enault, C. and Bretaudeau, F., "Traitement d'Images de Thermographie Infra-Rouge: Lissage Local et Interpolation Temporelle," ONERA Rapport Technique 8/7254 SN, June 1988.
9. Gartenberg, E. and Roberts, A.S. Jr., "Influence of Temperature Gradients on the Measurement Accuracy of IR Imaging Systems," International Conference on Thermal Sensing and Imaging Diagnostic Applications, Thermosense XII, SPIE Vol. 1313, April 1989, pp. 218-224, see also 6th Applied Aerodynamics Conference, AIAA, June 1988, pp. 121-128.
10. de Luca, L., Cardone, G. and Carlomagno, G.M., "Theoretical and Experimental Analysis of the Modulation Response of a Sampled IR Imaging System," International Conference on Thermal Sensing and Imaging Diagnostic Applications, Thermosense XII, SPIE Vol. 1313, April 1989, pp. 259-268.
11. Wolfe, W.L. and Zissis, G.J., (ed)., Infrared Handbook, Environmental Research Institute of Michigan, 1985, ch. 7.
12. Gauffre, G., "Detection de la Transition Laminaire Turbulent par Thermographie Infrarouge," La Recherche Aerospatiale, ONERA, No. 1988-2, pp. 11-22; available also in English edition.
13. Balageas, D., Boscher, D., Deom, A., Fournier, J. et Henry, R., "La Thermographie Infrarouge: un Outil Quantitatif a la Disposition du Thermicien," Revue Generale de Thermique, No. 322, October 1988, pp. 501-510; also, ONERA T.P. No. 1989-3.
14. Balageas, D., Boscher, D., Delpech, P., Deom, A., Fournier, J., Gardette, G., Lempereur, C., Berthoumieux, P. et Mathe, J.M., "Application de la Thermographie Infrarouge a la Mesure des Flux Thermiques en Soufflerie," ONERA T.P. No. 1989-192.
15. Balageas, D., Boscher, D., Delpech, P. and Deom, A., " Determination des Coefficients de Transfert Convectif sur une Maquette en Soufflerie par Thermographie Infrarouge Stimulee," ONERA T.P. No. 1989-218.
16. Allegre, J., Dubreuilh, X.H. and Raffin, M., "Measurement of Aerodynamic Heat Rates by Infrared Thermographic Technique at Rarefied Flow Conditions," Rarefied Gas Dynamics: Physical Phenomena, Progress in Astronautics and Aeronautics, Vol 117, AIAA, 1988, pp. 157-167.
17. Monti, R., "Thermography," in Flow Visualization and Digital Image Processing, Lecture Series 1986-09, von Karman Institute for Fluid Dynamics, Rhode Saint-Genese, Belgium.
18. Monti, R., "Thermography," Handbook of Flow Visualization, Wen-Jei Yang editor, Hemisphere, New-York 1989, pp. 331-353.
19. Carlomagno, G.M. and de Luca, L., "Infrared Thermography in Heat Transfer," Handbook of Flow Visualization, Wen-Jei Yang editor, Hemisphere, New-York 1989, pp. 531-553.
20. de Luca, L., Carlomagno, G.M. and Buresti, G., "Boundary Layer Diagnostics by Means of an Infrared Scanning Radiometer," Experiments in Fluids, Vol 9, Springer-Verlag 1990, pp. 121-128.
21. Carlomagno, G.M., de Luca, L. and Alziary, T.,"Heat Transfer Measurements with an Infrared Camera in Hypersonic Flow," Computers and Experiments in Fluid Flow, 4th. International Conference on Computational Methods and Experimental Measurements, Springer-Verlag 1989, pp. 467-476.

22. Wendt J., "Infrared Thermography," in The Second Joint Europe/US Short Course in Hypersonics, U.S. Air Force Academy, Colorado Springs, January 1989.
23. Simeonides, G., Van Lierde, P., Van der Stiechele, J., Capriotti, D. and Wendt, J.F., "Infrared Thermography in Blowdown and Intermittent Facilities," AIAA Paper 89-0042; see also, Journal of Thermophysics, Vol.4, AIAA, April 1990, pp. 143-148.
24. Thomann, H. and Frisk, B., "Measurement of Heat Transfer with an Infrared Camera," Int. Journal Heat Mass Transfer, Vol. 11, 1968, pp. 819-826.
25. Eckert, E.R.G. and Drake, R.M. Jr., Analysis of Heat and Mass Transfer, 2nd. ed., McGraw-Hill, New-York, 1972, pp. 169-172.
26. Jones, R.A. and Hunt, J.L., "Use of Fusible Temperature Indicators for Obtaining Quantitative Aerodynamic Heat-Transfer Data," NASA TR R-230, Washington D.C., February 1966.
27. Balageas, D.L. and Ory, D., "Improvements in the Determination of Convective Transfers from Infrared Thermography," La Recherche Aerospatiale, Vol. 1980-3, ONERA, June 1980, pp. 73-78.
28. Schepers, H.J., "Heat Transfer Investigations of Axisymmetric Bodies at Hypersonic Speeds by Means of Infrared Measurement," NASA TT F-14,509, Washington, D.C., August 1972. Translation from German of DLR-Mitt-71-19, October 1971.
29. Compton, D.L., "Convective Heating Measurement by Means of an Infrared Camera," Space Shuttle Aerothermodynamics Technology Conference, Volume II-Heating, NASA TM X-2507, February 1972, pp. 645-660. See also "Use of an Infrared-Imaging Camera to Obtain Convective Heating Distributions," AIAA Journal, Vol 10, August 1972, pp. 1130-1132.
30. Bynum, D.S., Hube, F.K., Key, C.M. and Dyer, "Measurement and Mapping of Aerodynamic Heating in VKF Tunnel B with an Infrared Camera," AEDC-TR-76-54, Arnold Air Force Station, Tennessee, November 1976.
31. Noble, J.A. and Boylan, D.E., "Heat-Transfer Measurements on a 5-deg Sharp Cone Using Infrared Scanning and On-Board Discrete Sensor Technique," AEDC-TR-78-V51, Arnold Air Force Station, Tennessee, December 1978.
32. Boylan, D.E., Carver, D,B., Stallings, D.W. and Trimmer, L.L., "Measurement and Mapping of Aerodynamic Heating Using a Remote Infrared Scanning Camera in Continuous Wind Tunnels," Proceedings 10th Aerodynamic Testing Conference, AIAA, April 1978, pp. 213-231.
33. Stallings D.W. and Whetsel, R.G., "Use of Infrared Imagery in Continuous Flow Wind Tunnels," Thermal Infrared Sensing Diagnostics, Thermosense V, SPIE Vol. 371, October 1982, pp. 203-210.
34. Stallings, D.W. and Carver, D.B., "Infrared and Phase-Change Paint Measurements of Heat Transfer on the Space Shuttle Orbiter," AEDC-TSR-78-V13, Arnold Air Force Station, Tennessee, June 1978.
35. Martinez, A., Dye, W.H., Vaughn, J.E., Hersey, D.W. and Lutz, G.R., "Results of Test OH69 Obtained in the AEDC VKF Hypersonic Tunnel B, Using the Infrared Scanning Method to Obtain Heat Transfer Data on the 0.040 Scale Model 82-0 of the Space Shuttle Forebody," Vols. I and II, NASA CR-151410 and NASA CR-151141, July 1978.
36. Hender, D.R. and Okabe, C.M., "Expanded Uses of Infrared Scanning Data in Aerodynamic Heating Tests," AIAA Paper 83-1542, June 1983.
37. Schlichting, pp. 334-335, 713-714.
38. Peake, D.J., Bowker, A.J., Lockyear, S.J. and Ellis, F.A., "Non-Obtrusive Detection of Transition Region Using an Infra-Red Camera," in AGARD-CP-224, May 1977.
39. Collier, A.S., Lafferty, J.F., Scott, S.S. and Witte, D.W., "Aerodynamic Heat Transfer Testing in Hypersonic Wind Tunnels Using an Infrared Imaging System," AIAA Paper 90-0189, January 1990.
40. Hall, R.M., Obara, C.J., Carraway, D.L., Johnson, C.B., Wright, R.E. Jr., Covell, P.F. and Azzazy, M., "Comparisons of Boundary-Layer Transition Measurement Techniques in the Langley Unitary Plan Wind Tunnel," AIAA Paper 89-2205, July 1989.
41. Bendettini, A. and Peake, D.J., "Diagnosis of Separated Flow Regions on Wind-Tunnel Models Using an Infrared Camera," International Conference on Instrumentation in Aerospace Simulation Facilities, (ICIASF 79), IEEE , September 1979, pp. 171-185.

42. Arai, N. and Sato, K., "Nonintrusive Measurement of Surface Temperature Distributions," Sixteenth International Symposium on Space Technology and Science, AGNE Publishing, Tokyo, Vol. 1, Part 2, May 1988, pp. 929-934.
43. Henckels, A. and Maurer, F., "Application of Infra-red Thermography in a Hypersonic Wind Tunnel," International Conference on Instrumentation in Aerospace Facilities, (ICIASF 89), IEEE, September 1989, pp. 516-524.
44. Byron, S.L. and Edsinger, L.E., "Preliminary Analysis of Remote Infrared Imagery of Shuttle During Entry - An Aerothermodynamic Flight Experiment," NASA TM 73251. Washington, D.C., August 1977.
45. Anon. "Infrared Imagery of Shuttle (IRIS)," Task 1 Final Report, Martin Marietta Corp., NASA CR-152123, August 1977.
46. Chocol, C.J., "Remote Infrared Imagery of Shuttle During Entry," Joint Automatic Control Conference, AICE, June 1979, pp. 251-255.
47. Green, M.J., Budnik, M.P., Yang, L. and Chiasson, M.P., "Supporting Flight-Data Analysis for Space-Shuttle Orbiter Experiments at NASA Ames Research Center," NASA TM-84345, Washington, D.C., April 1983.
48. Myrick, D.L. and Kantsios, A.G., "Incorporating Geometric and Radiative Effects into Infrared Scanning Computer Analysis," Thermosense V, SPIE Vol. 371, 1982, pp. 211-215.
49. Throckmorton, D.A., Zoby, E.V. and Kantsios, A.G., "The Shuttle Infrared Leeside Temperature Sensing (SILTS) Experiment," AIAA Paper 85-0328, January 1985.
50. Throckmorton, D.A., Dunavant, J.C. and Myrick, D.L., "Shuttle Infrared Leeside Temperature Sensing (SILTS) Experiment - STS 61-C Results," AIAA Paper 88-2668, June 1988.
51. Throckmorton, D.A., Zoby, E.V., Dunavant, J.C. and Myrick, D.L., "Shuttle Infrared Leeside Temperature Sensing (SILTS) Experiment - STS-28 Preliminary Results," AIAA Paper 90-1741, June 1990.
52. Elsenaar, A., Rohne, P.B., Rozendal, D. and Poestkoe, R., "Instrumentation Requirements for Laminar Flow Research in the NLR High Speed Wind Tunnel Test," International Congress on Instrumentation in Aerospace Simulation Facilities (ICIASF 89), IEEE, September 1989, pp. 365-373.
53. Elsenaar, A., "The Windtunnel as a Tool for Laminar Flow Research," 17th Congress of the International Council of the Aeronautical Sciences (ICAS 1990), AIAA, September 1990, pp. 174-185.
54. Korner, H. and Horstmann, K.H., "The Use of Airplanes for Aerodynamic Research at DFVLR-Institute for Design Aerodynamics," Festschrift for B.H. Gothert's 80th Birthday, University of Tennessee, Space Institute, Tullahoma, October 1987.
55. Holmes, B.J., Obara, C.J., Manuel, G.S. and Lee, C.C., "Developments in Flow Visualization Methods for Flight Research," Flow Visualization V, International Symposium, Hemisphere, Washington, D.C., 1990.
56. Nitsche, W. and Szodruch, J., "Concepts and Results for Laminar Flow research in Wind Tunnel and Flight Experiments," 17th Congress of the International Council of the Aeronautical Sciences (ICAS 1990) , AIAA, September 1990, pp. 197-209.
57. Korner, H., Horstmann, K.H., Koster, H., Quast, A. and Redeker, G., "Laminarization of Transport Aircraft Wings, A German View," AIAA Paper 87-0085.
58. Korner H., "Natural Laminar Flow Research for Subsonic Transport Aircraft in FRG," 16th International Congress of the Aeronautical Sciences (ICAS 1988), AIAA, 1988.
59. Greff, E., "Aerodynamic Design for a Regional Aircraft," 17th Congress of the International Council of the Aeronautical Sciences (ICAS 1990), AIAA, September 1990, pp. 1251-1265.
60. Schmitt, R.L. and Schanetz, B.P., "Experimental investigation of Three Dimensional Separation on an Ellipsoid-Cylinder Body at Incidence", AIAA Paper 85-1686, July 1985.
61. Quast, A., "Detection of Transition by Infrared Image Technique," International Congress on Instrumentation in Aerospace Facilities (ICIASF 87), IEEE, June 1987, pp. 125-134, see also "Bestimmung des laminar-turbulent Umschlags mit Hilfe der Infrarottechnik," DFVLR Braunschweig IB 129 - 86 / 6, October 1987.
62. Gartenberg, E., Roberts, A.S.Jr., and McRee, G.J., "Infrared Imaging and Tufts Studies of Boundary Layer Regimes on a NACA 0012 Airfoil," International Congress on Instrumentation in Aerospace Simulation Facilities (ICIASF 89), IEEE, September 1989, pp. 168-178.

63. Carlomagno, G.M., De Luca, L., Buresti, G., and Lombardi, G., "Characterization of Boundary Layer Conditions in Wind Tunnel Tests Through IR Thermography Imaging," Applications of Infrared Technology, SPIE Vol. 918, June 1988, pp. 23-29.
64. Heath, D.M., Winfree, W.P., Carraway, D.L. and Heyman, J.S., "Remote Noncontacting Measurements of Heat Transfer Coefficients for Detection of Boundary Layer Transition in Wind Tunnel Tests," International Congress on Instrumentation in Aerospace Simulation Facilities (ICIASF 89), IEEE, September 1989, pp. 135-139.
65. Monti, R. and Zuppardi, G., " Computerized Thermographic Technique for the Detection of Boundary Layer Separation," Aerodynamic Data Accuracy and Quality: Requirements and Capabilities in Wind Tunnel Testing, AGARD-CP-429, September 1987, ch. 30.
66. Crowder, J.P., "Infrared Cameras for Detection of Boundary Layer Transition in Transonic and Subsonic Wind Tunnels," AIAA Paper 90-1450, June 1990.
67. Brandon, J.M., Manuel, G.S., Wright, R.E. Jr., and Holmes, B.J., "In-Flight Flow Visualization Using Infrared Imaging," AIAA Paper 88-2111, May 1988; see also Journal of Aircraft, Vol. 27, AIAA, July 1990, pp. 612-618.
68. Horstmann, K.H., Quast, A. and Redeker, G., "Flight and Wind-Tunnel Investigations on Boundary-Layer Transition," 16th Congress of the International Council of the Aeronautical Sciences (ICAS 1988), AIAA, August 1988, pp. 979-986; see also Journal of Aircraft, Vol. 27, AIAA, February 1990, pp. 146-150.
69. Schmitt, V., Reneaux J. and Thibert, J.J., "Design and Experimental Investigation of a Laminar Horizontal Tail," AIAA Paper 90-3042, August 1990.
70. Redeker, G., Horstmann, K.H., Koster, H., Thiede, P. and Szodruch, J., "Design of a Natural Laminar Flow Glove for a Transport Aircraft," 8th Applied Aerodynamics Conference, AIAA, August 1990, pp. 375-384.
71. Horstmann, K.H., Redeker G., Quast, A., Dressler, U. and Bieler, H.,"Flight Tests with a Natural Laminar Flow Glove on a Transport Aircraft," Ibid., pp. 385-392.
72. Henke, R., Munch, F.X., and Quast, A., "Natural Laminar Flow: a Wind Tunnel Test Campaign and Comparison with Flight Test Data," Ibid., pp. 393-400.
73. Horstmann, K.H., Redeker, G. and Miley, S.J., "Flight Investigations of Tollmien-Schlichting Waves on an Aircraft Wing," 17th Congress of the International Council of the Aeronautical Sciences (ICAS 1990), AIAA, September 1990, pp. 186-192.
74. Henke, R. and Munch, F.X., "Laminar Flow Experiments with a Large Half Model in Transonic Flow," Ibid., pp. 1090-1097.
75. Thibert, J.J., Reneaux, J. and Schmitt, V., "ONERA Activities on Drag Reduction," Ibid., pp. 1053-1064.
76. Seraudie, A., Blanchard, A. and Dor, J.B., "Qualification d'Essais en Ambiance Cryogenique a la Soufflerie T2," presented at the 23eme Colloque d'Aerodynamique Appliquee, Association Aeronautique et Astronautique de France Note Technique No. 86-07, Modane, Novembre 1986.
77. Gartenberg, E., Johnson, W.G. Jr., Johnson, C.B., Carraway, D.L. and Wright, R.E., "Transition Detection Studies in the Cryogenic Environment," 8th Applied Aerodynamics Conference, AIAA, August 1990, pp. 234-244.
78. Blair, M.F. and Lander, R.D., "New Techniques for Measuring Film Cooling Effectiveness," Journal of Heat Transfer, ASME, Vol. 97, November 1975, pp. 539-543.
79. Sasaki, M., Kumagai, T. and Hamano, M., "Film Cooling Effectiveness for Injection From Multirow Holes," Journal of Engineering for Power, ASME, Vol. 101, January 1979, pp. 101-108.
80. Borg, S.E., Wright, R.E. Jr., Alderfer, D.W. and Whipple, J.C., "The Utilization of an Infrared Imaging System as a Cooling Slot Blockage Detector in the Inspection of a Transpiration Cooled Nozzle," NASA TM-102608, January 1990.
81. Braunling, W., Quast, A. and Dietrichs, H.-J., "Detection of Separation Bubbles by Infrared Images in Transonic Turbine Cascades," Journal of Turbomachinery, ASME, Vol. 110, October 1988, pp. 504- 511.
82. Streby, G.D., "Combustor Flow Visualization Using Innovative Infrared Thermographic Techniques," Wright Research Development Center WRDC-TR-89-2015, March 1989.

83. Byington, C.S., Burton Northam, G. and Capriotti, D.P., "Transpiration Cooling in the Locality of a Transverse Fuel Jet for Supersonic Combustors," AIAA Paper 90-2341, July 1990.
84. Flaig, J.W., "Infrared Flow Visualization for VTOL Applications," AIAA Paper 77-618, June 1977; see also "USN / FMOD FRG VAK-191K Joint Flight Test Program, Volume 13, IR Flow Visualization," Naval Air Systems Command NAVAIR-13R-76, August 1976.
85. Dries, J.W. and Ferrante, J., "Exhaust Flow Visualization of the McDonnell-Douglas Lift / Cruise Fan V/STOL Aircraft Model," Naval Research Laboratory Instruction Book 174, Washington, D.C., February 1980.
86. Witten, A.J. and Courville, G.E., "Investigation of Aeroacoustic Mechanisms by Remote Thermal Imaging," Thermal Infrared Sensing for Diagnostic and Control, Thermosense X, SPIE Vol. 934, April 1988, pp. 207-214.
87. Meroney, R.N., "Studying the Convective Heat Transfer from a Building Model with Infrared Camera Techniques," ASME Transaction 78-WA/HI-58.
88. Page, R.H., Ostowari, C. and Carbone, J.S., "Radial Jet Flow," Flow Visualization IV, International Symposium, Hemisphere, Washington, D.C., 1987, pp. 513-521.
89. Carlomagno, G.M. and de Luca, L. "Heat Transfer Measurements by Means of Infrared Thermography," Idem., pp. 611-616.
90. Eppich, H.M. and Kreatsoulas, J.C., "A Novel Infrared Thermography Heat Transfer Measurement Technique," AIAA Paper 89-0601, January 1989.
91. Spence, T.M., "Applications of Infrared Thermography in Convective Heat Transfer," M.S. Mech. Eng. Thesis, Naval Postgraduate School, Monterey, March 1986.
92. Henry, R. and Guffond, D., "Infrared Technique to Measure Skin Temperature on an Electrothermal De-icer, Comparison with Numerical Simulations," AIAA Paper 89-1989, January 1989; see also ONERA TP No. 1989-28.
93. Daryabeigi, K. and Alderfer, D.W., "Aerodynamic Applications of Infrared Thermography," 33rd International Technical Symposium on Optical and Optoelectronic Applied Science and Engineering, SPIE Paper 1157-20, August 1989.
94. Fuller P.W.W., "Gun Barrel Temperature Study Using Short Time Scan Thermal Imaging," International Congress on Instrumentation in Aerospace Simulation Facilities (ICIASF 89), IEEE, September 1989, pp. 159-167.
95. Schulze, B., Lange, R. and Craubner, S., "An Infrared Camera System for Detection of Boundary Layer Transition in the ETW," 2nd Cryogenic Technology Meeting, European Transonic Windtunnel GmbH and DFVLR, Koln, Germany, June 1988.

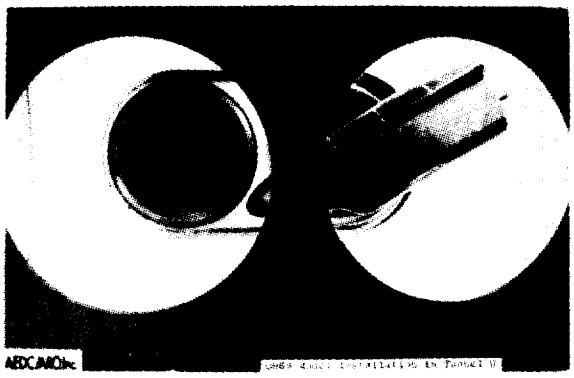

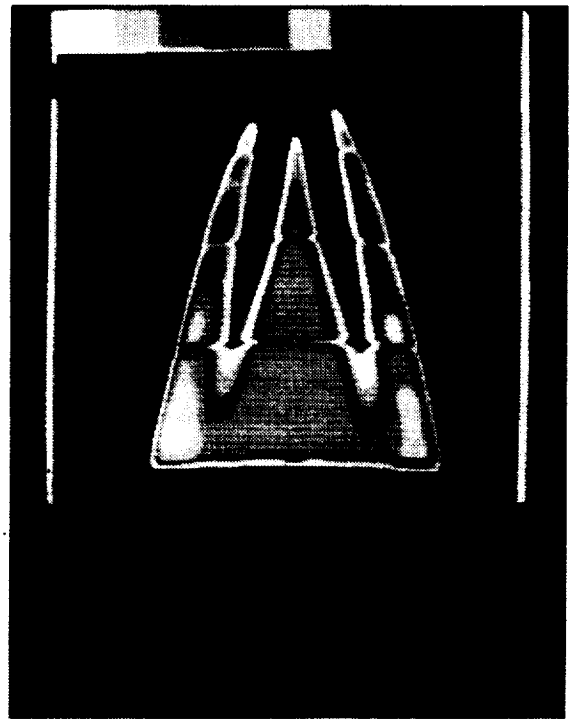

Fig. 1. a) Space Shuttle forebody model in Tunnel B at AEDC von Karman gas dynamics facility during hypersonic heating test. b) Typical heating pattern on the windward side as captured by the IR imaging system.[35]
Courtesy NASA, reprinted with permission.

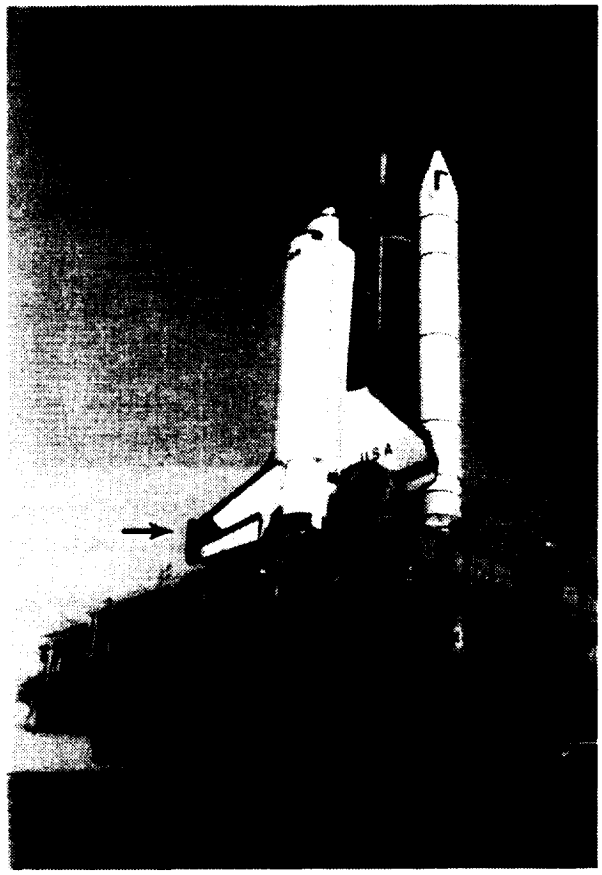

Fig. 2. Space Shuttle Columbia atop the Mobile Launcher Platform. The Shuttle Infrared Leeside Temperature Sensing (SILTS) pod is installed atop the vertical stabilizer.
Courtesy NASA, reprinted with permission.

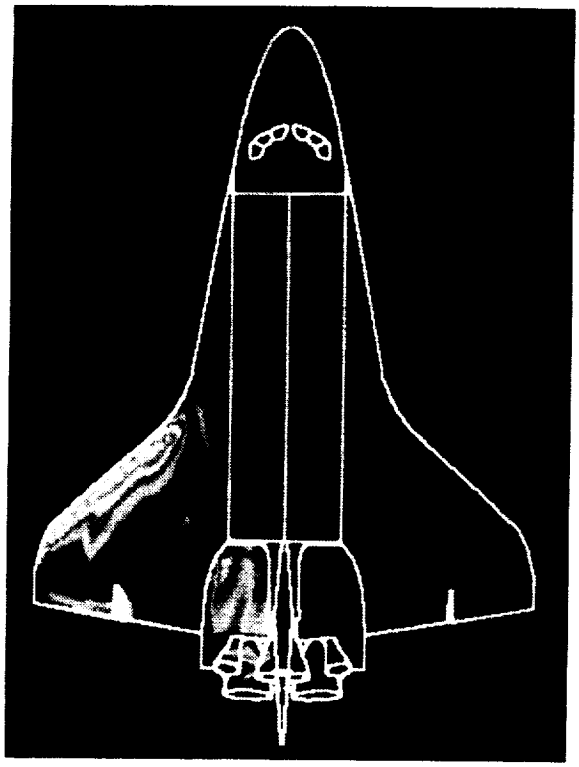

Fig. 3. SILTS data of Space Shuttle heating pattern during atmospheric re-entry, projected on the orbiter planform.[51]
Courtesy D. Throckmorton and V. Zoby, NASA Langley, reprinted with permission.

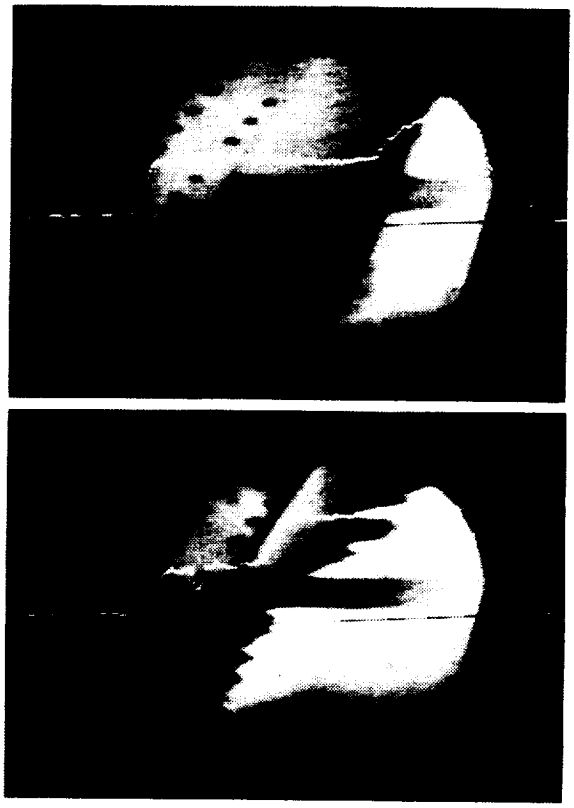

Fig. 5. Characteristic transition patterns.
a) Tollmien-Schlichting (TS) waves,[12] b) cross flow (CF).[69] Dark area indicates laminar regime and light area indicates turbulent regime. Notice the saw-teeth pattern characteristic to CF instability.
Courtesy G. Gauffre and V. Schmitt, ONERA Chatillon, reprinted with permission.

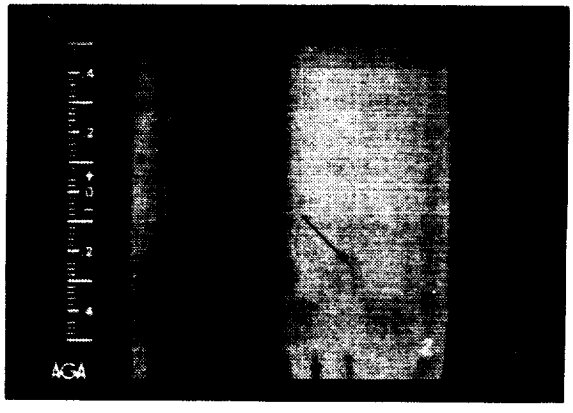

Fig. 4. Transition via laminar separation bubble. The bubble is indicated by the colder (darker) straight strip between the laminar (dark) and turbulent (light) areas.
Courtesy A. Quast, DLR Braunschweig, reprinted with permission.

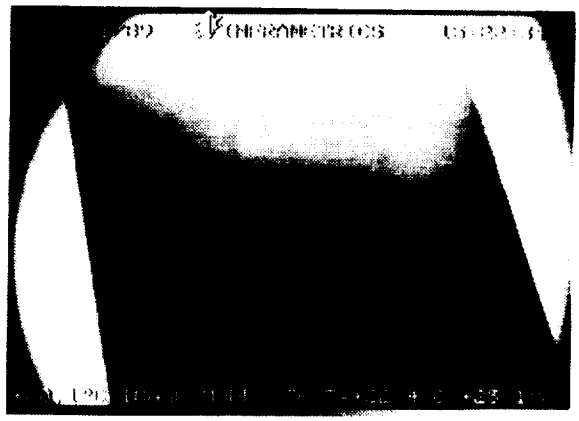

Fig. 6. Turbulent wedge and transition captured on a painted stainless steel model by injecting liquid nitrogen into the wind-tunnel flow.[66]
Courtesy J. Crowder, Boeing, reprinted with permission.

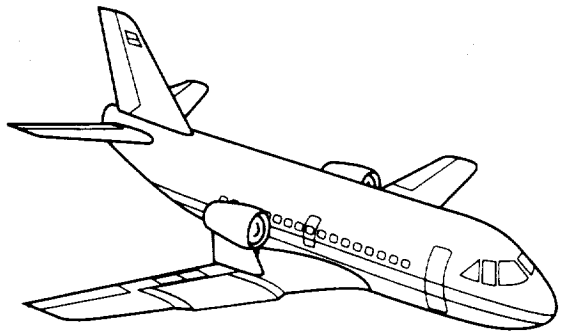

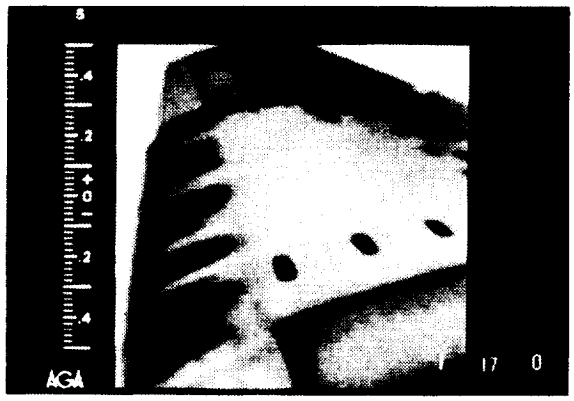

Fig. 7. The VFW-614 Advanced Technologies Testing Aircraft System. a) Schematic drawing; the laminar flow glove, marked gray, is outboard the engine pylon.[57] b) Close-up view of the wing area; notice the laminar glove and the IR cameras locations.[71] c) In-flight transition pattern induced by Tollmien-Schlichting waves and insect contamination (turbulent wedges). Courtesy A. Quast, DLR Braunschweig, reprinted with permission.

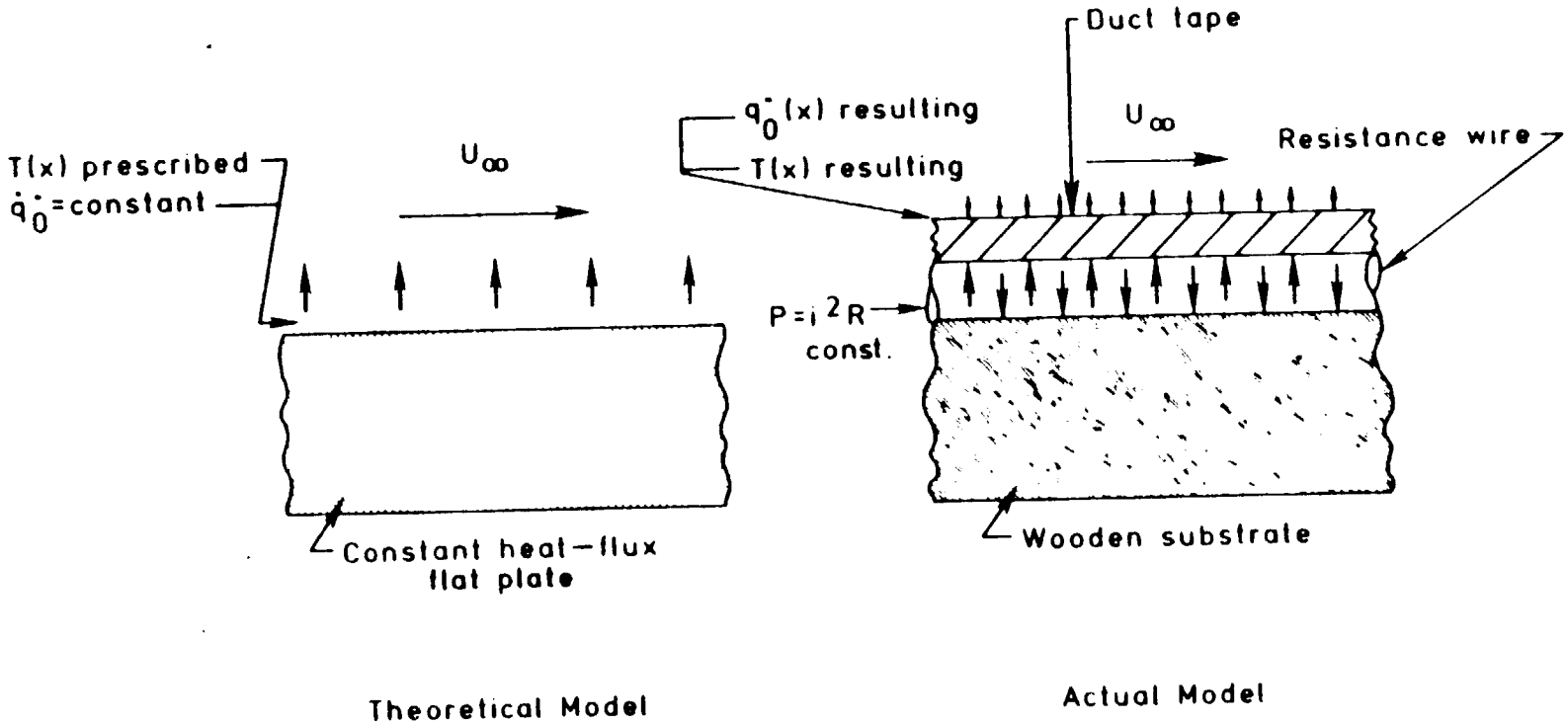

Fig. 5.6 Heated flat plate experiment: comparison between the theoretical constant heat flux model and constant power reality.

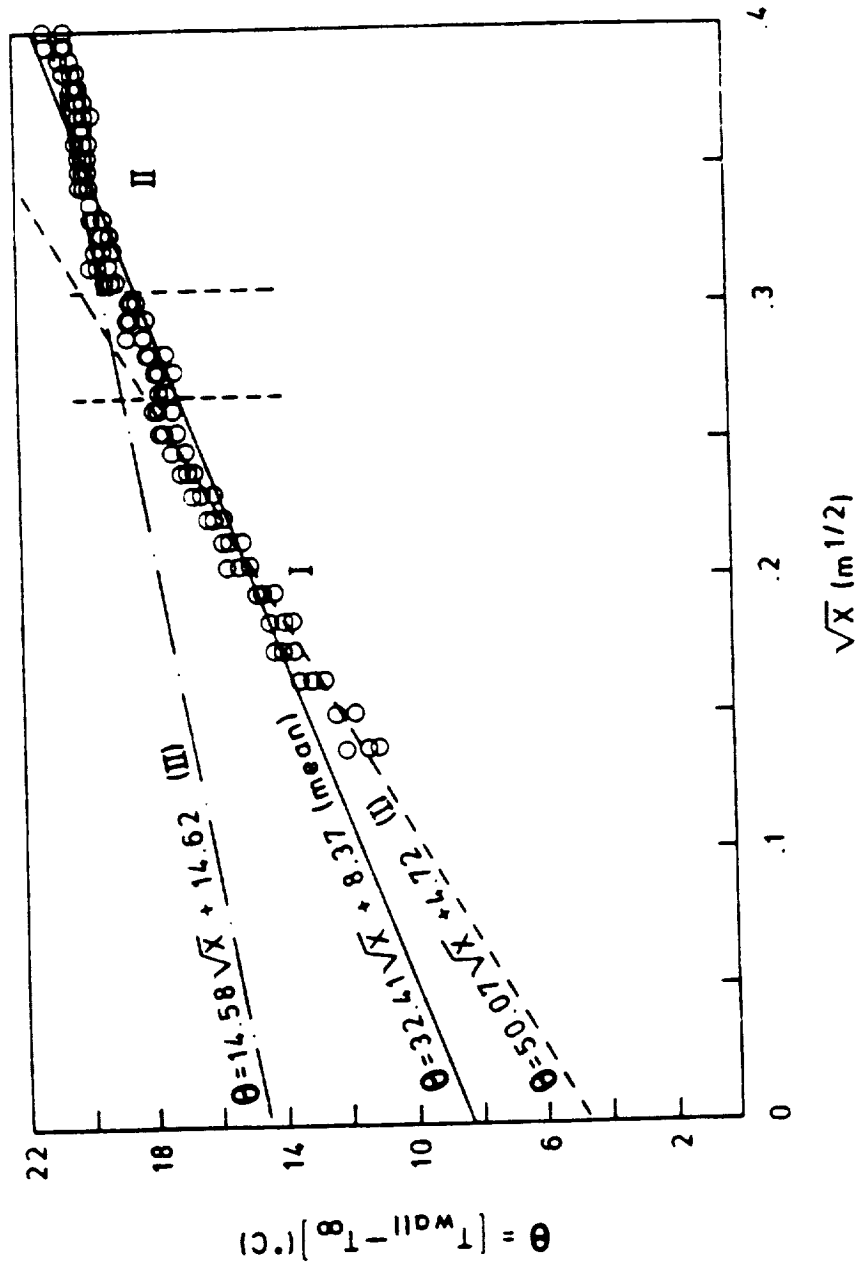

Fig. 5.5 Constant power heated flat plate experiment: adjusted temperature profile vs. square-root of distance from the leading edge. $Re_x = 1.233 \times 10^6 X(m)$

Data points of three different experiments.

condition. The model, assuming a general heat flux distribution chordwise and its analytical solution, was formulated by Klein and Tribus (1952). When simplified to the constant heat flux assumption, the solution reads

$$\theta(x) = 2.2019 \frac{\dot{q}_o''}{k_a} Pr^{-1/3} \left(\frac{\nu_a}{U}\right)^{1/2} x^{1/2}$$

$$= \text{const} \cdot x^{1/2} \qquad (5.1)$$

where $\theta(x)$ is the difference between the local wall temperature and the freestream air static temperature, $\dot{q}_o''$ is the wall heat flux, k_a is the air conductivity, Pr is the air Prandtl number, ν_a is the air kinematic viscosity, U is the freestream air velocity and x is the distance from the leading edge. According to this model, when the flat plate temperature distribution corrected by the ambient air temperature is plotted against the square-root of the distance from the leading edge, the slope of the line is an indication of the heat flux convected into the airstream. When this plotting is done for the present case, as shown in Fig. 5.5, its analysis shows that although the data is well correlated (r^2 is 0.945 with a variance of 0.38) the assumed linear behavior of the data is not uniform all along the coordinate scale. A closer look suggests one linear regression for the first 14 stations and another for the last 18 stations, leaving 6 stations in between as a transition zone. Following this approach, the variance of the data goes down, for the first group to 0.1 and for the second group to 0.05, which is significantly better. The question is what causes this change in the pattern behavior. An answer lies in the actual physical process taking place with this experimental set-up and its departure from the assumed model (see Eq. 5.1). As shown in Fig. 5.6, the theory assumes a flat plate "pumping" a constant amount of heat flux into the airstream. For a desired constant value of this heat flux, a certain prescribed temperature distribution should be

a temperature rise proportional to the square root of the distance from the leading edge.

(3) The leading edge experiences an abrupt increase in its temperature, due to its sharpness. This geometrical feature causes a finite amount of heat to be absorbed by a theoretically infinitesimal substrate mass, with the consequent real increase in temperature. The effect is further augumented by the fact that the heating wires being wrapped around the plate, the leading edge is well heated from all around its contour.

(4) The temperature distribution exhibits some irregularity around the coordinate x=8 cm. This is the region where the thermocouple junction was placed, a fact that caused a slight "bumpiness" (about 0.1 mm high and 8 mm long streamwise), on the overlaying duct tape surface. This geometrical feature initiated a directional emittance factor, which is usually lower than its normal counterpart, especially in the range of local inclination between 60° to 90° (Sparrow and Cess, 1978, p. 55). This effect, not being taken into account by the system's software, is ultimately (and falsely) interpreted as a local drop in temperature.

As a result of these considerations, it was decided to proceed with the analysis of the experiments, using only the data points starting at the coordinate x = 1.9 cm from the leading edge (the first 1.52 cm from the leading edge were ignored). The numerical values of these coordinates resulted from the fact that the data was extracted at each third consecutive pixel, which on the plate is equivalent to 3.8 mm.

In search for a model against which the experimental results can be evaluated, the physical reality suggests using the flat plate laminar boundary layer model with constant heat flux at its surface as the prescribed boundary

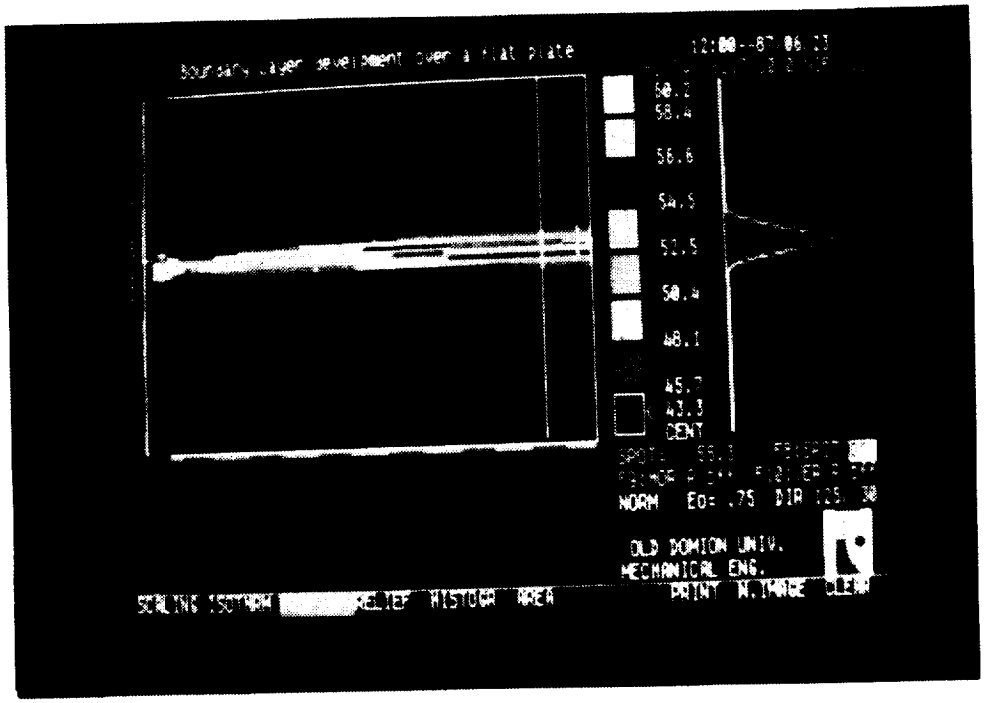

Fig. 5.4 Constant power heated flat plate experiment DISCO II® output with longitudinal and latitudinal temperature distributions. Air flows from left to right

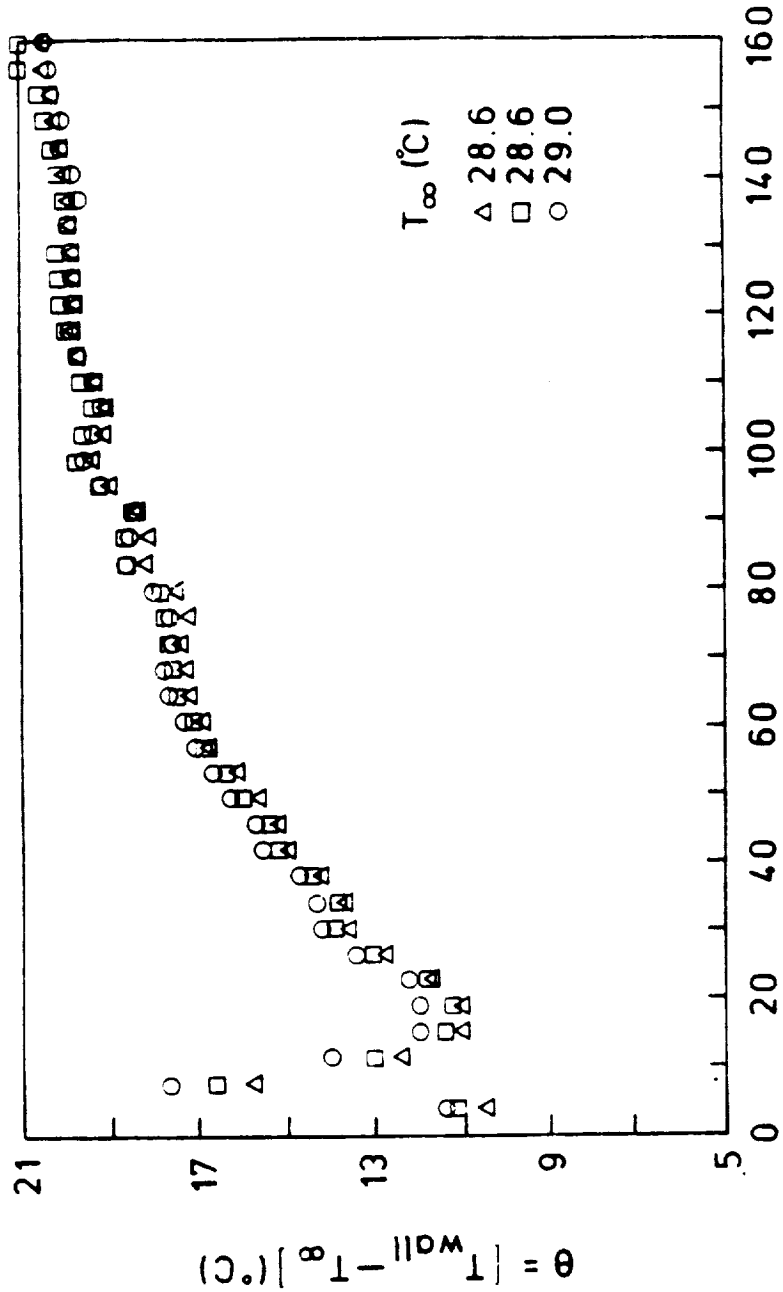

Fig. 5.3 Constant power heated flat plate experiment: adjusted temperature profile vs. distance from leading edge, $Re_x = 1.233 \times 10^6$ X(m)

results ensured that no further benefit would have come out of analyzing more profiles, except perhaps to establish a statistical variation measure for the data set.

5.3 Results and Discussion

The chordwise temperature profiles as obtained from the last three runs are shown in Fig. 5.3. The data in Fig. 5.3 was extracted from computer stored thermographies, an example of which is shown in Fig. 5.4. Note the longitudinal (chordwise) temperature distribution under the thermography and the latitudinal (spanwise) temperature distribution at three different stations along the chord, to the right of the thermography. The wind-tunnel air temperature for runs 1 and 2 was 28.6°C and for run 3, was 29.0°C. The actual wind tunnel air velocity was 20.9 m/sec during all three runs. The camera's field of view in this configuration was 16.5x16.5 cm, and the Reynolds number of that area of the plate scanned by the camera varied between zero (at the leading edge) to about 217000. This means that the phenomena addressed should be all under the laminar boundary layer regime, Re_{crit} = 500,000.

The data as presented in Fig. 5.3 displays the temperature profile along the plate reduced by the airflow temperature, versus the chordwise coordinate. A first evaluation of these profiles reveals the following:

(1) The information gathered from all three runs was quite reproducible, and the data points obtained from the different experiments almost coincide.

(2) The general qualitative behavior of the surface temperature distribution meets the expectations based on the laminar boundary layer theory, i.e.,

on the heat transfer process from the flat plate to the fluid and in general is disruptive to infrared measurements. The other concern was that long periods of heating, would affect the substrate to an unknown degree resulting in long cooling times between runs and irreproducible results. In this respect, the thermocouple used for emittance calibrations proved to be of significant help, in establishing the substrate initial conditions for each test.

According to the above mentioned guidelines, a typical experiment would run for less than one minute with the time split between the following steps.

(1) Wind-tunnel starting and achieving steady-state operation (approx. 15 secs.)

(2) Turning-on the power supply, and recording of the data. Turning-off the power supply (approx. 20 secs.)

(3) Keeping the wind-tunnel running to cool the plate (approx. 15 secs.) and stop its operation.

The working point of the various systems participating in this experiment was determined in previous runs. The nominal test conditions were established to be:

(1) Wind tunnel air speed: 21 m/sec

(2) Electric current through the heating wire: 345 mA. Total resistance of the heating wire: 135 Ω

A total of 20 tests were performed. Of these, eleven tests were recorded. Since the results of all the runs were very much alike, only the last three were picked-up for data analysis. The reproducibility of the

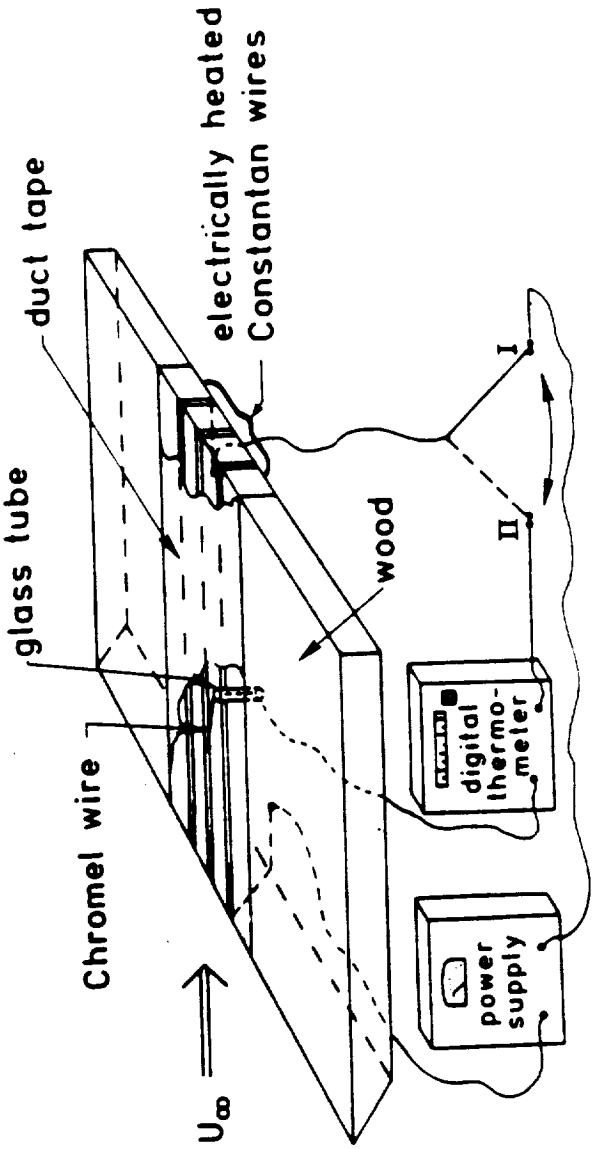

I ELECTRICAL HEATING CIRCUIT
II TEMPERATURE MEASUREMENT CIRCUIT

Fig. 5.2 Cutaway of the heated flat plate

stability principle. The accuracy of both devices was established to be within 0.5°.

The target flat plate was placed in the wind-tunnel at +0.5 degree angle of attack in order to be on the safe side regarding transition. The active heating of the target plate was achieved locally, at one third of the span, by wrapping chordwise a 0.00397" Constantan wire three times around the plate at 2 mm pitch, and connecting it to a power supply. To ensure uniform surface texture, roughness and heating, these wires and the entire surrounding area in the field of view of the camera were covered chordwise with three adjacent strips of 2" wide duct tape. At 85 mm. from the leading edge, a Chromel wire was soldered to the Constantan wire and its lead was taken straight to the back of the plate through a very small hole that was drilled in the wood. As shown in Fig. 5.2, this layout permitted the experimenter to carry-out emittance calibrations of the duct-tape surface by providing the true surface temperature. Hence, the Constantan wire played a dual role in this experiment, either as a heating element when connected to the power supply, or as a thermocouple element when connected to a digital thermometer. The desired function was selected by switching between the two circuits.

5.2 The Experiment Description

The guiding rule in performing these experiments was to make them as short as possible. There were two reasons for this; one, concerning the wind-tunnel operation, the other concerning the substrate participation in the heat transfer process. Since the wind-tunnel used in this experiment is of closed circuit type, the longer the operation period the higher is its air temperature. At room temperature, the initial rise of the air temperature in the wind-tunnel is about 1.2°C/min. This phenomenon has a negative influence

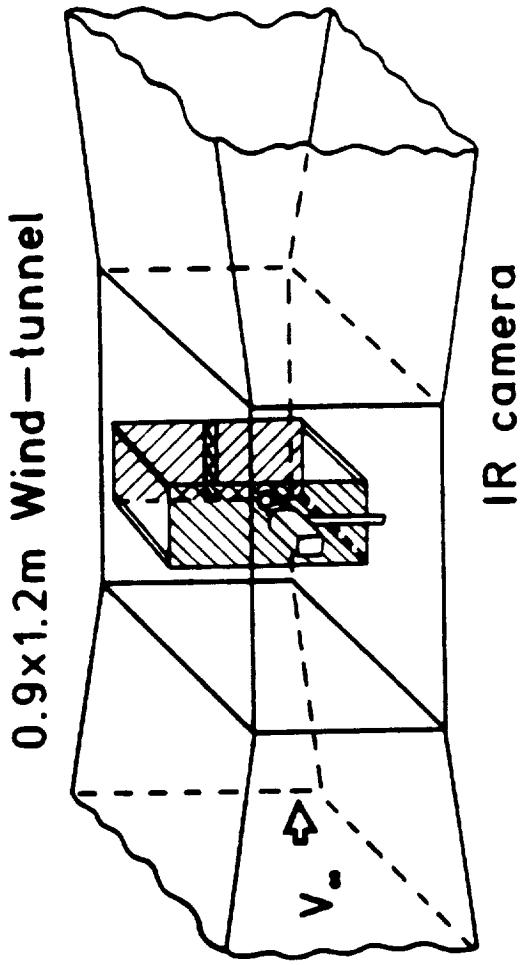

Fig. 5.1 Layout for IR surface measurements of a heated flat plate in a uniform freestream

Chapter 5

THE FLAT PLATE EXPERIMENT

Following the heated wire experiments that essentially involved only one mode of heat transfer namely convection, the attention turned to a more general type of experiment in which all three modes were involved. The choice was a laminar flat plate experiment which was designed to measure surface temperatures on an actively heated surface subjected to a uniform free-stream flow. The purpose was to produce an "aerodynamic" target whose temperature distribution as measured by the infrared imaging system could be assessed by analytic results from velocity and thermal boundary layer analysis.

5.1 The Experimental Set-Up

The target flat plate measured 32 cm. chordwise, 90 cm. spanwise, was made of wood, and had a sharp leading edge of the type assumed in the Blasius analysis of the boundary layer. The IR imaging camera was placed laterally at 55 cm. from the target, behind a second plate (parallel to the first one), with a circular hole through which the camera could view the target. This was done in order to prevent the vortices shedded from the camera from interfering with the flow over the target plate. The experiments were carried out in a 0.9x1.2 m (3'x4') low speed wind-tunnel, where the entire assembly was placed vertically as shown in Fig. 5.1. The zero angle of attack of the plates was determined by using a cylindrical two-hole differential pressure probe connected to a U-shape glass manometer. In order to eliminate errors associated with geometrical misalignments, the zero angle of attack was established from the mean of two readings, with the pressure probe at its normal position and then rotated 180° around its axis. Separately this measurement was done with a vane-type indicator working on the weathercock

in the wider context of better understanding the complexity of convective heat transfer processes.

velocity behavior U to be quite sensitive to the scatter of the temperature measurements. In spite of this fact the results of the experiments with the higher heating rates (and thus the best correlated data) prove that the concept of deducing velocity information is viable.

The encouraging aspect of this approach is that as the Reynolds number increases with the velocity, so does the heat transfer coefficient, on a power law basis (Morgan, 1975). The net result of this feature is to increase substantially the accuracy of the velocity predictions from the temperature measurements.

4.5 Summary

This set of experiments showed that using an infrared imaging system, one can detect local temperature variations, and hence Nusselt number variations, that may occur over a very limited portion of the camera's field of view. The concept proved to be applicable in the core region of the flow as well as in the entrained part of it. The capability of accurately tracking temperature variations was found to be in this case as high as 350 K/m. A question still to be answered is whether or not this limit is set by the actual value of the temperature gradient, or by the variation of the temperature in the field of view of the IR imaging camera. The inverse approach of using temperature measurements in conjunction with heat transfer correlations to deduce local velocities was shown to be possible in principle. This method shows promise for use in aerodynamic research: (1) provided the wire overheat is high enough to get good signal to noise ratio measurements, (2) the temperature gradient problem is solved by appropriate calibrations, and, (3) more accurate forced convective heat transfer correlation may be found. The last condition should be viewed not only in the perspective of this particular research, but

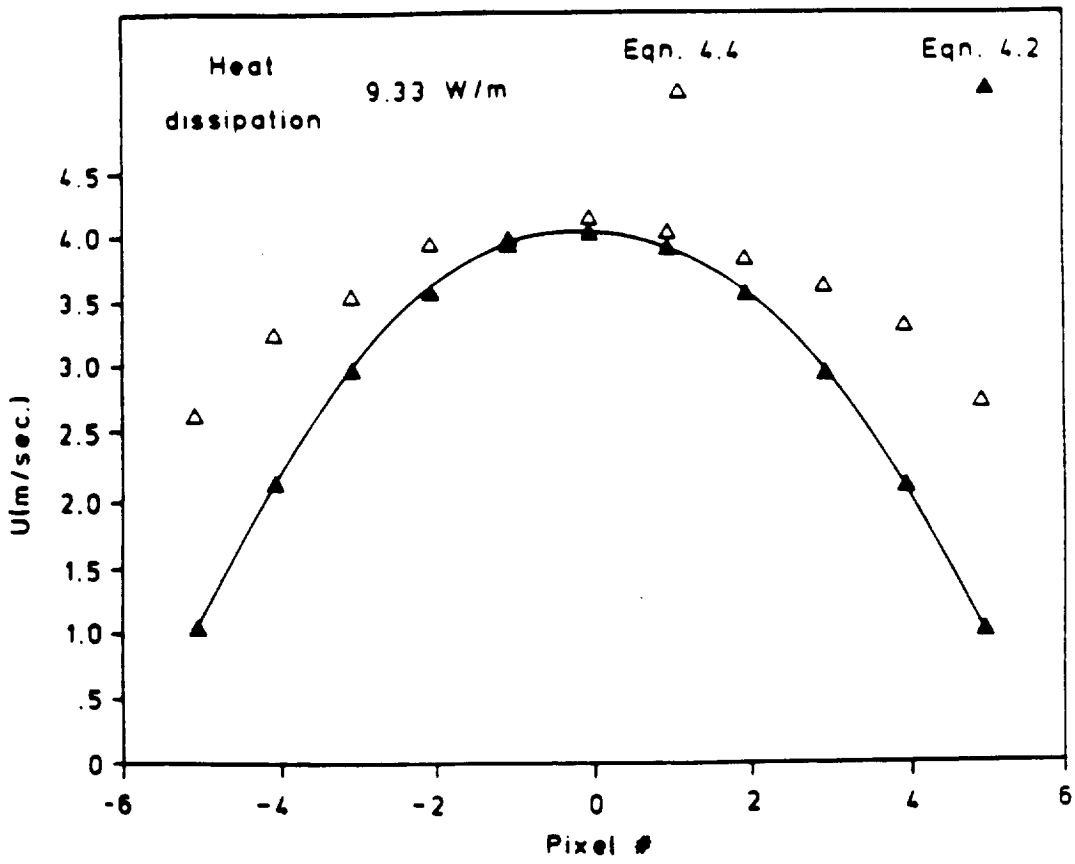

Fig. 4.12 Velocity profile as deduced from the heated-wire laminar-jet measurements (highest heating rate)

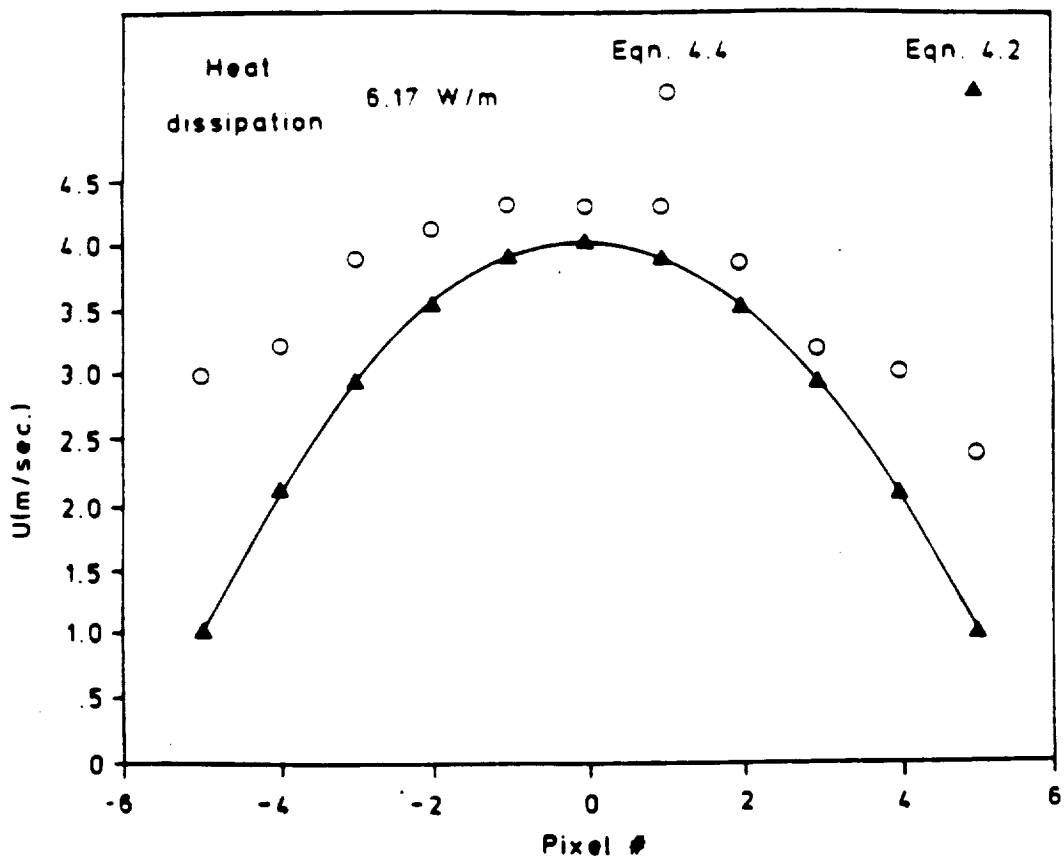

Fig. 4.11 Velocity profile as deduced from the heated—wire laminar—jet measurements (intermediate heating rate)

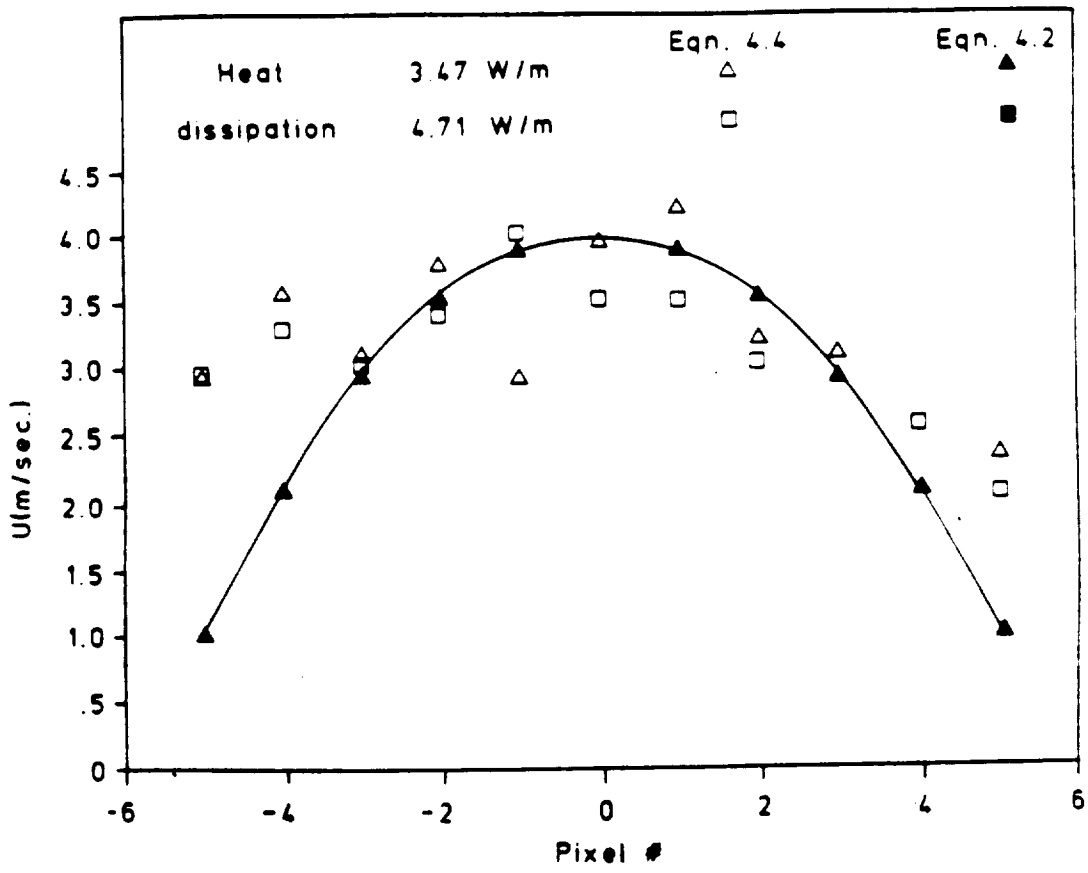

Fig. 4.10 Velocity profiles as deduced from the heated-wire laminar-jet measurements (lower heating rates)

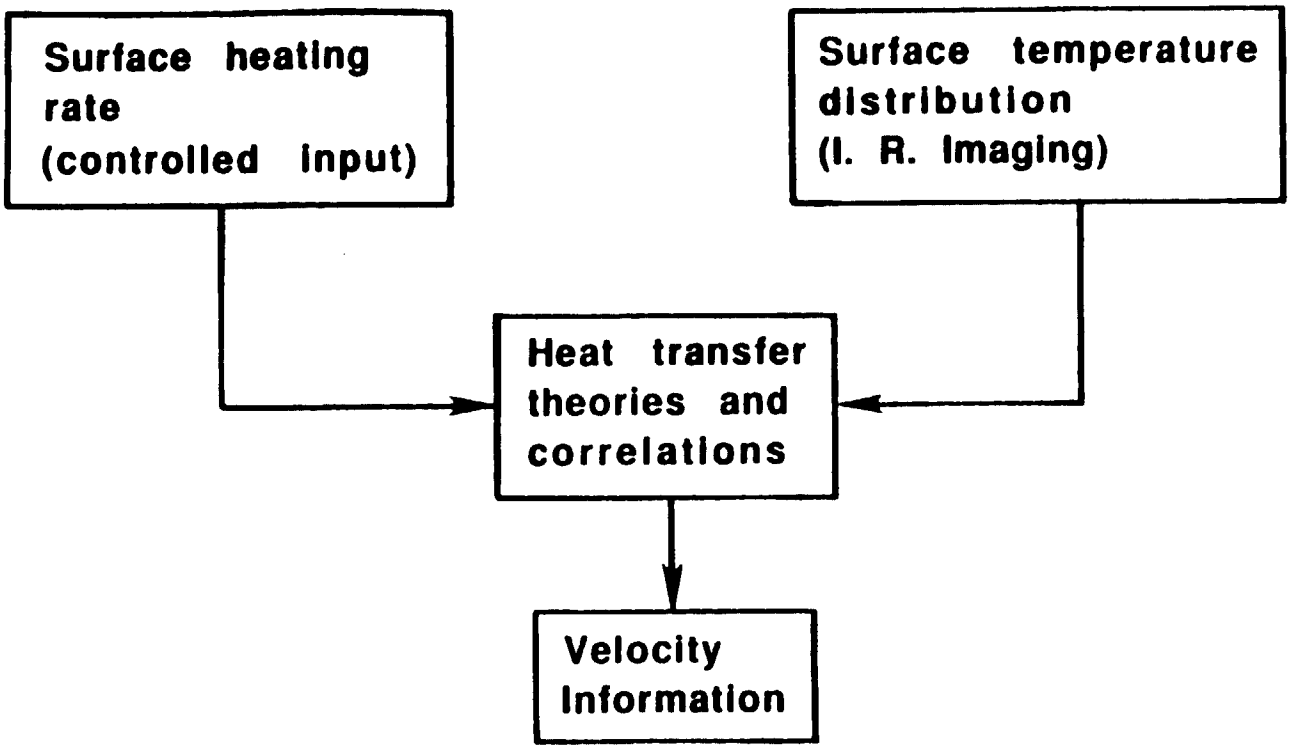

Fig. 4.9 The concept of flowfield velocity deduction through Infrared Imaging of the surface

decreases, the discrepancy between predictions based on Morgan's correlations and the data obtained increases. It may reach as much as 30% for Ra numbers as low as 300. In the present case, the Ra numbers were even lower, typically 10^{-3}.

The deduction of the velocity profile from the measured temperature profile through Nu-Re correlations is also possible. This time, the process is reversed and assuming the correct correlation is available, the known differential temperature is used to calculate the velocity that would produce it. This approach is schematically shown in Fig. 4.9 and quantitatively described in Appendix A2 item 5. The results for the first two experiments (lower heating rates) are presented in Fig. 4.10 while the results for the last two experiments (with the highest heating rate) are presented in Figs. 4.11 and 4.12. For the predicted velocity values, Eq. (4.3) was reformulated to express the local jet velocity U(r) in terms of the local temperature difference $\Delta T(r)$ between the heated wire and the air

$$U(r) = \frac{0.909\ \nu_a}{R}\left[\frac{\dot{q}}{\pi\ k_a\ \Delta T(r)}\right]^{2.604} \qquad (4.4)$$

Once again the reader is reminded that the two most peripheral points in each graph should be regarded more as a mathematical feature (arising from the assumed parabolic distribution) than an actual physical reality. A comparison between Figs. 4.10-4.12 only emphasizes how important is in this case to get well correlated temperature measurements before proceedings with the data processing (see Table 4.2). The explanation of the higher scatter of the deduced velocities (Fig. 4.10) than that of the temperature data from which they were deduced (Fig. 4.6) lies in the behavior of the Nu-Re correlations. These correlations assume a behavior like, $Nu \sim Re^n$ $0 < n < 1$. In the former case one gets $\Delta T \sim U^{-n}$ while in the latter $U \sim (\Delta T)^{-1/n}$, thus causing the deduced

Table 4.4 Mean temperature difference between the heated wire under free convection and the ambient air as a function of the wire heat dissipation.

$\dot{q}''_o$ (w/m wire)	ΔT predicted (K) Nu-Gr corr.*	$\Delta\bar{T}$ (K) Experimental
3.47	65	25.6
4.71	86	34.5
6.17	110	44.8
9.33	161	63.9

*See Appendix A2 item 3.

processes on the raw (detector) signal, that practically nothing is known about the transfer function operating on it. First, there is the IR imaging camera, then its accompanying analog processor and finally the computer digitizer and its software. (Several attempts to get some information about these transfer functions from the suppliers were not answered). Therefore, there is no choice left but to look at this system as a "black box" and to assess its performance by controlled experiments, even though this task is double complicated because of the uncertainty induced at the same time by both the measurement apparatus and the reference data. In any case, the trend in Fig. 4.8 shows that the accuracy of the deduced Nusselt numbers from temperature measurements performed with the infrared imaging system is adversely influenced by the existence of a temperature gradient at the location of interest. It also confirms that this system may be able to track accurately temperature variations up to about 350 K/m which is in good agreement with the findings of Stallings and Whetsel (1984). Furthermore, according to the evidence presented, at high temperature gradients the indicated temperature is always lower than the actual one. This suggests that it is possible to produce a calibration curve similar to Fig. 4.8 and use it to correct the experimental measurements prior to processing the data.

The uncertainty with respect to the accuracy of heat transfer correlations is further emphasized by the results measured on the uncooled portions of the wire. Although the free convection heat transfer was out of the scope of the present study, it was interesting to observe that on those segments, the predicted Nusselt number as regressed by Morgan, grossly underestimates the actual heat transfer process, as it is shown in Table 4.4.

The verity of the present findings are indirectly supported by Fand et al. (1977) where it is shown that as the Rayleigh number (Ra = Gr Pr)

heating rate is known and constant, the dissipation is effected solely by convection, and the actual wire temperatures are higher than the measured ones. Therefore, Nusselt numbers that are deduced based on this kind of information should be corrected to actual values by substrating the error inherently associated with this type of measurements.

One question that remains open on this issue is whether the infrared camera limitation to track high temperature gradients is a function of the absolute value of the gradient itself (K/m), or of the variation of the temperature in the instantaneous field of view (K/IFOV or K/rad). To answer this problem, it would be necessary to undertake another set of experiments, deviating from the objectives set-out for this research. However, the resemblance between Figs. 4.8 and 3.2 relating the minimum detectable temperature difference is remarkable. Indeed, the prediction made on the basis of the IR imaging camera operational characteristics about its inability to accurately resolve high temperature gradients turned out to be true.

The quantitative estimation of the performance of the infrared imaging system in this case is a very difficult task. The first difficulty refers to the reliability of the heat transfer data chosen to be the reference. As Morgan points out, "The percent coefficient of variation of the Nusselt number for a given Reynolds number for the experimental data varies from 10% to 29% depending on the Reynolds number, whereas that for the various correlations varies from 10% to 46%". Based on the present measurements, and referring only to those performed in near zero temperature gradient regions, it was found out that the experimental Nusselt number based on infrared imaging system measurements could further vary by as much as 3.3% from the predicted one by Eq. (4.1) to which Morgan's remark refers. The second difficulty refers to the fact that the experimental data set resulted from a series of

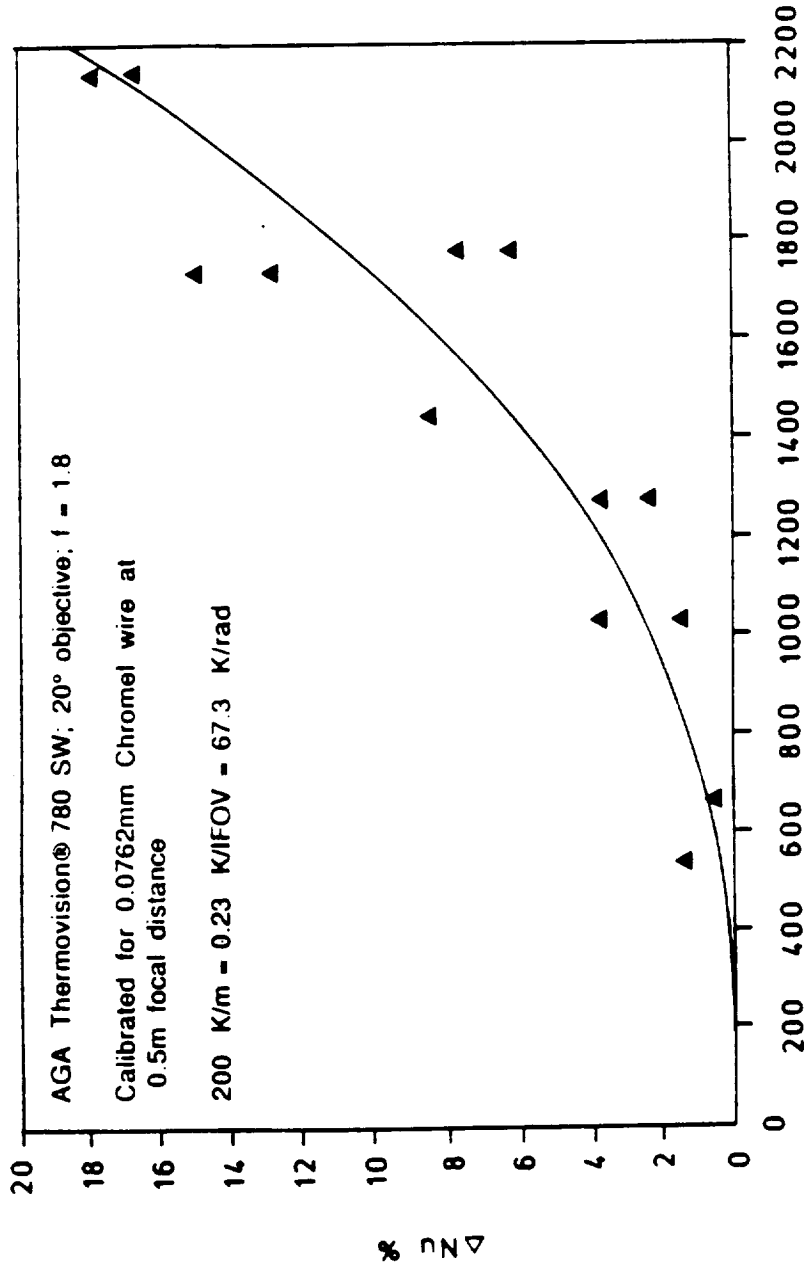

Fig. 4.8 Error in the experimental Nusselt number due to the IR camera limitation in tracking the high gradient temperature distribution, IFOV=0.0034 rad

In this case, it will be easier to evaluate the influence of the temperature field gradient on the measurement accuracy, because of the position dependence of the temperature gradient along the wire. For this, it was assumed that the actual wire temperature distributions could be approximated by a cosine-type function between X = 0 at the maximum wire temperature and X = $\ell/2$ at the minimum wire temperature (0 and π radians respectively). This approximation function was suggested by the experimental data shape. While doing this, it was assumed that the temperature measurements are essentially correct in regions with no sharp gradients (Stallings and Whetsel, 1982). The approximating functions are presented in Appendix A3. The final result is presented in Fig. 4.8, where the estimated error in the measured Nusselt number relative to the expected values from Eq. (4.1) are shown versus the temperature gradient along the wire at the location of measurement. The Nusselt number error shown in Fig. 4.8 was uniformly adjusted by the difference between the experimental and the correlation values found at the point with zero temperature gradient. This small discrepancy (see Fig. 4.7) was assumed to be a systematic error applying all along the set of data belonging to the same experiment. The data points for Fig. 4.8 were taken from the last two experiments (with the higher heating rates) were the signal to noise ratio was previously found to be high enough to produce well correlated data. Data points for the two most peripheral points in each experiment, to which reference was made previously, have been excluded. The line in Fig. 4.8 should not be interpreted as the regression curve on the data points. It is rather shown there with the purpose of indicating the trend of the findings. The conclusion of this analysis is that Nusselt numbers values deduced from the IR imaging system temperature measurements will always be higher than the actual ones. The explanation lays in the fact that the

Table 4.3 Nusselt number comparison for the laminar flow jet using the heated wire technique for experiment #4 (highest overheat).

Pixel #	Re* [Actual]	Nu(correlation) [= 0.795 $Re^{0.384}$]	Nu [Actual]	$\frac{Nu(act)-Nu\ (cor)}{Nu(cor)}$ [%]
0	17.018	2.361	2.384	0.9
+1	16.508	2.333	2.357	1.0
-1	16.508	2.333	2.337	0.2
+2	14.976	2.248	2.312	2.9
-2	14.976	2.248	2.337	4.0
+3	12.423	2.092	2.268	8.0
-3	12.423	2.092	2.244	7.3
+4	8.892	1.840	2.180	18.4
-4	8.892	1.840	2.163	17.6
+5	4.297	1.397	2.029	45.2
-5	4.297	1.397	2.009	43.8

*Decreasing Reynolds number coincides with increasing temperature gradient due to the velocity distribution of the flowfield. (See Figure 4.7 and Appendix A3)

influence on the results. The radiation effect was found to be negligible. Because of the moderate wire overheat values, the emittance was assumed constant and, according to Kirchhoff rule, the absorbtance could be taken to be the same as the emittance (Eckert and Drake, 1972, p. 612). Thus, even for an overheat of, say, 80K above the room ambient the radiation effect turned out to be three orders of magnitudes lower than the generated heat. In order to estimate the possible heat conduction contribution, the measured temperature profile of the experiment with the highest overheat was approximated by a polynomial function that indicated a maximum temperature gradient of 2524K/m. With a mean wire thermal conductivity of 50 w/mK, the conductive loss for a wire element between two adjacent sampling points is still two order of magnitudes lower than the generated heat and the influence of this mechanism can be discarded too.

Table 4.3 presents in a tabular form the departure of the Nusselt number as deduced from the temperature and heating rate data of experiment #4 from the Nusselt number as predicted by Eq. (4.1), and assuming the parabolic velocity distribution inside the jet. The positive departure values exhibited by the results raises the suspicion that the infrared imaging system may have difficulty in accurately mapping high gradient temperature fields. Stallings and Whetsel (1982) came to a similar conclusion using a similar camera (Thermovision® 680) to map the temperature variation along a bar with an almost constant temperature gradient. Their data show that while the system could track temperature gradients of 109K/m (5R/in) with a ±1% error, at 262K/m (12R/in) this error increased to -1.5%, but they did not pursue this issue to determine the dependency of the error on the temperature gradient of the measured field, as may be done in the present circumstances.

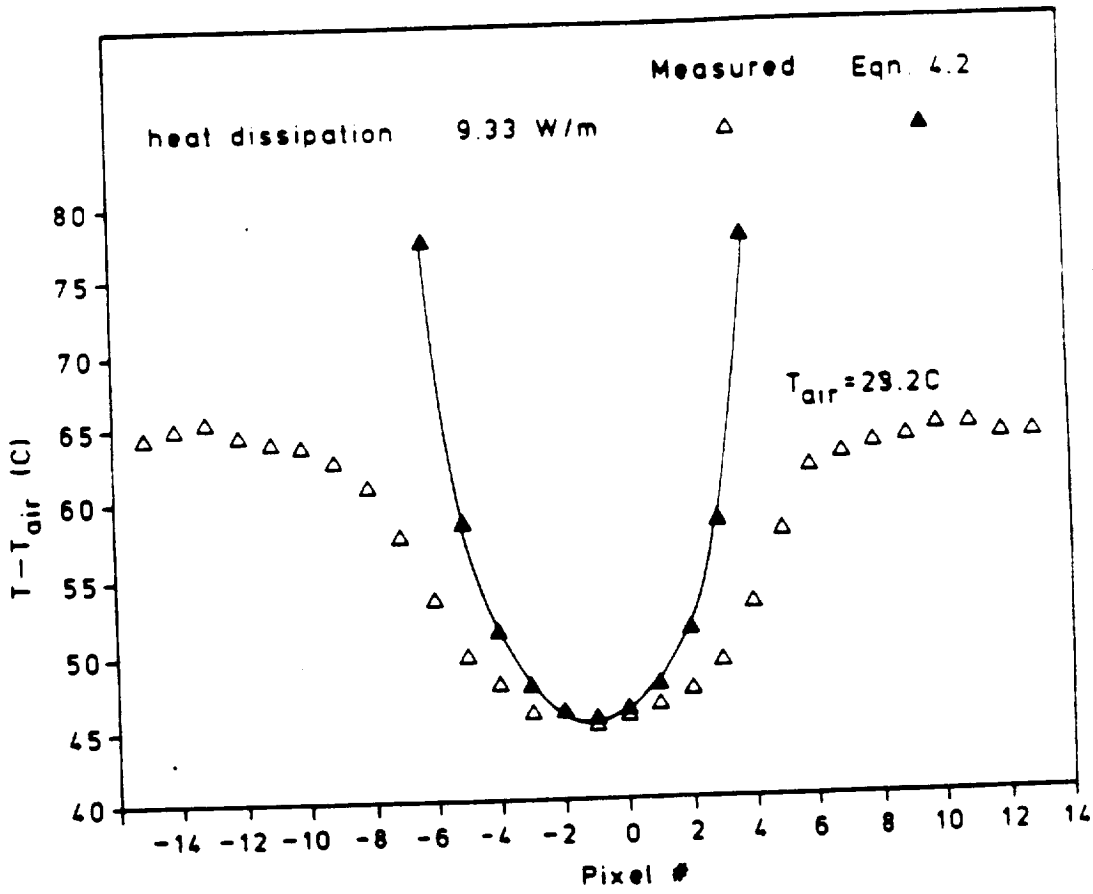

Fig. 4.7 Heated wire temperature difference distribution when exposed to a laminar jet. 1 pixel=1.154 mm. (highest heating rate)

Table 4.2 The coefficient of determination r^2 for the temperature measurements made with the infrared imaging system using the heated wire technique at various levels of heating rates, exposed to a circular jet.

Experiment #	Heating rate [w/m wire]	r^{2*} [%]
1	3.47	41.0
2	4.71	53.1
3	6.17	80.1
4	9.33	98.2

*Adjusted for degree of freedom.

where U(r) is the local air velocity inside the jet, U_{max} is the maximum air velocity at the center of the pipe, r is the radial coordinate and R is the internal radius of the pipe. In this case, U_{max} = 4 m/sec. The final result that correlates the temperature difference between the heated wire $\Delta T(r)$ and the airflow (see Appendix A, Eq. A7) is given by

$$\Delta T(r) = \frac{\dot{q}}{0.795\pi\, k_a} \left\{ \frac{\nu_a}{2U_{max}\left[1 - \left(\frac{r}{R}\right)^2\right]R} \right\}^{0.384} \qquad (4.3)$$

where $\dot{q}$ is the electrical heat generation per unit length of wire, k_a is the heat conductivity of the air and ν_a is the kinematic viscosity coefficient of the air. The Reynolds number at the computed points varied roughly between 4 to 20. Figure 4.6 indicates that increasing the wire overheat value improves the signal to noise ratio and the resulting acquired data is better correlated. The quantitative evidence is presented in Table 4.2 where r^2 is the (statistical) coefficient of determination (see Appendix A, Eq. A.4). On the negative side, high overheating may cause changes in surface emittance, excessive wire elongation (with resulting vibrations) and thermal contamination of the flow. Thus, the overheat value should not be set to exaggerated values. A second observation relates to the fact that the measured temperature values systematically depart from the expected values according to Eq. (4.3.). These trends become more evident in the data from the experiment with the highest heating level presented in Fig. 4.7, where the wire temperature difference is graphed in order to make the results more meaningful for heat transfer evaluations.

Since the correlation given by Eq. (4.1) accounts only for the forced convective heat transfer, the magnitudes of the other two heat transfer modes, namely conduction and radiation, were estimated in order to assess their

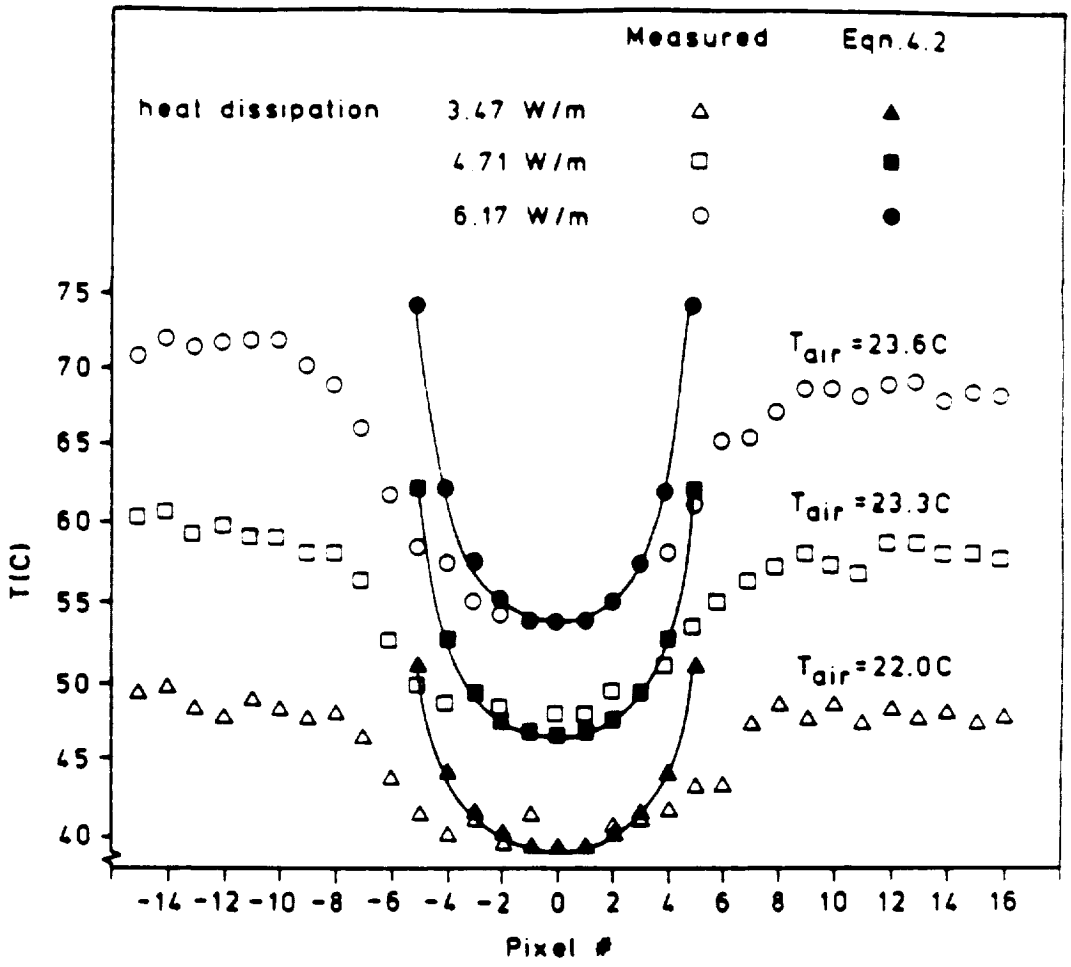

Fig. 4.6 Heated wire temperature distribution when exposed to a laminar jet. (lower heating rates) 1 pixel=1.154mm

cooled section of the wire length indicating the jet width will be the same too, under the assumption of negligible radiation and conduction. Hence, the "wavelength" of the wire exhibiting a varying temperature distribution will be the same in all four experiments. The validity of this assumption is examined next.

4.4 Results and Discussion

The raw data of the initial experiments at the three lower heating rates are presented in Fig. 4.6. The darkened symbols are given for comparison and represent the expected temperature distribution along the section of the wire directly exposed to the laminar flow. The respective temperatures were predicted from the relation,

$$Nu = 0.795\ Re^{0.384},\quad 1 < Re < 35 \tag{4.1}$$

which is a cross-flow correlation deduced by Morgan (1975) through statistical analysis of some 200 independent experimental and theoretical studies. Although Eq. (4.1) refers to two-dimensional flows, and the circular jet is a three-dimensional flow, it is still possible to use this equation in the present application because the wire diameter is almost three orders of magnitude thinner than the jet. Thus, it is assumed that the wire is on the plane of symmetry of the jet, where the flow, locally can be assumed two-dimensional. The air velocities to be used in Eq. (4.1) were calculated assuming parabolic velocity distribution as predicted by the viscous-flow theory

$$U(r) = U_{max}\left[1 - \left(\frac{r}{R}\right)^2\right] \tag{4.2}$$

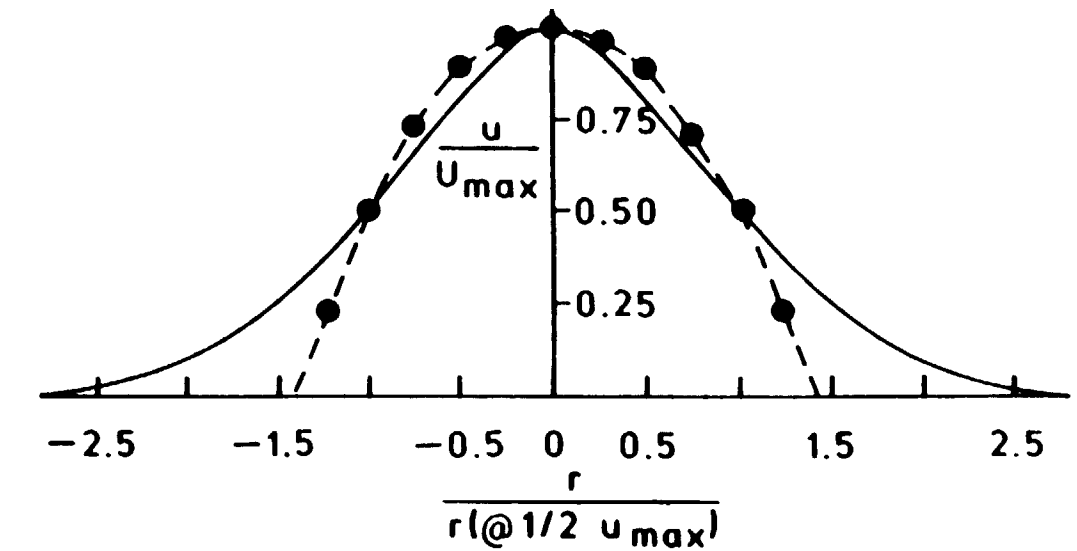

Fig. 4.5 Comparison of the normalized velocity distribution in a circular turbulent jet with a fully developed laminar flow in a pipe (parabolic distribution).

the periphery, the jet will experience an enlargement due to the mixing effect. The magnitude of this singular enlargement cannot be predicted in a straightforward way from the theory. Due to mathematical boundary conditions required for solution, it may be assumed that the jet issues from a round slit in an infinite wall. One of the techniques to match the theory with the reality is to assume the nozzle moved back with the wall a "virtual" distance that is calculated through a suitable matching criterion. For example, it can be done by matching the volumetric rate of flow between the actual jet and the assumed one (Blevin, 1984, p. 232). This analysis indicates that the actual flowfield behavior around the wire lies somewhere between the parabolic and the circular jet velocity profiles. The two normalized velocity profiles, parabolic versus circular jet, are shown for comparison in Fig. 4.5, where the positions of the indicated points on the theoretical parabolic distribution coincide with the actual temperature measurement locations as shown in Figs. 4.6 and 4.7 with an error smaller than 2.7% (These figures will be discussed in detail in the next section). This comparison suggests that the uncertainty with regard to the actual flow velocity may be too large at the two (symmetrical) most peripheral points and the data there should be treated cautiously. Another point emerging from Fig. 4.5 is that the effective radius of the circular jet flow is about 1.8 times the radius of the pipe. This fact is directly supported by the experimental evidence presented in the next section in Figs. 4.6 and 4.7, where the cooled section of the wire is larger than the internal radius of the pipe. Assuming that the extent of the cooled section is an indication of the extent of the actual flowfield, it can be inferred that the capability of the infrared imaging system to map the core as well as the entrained flow regions is demonstrated. Indeed, if one assumes the flow velocities to be approximately the same in all four experiments, the

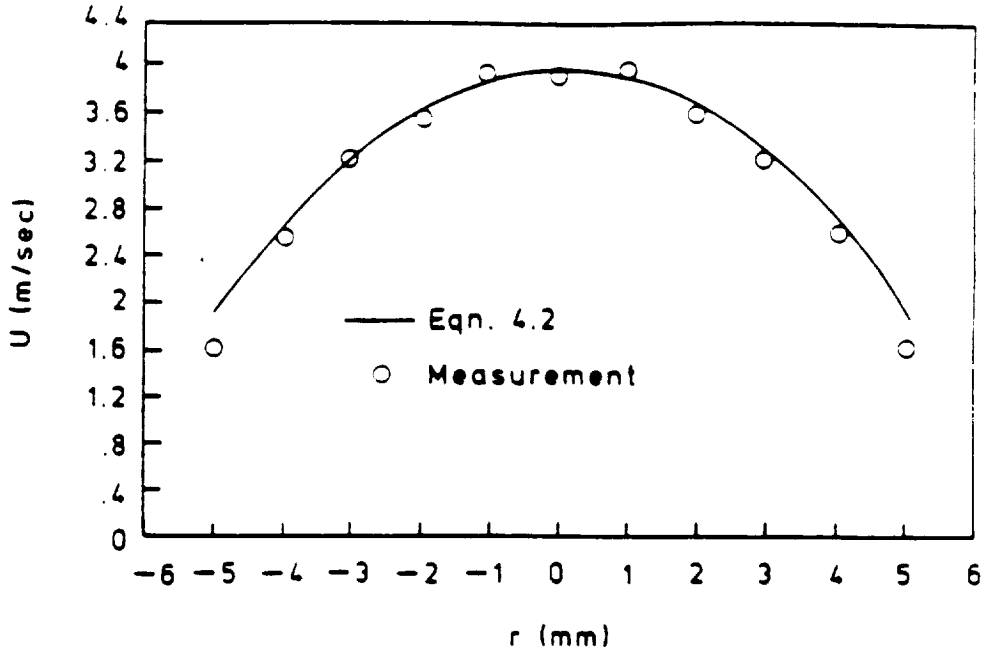

Fig. 4.4 Laminar flow jet experiment: Parabolic velocity distribution vs. Pitot-tube measurements

assumed the same, due to the viscous interaction between the flow and the still surrounding air. This interaction causes the well-known entrainment effect which affects the flow velocity profile especially at its periphery. Since the air velocities near the pipe wall fall to extremely low values that are difficult to measure, an attempt is made to estimate the velocity profile perpendicular to the wire. According to Blevins (1984, p. 231) a circular jet is fully laminar for Reynolds numbers up to 1000 and fully turbulent for Reynolds numbers above 3000. This Reynolds number is based on the diameter of the nozzle from which the jet issues. Regardless of the jet type of flow, whether laminar or turbulent, both of them exhibit the same type of behavior with regard to the main parameters of interest: the jet width increases linearly with the axial distance (X) while the centerline velocity decreases with inverse proportionality to the axial distance (1/X), see Schlichting (1968), p. 686. To this, it must be added that in both cases the flow pattern fully establishes itself only after a certain distance downstream from the pipe exit. In this case of intermediate Reynolds number of 1700, the distinction between laminar and turbulent jets is more of a semantic matter. The difference is whether one assumes the transition to be an "entrainment" phenomenon (laminar) or a "mixing" one (turbulent). Therefore, and for these experiments only, further reference will be made simply to "the circular jet". It is assumed that the coreflow is very much like the one in the pipe, the fractional change in the centerline velocity at the wire being of the order of magnitude of 10^{-3} relative to the nominal velocity in the pipe. This assumption was supported by measurements of the coreflow at the mouth of the pipe performed with a static Pitot-tube connected to a U-shaped glass manometer inclined 85.3° from the vertical. The measured core velocity distribution versus the parabolic velocity profile is shown in Fig. 4.4. At

correction for its discharge coefficient. The throat diameter of tne nozzle was 0.8 mm (0.0315"), and the nominal absolute air pressure upstream the nozzle was 304510 N/m^2 (31 psig). This pressure was adjusted to account for the nozzle discharge coefficient and variations in the air temperature, to get a nominal centerline velocity of 4 m/sec, determined from Pitot-tube measurements (see Sec. 4.3).

4.2 The Experiment Description

The experiments were carried-out at four different levels of heating corresponding to dissipation rates of 3.47, 4.71, 6.17 and 9.33 watts/m of Chromel wire. The area of interest i.e., that part of the wire that was directly cooled by the air jet, was about one tenth the field of view of the IR imaging camera. This design was made purposely to evaluate the system's capability to resolve localized temperature changes in the field of view.

For each separate experiment, nine consecutive frames were taken at a rate of 0.7 Hz and their average was stored as a single frame on tne computer's diskette for later analysis. During each experiment, the range and level of the camera were carefully set according to the target luminosity in order to minimize the background noise, and at the same time to prevent the detector from being under or overexposed (saturated) to the target photons. In either case, the output ceases to be proportional to the fourth power of the target temperature.

4.3 The Flowfield

As previously explained, the wire was placed at the mouth of a pipe designed to produce a laminar flow, implying a parabolic velocity profile inside the pipe. However, the behavior at the exit of the pipe can hardly be

The Chromel wire length was 40 cm and the Constantan wire length was 10 cm. The thermocouple assembly was hung between two vertical bars 50 cm apart. The length to diameter ratio of the Chromel wire was 5250:1, so that the influence of the heat conduction (on the central area of interest) to the supports can be neglected. The wire was heated by a D.C. electric current passing through it. A cardboard screen was placed behind the wire to provide a uniform background for the IR imaging camera (see Sec. 2.1). As shown in Fig. 4.2, the pipe exit was placed at 2 mm distance from the heated wire, at the center of the Chromel section. The air-supply pipe had a 13.3 mm (0.545") internal diameter, a 15.9 mm (0.625") outer diameter and a straight section of 80 cm, thus getting a length to diameter ratio of 60. The nominal mean air velocity in the pipe was about 2 m/sec, and the corresponding Reynolds number based on the pipe diameter was about 1700, which is well under the critical Reynolds number of 2300. The length of the straight section was considered enough to provide fully developed laminar flow inside the pipe, just before its mouth. According to an approximate analysis by Schiller (Schlichting, 1968, p. 231) a length to diameter ratio of 49 could be considered satisfactory for the actual Reynolds number. According to another analysis by Langahaar (Kays and Crawford, 1980, p. 67), this design is acceptable within a margin of 5% off the ultimate coefficient of friction for fully developed flow. Three fine-mesh screens, (each rotated at 45° with respect to the others) were placed at the entry of the straight section of the tube in order to break down any large vortices or non-uniformities that might exist in the flow. The air was supplied by a standard 100 psi low-pressure system (of the type that is commonly in use in laboratories and workshops). The air mass-flow rate was adjusted using a pressure regulator and by taking total pressure and temperature measurements upstream from a sonic nozzle with the suitable

Table 4.1 Calibration of the Apparent Wire Emittance with the Disco II® Computer Program

T_{wire} (°C) actual	Emittance Disco II®	Transmittance Disco II®	T_{wire} (°C) Disco II®	Emittance apparent
75.4	0.05	1.00	56.1	0.050
75.4	0.04	1.00	61.4	0.040
75.4	0.03	1.00	69.4	0.030
75.4	0.03	0.90	72.3	0.0270
75.4	0.03	0.85	74.0	0.0255
75.4	0.03	0.83	74.8	0.0249
75.4	0.03	0.82	75.2	0.0246
75.4	0.03	0.81	75.5	0.0243

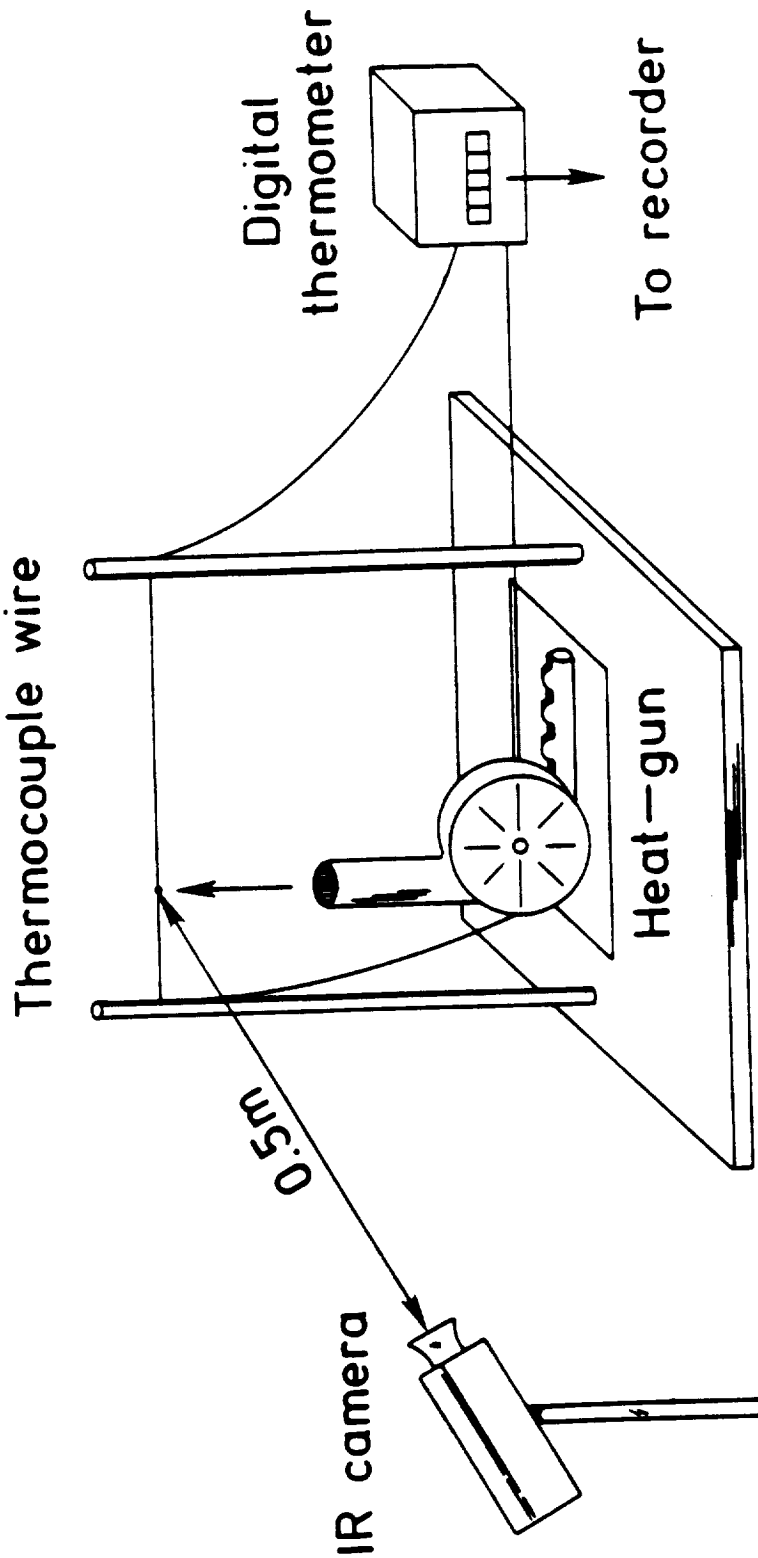

Fig. 4.3 Set—up for wire emittance calibration.

Calibrations for surface emittance properties are usually quite tedious processes. As shown in Fig. 4.3, the calibrations were performed by aiming a working heat-gun at the wire segment including the thermocouple junction, thus getting a direct reading of the wire temperature. Previously, the heat gun position was carefully adjusted in order to get locally a uniform (flat) temperature distribution of the wire in the region adjacent to the thermocouple junction, within ±0.2°C. The hot air temperature distribution in that region was double checked for uniformity, independently, with another thermocouple, and the mean hot air temperature was measured with a mercury thermometer. The accuracy of each of these devices was ±0.2°C. In parallel, the wire was thermographed by the AGA system and the temperature of the Chromel wire adjacent to the thermocouple junction was analysed with the Disco II® software on the dedicated microcomputer. The emittance input of the wire was adjusted until the temperature result from the computation equaled that of the thermocouple readout. Since the Disco II® computer program that was used to analyze the thermographies could read only emittance values down to two decimal digits, recourse was made to the atmospheric transmittance factor to finally adjust the emittance value. This result was checked with another software package supplied by AGA and run on an HP-41 CV programmable calculator with identical results. Thus, for the 0.0762 mm (0.003") diameter Chromel wire at 0.5 m distance from the IR imaging camera and moderately overheated (say around 350K), this apparent emittance has a value of 0.0244, as indicated by the HP 41 CV calculator run program. With the Disco II® software, the emittance value was set at 0.03 and the transmittance at 0.82, to get an equivalent apparent emittance value of 0.0246. The sequence of steps for one such wire calibration is given in Table 4.1.

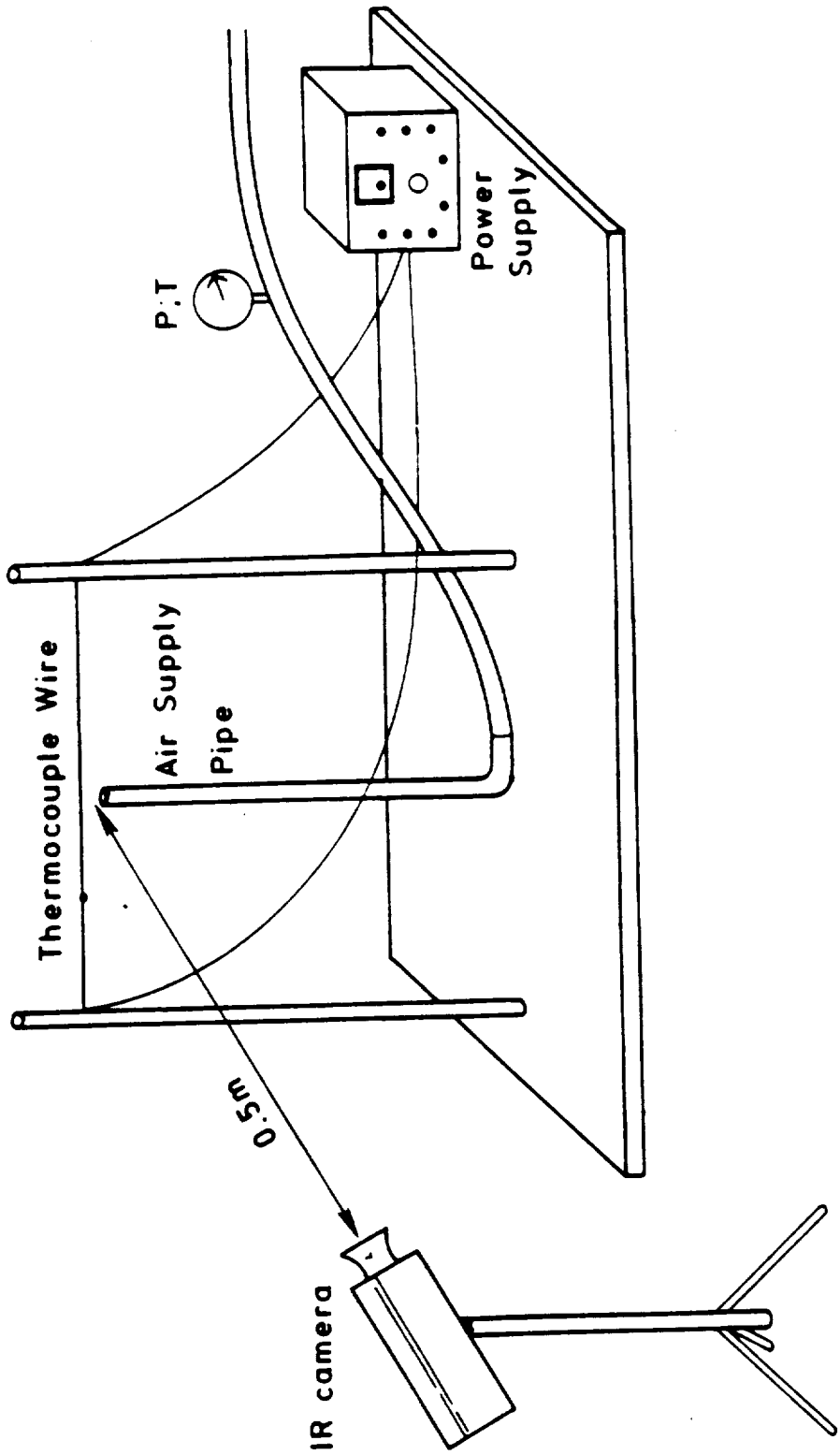

Fig. 4.2 Set—up for the heated wire laminar jet experiment

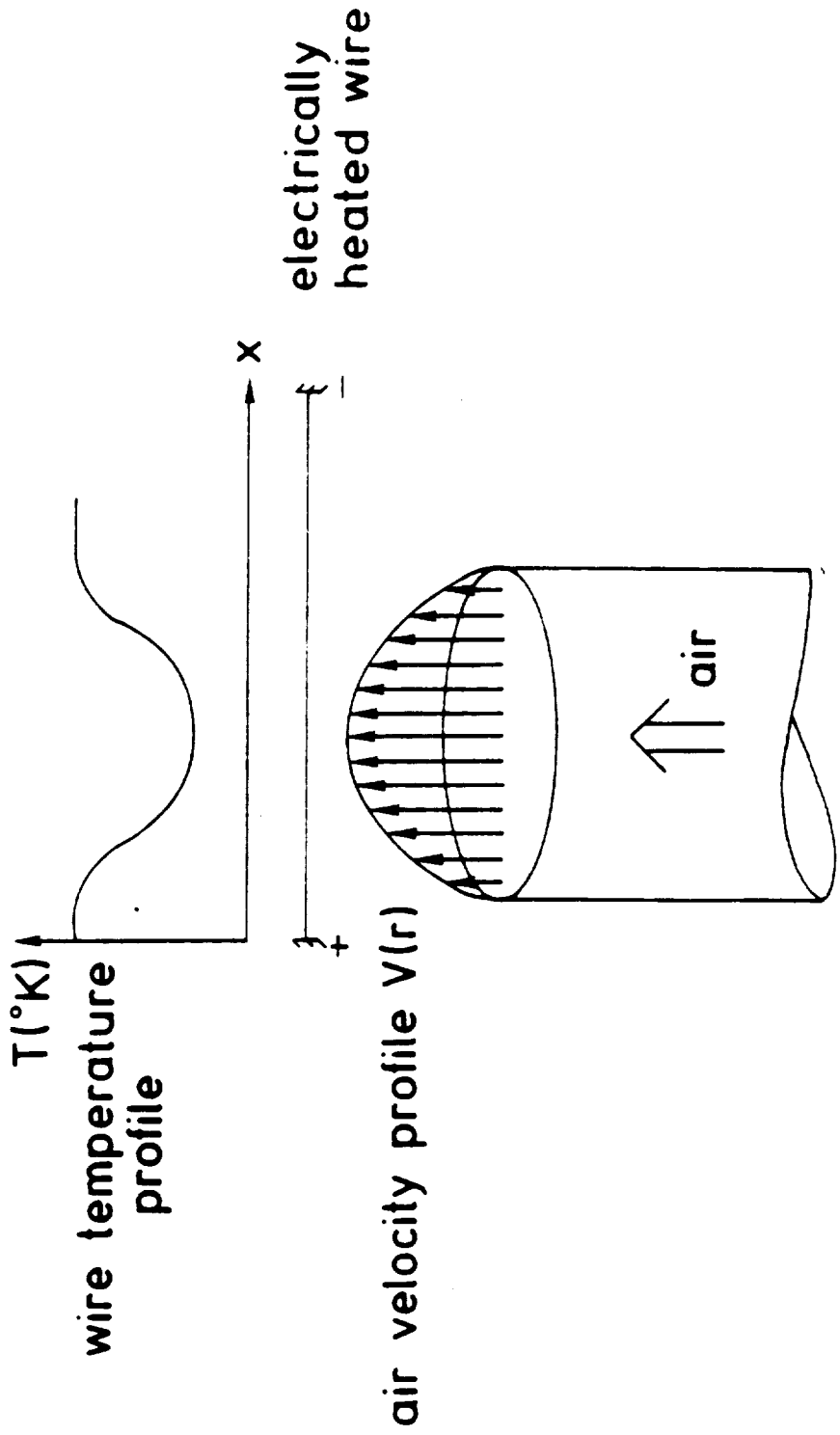

Fig. 4.1 Enlarged schematics of the heated wire laminar flow air jet experiment

Chapter 4

THE LAMINAR FLOW JET EXPERIMENT

Following the promising preliminary evaluation, the next step was to assess the capability of the IR imaging method to produce relevant quantitative results. For this purpose the research was focused on the mapping of a laminar flow air jet using the heated wire concept, which is shown in Fig. 4.1. The ordered behavior of this flow offered the convenience of comparing well understood experimental and theoretical results. The measured temperatures were used in conjunction with heat transfer correlations in order to deduce the air velocity distribution within the jet. In particular, this flowfield offered the opportunity to test the capability of the system to map high gradient temperature distributions.

4.1 The Experimental Set-up

In this experiment, the infrared imaging camera scanned the temperature distribution along a thin, electrically heated Chromel wire, a small part of which was placed diametrically at the exit of a pipe from which a laminar flow air jet discharged into the atmosphere. The camera was placed at a distance of 0.5 m from the wire. At this distance, it has a spatial resolution of 0.0034 radians and its field of view was 15x15 cm. As shown in Fig. 4.2, the Chromel wire, 0.0762 mm in diameter (0.003"), was part of a Chromel-Constantan thermocouple assembly that offered the opportunity to perform in-situ calibration for the surface emittance value. The knowledge of this value is critical when the objective is to determine surface temperatures and air velocities from infrared thermographies.

3.6 Summary

Use of infrared imaging systems requires the understanding of their principles of operations, as well as the characteristics of the specific system which is placed in service. These systems do not measure the temperature of the object being scanned. Rather they have a voltage output which is proportional to the photons number coming from the target and hitting the detector. This input may be attenuated by a multitude of factors, among them the surface emittance and the atmospheric attenuation. Therefore, in extracting quantitative data from system readings, it is the responsability of the experimenter to account for all the possible influences that may have influenced the result. Also, it was shown that the IR imaging systems may experience difficulties in mapping high temperature gradient fields.

so does its angle and the signal modulation, until the detector response reaches a plateau characteristic to resolved targets, as shown in Fig. 3.3c.

With the above background information, the behavior of the curve for the minimum resolvable temperature difference, shown in Fig. 3.2 may be understood. As the slits frequency increases, the modulation of each individual slit decreases, and one needs a higher temperature difference between the two plates in order to get a minimum modulation of the signal, enough to be detected by the detector.

From the practical point of view, this behavior suggests that the IR imaging camera may have difficulty in tracking high gradient temperature fields. Visually, this may be explained in the following way: Let's approximate the temperature distribution of a target by a series of constant temperature strips. As the temperature gradient increases, the width of these strips decreases and therefore their individual modulation decreases. Thus, as the IR imaging camera scans such an object, the error of the measurement will increase. In fact, the graph showing the dependency of the error in the measurement of a high gradient temperature field will look very much like that in Fig. 3.2, with the abscissa representing the gradient of temperature and the ordinate representing the mesurement error.

Before concluding this chapter, it is well to remember that the infrared radiation includes diffraction behavior, which is typical to electromagnetic phenomena. This means that the signal modulation will not be full even if the target is just resolved, since energy from the surroundings will still reach the detector. As a rule of thumb, the target area to be scanned for full modulation should be at least three times that of the instantaneous field of view (IFOV).

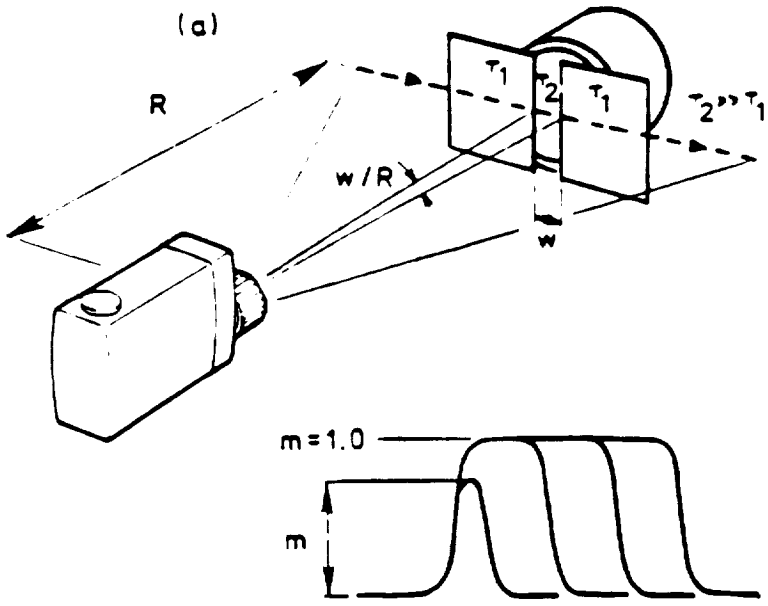

(b) LINE SCAN VIDEO SIGNAL

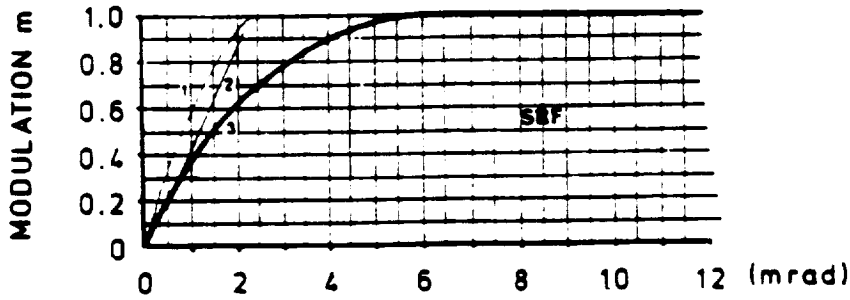

(c) SLIT ANGLE w/R

1) Ideal SRF for circular detector
2) Ideal SRF for square detector
3) Typical measured SRF

Fig. 3.3 The slit response function test set-up and results (after Ohman)

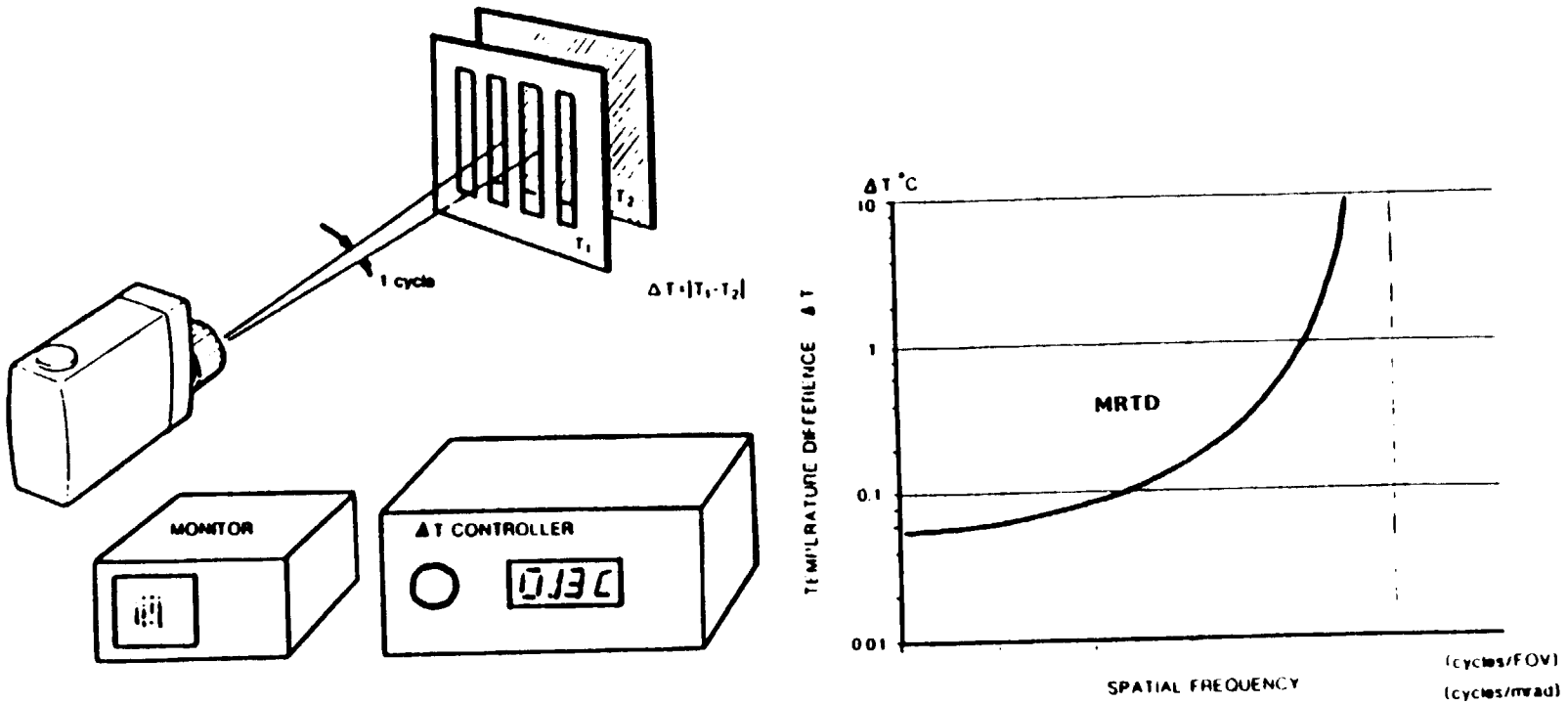

Fig. 3.2 The minimum resolvable temperature difference test set—up and result (after Ohman)

3.5 The Resolution Problem

The essence of a successful design for an infrared imaging system lies in the answer to the resolution problem. This problem has two aspects: the minimum resolvable temperature difference and the slit response function.

The minimum resolvable temperature difference (MRTD) is the result of a standardized test designed to evaluate the camera performance in this respect. The test target is a plate with four slits of varible widtn which is placed in front of another uniform plate. The temperature of both plates is independently adjustable. By varying the width of the slits and recording the respective temperature difference between the plates, where the pattern becomes indistinquishable to the camera, one obtains a graph as shown in Fig. 3.2. The lowest point of the curve is the temperature difference at zero slit spatial frequency and represents the system sensitivity. The test is usually run at 30°C, and for the present system, this sensitivity is about 0.2°C. A second parameter is the highest possible resolution, which can be represented by a vertical line that is asymptote to the rising curve. To understand this behavior, one must understand the slit response function (SRF) of the camera. As it can be seen in Fig. 3.3a, the test target in this case consists of a temperature adjustable plate covered by another plate with a slit of a variable width. As the slit width is increased, so is its angle as viewed from the detector. This angle can be less, equal or greater than the field of view of the detector which is called the instantaneous field of view (IFOV). Slits that are smaller than the IFOV are called unresolved. When the camera scans an object that is unresolved, the radiation falling on the detector comes partially from the target and partially from the surroundings. As a result, as shown in Fig. 3.3b, the signal modulation from an unresolved slit is smaller than one coming from a resolved slit. As the slit width increases,

where $e_{b\lambda}$ is the spectral emissive power of the black body radiation, h is Planck's constant, k is Boltzmann's constant, c_o is the speed of light in vacuum, n is the refraction index of the medium, λ is the respective wavelength and T is the absolute temperature. When Planck's formula is divided by the energy of a single photon $h\, c_o/\lambda = h\nu$ we obtain the spectral photon emittance for a blackbody $N_{\lambda b}$

$$N_{\lambda b} = \frac{2\pi c_o}{n^2\, \lambda^4 [\exp(hc_o/n\lambda kT)-1]} \qquad (3.2)$$

From here, one gets directly the formula commonly used to express the calibration curve behavior,

$$I = \frac{A}{C\, \exp(B/T-1)} \qquad (3.3)$$

where I is the "thermal value" corresponding to temperature T and A, B, and C are constants (AGA, 1984). The thermal value I is measured in isothermal units (IU) which is a practical unit of measurement. The relationship between the thermal value and the received photon flux is linear. However, the relationship between the thermal value and the object temperature is obviously non-linear.

Finally, it should be mentioned that the radiation coming from a certain spot to the detector has three components: object radiation, reflected radiation and atmospheric participation. The camera has no way to distinquish between the three, and its output is an "integrated" one. It is indeed the duty of the operator to account for the various contributions causing the final output signal. As a corollary, it can be said that the measurement of temperatures using infrared imaging techniques is not a method that can be applied without expert attention to detail.

the IR radiation all along its spectrum, the matching of the detector has also to fit the "atmospheric windows". This is the term used to denote the wavelength of IR radiation for which the atmosphere is transparent. In the present case, the sensor is made of Indium Antimonide (InSb), which is classified as a semiconductor element with a spectral response in the 1.7 to 5.8 μ range. However, the spectral response of the camera (as a system) is purposely reduced to the 3.5 to 5.6 μ by special coatings on the objective lens. Its operational temperature detection range is between -20°C to 850°C. The field of view (FOV) of the objective lens of the camera is 20°. The area projected at any one time on the detector is subtended by an angle of 0.0035 radians, which is also called the instantaneous field of view (IFOV). With a scanning rate of 25 fields per seconds, each field having 100 lines and 130 columns, the scanning rate is 325,000 IFOV/sec, or 3 μ sec per IFOV. With a time constant of approximately 0.2 μ sec (Levinstein 1977), the InSb detector matches the camera needs. Since the camera design probably started from the detector characteristics, it is clear that they are the bottleneck for the upper limit of the scanning rate.

The InSb is a linear photon counting photovoltaic detector. These detectors are sensitive to the number of photons hitting them (rather than their energy), once their energy exceeds the energy threshold of the semiconductor material. In general, the effect of cooling the detector is to decrease this cut-off wavelength. The calibration curves of the IR imaging camera can be derived directly from the Planck's formula (Sparrow and Cess 1978, p.6)

$$e_{b\lambda}(T) = \frac{2\pi hc_o^2}{n^2 \lambda^5 [\exp(hc_o/n\lambda kT)-1]} \qquad (3.1)$$

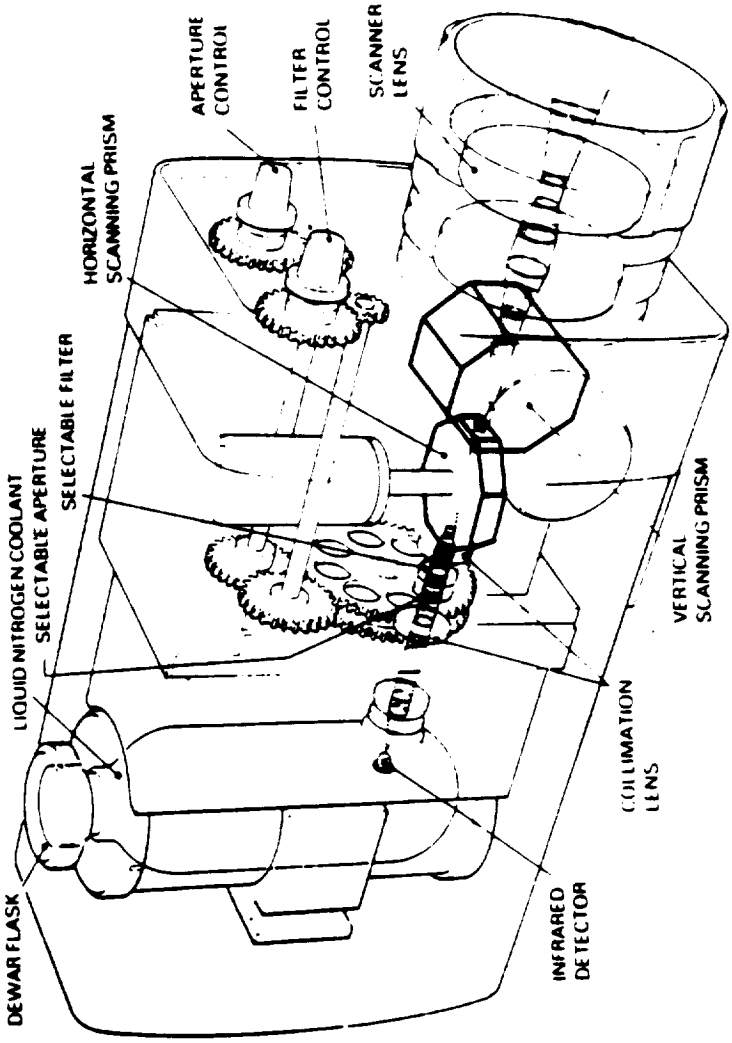

Fig. 3.1 Infrared imaging camera cutaway
AGA Thermovision® 782

As can be seen in Fig. 3.1, the scanning mechanism consists of two mutually perpendicular prisms. The horizontal one rotates at three rps. Its optical output is passed to the vertical one which rotates at 300 rps. Thus, we get the "lines" and the "columns" of the scanned scene, which is called a field. Each field has 70 active lines (100 all together) and 130 active columns. For visual display reasons, the vertical and horizontal motors are synchronized in such a way that four fields produce one interlaced frame. With a scanning rate of 25 fields per second, 25/4 completely interlaced picture frames per second are thus obtained. The output from the vertical prism is focused onto the single element semiconductor detector, which is located in the wall of a Dewar chamber, and is maintained at 77K by liquid nitrogen. The detector produces an electronic output proportional to the incoming infrared radiation. After amplification, the signal is sent via a cable to the display unit, where absolute or relative temperature measurements can be made.

Throughout this research, the data was aquired only in the "field" mode, to take advantage of the higher scanning rate associated with that mode (25 images per second). More information about the system and the way it operates can be found in the AGA Thermovision® 782 Operating Manual (1984).

3.4 Physical Aspects of the Camera Operation

The operational characteristics of an IR imaging camera are largely dependent upon the detector characteristics and performance. Each kind of detector has its own narrow range of detection in the IR spectrum according to its chemical composition. Therefore, it is important to find out a priori whether the expected targets do have a radiation component that matches the detector characteristics. Secondly, since the atmosphere does not transmit

record single images, or an image that is the average of several images, or to record a series of up to 16 images at a time at a frequency of 1.5 Hz or lower. A key feature of this program is the gradual assignment of eight tones of artificial colors (from black through blue, green, red, etc. to white), for corresponding gray shades in the original image, thus producing an artificial sensation of the temperatures in the scanned field. The main advantage of such a system is the cross-hair cursor that can easily be moved on the screen and allows the operator to get precise temperature readings at defined locations of interest. Although the Disco® 2.0 was written specifically for the BMC IF800 computer, and although the latter has a quite obsolete architecture, together they make-up a quite versatile system that offers an abundance of processing options, from which only the main ones have been reported here.

3.3 The Infrared Imaging Camera

The infrared imaging camera converts electromagnetic thermal energy radiated from the scene contained in its field of view, into electronic video signals. These signals are electronically amplified and transmitted to the black and white display unit where the signals are further amplified, and the resulting image is displayed on the screen. The camera, or the scanner, comprises the following main subsystems:

(a) Electro-optical scanning mechanism

(b) Infrared detector attached to a liquid nitrogen Dewar flask

(c) Control electronics and preamplifier.

different requirements from an IR system when it is used for night vision imaging versus imaging for temperature measurements, and the inherent changes to be made in the former in order to realize the latter. A state of the art review of infrared detectors is given by Levinstein (1977). Although written twelve years ago, the article is still relevant as some of the detectors described there are still in use. With regard to the quantitative determination of surface temperatures using an infrared camera, Hsieh and Ellingson (1977) propose a method that also includes the surface reflection problem.

Before proceeding with the description of the technical aspects of infrared imaging systems, it is worthwhile to draw attention to the proceedings of Thermosense V (1982), that contains a few papers concerned with the practical aspects of temperature measurements using these systems.

3.2 The Infrared Imaging System

The infrared imaging system used in this investigation was an AGA Thermovision® 782. The basic system consisted of the scanner and a black and white display unit that allows direct or relative temperature measurements. The output from the scanner can be directly recorded on a modified vidicon recorder (VCR) for later playback. This device was of very little use mainly because of two limitations: frames could not be addressed individually; and a lack of a time base that could be recorded on the tape. The basic system was connected through a data link to a microcomputer BMC IF800 dedicated to the analysis of the thermographies. A Disco® 2.0 software package is used for the image processing and completely occupies a 5 1/4" floppy disk in a read-only storage mode. Up to 36 individual images can be stored on a second floppy disk in a read and write access storage mode. The user has the option to

Chapter 3

THE INFRARED IMAGING SYSTEM

A measurement system can be useful only to the extent that the operator understands the capabilities and limitations of his device. Although easy to use, the infrared imaging systems are very complex electro-optical devices and their output is influenced by a myriad of factors besides the target surface temperature. Since, in general, aeronautical engineers are not too familiar with these systems, it is the purpose of this chapter to review the main points of interest related to their performance.

3.1 Some Useful References

Infrared imaging systems work on the principles of radiation heat transfer. This type of heat transfer is based solely on the fourth power temperature difference between the body of interest and its surroundings, and takes place through electromagnetic radiation at wavelengths between 0.3μ to 50μ (where $\mu = 10^{-6}$ m), known as the infrared spectrum. As the name implies, the IR imaging systems detect this radiation and through electronic processing of the signals, produce an artificial video picture of the area scanned in which darker shades are associated with lower temperatures and lighter shades with higher temperatures.

The infrared imaging systems used for surface temperature measurements were developed during the sixties as derivatives of the military passive night vision systems. Although the requirements from the two types are somewhat different, the operational principles are the same. Lloyd (1975) gives an excellent overall account of the subject as viewed from his perspective as an engineer who worked for many years on research and development of such systems at Honeywell Inc. In a short note, Ohman gives a clear presentation of the

2.3 Summary

The preliminary experiments carried out at this stage were critical to the definition and continuation of the main research tasks. Not only was it true that the bulk of the work carried out later stemmed directly from this stage, but also most of the instrumentation and measurement interpretation problems encountered when using infrared imaging systems in aerodynamic research, were crystalized during this stage.

there is a jump in the wall temperature, that can be explained by the fact that at the corner, the flow has no velocity components and therefore, the convective heat transfer there should be minimal. The second feature was that at the point where the reattachment was believed to take place ($x \approx 15$ cm), the temperature passed through a local minimum. It is a well known fact that the heat transfer coefficient in such a flow is the highest at the turbulent reattachment point (Merzkirch et al., 1988), thus explaining the minimum temperature value there. The third feature was that downstream from the reattachment point, the influence of the development of the turbulent boundary layer can be observed on the wall temperature distribution. The fourth and last feature of this experiment was that the assumed reattachment point occurred between six to seven step heights downstream of the step. For a Reynolds number based on the height of the step of approximately 17500, this result is in excellent agreement with the findings of Eaton and Johnston (1981). The results of this experiment showed that separated flows can be detected with infrared imaging systems by mapping the surface of interest. This conclusion led to the experiment described in Chap. 6 where the footprints of the airflow about a NACA 0012 airfoil were studied all the way from the fully attached regime at zero angle of attack up to the post stall regime.

Before proceeding further with the analysis of the main series of experiments, it is essential to explain the operational principles of the infrared imaging system, in order to understand its limitations from an aerodynamic research point of view.

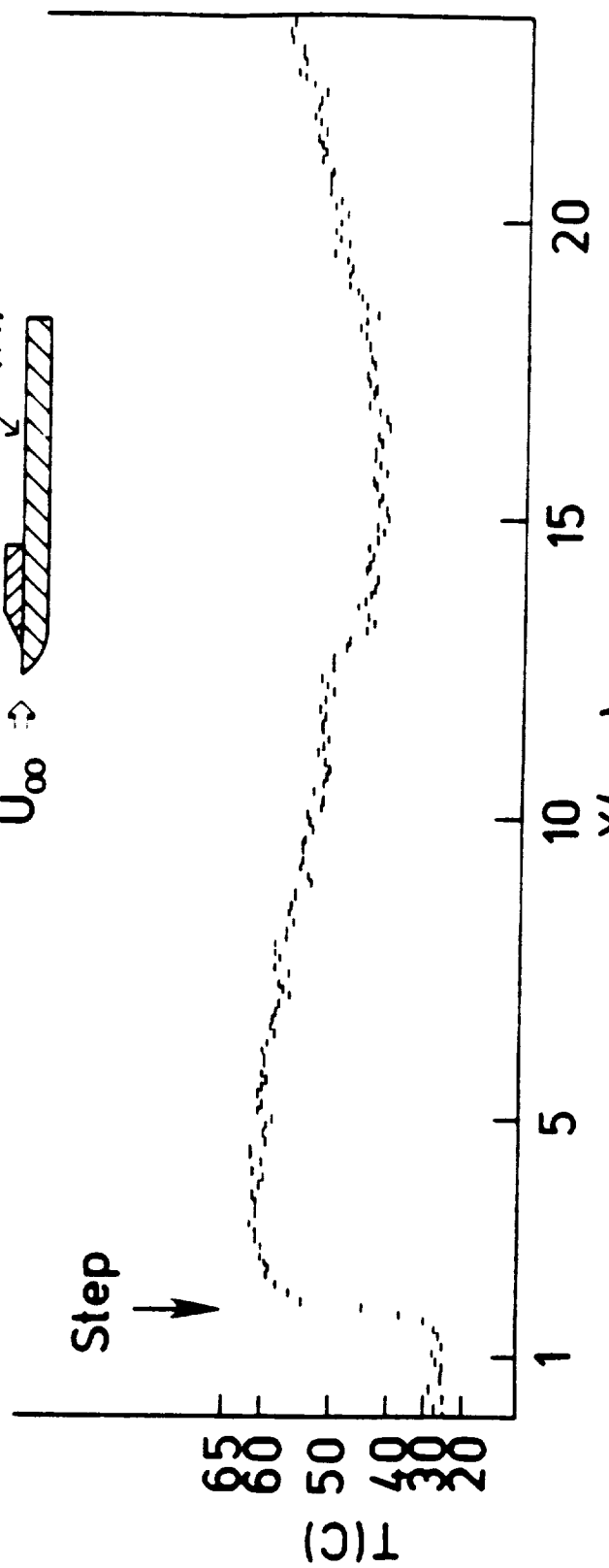

Fig. 2.3 Temperature distribution over a heated plate with a rear facing step. V_{air} =14 m/sec, Step height=2 cm

0.9x1.2m (3'x4') wind-tunnel. It is a low speed, return circuit wind tunnel driven by a 100 HP electric motor. The surface was warmed by a Constantan wire closely wrapped three times chordwise around the plate with a duct tape covering it in order to ensure uniform emittance and a smooth surface. The original idea was to produce a constant heat flux flat plate. However, it became very quickly apparent that the boundary condition produced is of constant power heating type. The difference between the two is that in the former case a constant heat rate is dissipated into the freestream through the boundary layer, while in the latter the airflow, the surroundings and the substrate share the constant heat rate dissipated by the wires. The measured wall temperature distribution was considered physically realistic due to its similarity to the constant heat flux case (Gartenberg et al., 1987), except for the fact that after an initial raise with the square root of the distance from the leading edge it leveled off, instead of continuing the initial trend (Kays and Crowford, 1980, p. 151). It was concluded that this behavior was the result of an ever increasing thermal involvement of the substrate, as the laminar boundary layer thickens and the convective cooling becomes less effective. At this stage, it was felt that this experiment should be revisited with a wedge type leading edge that would permit comparison of the experimental with analytic results. Further details are given in Chap. 5.

The last preliminary experiment was to monitor the wall temperature distribution for air flow over a rearward facing step to observe separated flow effects. The rearward facing step was produced by placing a right angle trapezoidal wedge on the flat plate previously mentioned, at 5 cm from the leading edge and parallel to it. The step height was 2 cm. The measured wall temperatures are reproduced in Fig. 2.3. Four features of the results were particularly encouraging. The first was that just at the foot of the step

of the mass per unit length with the specific heat) should be low in order to minimize the temperature time response to changes in local velocities. As already known, all these requirements led to the Chromel wire as the most suitable choice. On an absolute basis there are materials that fit better to the criteria established above. However, they fall into the category of rare metals, and thus their availability and price made their use in this case prohibitive.

Another problem that arose during the heated wire experiments was the background radiation interference. Since (as we have seen previously) the wire is unresolved by the camera, photons originating from the background surface will hit the detector together with the photons from the target wire. The problem is aggravated with increasing background temperature and spatial nonuniformity. To prevent problems associated with background interference, its surface temperature should be kept at least uniform and preferrably low. All these factors indicate that the actual experiments should be run under the same background conditions at which the calibration was carried out. This is the reason why later, the laminar flow jet experiments (Chap. 4) were carried out against a uniform background made out of cardboard paper held at constant temperature by the air conditioning system of the laboratory.

2.2 Surface Measurements for Boundary Layer Research

A second series of preliminary experiments was concerned with detecting the laminar boundary layer development over a warmed flat plate. The experimental set-up is identical with that shown in Fig. 5.1 except for the fact that the leading edge was curved and not sharp as it should be in order to reproduce a Blasius type flow field. The experiments were carried out in a

Minimization of this factor is essential when velocity information is deduced from the temperature measurements. After trial-and-error experimentations, it was decided that a 0.0762 mm (0.003") diameter Chromel wire would be the best compromise for the present task. At this point yet another problem was to be faced involving the wire surface emittance calibration. The Chromel wire has a highly polished surface with a typical emittance of 0.05. However, using this value to determine temperatures with the IR imaging system will result, as previously noted, in lower than actual values because the wire is unresolved by the camera. In order to get true temperature readings, an "apparent emittance" lower than the actual should be used. The calibration procedure is described in Chap. 4. In this context, it should be emphasized that for optically unresolved targets, the distance from the camera determines the fraction of the instantaneous field of view the target will cover on the focal plane. Therefore, emittance calibrations for unresolved targets are valid only for the specific distance at which they were carried out.

The choice of the wire material should be made after a careful screening of its physical properties: the material should have a high electrical resistivity in order to dissipate enough heat to raise its temperature and be visible with the IR imaging camera. Also, the temperature coefficient of electrical resistance should be low so that the wire will uniformly dissipate the heat lengthwise, even if the temperatures vary locally. The material should be chemically stable, otherwise corrosion may change the emittance, and thus accurate continuous temperature measurements may not be possible. The coefficient of thermal expansion should be low in order to prevent elongation due to the heating that may cause vibrations. The wire thermal conductivity should be low in order to prevent equalization of the temperature along the wire through conduction. Finally, the wire thermal capacitance (the product

Reynolds number. These heat transfer features are of course washed downstream with the flow causing the wake to be a zone of very intense turbulent mixing with peak values at the edges, thus determining the temperature shape along the wire as shown in Fig. 2.2.

An important factor that arose during this stage of the research was the choice of the wire material. From the flowfield point of view, a thinner wire is more desirable. However, for lengths of wire herewith under consideration (tens of centimeters), a too thin wire may break easily. Also, a thin wire may not be resolved by the camera i.e., its surface may not be large enough in order to be projected on the whole area of the camera detector. Therefore, the infrared imaging system wrongly assumes that the photons reaching the detector come from an area which is equivalent at least to the instantaneous field of view of the camera for that focal distance, thus giving false lower temperature readings of the wire. (This aspect of the temperature measurements with the infrared imaging system will be addressed in greater detail in the next chapter).

At this point, it seems that increasing the wire diameter may be a partial solution to the spatial resolution problem of the IR imaging camera but this is not completely true. A larger wire will disturb the flowfield, and also, as the wire diameter becomes larger, the spurious reflections from the surroundings to the camera start to play an important role in the signal to noise ratio the camera receives. A separate set of experimental runs with a variety of wire sizes revealed that at 0.381 mm diameter (0.015") the signal to noise ratio becomes unacceptably large. For example, the presence of people in the laboratory could be detected through their body heat reflection from the wire into the camera. Later it was found that smaller diameters were also desirable in order to minimize the heat conduction along the wire.

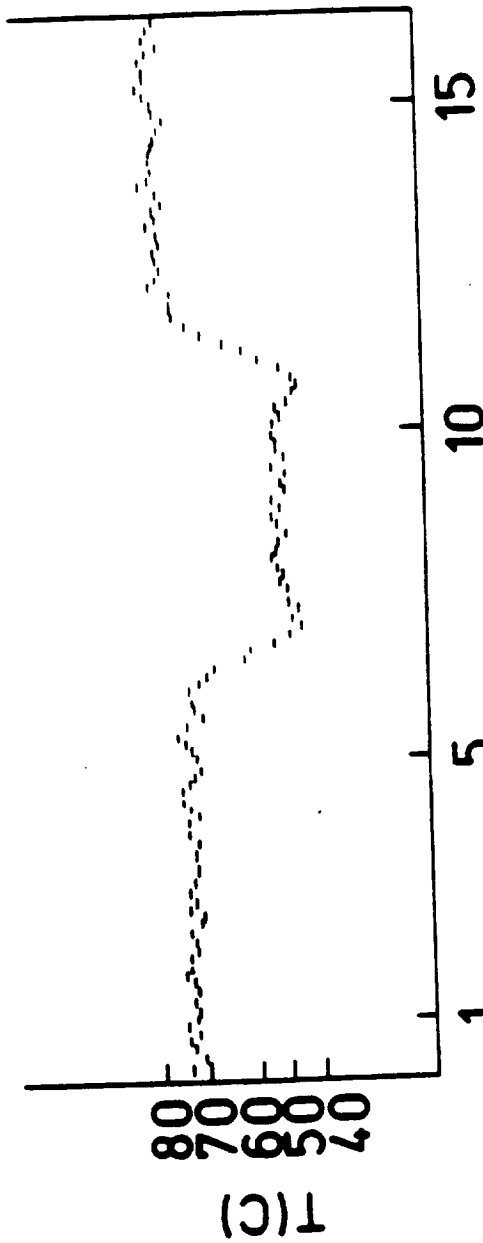

Fig. 2.2 The wake of a 10 cm diameter cylinder as captured on a heated wire placed 5 cylinder diameters downstream. Re_D=90,000

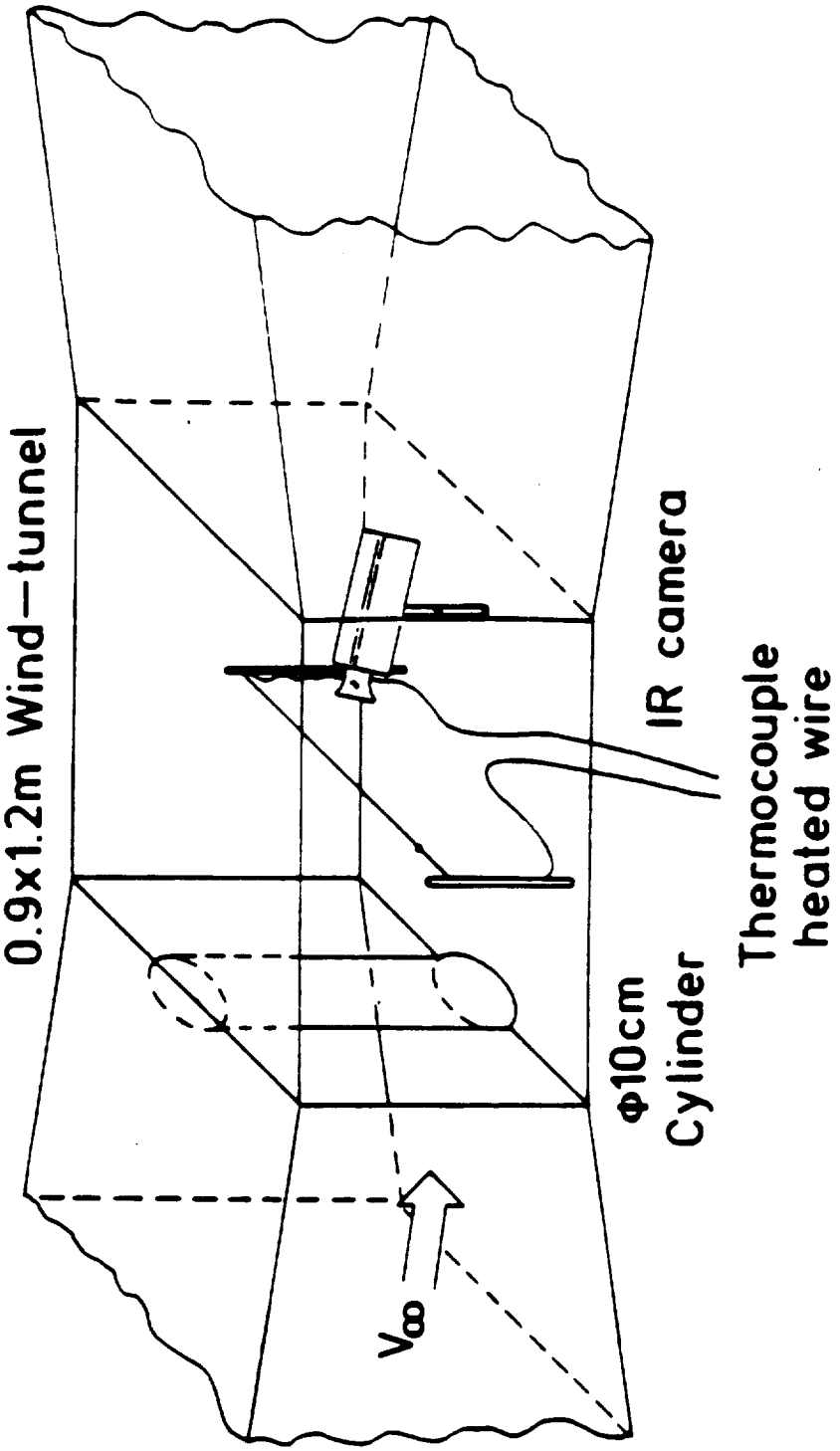

Fig. 2.1 Experimental layout for IR measurements of a heated wire in the wake of a cylinder

experimental set-up was identical to that shown in Fig. 4.3 with the addition that the wire was electrically heated. The measured temperature distribution along the wire was symmetrical with a minimum at the center of the jet, where the experimentally determined coefficient of heat transfer on the wire was in good agreement with the value predicted by a standard correlation (Morgan, 1975). Although the result was considered physically correct, the opinion was that the heat-gun flow was not controllable enough in order to produce a flow field suitable for a thorough investigation. As a result, the conclusions drawn from this preliminary experiment led directly to the laminar flow jet experiment described in Chap. 4.

In the second experiment, cylinder wakes were mapped using a heated wire placed downstream, and again the temperature distribution was found with the infrared imaging system. The set-up as installed in the 0.9x1.2 m (3'x4') low speed wind tunnel in which the experiments were carried out is shown in Fig. 2.1. A 10 cm diameter cylinder was tested at a Reynolds number of 90,000, the wire being placed at 5 and 10 diameters downstream from the cylinder. A second cylinder, 2 cm in diameter, was tested at a Reynolds number of 18,000, the wire being placed at 8, 16, 24 and 32 diameters downstream. In all cases, the qualitative results were self-consistent and agreed with the physical expectations. A sample result is shown in Fig. 2.2 where the temperature is plotted as a function of the lengthwise wire coordinate. According to Schmidt and Werner (Schlichting, 1968, p. 298), the heat transfer rate on the leeside of a cylinder, where the flow is separated, is equal to, or higher, than that on the windward side. The behaviour of the heat transfer rate in the separated flow area of the cylinder is dependent on the Reynolds number based on the cylinder diameter. In particular, just after the separation point, there is a jump in the heat transfer rate which is even more sensitive to the

Chapter 2

THE PRELIMINARY EXPERIMENTS

Since the main objective of this research was to extend the use of infrared imaging systems to a few important aerodynamic subjects of interest, the first step was to carry out initial experiments, where the suitability of the measurement technique could be easily judged according to the results. The initial experiments and the results are described in detail in Gartenberg et al. (1987) and only the more interesting results are reproduced here. A review is made of the main ideas behind each experiment and of the way the results were evaluated.

2.1 The Heated Wire Technique

The first concept to be tested was the use of a thin, electrically heated wire as an air velocity detector. The idea was that by measuring temperatures along the wire while it is immersed in a flow with position dependent velocities, one may deduce the local velocities through Nusselt number correlations. This approach is useful when investigating shear flows, jets, boundary layer and confined flows, wakes etc. In such cases, the local heat transfer coefficient is mostly a function of the normal velocity component relative to the wire (Morgan, 1975); but even with this restriction, the method may be extremely useful to map flowfields unintrusively, since a 0.0762 mm (0.003") slightly heated wire will not have any significant influence on the surrounding flow. Two experiments were performed in this category: mapping of an air jet and mapping of the wake behind a circular cylinder.

In the first experiment, the 0.0762 mm (0.003") heated wire was placed at 30 cm from the exit of a working heat-gun throwing cold air at 2.5 m/sec. The

The experimental work carried out under this program followed very closely the preceding stated purposes. Chapter 2 contains a brief review of an initial set of experiments that were aimed toward checking the feasibility of the objectives with regard to the heated wire concept and tracking the boundary layer behavior by surface thermography. Chapter 3 is a short description of the infrared imaging system, emphasizing the IR imaging camera operation principles. Chapter 4 describes the evaluation of the heated wire concept using a laminar circular jet as a test case. Chapter 5 presents the experimental results and an analysis of the laminar, thermal boundary layer, which develops over a flat plate, using surface thermography. Chapter 6 is a study of the boundary layer regimes over a NACA 0012 airfoil from zero angle of attack up to separation, employing also tufts that could be observed both visually and with the IR imaging system. Finally, in Chap. 7 the conclusion from this research are drawn and recommendations for further work are made.

With the realization that IR imaging systems can produce more useful data in aerodynamic research than has been generally appreciated, this work explores the extent to which these systems can be made useful in advancing the understanding of aerodynamic flow phenomena. As a result, the plan of research incorporated specific experimental objectives set out to produce an improved understanding regarding the detection of the low speed viscous interaction characteristics using IR imaging systems. Specifically, the following topics were identified to be pursued:

1. Feasibility and validation studies of the heated wire concept.

   This method calls for placing a very thin and very long heated wire perpendicular to the velocity vector of an airflow of interest. By tracking the temperature distribution along the wire with the IR imaging camera, it is possible to capture the main features of the flowfield. Furthermore, by using appropriate Nusselt number correlations, the velocity distribution perpendicular to the wire may be deduced.

2. Boundary layer development over a body of interest.

   Experiments and model analysis were planned so that by measuring with the infrared imaging system the wall temperatures of an actively heated body immersed in an airflow, the development of the thermal boundary layer can be tracked.

3. Detection of boundary layer flow regimes over airfoils.

   The purpose in this experiment is to expand the applicability of infrared imaging systems to the detection of separation, beyond the detection of transition, e.g., Quast (1987).

For a constant Prandtl number, which is frequently the case in aerodynamics, Eq. (1.1) can be rewritten as

$$\frac{h\ x}{k_a} = \text{Constant} \cdot \left(\frac{U \cdot x}{\nu_a}\right)^m, \quad 0<m<1 \tag{1.2}$$

Let's assume a constant properties flows, as is the case in the subsonic regime where the temperature doesn't change appreciably throughout the flowfield. Then, Eq. (1.2) can be expressed

$$h = h\ (U,\ x) \tag{1.3}$$

where h is the local heat transfer coefficient, x is the coordinate location of the point of interest on the configuration surface, k_a is the air conductivity, U is the local freestream velocity and ν_a is the air kinematic viscosity. This expression shows that the local heat transfer coefficient, h, between a surface and a surrounding flow is a function of the freestream flow velocity and the configuration geometry, x, if the air properties remain constant. On the other hand, the heat transfer coefficient h is defined by Newton's law:

$$\dot{q}_o'' = h\ (T_w - T_\infty) \tag{1.4}$$

where q_o'' is the local heat flux, T_w is the local wall temperature and T_∞ is the freestream static temperature.

Equations (1.3) and (1.4) are the basic formulae to be used for aerodynamic research using infrared imaging systems. Measurement of the surface temperature distribution on the body of interest with the IR imaging system, and knowledge of the geometry, the freestream temperature and eventually the heat flux, may provide enough data to deduce useful information about the flow-body interaction. The thrust of the present research utilized this second approach.

concerned with the shuttle entry measurements concentrate on technical descriptions of the systems and the projected experiments but give no results. The other papers either go into lengthy descriptions of the infrared imaging sytem itself, or use them to produce artificially colored pictures, while the quantitative data was either acquired or heavily backed-up by thermocouples. Each one of the references adds a little bit of information, but none of them gives a complete picture, and this is the reason why every single reference that was found was listed. Of all the references, the most useful ones are those of Boylan et al. (1978) from Arnold Air Force Station, Tennessee, and Quast (1987) from DFVLR in West Germany.

1.4 The Present Work

Considering the potential applications of infrared imaging systems in aerodynamic research, there are at least two distinct paths that may be followed. The first and the simplest one is to follow the Reynolds analogy between the heat transfer and the skin friction. Temperature measurements can be performed in order to deduce Stanton numbers and subsequently skin friction coefficients. This approach works in fully developed laminar and turbulent flows, but it is not applicable in the region of the transition itself and in separated flows.

The second approach is more fundamental and goes back to the basics of the convective heat transfer. As is well known, the dimensionless heat transfer coefficient, the Nusselt number (Nu), is usually expressed as a function of the Reynolds number (Re) and the Prandtl number (Pr):

$$Nu = \text{Constant} \cdot Re^{m} Pr^{n} \qquad (1.1)$$

aircraft and some helicopters. The results show the very complicated airflow patterns that develop in ground effect and at low speeds. No follow-up of this experiment could be found.

1.2 University Research

Applicable references from universities around the world are very meager. Most of the investigations were done in the United States. It seems that Champagne et al. (1967) were first to use a microscope-pyrometer to make temperature measurements along a scaled-up hot-wire probe to determine the extent of the heat conduction to the supports. Meroney (1978) used an infrared imaging system to make heat transfer studies on model buildings in a wind tunnel. He proved the concept by estimating convection heat transfer coefficients but didn't proceed further because of lack of a suitable data processing system. Page et al. (1986) used an infrared imaging system to determine the temperature distribution in a heated jet at the stagnation point region. A similar research was done by Carlomagno and De Luca (1986) in Italy expanding the research to an array of jets and determining heat transfer coefficients from the temperature measurements. Finally, Spence (1986) used the infrared thermography to determine heat transfer coefficients on double wedge jet vanes used for missiles thrust vector control.

1.3 Perspective on the Literature Survey

The paucity of works documented in archival journals is a good indication regarding the immaturity of the infrared imaging method in aerodynamic research. Only three works, out of all those reviewed, have been documented in recognized scientific journals (e.g., Int. J. Heat Mass Transfer, J. Fluid Mechanics, AIAA J.). Furthermore, the relatively long reference list reviewed in this chapter is misleading with regard to its usefulness. The papers

that study in the light of the following experiment objectives: (a) determine the actual heating rate distribution on the lower surface, (b) the location of the boundary layer transition, and (c) location and extent of flow separation in front of the control surfaces. Green et al. (1983) give a detailed description of how the system works, together with a few representative results. However, no detailed presentation of the results or their processing followed up. Meanwhile, this research was cancelled, on financial grounds. In a second and completely separate experiment, the objective was set to be the measurement of surface temperatures on the leeside of the shuttle. In this case, an infrared imaging system is mounted in a pod on the tail of the Space Shuttle Columbia, from where it scans the orbiter's wings and fuselage. This experiment is of interest because of the highly vortical nature of the separated flow over the wings which would impinge on the leeside surfaces. The final objective is to compare the measurements with results of CFD codes (Anon, Aviation Week and Space Technology, Dec. 7, 1987). As in the previous case, no results have yet been published from this unique experiment. Contributing to the design of the pod, heat transfer measurements were performed by Nutt (1979). The radiation estimation calculations were done by Myrick and Kantsios (1982); the description of the infrared imaging system is given by Myrick and Throckmorton (1985); and, the overall experiment description is provided by Throckmorton et al. (1985).

Two more noteworthy papers related to infrared imaging applications to flight testing are: one by Brandon, et al. (1988) from NASA Langley Research Center in which results relating to in-flight transition detection as well as mapping a vortex "footprint" on the airplane wing are described. Another paper is by Flaig (1977) from the Naval Air Systems Command, in which an infrared imaging system was used to map exhaust gases from a hovering VTOL

scanning direction is much poorer than across it. Tests were also carried out to determine the system spatial resolution using different size circular targets at the same temperature. Furthermore, an extensive measurement error analysis was carried out based on the work of Carter (1975). From all the aeronautical engineering groups using infrared imaging systems, the group at Arnold Air Force Station probably accomplished the most comprehensive analysis concerning the performance and limitations of this system in wind-tunnel testings. In two other papers, Stallings et al. (1979) and Stallings and Whetsel (1982) repeated some of the findings reported in the previous paper. Using the knowledge and facilities developed at Arnold Air Force Station, Martinez et al. (1978) performed heating experiments and measurements using an infrared imaging system on a 0.040 scale model of the Space Shuttle. These measurements served the Rockwell Corporation in the design of the thermal protection system of the orbiter and can be considered as one of the very few but nonetheless great contributions using an infrared imaging system in aeronautical engineering. Hender and Okabe (1983) made further use of that expertise to carry out heating measurements on a wedge type model made of an elastomer bonded to an aluminium base. It was found that for the wedge configuration, the semi-infinite slab assumption breaks down when deducing heat transfer data. Although the outcome could be predicted a priori, its extent could hardly be so, and for such cases an infrared imaging system may be the cheapest and fastest means to obtain quantitative data.

Two other applications relating to the Space Shuttle, concern mapping surface temperatures during the entry phase. In one of them, the temperatures on the windward side of the orbiters were measured with a telescopic infrared imaging system mounted on an airborne observatory. The feasibility analysis was performed by Swenson and Edsinger (1977). Later, Chocol (1979) reviewed

compared with the thermographies in order to determine the cooling effectiveness of the various configurations being tested (simple versus multirow holes). The research was performed in support of jet engines turbine design efforts, but no directly applicable results have been reported.

1.1.5 U.S.A.

Most of the infrared imaging systems applications in aeronautical engineering reported by national laboratories are linked to the Space Shuttle program. The beginning goes back to the initial design phases of the shuttle when the prediction of the heat transfer rates during the entry phase were of major concern. The first experiments were performed by Compton (1972) at NASA Ames. This experimental program was very similar to that of Thomann and Frisk (1967) in Sweden, except for the fact that extensive use of computers was made for both data aquisition and data reduction. However, the bulk of the experiments were carried out later on at Arnold Air Force Station in Tennessee. The initial study and set-up of the experimental system was done by Bynum et al. (1976). The study, which provided surface temperatures and heat transfer data, was still general in nature, the measurements being performed on a cone and a hemisphere at a Mach number of 8.0. Later, Stallings and Carver (1978) embarked on a program to make heat transfer measurements on Space Shuttle scale models, using an infrared imaging system and the phase-change paint method. Besides the obvious and original contribution to the Space Shuttle design, this group was the first to report the difficulties associated with infrared imaging system measurements. In a very extensive testing program, Boylan et al. (1978) evaluated the influence of the infrared imaging system optics on the overall performance. It was also showed that the system capability to map a step temperature change along the

wind tunnels that will allow transition studies at higher Reynolds numbers in ground test facilities. A first effort in this direction was to carry-out experiments at 240K. A short and succinct enumeration of the difficulties encountered when making IR measurements in cryogenic environments is given by Seraudie et al. (1988). A further contribution to the use of infrared imaging systems was made by Balageas and Ory (1985), who reviewed the previously mentioned semi-infinite slab assumption and showed in which cases it can lead to significant errors. To refine the calculation methods, a technique was developed that takes into account the curvature of the wing, its skin thickness, as well as the thermal boundary conditions at the back of the skin.

1.1.3 West Germany

According to a survey by Mordoff (1988), the Deutsche Forschungs-und Versuchsanstalt fur Luft-und Raumfahrt (DFVLR) conducts an extensive and systematic experimental program designed to prepare a data base of flow regime characteristics of wings and airfoils. The program includes both wind tunnel and flight tests (Quast, 1987), the infrared imaging system being the transition detection tool. Laminar flow data were recorded at Mach numbers varying up to 0.7, altitudes up to 10,000 m and sweep angles up to 23 degrees. Further tests are planned to be carried out in order to expand the range of the parameters of interest.

1.1.4 Japan

A study concerning the film cooling effectiveness of injection from multirow holes was carried out at the National Aerospace Laboratory by Sasaki et al. (1979). In this study, an infrared imaging system was used as a visualization means for the spreading of the injection fluid. All the temperature measurements were done by thermocouples and their results were

results from the heat-conduction theory (e.g., Eckert and Drake, 1972, pp. 168-176). This concept and the data reduction method was later adopted with little or no change at all by most of the groups working on this subject. However, Thomann and Frisk were not the first investigators to make the semi-infinite slab assmuption to deduce heat transfer rates from surface temperature measurements. This idea was borrowed from the phase change paint technique which later evolved into the thermographic phosphorescent paint technique. The interested reader can consult Jones and Hunt (1966) and Throckmorton (1972) regarding to the data reduction procedures originating from this technique.

1.1.2 France

The French at the Office National d'Etudes et de Recherches Aerospatiales (ONERA), were the first to realize the potential of infrared imaging systems to detect the laminar to turbulent boundary layer transition in the low subsonic regime (Bouchardy et al., 1983). This application is made possible by the fact that at the transition point there is an order of magnitude increase in the convective heat transfer rate. Thus, the transition line can be seen on an infrared imaging system display as a jump in the skin temperature going from low values in the laminar zone to high values in the turbulent zone, where the skin temperature is intially at the free stream temperature. Because at very low Mach numbers the temperature differences may not have been high enough to generate a good contrast on the IR thermography, the authors analyzed the raw data by applying digital image processing techniques. The effort was beneficial to other researchers as well, who made successful use of that capability (Schmitt and Chanetz, 1985). Lately, the effort at ONERA is concentrated on developing this method for use in cryogenic

flow, the boundary layer flow and the substrate thermal diffusion. This aspect was recognized a long time ago and led directly to the introduction of hot-wire and hot-film gages for boundary layer research. However, these sensors (like most of the others) can provide information that can be related only to their locations, and this is one of their shortcomings. It is the capability of infrared imaging systems to scan large areas in a dynamic fashion, and produce quantitative results related to the surface temperature that make them an attractive alternative aerodynamic research tool. Unfortunately, conservative thinking played a major role in the failure to recognize the full research potential of these systems. The following literature survey will point to the very few applications the infrared imaging systems have seen. The survey is divided in two parts: aeronautical research establishments and universities. The big gap in financial, manpower and time resources between the two had a clear impact on the span of the research output.

1.1 Research at Aeronautical Establishments

1.1.1 Sweden

It seems that the first use of an infrared imaging system for aerodynamic research was made at the Aeronautical Research Institute of Sweden by Thomann and Frisk* (1967) which used an IR system to measure surface temperatures on a model in a hypersonic wind tunnel and to deduce heat transfer rates from the data. For reducing the data, the material beneath the model's skin was assumed to be a semi-infinite slab. This allowed to use well-known analytical

*Complete citations are found in the alphabetical list of references section.

Chapter 1

INTRODUCTION

A quarter of a century after infrared imaging systems were introduced commercially, they are still rarely used in aerodynamic research. The perception of these systems as an exotic tool limited their application to a few specific tasks. This reality is rooted in the history and in the everyday practice of aeronautical engineering. Since the primal interest is on the forces acting on a given body, pressure measurements come out as the natural measurements choice. This traditional approach is very useful in design studies that are mainly concerned with forces and moments impressed on the body by the external flow. However, it has little to offer when it comes to understanding and analyzing the interaction between the body and the viscous fluid that takes place through the boundary layer. When viewed globally, the two views are, of course, interconnected because the geometry of the body and the freestream velocity will determine not only the pressure-dependent forces but also the character of the boundary layer whether laminar, turbulent, or separated. In the case of attached boundary layer flow, its regime, whether laminar or turbulent, will determine the magnitude of the skin friction drag. However, a separated boundary layer completely alters the external flowfield about the body and totally changes the pressure distribution on it. Thus, there is the need for a complimentary measurement technique that will offer insight into the whole picture of the fluid-body interaction.

In the same way that the pressure distribution reflects the momentum exchange between a fluid and a body, the temperature distribution reflects the energy exchange between the two. The difference is that the energy exchange process is related to all of the interaction aspects related to the external

D	value based on diameter
f	value at film temperature
v	constant volume value
w	wall
x	value based on distance from the leading edge
λ	radiation spectral value
∞	freestream property

Ra	Rayleigh number
Re	Reynolds number
r	radial position
r^2	statistical coeffcient of determination
s	airfoil surface arc length
St	Stanton number
T	temperature
U	freestream velocity
x	distance from the leading edge

Greek Symbols

α	thermal diffusivity or angle of attack
δ	boundary layer thickness
ε	emittance
θ	reduced wall temperature
λ	radiation wavelength
μ	absolute viscosity of the air
ν	kinematic viscosity of the air or photon frequency
ρ	density
σ	Stefan-Boltzmann constant or standard deviation
Φ	viscous dissipation function

Subscripts

a	air
b	black body radiation
c	value based on chord length

NOMENCLATURE

A	cross section area or circumferential area
c	specific heat or constant in the power function freestream velocity distribution
c_f	skin friction coefficient
c_o	speed of light in vacuum
d	diameter
e	radiation emissive power
F	body force
Gr	Grashof number
h	convective heat transfer coefficient or Plank constant
I	thermal value
i	electrical current
k	thermal conductivity or Boltzmann constant or constant in the power function wall temperature distribution
ℓ	length
m	mass
N	photon emittance number
n	medium index of refraction or degrees of freedom
Nu	Nusselt number
P	number of the coefficients fit in the regression equation
p	pressure
Pr	Prandtl number
$\dot{q}$	heat generation rate
$\dot{q}''_o$	heat flux
R	pipe radius or electrical resistance

TABLE OF CONTENTS

PREFACE

This is a report of a research that was aimed at proving concepts, and as such was exploratory in nature. In order to keep the cost of the program within the assigned limits of the budget, some measurements were made with devices that were readily available in the laboratory. Some of these devices had an accuracy that may be judged as too coarse. At that time, the opinion was that as long as the measurement errors could be established quantitatively, they sufficed for achieving the research purposes and paved the way for future investigators to apply the developed methods to their own research.

SUMMARY

An experimental program was aimed at identifying areas in low speed aerodynamic research where infrared imaging systems can make significant contributions. Implementing a new technique, a long electrically heated wire was placed across a laminar jet. By measuring the temperature distribution along the wire with the IR imaging camera, the flow behavior was identified. Furthermore, using Nusselt number correlations, the velocity distribution could be deduced. The same approach was used to survey wakes behind cylinders in a wind-tunnel. This method is suited to investigate flows with position dependent velocities, e. g., boundary layers, confined flows, jets, wakes and shear layers. It was found that the IR imaging camera cannot accurately track high gradient temperature fields. A correction procedure was devised to account for this limitation. Other wind-tunnel experiments included tracking the development of the laminar boundary layer over a warmed flat plate by measuring the chordwise temperature distribution. This technique was applied also to the flow downstream from a rearward facing step. Finally, the IR imaging system was used to study boundary layer behavior over an airfoil at angles of attack from zero up to separation. The results were confirmed with tufts observable both visually and with the IR imaging camera.

NASA Contractor Report 181839

Low-Speed Flowfield Characterization by Infrared Measurements of Surface Temperatures

E. Gartenberg, A.S. Roberts, Jr. and G.J. McRee

Old Dominion University Research Foundation
Norfolk, Virginia 23529

Contract NAG1-735
May 1989

National Aeronautics and
Space Administration

Langley Research Center
Hampton, Virginia 23665

maintained (or obtained) in order to compensate for the fact that the boundary layer thickens and heats up streamwise. In this case, the constant heat generation rate is shared mainly by two participating media, the wooden substrate by conduction and the airflow by convection. Heat transfer by radiation is also taking part, but is insignificant. Since the air cooling by convection is more effective on the forward part of the plate, (due to the thin boundary layer), the heat transfer by conduction to the substrate is less than on the aft part of the plate, where the boundary layer is thick and the convective heat transfer is much poorer. The estimation of the boundary layer behavior will show that between the first and the last station of the first data group, it thickens by 90% (from 0.60 mm. to 1.15 mm) while with respect to the second data group, it continues to thicken but only by 30% (from 1.35 mm. to 1.75 mm.) (see Appendix B, Eq. B7).

Looking more attentively at Fig. 5.5, one may further observe that the general trend of the slope of θ vs. $x^{1/2}$ is to decrease gradually from the leading edge downstream, at the same time that the overheat of the substrate is going up. This feature is an additional evidence to the ever increasing participation of the substrate due to the gradual decreasing effectiveness of the convective cooling, and it happens in spite of the fact that the wood qualifies as a heat insulator.

The thermal energy analysis performed on the flat plate is summarized in Table 5.1. The convective heat transfer was calculated from the temperature regressions given in Fig. 5.5. It is a superposition of the heat flux as generated by a constant temperature distribution (Kays and Crawford, 1980, p. 139)

$$Nu_x = 0.332\ Pr^{1/3}\ Re_x^{1/2} \qquad (5.2)$$

Table 5.1 Mean values analysis of the heat dissipation modes on a flat plate heated at constant wall power generation placed in an airstream at zero angle of attack $Re_x = 1.233 \times 10^6 \, x \, (m)$.

Data points	x	$\dot{q}''_{o\ conv}$	$\frac{\dot{q}''_{o\ conv}}{\dot{q}''_{o\ gen}}$	$\dot{q}''_{o\ rad}$	$\frac{\dot{q}''_{o\ rad}}{\dot{q}''_{o\ gen}}$	$\dot{q}''_{o\ cond}$	$\frac{\dot{q}''_{o\ cond}}{\dot{q}''_{o\ gen}}$
	(1)	(2)		(3)		(4)	
All	1.9 → 159.9	767	18%	82	2%	3335	80%
1st group	1.9 → 68.5	930	22%	73	2%	3181	76%
2nd group	95.2 → 159.9	546	13%	103	2%	3535	85%

(1) distance from the leading edge (mm)

(2) based on Eqs. (5.1) and (5.2) (W/m^2)

(3) based on Eq. (5.9) mean value (W/m^2)

(4) $\dot{q}''_o$ conducted = $\dot{q}''_o$ generated - ($\dot{q}''_o$ convected + $\dot{q}''_o$ radiated), mean value (W/m^2)

conv - convected

gen - generated

rad - radiated

cond - conducted

(where Nu_x is the local Nusselt number, Pr is the air Prandtl number and Re_x is the local Reynolds number), and a constant heat flux as deduced from Eq. 5.1. Thus, the regressions of Fig. 5.5 present two aspects of the convective heat transfer. The first is contained in the point of intercept of the regression line with the θ-axis and is indicative of the level of overheat of the substrate that can be accounted for through Eq. 5.2. The second is contained in the slope of the regression line, and is indicative of the variation in the chordwise temperature distribution, that in this case can be accounted through the constant heat flux model as given by Eq. 5.1.

The quantitative evaluation of the experiment shows that the mean electrically generated power was 949 W/m^2. Locally, along the centerline wire, where the temperature measurements were made, the value of the electrically generated power was 4184 W/m^2 (see Fig. 5.4). As the balance of energy analysis shows (see Table 5.1), the highest value of the mean heat flux convected into the air along that wire was 930 W/m^2. This value is of the same magnitude to the solar heat flux at the earth surface. Therefore, this heating is thought to affect the boundary layer on the flat plate about the same as it occurs in reality over the wing of an airplane.

5.4 The Infrared Imaging System as a CFD Codes Validation Tool

The interaction between a solid body and a surrounding flowfield of different temperature has both a momentum and an energy exchange aspect. The former is responsible for the velocity distribution around the body while the latter is responsible for the heat flux distribution over its surface. This heat flux will continuously change the temperature distribution of the body substrate and particularly of its surface. Thus, in general, even under steady flow with constant free-stream temperature conditions, the surface

temperature distribution of a body may remain time dependent for significant periods of time.

Since the prediction of aerodynamic and aerothermal loads by computational means is and will be one of the main research topics in aerodynamics, there is a clear need for an experimental method to provide data for comparison and validation of the CFD codes. Viewed from this perspective, the infrared imaging systems are ideal tools for such tasks since they do not require instrumented models, nor any specialized instrumentation conduits in the wind tunnel or on the tested aircraft.

From a general stand point of view, the complete calculation of the interaction between an arbitrary body and the fluid flow requires the following steps: first, the Euler equation

$$\rho \frac{D\vec{U}}{Dt} = \vec{F} - \text{grad } p \qquad (5.3)$$

is solved for the external flow, yielding the flow velocity distribution around the body. Here, this equation is given in the incompressible flow formulation where, $\vec{U}$ is the air velocity vector, ρ is the air density, D/Dt is the total derivative operator, $\vec{F}$ is the body force and, p is the pressure.

Next, the Navier-Stokes equation can be solved, perhaps in boundary layer approximation. This equation differs from the Euler equation by the inclusion of the viscous terms $\mu_a \nabla^2 \vec{U}$. Again, in the incompressible flow formulation it can be expressed as

$$\rho \frac{D\vec{U}}{Dt} = \vec{F} - \text{grad } p + \mu_a \nabla^2 \vec{U} \qquad (5.4)$$

where ∇^2 stands for the Laplacian operator and μ_a is the air viscosity. Now with the velocity distribution known around the body, one may solve the energy

equation for the temperature distribution in the flow field. Once again invoking the incompressiblity argument and assuming constant properties flow, the energy equation as derived from its internal energy formulation can be expressed in terms of the air temperature field as

$$\rho\, c_v \frac{DT}{Dt} = k_a \nabla^2 T + \mu \Phi \qquad (5.5)$$

where c_v is the air specific heat at constant volume, k_a is the air thermal conductivity, T is the air temperature and, Φ is the viscous dissipation function (Schlichting, 1968, p. 254).

All the above mentioned equations with the addition of the continuity equation, can in principle be solved for the five parameters that uniquely determine the flowfield behavior namely $\vec{U}$, p and T. For the present purposes, the energy equation solution is of the main interest, since it is the temperature gradient of the air in the boundary layer at the wall that determines the heat flux into the body through the Fourier heat conduction law

$$\vec{q}_o'' = - k_a \text{ grad } T \qquad (5.6)$$

where $\vec{q}_o''$ is the heat flux. In order to obtain the temperature distribution on the body surface, it must be remembered that its surface is the solid boundary with respect to the fluid. Therefore, the heat conduction equation

$$\frac{\partial T}{\partial t} = \alpha \nabla^2 T \qquad (5.7)$$

where α is the thermal diffusivity of the substrate, must be solved for the solid body in order to determine the surface temperature distribution. Boundary conditions do play a special role. For example, besides the convective heat transfer, heat sources, sinks and thermal radiation effects may occur at the solid boundary.

The convection effect is more conveniently expressed through the Newton law

$$\dot{q}_0'' = h\,(T_w - T_\infty) \qquad (5.8)$$

rather than through the Fourier conduction law. Sometimes, the combination of the two laws is used to determine the convective heat transfer coefficient h, as a function of the difference between the solid wall temperature T_w and the air freestream temperature T_∞.

The radiation heat transfer obeys the well known Stefan-Boltzmann equation

$$\dot{q}_0'' = \varepsilon\,\sigma\,T_w^4 \qquad (5.9)$$

where σ is the Stefan-Boltzmann constant and ε is the radiation surface emittance factor.

Schematically, this procedure is summarized in Fig. 5.7, which shows why, in general, this process is unsteady even for steady state flow conditions. The evolving nature of the temperature field of the substrate continuously changes the temperature gradient in the boundary layer and the resulting heat flux.

Once the body surface temperature distribution is predicted, it is possible in principle to construct a synthetic temperature distribution of the body surface, as it is assumed that it will be produced by the infrared imaging system in a test run at identical conditions with those of the calculation. Still to be remembered at this stage is the fact that the configuration geometry, the model material and its finish, and the IR imaging camera specifications, all these factors influence the final thermographic experimental result, and they should be taken into account when computing and synthesizing the predicted temperature distribution (Gartenberg and Roberts, 1988).

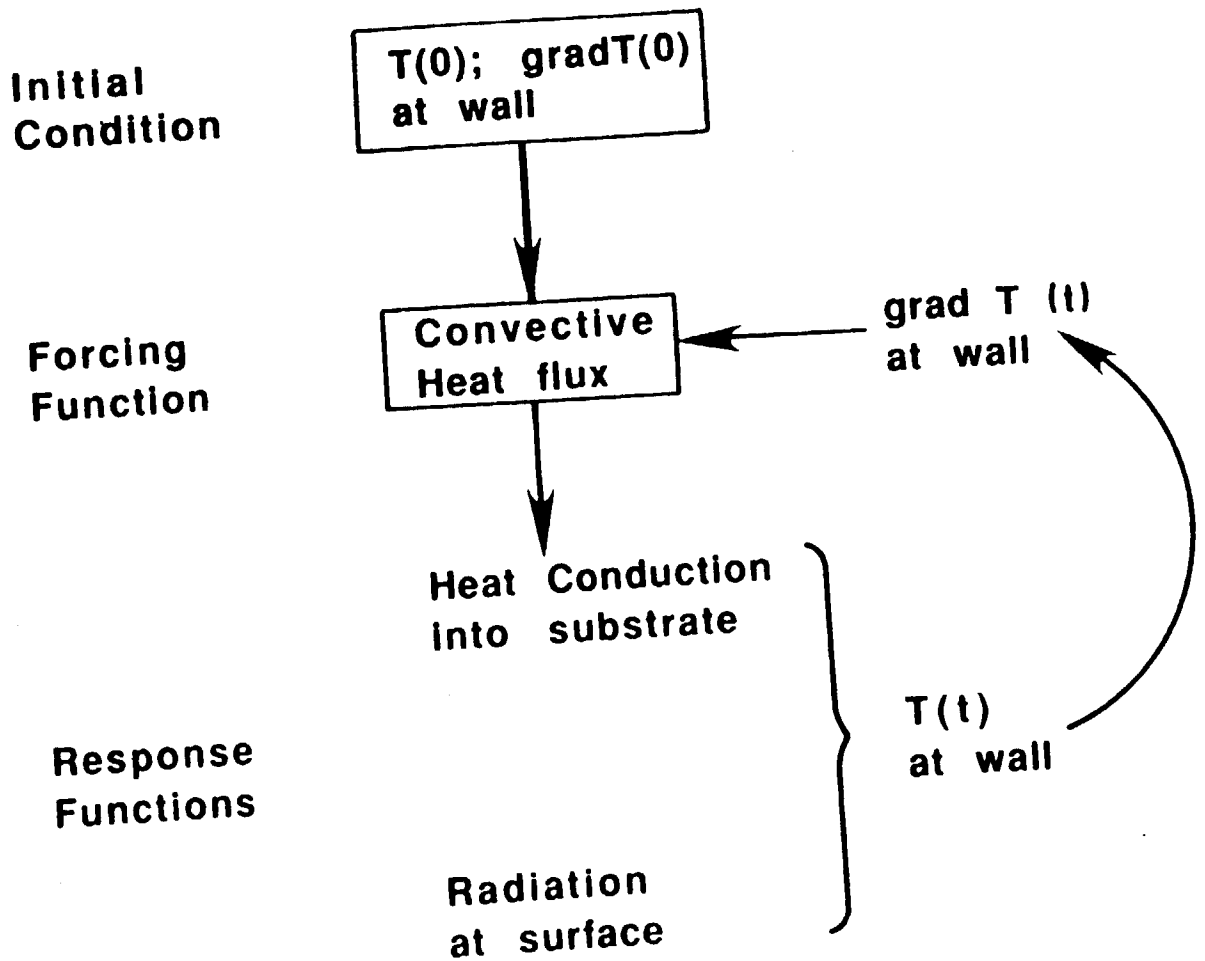

Fig. 5.7 The closed loop of surface temperature distribution in a body–airflow interaction

Hence, through a complete set of aerodynamic and heat transfer calculations, it is possible to come up with computed results that are relatively easy to compare with experimental data obtained as thermographies. The whole concept is presented in Fig. 5.8.

5.5 Summary

The infrared imaging system is an effective, non-intrusive device for measurement of surface temperatures with position and time dependent temperature distributions. Its capability of mapping rapidly entire surfaces is unmatched by any other means existing today. Furthermore, for aerodynamic configurations, the surface temperatures provide important information about body interaction with the external airflow. This was basically shown for the case of a flat plate in the laminar boundary layer regime at constant wall heat generation rate.

The concept of using infrared imaging systems in aerodynamic research as a direct CFD codes validation tool was introduced. In general, it can be stated that the surface temperatures of a body in a flowfield is time dependent even for steady state flows.

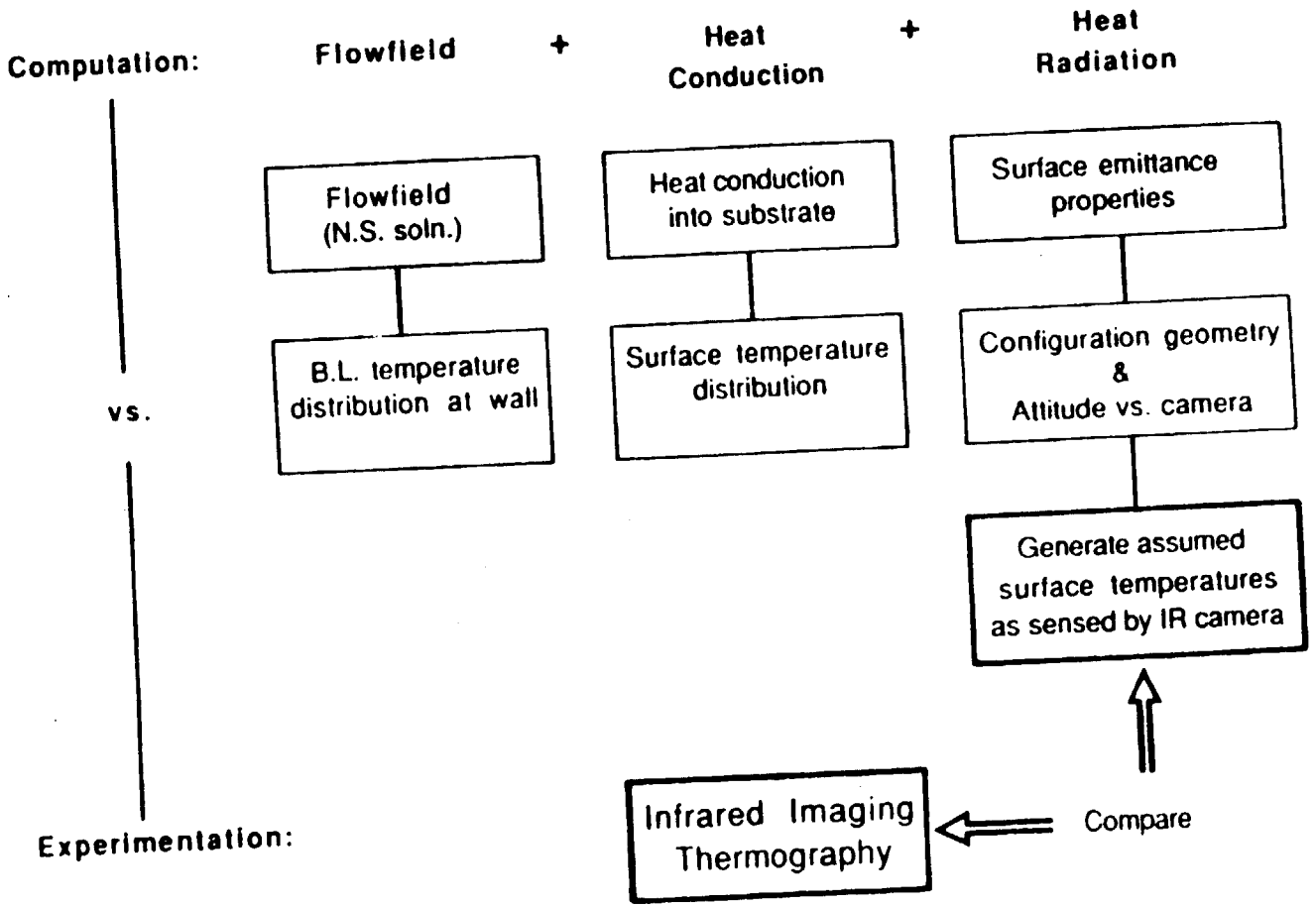

Fig. 5.8 Proposed method for infrared imaging evaluation of aerodynamic calculations

Chapter 6

BOUNDARY LAYER REGIMES ON A NACA 0012 AIRFOIL

The next step after the flat plate laminar boundary layer experiment was to expand the investigation to a two-dimensional NACA 0012 airfoil at various angles of attack from zero up to a post separation angle. Such an experiment offered the opportunity to validate the applicability of infrared imaging systems to aerodynamic research on a real aerodynamic geometry, and to provide some new information, for boundary layer flows extending all the way from fully attached laminar regime through transition to turbulence, and up to separation. Furthermore, the extension of this method to three-dimensional geometries and higher Reynolds numbers flows can be easily implemented following the success of these experiments.

6.1 The Experiment Viewed in Perspective

The detection of boundary layer transition from laminar to turbulent regime or its separation from the surface of interest, is one of the most challenging subjects in aerodynamics. Almost any available experimental technique is used for this kind of studies: smoke visualization, laser Doppler velocimeters, tufts, chemical sublimation (acenaphtene), oil flow, hot films and hot wires, phase change paints, liquid crystal paints, pressure measurements, optical techniques etc. With all these methods, the subject is far from being closed and the search for more rewarding techniques is still going on. As was already pointed out in the literature survey, infrared imaging systems have already been successfully used in the recent past to detect transition both in flight and in wind-tunnel testing. However, detection of separation with IR imaging systems is still an open subject because the heat transfer behavior itself in separated flows still resists

accurate prediction. Also, no validation of the IR imaging system findings was done in the very same experiments by any independent means. Therefore, trying to detect both the transition and the separation in the same experiment can enhance the usefulness of infrared imaging systems for aerodynamic research.

6.2 The Experimental Set-Up

As shown in Fig. 6.1, the experimental system consisted of a NACA 0012 airfoil mounted vertically at one end of a rotating arm, at the other end of which was mounted the infrared imaging camera. The set-up was installed in a 0.9x1.2 m (3'x4') low speed, closed circuit wind tunnel. As the arm rotated around its center, the airfoil changed its angle of attack, but the camera remained in a fixed, perpendicular position relative to the airfoil chord. The angle of attack α, could be fixed within ±0.5 degree of the desired value. The airfoil had a chord of 0.3048 m (one foot), an aspect ratio of 1.5 and it was clamped between two end plates measuring 35.5 x 7.62 cm (14"x3") in order to reduce the three-dimensional flow effects of the tips. At zero angle of attack the airfoil was at a distance of about 10 cm from the wind-tunnel side wall, and the camera was similarly spaced near the opposite wall. While this arrangement did affect the airflow around the airfoil (by blockage and by wall proximity), the basic objective of the experiment, to detect the foot-prints of the boundary layer behavior with the IR imaging camera, was not hampered. The observations are reported as they were made i.e., with no corrections to account for the wall proximity. In order to eliminate any possible spurious reflections from the airfoil to the camera, a 0.152 mm thick black matte paper was bonded to its surface with double-sided Scotch® tape wrapped chordwise around the airfoil with a 3 cm pitch. Figure 6.2 displays the following features of the airfoil:

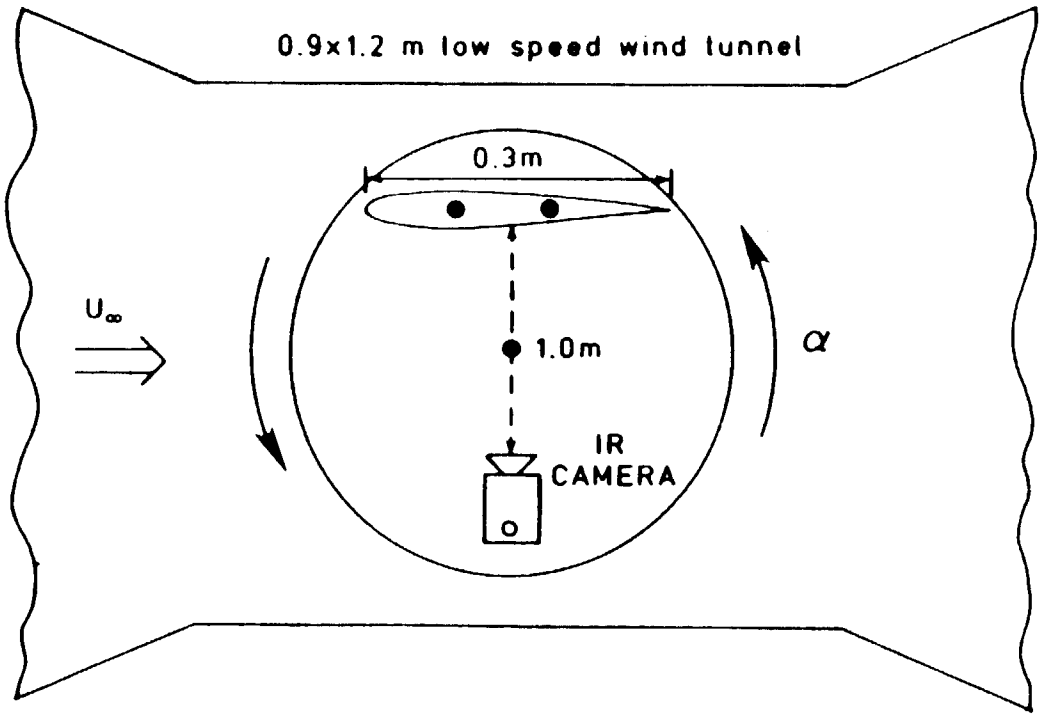

Fig. 6.1 Schematic top-view of the IR camera-airfoil mounting on a turntable used for wind tunnel flow separation studies

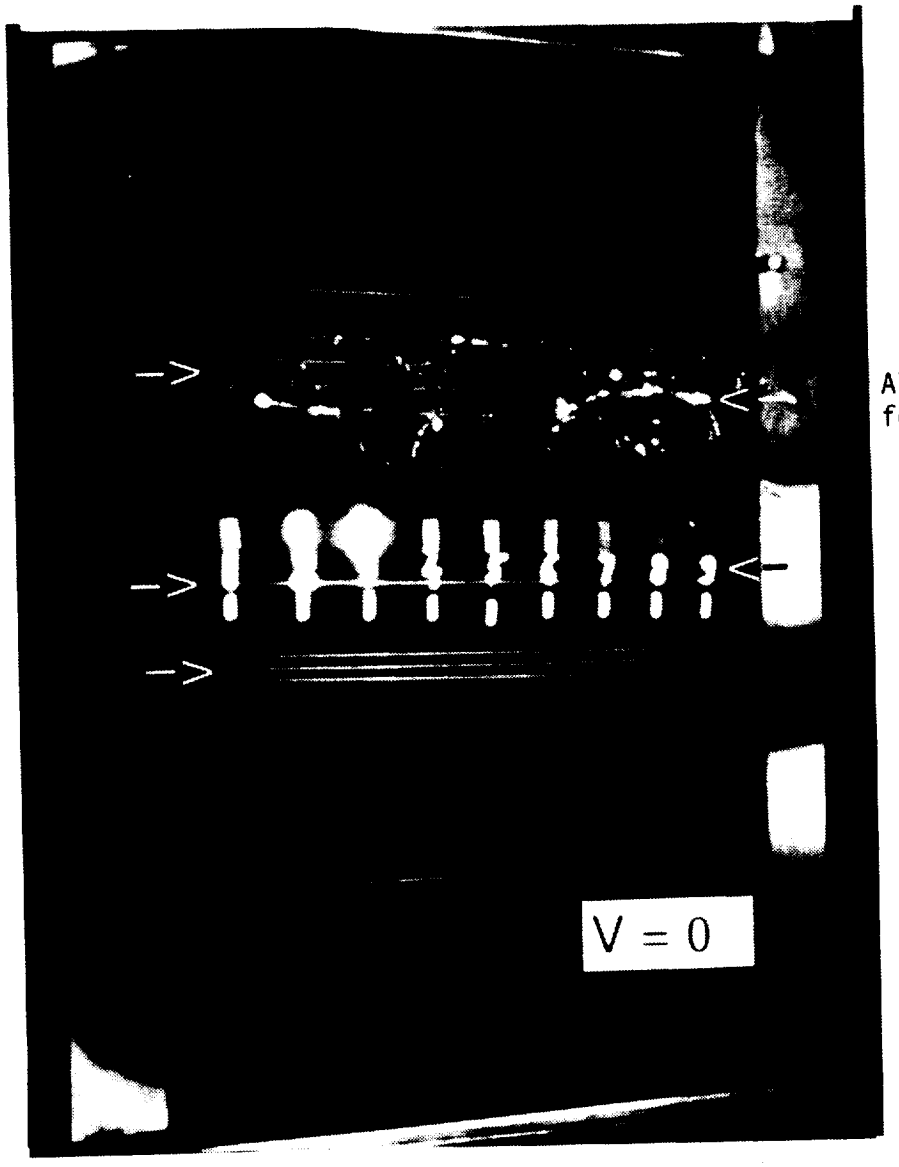

Fig. 6.2 NACA 0012 airfoil with aluminum foil tufts in still air.

(1) Decimal subdivision of the upper surface arc length (further referred to as "s") was provided, where the lower and the upper divisions were marked respectively with highly reflective silver paint and ultrafine gold leaf to be visible on the IR imaging system display. A posteriori, it can be concluded (see Fig. 6.4) that both the silver paint and the gold leaf markings performed equally well, and since the silver paint is easier to apply it may be considered as the preferable choice.

(2) Above the arc subdivisions, four rows of aluminum foil tufts 0.0254mm thick and 2mm wide, observable both visually and with the infrared imaging system, were threaded through the paper in increments of one-tenth of the surface arc length (0.1s).

(3) The surface was locally warmed by passing an electric current through a 0.127mm (0.005") Constantan wire that had been wrapped chordwise around the airfoil underneath the black paper, at the following locations:

   (a) directly under the arc markings and under the tufts - to enhance their observability with the IR imaging camera by providing a "low temperature/low emittance" target against a "high temperature/high emittance background.

   (b) below the arc markings - to allow tracking the boundary layer development through chordwise temperature measurements on a smooth, uncontaminated airfoil surface. The idea to use this layout was suggested by the encouraging results obtained earlier with this method in observing the footprints of the development of a laminar boundary layer over a flat plate (Gartenberg et al., 1988).

The mean heating flux was approximately 500 W/m^2, with no noticeable effect on the boundary layer based on the localized and smooth behavior of the chordwise surface temperature under the arc markings (item (a) above). The span-wise coordinates of these heating wires can be seen on Fig. 6.2, marked by pencil on the black paper just below the arc markings. The uppermost and lowest lines demark the field of view of the camera.

6.3 The Experiment Description

The airfoil angle of attack was varied between 0° and 16°. Photographs of the airfoil surface were taken under steady state conditions with a 35 mm single lens reflex (SLR) camera, and of the IR imaging system display unit (oscilloscope face) using a Polaroid camera. In a separate series of experiments, the airfoil angle of attack was varied between 0° and 16° in increments of 2° at 2 seconds intervals, and the thermographies were recorded on 5 1/4" diskettes by the system's dedicated microcomputer.

The rationale behind the above steps was to validate by visual observations the tufts patterns taken with the IR imaging system, and to validate the temperature analysis performed on the microcomputer against observations of the airfoil surface and the tufts made with the IR imaging system display unit. In this way, future investigations can rely entirely on observations performed with the IR imaging system. While it is true that the tufts themselves induce an early transition, their contribution to the detection of separation is self evident. Furthermore, transition induced by the tufts can be clearly seen on the IR imaging display.

The wind tunnel experiments were carried out at a nominal Reynolds number (Re_c) of 375,000, based on the airfoil chord. As the wind tunnel air heats up during operation, two opposite thermal effects take place concurrently on the

airfoil surface: convective cooling of the electrically heated surfaces and convective heating of the cooler surfaces due to the heating of the free stream wind-tunnel air above ambient conditions. The lateral conduction of heat was negligible, as it could be traced back on the thermographies.

The heating-up of the wind-tunnel during its operation had a negative effect on the quantative interpretation of the computerized thermographies. In principle, the aim of this experiments is to look for surface temperature differences caused by changes in boundary layer regime. Qualitatively, the change should be from lower surface temperatures under the laminar regime to higher temperatures under the turbulent (see next section). However, at the same time there is an additional heating effect due to the heating of the freestream air in the wind tunnel. Thus, extracting temperature differences from thermographies taken at different angles of attack, loses its meaningfulness due to the lack of a common freestream temperature. In other words, as the angle of attack of the airfoil is increased, there is an increase in surface temperatures due to changes in the boundary layer regime, and at the same time an additional change due to the air heat-up. Therefore, a posteriori, it can be remarked that the computerized thermographies could not be meaningfully interpreted and their use was discarded. At the same time, it is emphasized that the concept of analyzing transition and separation data through substraction of thermographies is sound and can work if the experiments are carried out in a thermally stable wind-tunnel. Also, this argument has nothing to do with regard to the determination of the transition line from the thermographies. On the contrary, the heating-up of the air only enhances the demarcation line of the transition.

6.4 Results and Discussion

The results reported herein are based on the observations made over 20 different experiments. Figure 6.3 shows a sequence of the airfoil photographs taken of the airfoil surface with a 35 mm SLR camera, for angles of attack varying between zero to 13 degrees. These pictures partially document the tufts behavior as they could be observed visually. The word "partially" is used here because continuous visual observation of the tufts offers more information than still photographs, especially with regard to the unsteady behavior of the flow. Figure 6.4 shows a similar sequence of pictures, this time as observed on the infrared imaging system display. These thermographies were taken with the display unit set to the inverted mode which produces darker shades for higher temperatures. This choice was dictated by the fact that the tufts status can be better seen in the inverted mode than in the normal mode. Thus, in Fig. 6.4, the darker shades represent higher apparent temperatures than the lighter shades. The pictures were taken with a Polaroid® camera and later reproduced with a 35mm SLR camera. These pictures prove that the tufts behavior is simultaneously observable visually and with the IR imaging camera, and therefore it is sufficient for future experiments to rely solely upon one set of photographies only, namely those taken from the IR imaging system display.

Before going into the analysis of the main results, the facts on which the transition detection by thermography is based will be briefly reviewed. According to the Reynolds analogy

$$St = \frac{c_f}{2} \quad \text{or} \quad \frac{Nu}{Re\ Pr} = \frac{c_f}{2} \tag{6.1}$$

and under the assumption Pr = 1

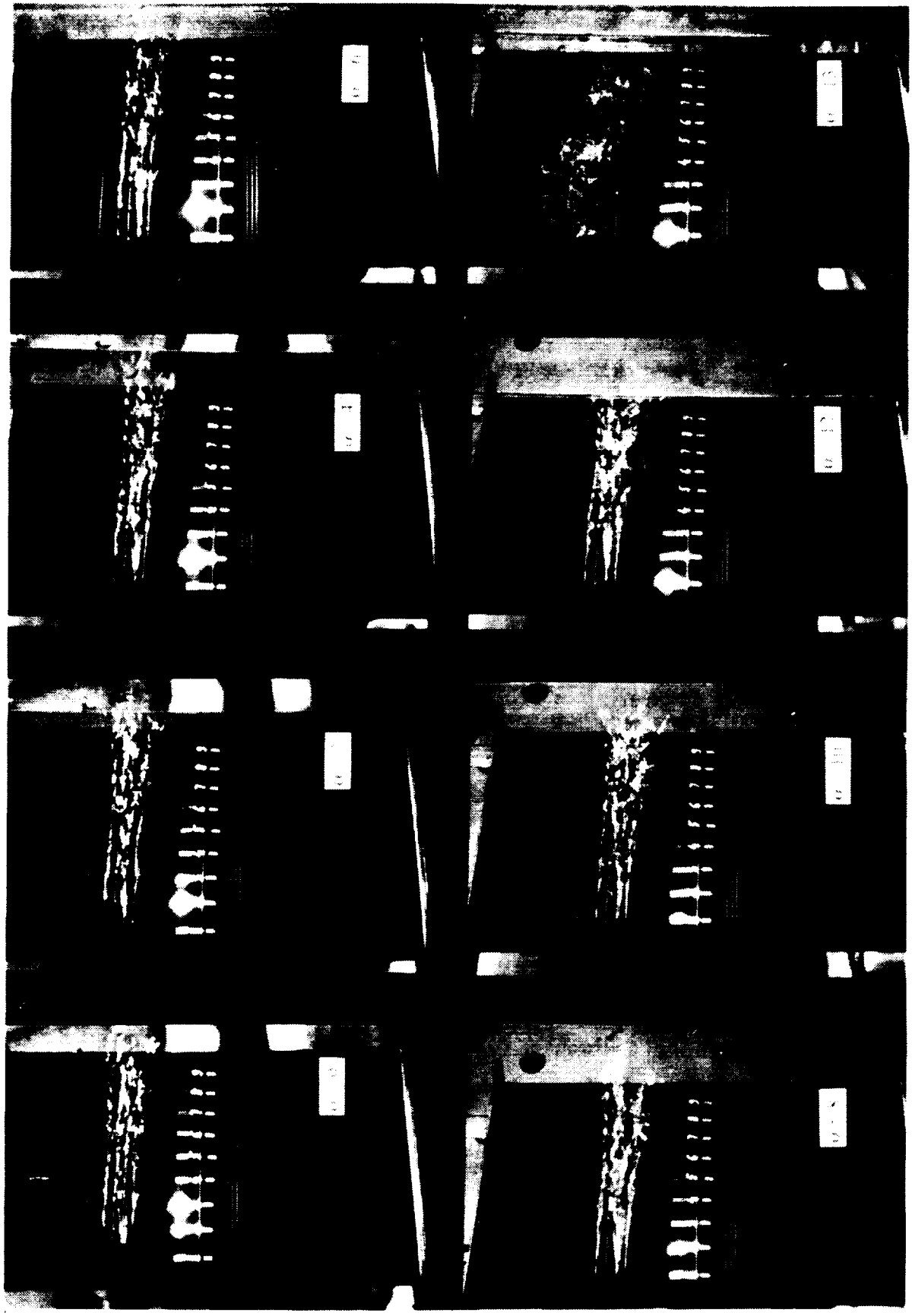

Fig. 6.3 NACA0012 airfoil with aluminum tufts at various angles of attack in wall proximity. Re_c = 375000. 35mm SLR camera photos. Air flows from left to right.

Fig. 6.4 NACA0012 airfoil with aluminum tufts at various angles of attack in wall proximity. Re_c = 375000. Photographs of the infrared imaging display in inverted mode. Air flows from left to right.

$$h = \frac{1}{2} c_f \cdot \frac{U \cdot k_a}{\nu_a} \qquad (6.2)$$

where h is the local heat transfer coefficient c_f is the local skin friction coefficient, U is the freestream velocity, ν_a is the air kinematic viscosity and k_a is its conductivity. According to Eq. (6.2), the local heat transfer coefficient is directly proportional to the local skin friction coefficient. Since during transition from laminar to turbulent regime, the skin friction coefficient jumps approximately by an order of magnitude, by Reynolds analogy the heat transfer coefficient also jumps by an order of magnitude. Thus, a clear "jump" in the wall temperature should be seen on the thermography as transition is induced. The temperature jump was shown to mark the transition region by prior workers (Bouchardy et al.; 1983, Quast, 1987), and can clearly be seen in Fig. 6.4, for example at $\alpha = 4°$ at the 0.35s location, on the arc markings.

The main experimental results are discussed after giving a brief description of what is believed to happen on the NACA 0012 airfoil at relevant Reynolds numbers (375,000), as the angle of attack is increased from zero up to separation. This account is based on the visual tufts observation in these experiments as well as on the accounts of Carr et al. (1977, p. 3), McCullough and Gault (1975), and Thwaites (1987) pp. 200-205. At zero angle of attack, the flow is usually laminar over most of the airfoil. As the flow approaches the trailing edge, the laminar boundary layer separates with subsequent transition to turbulent flow. The expansion of the turbulent motion causes reattachment of the boundary layer as a turbulent one which remains attached up to the trailing edge. This localized region of laminar separated flow is called the laminar separation bubble. The air motion inside this bubble is circulatory with typical velocities of one order of magnitude lower than that

of the free stream velocity (Brendel and Mueller, 1988). The length of the bubble is a few percent of the chord. As the angle of attack is increased, the bubble and the transition region above it move upstream, thus increasing the airfoil area subjected to turbulent flow. At a certain point, the turbulent boundary layer fails to negotiate the adverse pressure gradients and part of the turbulent boundary layer separates, usualy near the trailing edge. This phenomenon is known as turbulent separation. As the angle of attack is further increased, the bubble moves upstream as does the point of turbulent separation, thus causing the gradient of the lift curve versus the angle of attack to decrease. As the bubble reaches the leading edge, and the angle of attack is still increased, the separation point of the turbulent boundary layer continuously moves upstream, the bubble remaining relatively small and attached close to the leading edge. At a certain angle of attack (stall angle), the adverse pressure gradient can reach values where reattachement of the turbulent boundary layer is no longer possible. This causes the bubble to burst over the entire surface of the airfoil from the leading to the trailing edge, causing what is known as "leading-edge bubble-bursting stall."

The main findings of the experiments (visual and IR imaging observations) are summarized below, followed by a discussion of some interesting points worthy of elaboration:

$\alpha = 0$ Laminar flow up to 0.8s on the clean surface,
Tufts induced transition at 0.6s

$\alpha = 2°$ Transition at 0.7s on the clean airfoil (lower part),
Tufts induced transition at 0.5s,
High amplitude tufts fluttering after 0.7s

$\alpha = 4°$ Transition at 0.5s on the clean airfoil,
Tufts induced transition at 0.3s,
Higher amplitude tufts fluttering after 0.7s

$\alpha = 6°$ Transition at 0.2s on the clean airfoil,
Tufts induced transition at 0.2s,
Turbulent separation seen on tufts at 0.8s

$\alpha = 8°$ Transition at 0.1s on all the airfoil,
Turbulent separation at 0.7s

$\alpha = 10°$ Fully developed turbulent flow all over the airfoil,
Turbulent separation at 0.6s

$\alpha = 12°$ Turbulent separation at 0.3s with flow buffeting,
"Steady" separation at 0.5s

$\alpha = 13°$ Bubble burst; complete separation.

A first observation relates to the fact that the region of flow reversal due to separation could be very well seen in the tufts motion. Similarly, fully developed turbulent boundary layer flow could be identified in the tufts motion as a considerable increase in the flutter amplitude. As indicated by the tufts behavior, the turbulent boundary layer separation point was not stable with respect to time. Just after the separation had first been observed, oscillations of the separation line back and forth over at least one-tenth of the surface could be observed. Just prior to separation, these oscillations grew in amplitude up to one quarter of the surface.

A second observation refers to the detection of the laminar separation bubble. In Fig. 6.4, this bubble can clearly be seen on the $\alpha = 6°$ thermography at 0.15s as a lighter shade curved strip. Since at the separation point the first derivative of the velocity, $\partial u/\partial y$, is zero, so is the local

skin friction coefficient c_f, and also the heat transfer coefficient h. Therefore, the bubble appears as an area of lower temperatures due to the lower local convective heating on a cool surface. However, its observability depends on a very fine tuning of the "thermal level" knob of the display unit, which may be detrimental to the capture of other features, and may raise questions with regard to the reproducibility under any arbitrary conditions. Incidentally, the extent of the bubble for $\alpha = 6°$ can clearly be seen in this case to be about 10% of the upper surface.

A third observation relates to the fact that for steady state conditions such as those under which the photographs in Fig. 6.4 were taken, no substrate heating was necessary for enhanced observability. It seems that the heating of the wind tunnel, which in this case was 1.2K/minute was more than enough to get a sharp image on the system's display. Also, the substrate chordwise heating can be seen to have a well defined and localized effect (see Fig. 6.4).

A fourth observation relates to the stall angle of attack. For the present test Reynolds number, stall at 13° is somewhat premature. Hansman and Craig (1987) for example report a stall angle of 14° for the NACA 0012 at a Reynolds number of 310,000. This premature stall could be expected considering the fact that the airfoil was placed near to and spanwise parallel to the wind tunnel wall. This assembly geometry caused the airfoil to operate "in ground effect" which has a net effect of increasing the actual angle of attack (Rae and Pope, 1984, p. 418). In order to check the correctness of this assumption, the airfoil was temporarily moved close to the center of the wind-tunnel. A few runs at the same Reynolds number showed repetitively that in this position the airfoil did indeed stall at 14 degrees.

A closer look at Fig. 6.4 provides more detailed insight and helps correlate the observations with the flowfield features. For this purpose, the clean, undisturbed surface of the airfoil in the lower half of each thermography is noted.

The thermographies for α = 0, 2 and 4 degrees clearly show two heated zones. The first, starting at the leading edge is the effect of the convective heating under the laminar boundary layer regime. The second, along the trailing edge and exhibiting a curved boundary shape is due to the effect of convective heating under the turbulent boundary layer regime. Just upstream of that curved boundary shape is the region where the transition from the laminar to turbulent regime takes place. As the angle of attack is increased from zero to two and from two to four degrees, the transition region advances upstream as expected. The next four thermographies from $\alpha = 6°$ to $\alpha = 12°$ display the flow regime where trailing edge turbulent separation is encountered. The main vortex resulting from the separation is located in that area, and since the turbulent mixing there is quite vigorous, the net effect is that heat is convected from the freesteam to the airfoil surface. In order to get a visual impression about the intensity of the turbulent mixing, the reader can consult Schlichting (1968, p. 36) where a visualization of a separated flow about an airfoil is reproduced from Prandtl-Tietjens. The value of the heat transfer coefficient in that area of separated flow is difficult to determine. However, measurements made by Schmidt and Wenner (see Schlichting, 1968, p. 298) on cylinders in the supercritical range (Re = 426,000) show a sixfold increase in the Nusselt number in the wake region immediately following the separation point, relative to the value immediately preceeding the separation point itself. This fact explains at least qualitatively why there is a net heating effect in the region affected by the

trailing edge turbulent separated flow. The thermographies taken at $\alpha = 6°$ and $\alpha = 8°$ show the separation bubble moving upstream, and remaining small as long as the flow remains attached on the forward part of the airfoil (Carr et al., 1977). As the angle of attack is further increased to $\alpha = 10°$ and $\alpha = 12°$, the stagnation point moves downward around the leading edge and followed by the bubble, thus getting out of the field of view of the IR imaging camera. As the angle of attack is increased to $\alpha = 13°$, the stall angle is reached. However, the separation process is not immediate. It was observed on the tufts motion that at this angle of attack, the flow was extremely unsteady, the points of turbulent separation violently moving back and forth stream-wise before the flow separated itself completely from the airfoil. The dynamics of the separation appeared as if the separated flow tried to penetrate into the attached flow region and "peel it off" from the surface. The separation occurred usually spontaneously, without any change in the airfoil condition, after a very few seconds from the moment the airfoil reached $\alpha = 13°$. The hystersis effect of the reattachment was also clearly seen, although no singular value for the reattachement angle could be fixed. It varied between 11 to 12 degrees. The reattachment itself was also preceded by extremely unsteady flow and strong buffeting. Usually, it could take the flow three to four failed attempts until it managed to reattach. These findings are documented in Fig. 6.5. Based on the tufts observation, it can be said only that the air motion in the separated flow regimes is that it was chaotically unsteady.

The experimental results have been compared with predictions of the Eppler code (Eppler and Sommers, 1980). This computer program is accepted today as a good code with regard to inviscid and viscous flow calculations about airfoils. The code was run at a Reynolds number of 400,000. There is

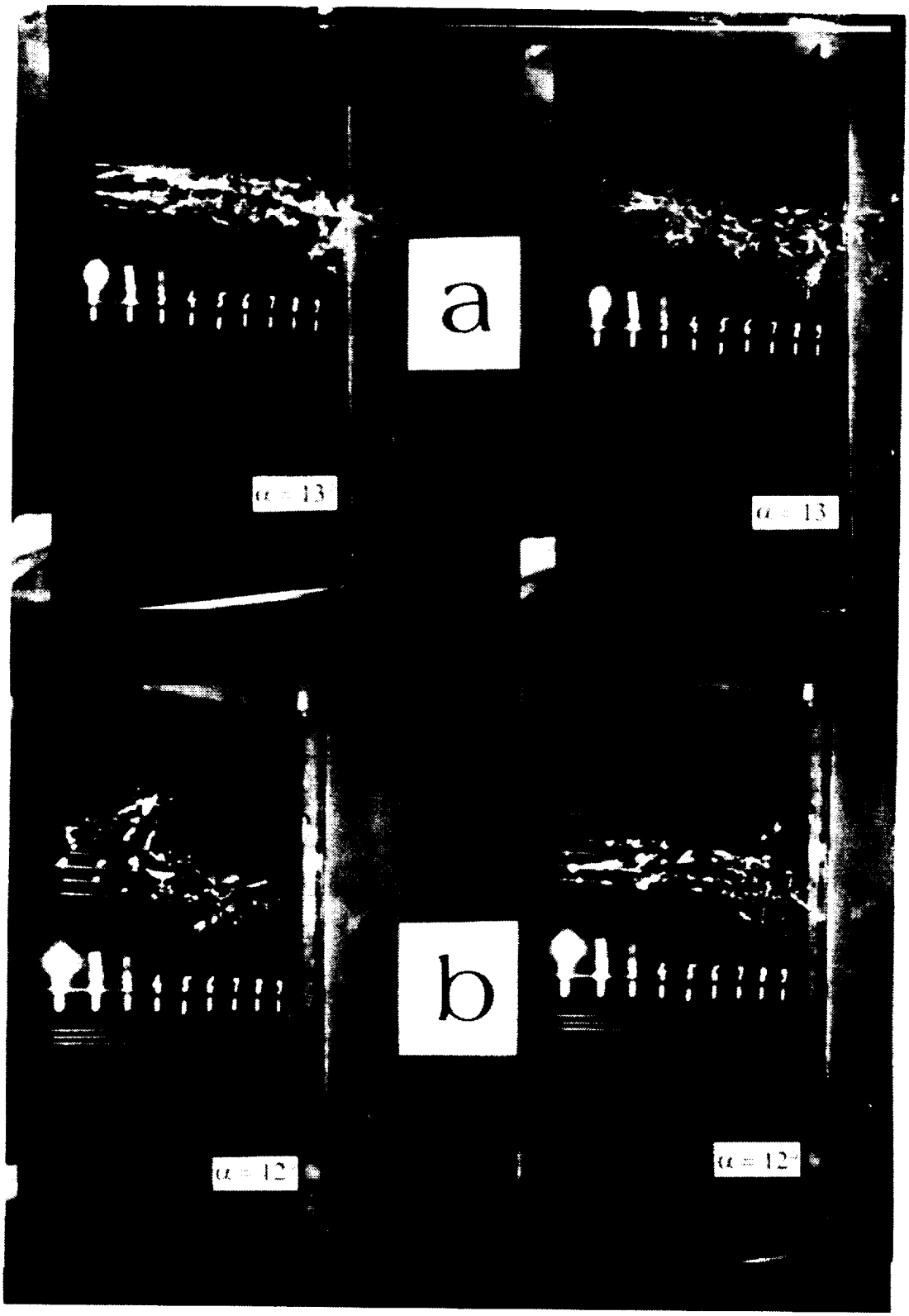

Fig. 6.5 NACA0012 airfoil (a) at separation (b) at reattachement incidence. Photographs for each set taken five seconds apart under identical conditions.

good agreement between the code prediction and the experimental results regarding the stall angle. The code predicts it at 14 degrees, while this experiment showed it to be 13 degrees near the wall and 14 degrees in the middle of the test section. At angles of attack below the stall, the code consistently underpredicted the extent of the turbulent separation as well as its onset. The experiment detected the separation onset at six degrees (say seven degrees to account for the wall proximity) while the code predicted it at ten degrees angle of attack. The degree of agreement between the experimental results and the code prediction regarding the extent to which the airfoil surface is affected by the turbulent flow varies with the angle of attack. Up to four degrees, the code underpredicted the extent of turbulent flow approximately by a factor of two (for partial support of this claim see Ladson 1988, p. 90, Fig. 30(a)). For six and eight degrees, the agreement starts to be very good (20% to 10% deviations) and from ten degrees and up the agreement is excellent. These results are summarized in Table 6.1.

This chapter will be concluded with a final remark concerning the interpretation of the thermographies. Looking at Fig. 6.4, one can observe that the temperature information contained in each individual thermography is not enough in order to allow a meaningful interpretation in itself. For example, the thermography taken at 10 degrees angle of attack can be ambiguously interpreted as indicating laminar flow with transition to turbulent flow at 0.75s, the actual case being transition to turbulent flow near the leading edge and separation at 0.75s (The tufts indicating the separation at 0.65s). However, a sequence of thermographies, covering the whole range of angles of attack, from zero up to separation, do provide enough data in order to evaluate the development of the boundary layer regime, from almost entirely laminar, through partially laminar, turbulent and separated and up to fully separated flow.

Table 6.1 Transition and separation studies over a NACA 0012 airfoil at different angles of attack: experiment vs. Eppler code (Re_c = 400,000)

α	s_{turb}[1] thermography	s_{turb} Eppler	$s_{separated}$[1] tufts	$s_{separated}$ Eppler
0°	0.2	0.4	0.0	0.0
2°	0.3	0.6	0.0	0.0
4°	0.5	0.8	0.0	0.0
6°	0.8	1.0	0.2	0.0
8°	0.9	1.0	0.3	0.0
10°	1.0	1.0	0.4	0.1
12°	1.0	1.0	0.7	0.5
14°	1.0	1.0	1.0	0.9

[1]In wall proximity.

6.5 Summary

The separation studies performed on the NACA 0012 airfoil showed that aluminium foil tufts can be observed with infrared imaging systems. This fact opens the possibility to use the infrared imaging system as a flow visualization and surface temperature measurement device at the same time. In agreement with other researchers, the laminar separation bubble and the transition were shown to be observable with the IR imaging system. A rather intense and localized heat transfer process is seen to exist on the upper airfoil surface under the turbulent separated regime. Both the flow separation and the reattachment were observed to be time-dependent phenomena. Regarding the complete separation dynamics, the observation of the tufts behavior indicated a "peeling off" effort of the separated flow region on that part of the boundary layer that is still attached.

Chapter 7

CLOSURE

7.1 Review of the Main Results

The essence of the heated wire technique is to place a very thin and very long electrically heated wire in an airflow, the measurement of the temperature distribution along the wire with the IR imaging camera being a direct indication of the flow speed behavior. Furthermore, since the heat conduction and radiation are negligible compared to the convection, Nusselt number correlations can be used to calculate that airflow velocity component that is perpendicular to the wire. This experimental method may be considered as non-intrusive since the wire end supports, and the IR imaging camera, can be placed out of the flowfield. More importantly, the wire itself is very long, very thin and slightly heated, and therefore it doesn't really disturb the flowfield significantly. This method is not to be confused with the hot wire technique, where the support itself is immersed in the flow at the point of interest.

The heated wire technique was evaluated using as a target flow a laminar flow circular jet. This type of flow produced large temperature gradients along the wire, up to 2200K/m. Starting at a temperature gradient of about 350K/m, it was observed that the IR imaging camera has difficulties in producing accurate temperature results. Furthermore, the measurement error grew nonlinearly with the temperature gradient. It was determined that this phenomenon is associated with the very nature of this IR imaging camera and probably has to do with its minimum resolvable temperature difference performance (Ohman). The roots of this behavior could be tracked through the field of view and instantaneous field of view to the size and the

characteristics of the camera detector element itself. However, this actual measurement error is always on the negative side of the output, i.e., the readings are always less than the true temperature. Since the measurement error is well behaving with respect to the temperature gradient, it is possible to produce a calibration curve of the error versus the temperature gradients. Therefore, at least to a first order, the experimental data can be corrected to get a temperature distribution that is closer to the reality. This process can be repeated by trial and error, until the final corrected temperature distribution produces such a temperature gradient distribution that when substracting the errors, corresponding to the adjusted temperature values, the original experimental distribution is recovered.

The inverse approach of using the temperature readings and Nusselt number correlations to deduce the velocity distribution of the jet was shown to work in principle. With regard to this approach, it was shown how important it is to work with accurate data, because of the great sensitivity of the velocity function to the temperature values. Unfortunately, error sources include not only the IR imaging system, but also the heat transfer correlations themselves. As it was found out from the literature survey, this subject is far from being completely understood and therefore this problem should be looked upon from the broader aspect of the convective heat transfer discipline. The heated wire concept was also shown to work for more general flowfields e.g., cylinder wakes in wind-tunnel experiments, with very promising results.

Infrared imaging thermography has been previously used to determine convective heat transfer rates without paying attention to the development of boundary layer flow. This work has shown that it is possible to track the thermal boundary layer development over a surface by measuring the surface

temperature distribution with the IR imaging system. The method was proved on a flat plate at zero angle of attack, slightly heated chordwise at a constant power rate. In analyzing the experimental results, it is important in this case to account for all of the three modes of heat transfer: convection, conduction and radiation. Also, it is important to remember that due to the development of the thermal boundary layer over the surface of interest, the balance between the relative contributions of the three may change. In general, the surface temperature distribution was shown to be time dependent even for steady state flows, due to the evolving nature of the substrate thermal coupling with boundary layer heat exchange. Therefore, a single thermography may not be enough in order to extract quantitative data about the flowfield, i.e., a time sequence is required. This method was also applied to the mapping of surface temperatures downstream a rearward facing step with very good results. The temperature profile correctly showed the lowest heat transfer rate to occur just after the step and the highest rate at the location of the turbulent boundary layer reattachment. Thereafter, the influence of the redevelopment of the turbulent boundary layer could be observed too.

These experiments suggest that the infrared imaging system may serve as an experimental tool for validation of CFD codes since the predicted temperature distribution may be corrected for the directional emittance effects of the radiation. As a result, the calculated surface temperature distribution as assumed to be produced by the IR imaging camera may be directly compared with the results of an actual thermography resulting from an experiment run under identical conditions. Generally, it is easier to run first the experiment and then to run the codes, since a precise tuning of the experimental condition may be sometimes an impossible task.

The concept of detecting low speed boundary layer transition over airfoils using IR imaging systems is about five years old. The present research extended the range of application to turbulent separation and laminar complete separation as well. It was shown to be possible to detect the various boundary layer regimes, i.e., laminar, transition bubble, turbulent and separated flow, all on one thermography imaging a NACA 0012 airfoil at 6 degrees angle of attack in ground effect at a chord Reynolds number of 375000. The development of tufts that can be observed both visually and with the IR imaging camera greatly enhances the capability of this tool in aerodynamic research, because the method may serve simultaneously in the temperature measurment and the visualization roles. Based on the observation of the tufts behavior, it was seen that the flow separation and reattachment are phenomena that develop in time. The flow prior to both of them is highly unstable and unsteady, a phenomenon commonly known as buffeting. With regard to the mechanism of the total flow separation, also known as leading edge laminar bubble burst, it was observed that there is a pulsating behavior of the turbulent separated boundary layer flow back and forth chordwise, that tries to "peel-off" the remaining portion of the attached flow from the airfoil surface.

Finally, the reader is reminded that the infrared imaging camera is basically a device sensitive to the number of photons originating from the instantaneous field of view which reach the detector. It is through this mechanism that the IR imaging camera output is sensitive to the surface temperature. Therefore, in extracting quantitative data from the thermographies it is important to remember the factors that may influence the readings, namely emittance values and reflections, directional emittance effects, depth of field and proper focusing etc.

7.2 Recommendations for Future Work

Since most of the work performed during this program was new in its nature, it is felt that each one of the various experiments reported herein should be revisited, concentrating on one at a time, stressing the depth rather than the span of the research.

The heated wire technique can be applied to virtually any kind of subsonic flow of interest. Boundary layers (laminar or turbulent), confined flows, free shear layers, wakes, jets etc. can be studied using this method. Of course, the first item to consider is the temperature gradient induced error. The precise behavior of this function is required before starting any new experiment. It should also be remembered that each calibration is valid only for the specific conditions under which it was performed. One question to be answered is whether there is a possibility to produce one universal curve that will show the measurement error as a function of the temperature change per instantaneous field of view rather than per unit length at the target. For a resolved target, this task may be easy to accomplish, and with some effort it may be possible even to determine a correction factor that will account for various degrees of unresolved targets. One method to check this possibility is to map the same target with various IR imaging camera objectives, thus changing both the field of view and its ratio to the instantaneous field of view. Referring to the heated wire experiments, it may be useful to know that the infrared imaging camera may be transformed to a one-dimensional scanning device by stopping the rotation of one of its scanning prisms. By stopping the horizontal prism for example, it is possible to get a scanning rate of 2500 Hz of a certain line, and this raises the possibility of making frequency response experiments using the heated wire technique.

One of the more serious problems with the inverse approach of deducing flow velocities from temperature measurements is that the heat transfer rate is greatly influenced by the free stream turbulence level (Schlichting, 1968, p. 299). Thus, it is possible to use a Nusselt number correlation based on the wire diameter and deduce results based on the assumption that the flow is laminar, while in reality the flow is turbulent and behaving differently with respect to the heat transfer mode. One of the problems with the laminar flow jet experiment was that at a diameter based pipe Reynolds number of about 1000, the flow starts its transition to turbulence, but fully accomplishes it only at a Reynolds number of about 3000 (Blevin, 1984, p. 231). Therefore, a change in the flow velocity, could produce different results not only because the velocity was changed, but also because the level of the turbulence was changed.

In general, it is felt that this method is very suitable for heat transfer research, such as the influence of the freestream turbulence level, or to study the process at low Reynolds or Grashof numbers.

With regard to using surface thermography for boundary layer research, it is very important to have agreement between the expected surface thermal response and the phenomenon investigated. A variety of possibilities are available including thin skin or solid models, that can be either cooled or heated prior to, or during the whole duration of the experiment in order to follow the development of the thermal boundary layer.

The boundary layer regime detection experiments should really concentrate on the separation signature. The infrared "visible" tufts method should be qualified also on flight tests, although some trouble can be expected in the air because the tufts will be unresolved by the camera. This fact, combined

with their low emittance may cause the tufts to become "invisible" to the IR imaging camera during flight tests. Regarding the flight tests, it should be emphasized that the ultimate goal in developing this experimental tool is that by scanning an airplane wing in flight, the test engineer will be able to determine the nature of boundary layer behavior at a specific station i.e., laminar, turbulent or separated.

7.3 Conclusions

The purpose of this study was to explore new applications in which infrared imaging systems could contribute to and enhance aerodynamic research. Two different experimental approaches have been studied: the heated wire technique and the surface thermography. The heated wire technique is a completely new approach to the study of flows with position dependent velocities such as jets, boundary layers, shear flows, wakes etc. A significant finding enabled the measurement error to be represented as a function of the temperature gradient, and provided a method of correction for the experimental results in order to get the actual temperature distribution. The use of surface thermography was extended to research on boundary layer flow detection spanning all the various flow regimes; laminar, transitional, turbulent and separated, and for the study of separated flows following a backward facing step. In order to confirm the thermographic results, a visualization method was developed using tufts detectable by the IR imaging camera, thus making this system a simultaneous, temperature measurement as well as a flow visualization tool.

REFERENCES

AGA Thermovision® 782 Operating Manual, 1984.

Anon, "Infrared Imaging System Will Record Flow Fields During Shuttle Reentry," Aviation Week and Space Technology, December 7, 1987, p. 65.

ASME: Fluid Meters, Their Theory and Application, ASME, 1971 (6th Edition).

Balageas, D. L. and Ory, D., "Improvements in the Determination of Convective Transfer From Infrared Thermography," La Recherche Aerospatiale, No. 1980-3, May-June 1980, pp. 73-79.

Blevins, R. D., Applied Fluid Dynamics Handbook, Van Nostrand, 1984.

Bouchardy, A-M., Durand, G. and Gauffre, G.," Processing of Infrared Thermal Images for Aerodynamic Research," Applications of Digital Image Processing, April 19-22, 1983, Geneva, Switzerland, SPIE, Vol. 397.

Boyland, D. E., Carver, D. B., Stallings, D. W. and Trimmer, L. L., "Measurement and Mapping of Aerodynamic Heating Using a Remote Infrared Scanning Camera in Continuous Flow Wind Tunnels," Proceedings of the AIAA 10th Aerodynamics Testing Conference, San Diego, California, April 19-21, 1978, pp. 213-231.

Brandon, J. M., Manuel, G. S. Wright, R. E. and Holmes, B. J., "In-flight Flow Visualization Using Infrared Imaging," AIAA 4th Flight Test Conference, May 18-20, 1988, San Diego, California, AIAA Paper No. 88-2111.

Brendel, M. and Mueller, T. J., "Boundary Layer Measurements on an Airfoil a Low Reynolds Numbers," AIAA Journal, Vol. 25, No. 7, July 1988, pp. 612-617.

Bynum, D. S., Hube, F. K., Key, C. M. and Dyer, P. M., "Measurement and Mapping of Aerodynamic Heating in VKF Tunnel B with Infrared Camera," AEDC TR-76-59, November 1976.

Carlomagno, G. M. and De Luca, L., "Heat Transfer Measurements by Means of Thermography," Proceedings of the 4th Flow Visualization Congress, Paris, August 1986, pp. 611-616.

Carr, L. W., McAlister, K. W. and McCroskey, W. J., "Analysis of the Development of Dynamic Stall Based on Oscillating Airfoil Experiments," NASA TN D-8382, January 1977.

Carter, L. D., "Supersonic Boundary-Layer Transition Detection Using Thermographic Phosphorescent Paint," M.S. Thesis, University of Tennessee, March 1975.

Champagne, F. H., Sleicher, C. A. and Wehrman, O. H., "Turbulence Measurements with Inclined Hot Wires," J. Fluid Mechanics (1967), Vol. 28, Part I, pp. 153-175.

Chocol, C. J., "Remote Infrared Imagery of Shuttle During Entry," Proceedings of the Joint Automatic Control Conference, Denver, Colorado, June 17-21, 1979, (AICE), pp. 251-255.

Compton, D. L., "Convective Heating Measurement by Means of an Infrared Camera," NASA TM X-2507, February 1972.

Compton, D. L., "Use of an Infrared-Imaging Camera to Obtain Convective Heating Distributions," AIAA Journal, Vol. 10, No. 8, 1972, pp. 1130-1132.

Eaton, J. K. and Johnston, J. P., A Review of Research on Subsonic Turbulent Flow Reattachment, AIAA Journal, Vol. 19, No. 9, Sept. 1981, pp. 1093-1100.

Eckert, E. R. G. and Drake, R. M., Jr., Analysis of Heat and Mass Transfer, McGraw-Hill, 1972 (Second Edition).

Eppler, R. and Sommers, D. M., "A Computer Program for the Design and Analysis of Low-Speed Airfoils," NASA TM 80210, August 1980; also see supplement to, NASA TM 81862, December 1980.

Fand, R. M., Morris, E. W. and Lou, M., "Natural Convection Heat Transfer from Horizontal Cylinders to Air, Water and Silicone Oils for Rayleigh Numbers Between $3x10^2$ and $2x10^7$," Int. J. Heat Mass Transfer, (1977) Vol. 20, pp. 1173-1184.

Flaig, J. W., "Infrared Flow Visualization for VTOL Applications," AIAA/NASA Ames V/STOL Conference, Palo Alto, California, June 6-8, 1977, pp. 314-321, AIAA Paper No. 77-618.

Gartenberg, E. and Roberts, A. S., Jr., "Phenomenological Aspects of Infrared Imaging in Aeronautical Research," AIAA/NASA/AFWAL Conference on Sensors and Measurements Techniques for Aeronautical Applications, September 7-9, 1988, Atlanta, Georgia, U.S.A, AIAA Paper No. 88-4674.

Gartenberg, E., Roberts, A. S., Jr. and McRee, G. J., "Aerodynamic Investigation by Infrared Imaging," Proceedings of the AIAA 6th Applied Aerodynamics Conference," June 6-8, 1988, Williamsburg, Virginia, AIAA-88-2523-CP.

Gartenberg, E. Roberts, A. S. Jr. and Selby, G. V., "Infrared Surface Imaging as a Flowfield Diagnostic Tool," Proceedings of the 12th International Congress on Instrumentation in Aerospace Simulation Facilities (ICIASF 87), June 22-25, 1987, Williamsburg, Virginia, pp. 393-349.

Green, M. J. Budnik, M. L. Young, L. and Chiasson, M. P., "Supporting Flight-Data Analysis for Space Shuttle Orbiter Experiments at NASA Ames Research Center," NASA TM 89395, April 1983.

Hansman, R. J., Jr. and Craig, A. P., "Low Reynolds Number Tests of NACA 64-210, NACA 0012 and Wortman FX67-K170 Airfoils in Rain," J. of Aircraft, Vol. 24, No. 8, August 1987, pp. 559-566.

Hender, D. R. and Okabe, C. M., "Expanded Uses of Infrared Scanning Data in Aerodynamic Heating Materials Tests," AIAA 18th, Thermophysics Conference, June 1-3, 1983, Montreal, Canada, AIAA Paper No. 83-1542.

Hsieh, C. K. and Ellingson, W. A., "A Quantitative Determination of Surface Temperatures Using an Infrared Camera," Modern Utilization of Infrared Technology III, SPIE Vol. 124 (1977) pp. 228-235.

Jones, R. A. and Hunt, J. L., "Use of Fusible Temperature Indicators for Obtaining Quantitative Aerodynamic Heat-Transfer Data," NASA TR R-230, February 1966.

Kays, W. M. and Crawford, M. E., Convective Heat and Mass Transfer, McGraw-Hill, 1980 (Second Edition).

Klein, J. and Tribus, M., "Forced Convection from Non-Isothermal Surfaces," University of Michigan Research Institute, August 1952, Project M 992-B.

Ladson, C. L., "Effects of Independent Variation of Mach and Reynolds Numbers on the Low-Speed Aerodynamic Characteristics of the NACA 0012 Airfoil Section," NASA Technical Memorandum 4078, October 1988.

Levinstein, H., "State of the Art of Infrared Detectors," Modern Utilization of Infrared Technology III, SPIE, Vol. 129, 1977, pp. 52-56.

Lloyd, J. M., Thermal Imaging Systems, Plenum Press, 1975.

Martinez, A., Dye, W. H., Vaughn, J. E., Hersey, D. W. and Lutz, G. R., "Results of Test OH69 Obtained in the AEDC VKF Hypersonic Tunnel B Using the Infrared Scanning Method to Obtain Heat Transfer Data on the 0.040 Scale Model 82-0 of the Space Shuttle Forebody," Vols. I and II, NASA CR-151410 and NASA CR-151411, July 1978.

McCullough, G. B. and Gault, D. E., "Examples of Three Representative Types of Airfoil-Section Stall at Low Speed," NACA TN 2502, September 1951.

Meroney, R. N., "Studying the Convective Heat Transfer from a Building Model with Infrared Camera Techniques," ASME Transactions 78-WA/HI-58.

Merzkirch, W., Page, R. H. and Fletcher, L.S., "A Survey of Heat Transfer in Compressible Separated and Reattached Flows," AIAA Journal, Vol. 26, No. 2, February 1988, pp. 144-150.

Mordoff, K., H., "German Researchers Seek to Improve Prediction of Laminar Flow Changes," Aviation Week and Space Technology, January 18, 1988, pp. 40-41.

Morgan, V. T., "The Overall Convective Heat Transfer from Smooth Circular Cylinders," Advances in Heat Transfer, Vol. 11, Academic Press, 1975.

Myrick, D. L. and Kantsios, A. G., "Incorporating Geometric and Radiative Effects into Infrared Scanning Computer Analysis," SPIE, Vol. 371, Thermosense V, 1982, pp. 211-215.

Myrick, D. L. and Throckmorton, D. A., "Comprehensive Analysis of Shuttle Orbiter Leeside Surface Infrared Imagery Obtained During Atmospheric Entry," International Conference on Thermal Infrared Sensing for Diagnostics and Control, Thermosense VII, SPIE, Vol. 581, Cambridge, Massachussets, September 12-20, 1985, pp. 116-121.

Nutt, K. W., "Space Shuttle Orbiter SILTS Pod Flow Angularity and Aerodynamic Heating Tests," AEDC TSR-79-V70, November 1979.

Ohman, C., "Measurement Versus Imaging in Thermography or What is Resolution," to be obtained from the author at AGEMA Infrared Systems AB, Development Department, Box 3, S-182 11 Danderyd, Sweden, or Eklund Infrared, 142 Sunset Avenue, Verona, NJ 07044.

Page, R. H., Ostowari, C. and Carbone, J. S., "Radial Jet Flow," Proceeding of the 4th Flow Visualization Congress, Paris, August 1986, pp. 513-521.

Quast, A., "Detection of Transition by Infrared Image Technique," Proceedings of the 12th International Congress on Instrumentation in Aerospace Simulation Facilities (ICIASF 87), Williamsburg, Virginia, June 22-25, 1987, pp. 125-139.

Sasaki, M., Takahara, K., Kumagai, T. and Hamano, M., "Film Cooling Effectiveness for Injection from Multirow Holes," Journal of Engineering for Power, January 1979, Vol. 101, pp. 101-108.

Schlichting, H., Boundary Layer Theory, McGraw-Hill, 1968.

Schmitt, R. L. and Chanetz, B., P., "Experimental Investigation of Three Dimensional Separation on an Ellipsoid-Cylinder Body at Incidence," AIAA 18th Fluid Dynamics and Plasmadynamics and Lasers Conference, July 16-18, 1985, Cincinnati, Ohio, AIAA-85-1686.

Seraudie, A., Blanchard, A. et. Dor, J. B., "Qualification d' Essais en Ambiance Cryogenique a la Soufflerie T2," 23eme Colloque d'Aerodynamique Appliquee, Modane, November 12-14, 1988. Association Aeronautique et Astronautique de France, Note Technique No. 86-07.

Sparrow, E. M. and Cess, R. D., Radiation Heat Transfer, Hemisphere (McGraw-Hill), 1978.

Spence, T. M., "Applications of Infrared Thermography in Convective Heat Transfer," M.S. Thesis, Naval Postgraduate School, Monterey, California, March 1986.

Stallings, D. W. and Carver, D. B., "Infrared and Phase-Change Paint Measurements of Heat Transfer on the Space Shuttle Orbiter," AEDC-TSR-78-V13, June 1978.

Stallings, D. W., Mathews, R. K. and Jenke, L. M., "Recent Developments in Aerothermodynamic Test Techniques at the AEDC von Karman Gas Dynamics Facility," International Congress on Instrumentation in Aerospace Facilities 8th (ICIASF79), Monterey, California, September 24-26, 1973, pp. 1-10.

Stallings, D. W. and Whetsel, R. G., "Use of Infrared Imagery in Continous Flow Wind Tunnels," Thermal Infrared Sensing Diagnostics (Thermosense V), Detroit, Michigan, October 25-27, 1982, SPIE, Vol. 371, pp. 203-210.

Swenson, B. L. and Edsinger, L. E., "Preliminary Analysis of Remote Infrared Imagery of Shuttle During Entry - An Aerothermodynamic Flight Experiment," NASA TM 73251, August 1977.

Thermosense V, (Proceedings of) SPIE, Vol. 371, 1982.

Thomann, H. and Frisk, B., "Measurement of Heat Transfer with an Infrared Camera," Int. J. Heat Mass Transfer, Vol. 11, Pergamon Press, 1968, pp. 819-826.

Throckmorton, D. A., "Heat Transfer Procedures in Phase B Shuttle Studies with Emphasis on Phase-Change Data Improvement," NASA TM X-2507, February 1972.

Throckmorton, D. A., Zoby, E. V. and Kantsios, A. G., "The Shuttle Infrared Leeside Temperature Sensing (SILTS) Experiment," AIAA 23rd Aerospace Sciences Meeting, January 14-17, 1985, Reno, Nevada, AIAA-85-0328.

Thwaites, B. (editor), Incompressible Aerodynamics, Dover, 1987.

APPENDICES

Appendix A

APPENDIX TO CHAPTER 4: THE LAMINAR FLOW JET EXPERIMENT

A1: Error Calculations

These calculations ignore the errors that may originate in the camera's difficulty to track high temperature gradients.

1. Wire temperature read-outs from Disco II.®

   (a) Due to uncertainty of the ambient temperature

   $\Delta T_a = 0.05^0C \quad \Delta T_w = 0.9^0C$

   (b) Due to emittance input accuracy (through the transmittance factor in Disco II). The transmittance last significant digit is 1%. A transmittance difference of 0.5% implies a

   $\Delta T_w = 0.2^0C$

   (c) Due to temperature induced changes in the surface emittance - unknown in nature

   (d) Due to improper focusings - practically zero.

   (e) Due to the AGA infrared camera accuracy $\Delta T_w = 0.2^0C$

   Therefore:

$$\Delta T_w = \sqrt{0.9^2 + 0.2^2 + 0.2^2} = 0.9^0C$$

2. Mean jet velocity assumed at a certain point (pixel)

   (a) Due to uncertainty in total pressure and temperature measurements ahead of the sonic nozzle:

   Δu = 0.09 m/sec.

   Note: The total temperature induced error is 2 orders of magnitudes lower than that induced by the pressure error. The pressure error has three contributions:

   i) reading accuracy ± 1 psig

   ii) pressure fluctuations ± 1 psig

   iii) Gage accuracy assumed a 3% i.e., ± 0.9 psig.

   Altogether this accounts for ± 1.68 psig.

   (b) Due to uncertainty in the nozzle's discharge coefficient 1%:

   Δu = 0.02 m/sec

   (c) Due to the camera's resolution (translates into half a pixel on the computer's screen)

   Δu = 0.36 m/sec

   Therefore:

   $$\Delta u = \sqrt{(0.09)^2 + (0.02)^2 + (0.36)^2} = 0.37 \text{ m/sec}$$

3. (a) Error in the calculated temperature profile due to velocity uncertainities: ±1% from the absolute temperature in deg K.

   (b) Error in deduced velocity from temperature measurements: ±15% from the local velocity.

The error in the calculated temperature was estimated with data from experiment #3 with $\Delta u = 0.37$ m/sec. The error in the deduced velocity was estimated in the same way with $\Delta T_w = 0.9K$.

4. The relatively high errors encountered in this experiment should be credited in their greatest part to the purpose of the experiment, that was to evaluate to what extent the IR imaging system can detect relatively high temperature changes that occur over a small portion of the camera field of view. When viewed in this light, the system's performance is quite satisfactory. This fact can be better understood by reconsidering the magnitude of the error induced by the uncertainty in determining the exact location of the measured spot (the "half pixel" uncertainty, see item above). If, for example, the jet would have been mapped along the whole width of the field of view of the IR imaging camera, this error could be reduced by an order of magnitude. This of course, would require a different objective lens.

5. The error in determining the velocity distribution in the core flow of the jet varied between 2.8% on the centerline and 12.5% near the wall. According to the manufcturer's specifications, the Pitot static tube may induce an error of ±2%. The rest of the error originates in the accuracy of reading of the difference between the water columns in the U-shaped manometer (±0.5 mm).

A2: Miscellaneous Calculations

(1) Radiation losses estimation:

$\alpha = \varepsilon = 0.05$

$$E = \varepsilon\sigma(T_w^4 - T_a^4)A = 0.05 \times 5.668 \times 10^{-8} \ (373^4 - 293^4) \cdot \pi \cdot 7.62 \times 10^{-5} \times 1.0$$

$= 0.008$ w/m length of wire.

(2) Conduction losses estimation (per pixel distance) for

$\dot{q}_{elec} = 9.33$ w/m (maximum heating rate):

1 pixel at 0.5 m focus = 1.154 mm.

$$\dot{Q} = -kA[\text{grad } T_{x_2} - \text{grad } T_{x_1}] \cdot \frac{1}{\Delta x_{1-2}}$$

$$T(^0C) = 78.1 - 10.2 \cos[\frac{x(mm)}{12.694} \pi]; \qquad (r^2 = 98.3\%; \quad \sigma = 1K)$$

$$\text{grad } T = 10.2 \ (\frac{\pi}{12.694 \times 10^{-3}}) \ \sin[\frac{x(mm)}{12.694} \pi] \ (K/m)$$

$$\dot{\Delta Q}_{\substack{\text{conduction} \\ \text{max}}} = 50 \cdot \frac{\pi}{4} [7.62 \times 10^{-5}]^2 \times 10.2 \frac{\pi}{12.694 \times 10^{-3}} [0.989 - 0.910] \frac{1}{1.154 \times 10^{-3}}$$

$= 3.97 \times 10^{-2}$ w/m length of wire

(3) The free convection estimations were based on Kays and Crawford (1980) p. 328:

$$Nu = 0.518 \ [1 - (\frac{0.599}{Pr})^{0.6}]^{-5/12} \ (Gr_D \ Pr)^{1/4} \qquad (A.1)$$

with the correction for thick boundary layer compared to the cylinder diameter

$$\bar{Nu} = \frac{2}{\ln (1 + 2/Nu)} \qquad (A.2)$$

The transcendental Eqs. for ΔT assuming $\overline{T_f}$ = 323K is

$$\Delta T = 887\, i^2 \ln\left[1 + \frac{2}{0.029(\Delta T)^{0.25}}\right] \qquad (A.3)$$

where i the electrical current in Amperes.

(4) The coefficient of determination r^2 (adjusted for degrees of freedom) is given by:

$$r^2 = 1 - \frac{\text{Sum of squares of the residuals } /(n-p)}{\text{Sum of squares of the total values } /(n-1)} \qquad (A.4)$$

where n is the degrees of freedom and p is the number of the coefficients fit in the regression equation.

(5) Calculation of the predicted wire temperatures in Figs. 4.6 and 4.7 and of the deduced velocity profiles in Figs. 4.10, 4.11 and 4.12.

The correlation (Eq. 4.1)

$$Nu = 0.795\, Re^{0.384} \qquad (A.5)$$

can be explicitly written

$$\frac{h\,d}{k_a} = 0.795 \left(\frac{U\,d}{\nu_a}\right)^{0.384} \qquad (A.6)$$

where h is the heat transfer coefficient, d is the wire diameter, k_a is the conductivity of the air, U is the local velocity of the air and ν_a is the kinematic viscosity of the air.

Defining $\Delta T = T_{wire} - T_{air}$

and

$$h = \frac{\dot{q}}{A\Delta T}$$

where $\dot{q}$ is the heat generated per unit length of wire ($\dot{q} = i^2R$) and $\dot{A}$ is the circumferential area of the wire per unit length ($A = \pi d$), one gets

$$\Delta T = \frac{\dot{q}}{0.795\pi\, k_a} \left(\frac{\nu_a}{d}\right)^{0.384} U^{-0.384} \qquad (A.7)$$

This formula was used as is to deduce air velocities from the wire temperature measurements (Figs. 4.10-4.12). To predict the wire temperatures in Figs. 4.6 and 4.7, the velocity profile was assumed to have a parabolic distribution:

$$U(r) = U_{max}\left[1-\left(\frac{r}{R}\right)^2\right] \qquad (A.8)$$

where U_{max} is the centerline velocity of the air in the pipe and has twice the value of the mean velocity.

A3: Approximating Functions for the Wire Temperature Distributions

Assuming a cosine function approximation for the temperature variation along the wire, with the maximum temperatures occurring at $X = 0, \ell$ (0 and 2π radians respectively), and the minimum at $X = \ell/2$ ($\pi/2$ radians), the temperature profile can be approximated by:

$$T(x) = 0.5\left[(T_{max} + T_{min}) + (T_{max} - T_{min})\cos\frac{2\pi x}{\ell}\right] \qquad (A.9)$$

In Figs. 4.6 and 4.7, zero radians correspond to pixel #-11, π radians to pixel #0, and 2π radians to pixel #11. Therefore

$$\text{grad } T(x) = -(T_{max} - T_{min})\frac{\pi}{\ell}\sin\frac{2\pi x}{\ell} \qquad (A.10)$$

The evaluation for the four experiments is given in Table A.1 below.

Table A.1 Approximating functions for the wire temperature distribution and temperature gradient

Experiment #	$\dot{q}$ w/m	T(X) °C	grad T(X) K/m
1	3.47	$43.6 + 4.6 \cos \frac{2\pi x}{\ell}$	$- 1138.4 \sin \frac{2\pi x}{\ell}$
2	4.71	$53.4 + 5.3 \cos \frac{2\pi x}{\ell}$	$- 1311.7 \sin \frac{2\pi x}{\ell}$
3	6.17	$61.7 + 7.7 \cos \frac{2\pi x}{\ell}$	$- 1905.6 \sin \frac{2\pi x}{\ell}$
4	9.33	$77.7 + 9.5 \cos \frac{2\pi x}{\ell}$	$- 2351.1 \sin \frac{2\pi x}{\ell}$

ℓ = 0.0254 m
Δx = 0.001154 m (1 pixel)

Appendix B

APPENDIX TO CHAPTER 5: THE FLAT PLATE EXPERIMENT

B1: Error Calculations

1.1 Surface temperature read-outs from Disco II (software package for IR data reduction)

(a) Due to uncertainty of the ambient temperature, practically zero ($\Delta T_\infty << \Delta T_w$).

(b) Due to uncertainty of emittance value.

$$\Delta\varepsilon = 0.02 \qquad \Delta T_w = 0.6^0C$$

(c) Due to temperature induced changes in the surface emittance - unknown in nature.

(d) Due to unproper focusing - practically zero.

(e) Due to the AGA camera resolution

$$\Delta T_w = 0.2^0C$$

(f) Due to error in location

$$\Delta T_w = 0.15^0C$$

Therefore,

$$\Delta T_w = \sqrt{0.6^2 + 0.2^2 + 0.15^2} = 0.65^0C$$

1.2 Error of the slope of θ vs $x^{1/2}$ (mean value)

$$\Delta \frac{d\theta}{d(x^{1/2})} = \frac{2x\ 0.65}{0.4 - 0.2} = 6.5\ \frac{^{0}C}{m^{1/2}}$$

1.3 Error of velocity measurement

Estimated at 2%

$$\Delta U = 21 \times 0.02 = 0.42\ m/sec$$

1.4 Error in the (calculated) convected heat flux (worst case);

$$\dot{q}''_o = \frac{d\theta}{d(x^{1/2})} \frac{k\ Pr^{1/3}\ U^{1/2}}{2.2019\ \nu^{1/2}}$$

$$\Delta\dot{q}''_o = \frac{k\ Pr^{1/3}}{2.2019\ \nu^{1/2}} \{U^{1/2} \cdot \Delta\left(\frac{d\theta}{d(x^{1/2})}\right) + \frac{d\theta}{d(x^{1/2})} \frac{1}{2\ U^{1/2}} \Delta U\}$$

$$= \frac{0.02709 \cdot 0.709^{1/3}}{2.2019 \cdot (16.95 \times 10^{-6})^{1/2}} (20.9^{1/2} \cdot 6.5 + \frac{50.07}{2 \cdot 20.9^{1/2}} \cdot 0.42)$$

$$= 2.66\ (29.72 + 2.3) = 85.2\ \frac{W}{m^2}$$

This is about one fifth of the mean convected heat-flux value and it comes almost entirely from the error in temperature measurements, which originate in the uncertainty of the emittance value (see items 1.1 and 1.2 above). This is a well known difficulty and is discussed in Sparrow and Cess (1978).

B2: Miscellaneous Calculations

1. Determination of the temperature distribution along a flat plate in the laminar boundary layer regime with constant heat flux, equation (5.1).

Starting from equation (9-39) in Kays and Crawford (1980)

$$T_o(x) - T_\infty = \frac{0.623}{k} Pr^{-1/3} Re^{-1/2} \int_0^x \left[1 - \left(\frac{\xi}{x}\right)^{3/4}\right]^{-2/3} \dot{q}_o''(\xi)\, d\xi \qquad (B.1)$$

for $\dot{q}_o''(\xi) = \text{const}$, and with $y = \frac{\xi}{x}$; $dy = \frac{1}{x} d\xi$ the integral becomes

$$x \int_0^1 \left(1 - y^{3/4}\right)^{-2/3} dy \qquad (B.2)$$

Now $z = y^{3/4}$ and $dz = \frac{3}{4} y^{-1/4} dy \rightarrow dy = \frac{4}{3} dz \left(y^{1/4}\right)$ and the integral becomes

$$x \int_0^1 (1 - z)^{-2/3} \cdot \frac{4}{3} z^{1/3} dz \qquad (B.3)$$

Since $\beta_1(m,n) = \int_0^1 z^{m-1}(1-z)^{n-1} dz = \beta_1(m,n) = \frac{\Gamma(m) \cdot \Gamma(n)}{\Gamma(m+n)}$, we get for the integral

$$\frac{4x}{3} \int_0^1 (1 - z)^{\frac{1}{3} - 1} z^{1\frac{1}{3} - 1} dz \qquad n = \frac{1}{3} \qquad m = 1\frac{1}{3} \qquad (B.4)$$

Since $\Gamma(n + 1) = n\,\Gamma(n) \rightarrow \Gamma(\frac{1}{3}) = 3\Gamma\left(1\frac{1}{3}\right)$, we get

$$\frac{4x}{3} \frac{3\Gamma(1\frac{1}{3})\ \Gamma(1\frac{1}{3})}{\Gamma\left(1\frac{2}{3}\right)} = \frac{4x}{3} \frac{3\left[\Gamma(1\frac{1}{3})\right]^2}{\Gamma(1\frac{2}{3})} = \frac{4x}{3} \frac{3(0.89338)^2}{0.90330} = 3.5343X \qquad (B.5)$$

Inserting this value for the integral in (B.1) and defining $\Theta(x) = T_o(x) - T_\infty$ one gets

$$\Theta(x) = 2.2019 \frac{\dot{q}_o''}{k} x\, Pr^{-1/3} Re^{-1/2} \qquad (B.6)$$

which is precisely equation (5.1).

2. Calculation of the velocity boundary layer thickness.

Following Schlichting, (1968) p. 26, the laminar velocity boundary layer thickness can be well approximated by

$$\delta = 5\ Re_x^{-1/2}\ x \text{ or}$$

$$\delta = 5\left(\frac{\nu}{u}\right)^{1/2} x^{1/2}$$

The numerical value for this experiment was calculated according to

$$\delta(m) = 0.004375\ [x(m)]^{1/2} \tag{B.7}$$

NASA

Report Documentation Page

1. Report No	2. Government Accession No.	3. Recipient's Catalog No.
NASA CR-181839		

4. Title and Subtitle

Low-Speed Flowfield Characterization by Infrared Measurements of Surface Temperatures

5. Report Date

May 1989

6. Performing Organization Code

7. Author(s)

E. Gartenberg, A. S. Roberts, Jr., and G. J. McRee

8. Performing Organization Report No.

10. Work Unit No.

505-61-01

9. Performing Organization Name and Address

Old Dominion University Research Foundation
P. O. Box 6369
Norfolk, VA 23508

11. Contract or Grant No.

NAG1-735

13. Type of Report and Period Covered

Contractor Report
1987-1989

12. Sponsoring Agency Name and Address

National Aeronautics and Space Administration
Langley Research Center
Hampton, VA 23665-5225

14. Sponsoring Agency Code

15. Supplementary Notes

Langley Technical Monitor: Debra L. Carraway
Final Report

16. Abstract An experimental program was aimed at identifying areas in low speed aerodynamic research where infrared imaging systems can make significant contributions. Implementing a new technique, a long electrically heated wire was placed across a laminar jet. By measuring the temperature distribution along the wire with the IR imaging camera, the flow behavior was identified. Furthermore, using Nusselt number correlations, the velocity distribution could be deduced. The same approach was used to survey wakes behind cylinders in a wind-tunnel. This method is suited to investigate flows with position dependent velocities, e. g., boundary layers, confined flows, jets, wakes and shear layers. It was found that the IR imaging camera cannot accurately track high gradient temperature fields. A correction procedure was devised to account for this limitation. Other wind-tunnel experiments included tracking the development of the laminar boundary layer over a warmed flat plate by measuring the chordwise temperature distribution. This technique was applied also to the flow downstream from a rearward facing step. Finally, the IR imaging system was used to study boundary layer behavior over an airfoil at angles of attack from zero up to separation. The results were confirmed with tufts observable both visually and with the IR imaging camera.

17. Key Words (Suggested by Author(s))

Infrared Imaging
Boundary Layer
Jets
Wakes
Separation

18. Distribution Statement

Unclassified - Unlimited

Subject Category 35

19. Security Classif. (of this report)	20. Security Classif. (of this page)	21. No. of pages	22. Price
Unclassified	Unclassified	140	A07